

# 13

## Photoinduced Electron Transfer in Zeolites

Kyung Byung Yoon

Sogang University, Seoul, Korea

### I. INTRODUCTION

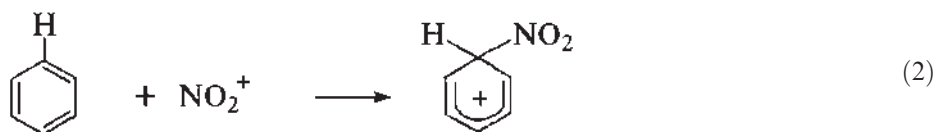
According to the long-inherited cosmological view of the Orient, the universe consists of yin (–) and yang (+) (1). They refer to entities that are richer in “negative spirits” and their counterparts that are richer in “positive spirits.” The knowledge of chemistry that has been accumulated during the last two centuries has also verified that matter consists of the two: those that are richer in negative-charge density and their counterparts that are richer in positive-charge density. In other words, matter consists of the two that are richer and poorer, respectively, in electron density. Accordingly, matter now can be categorized as electron richer or electron poorer. Consistent with this, in chemistry, compounds have commonly been divided into *bases* and *acids*, *nucleophiles* and *electrophiles*, and *reductants* and *oxidants* (2).

At first glance, the above three pairs of terms do not appear to be intimately interrelated since they have stemmed from three different views of chemical interactions among compounds. In fact, they describe a common classification in which the former represent relatively electron richer and the latter relatively electron poorer ones, respectively. The former are more generally categorized as electron donors (D) because they all donate electrons to the corresponding counterparts at the time of interaction. The latter are then categorized as electron acceptors (A). Consistent with the yin-yang theory, we can now say that matter consists of the two, i.e., D and A. It is then amazing to realize that a great part of chemistry deals with the physical and chemical interactions between D and A. Hence, categorization of compounds into D and A and investigation of the nature of interaction between them are the two most important steps toward understanding and subsequently applying chemistry.

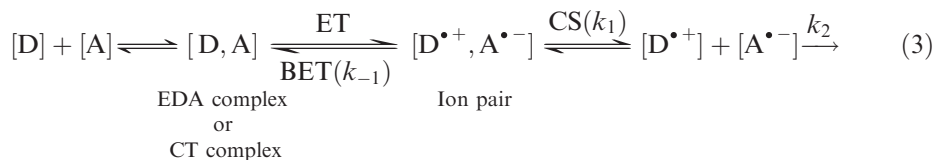
One of the two most important chemical interactions between D and A is the adduct formation, which is best represented by formation of water from hydroxide (D) and proton (A) [Eq. (1)]:



Formation of a Wheland intermediate between benzene (D) and nitronium ion ( $\text{NO}_2^+$ , A) during the initial step of nitration of benzene [Eq. (2)] is another good example for this type chemical interaction between D and A.



The other important type of reactions between them, which is of prime concern in this chapter, is electron transfer (ET) between the two interacting counterparts, the process of which can be generally described according to the following scheme:



where [D, A] represents the electron donor–acceptor (EDA) or the charge-transfer (CT) complex formed from D and A. The name of EDA complex was coined by Hildebrand (3), whereas that of CT complex was coined by Mulliken (4). The formation of CT complex may be omitted from the above formulation when the thermodynamic equilibrium is unfavorable for the complex formation or when the lifetime of the complexed state is very short.  $[\text{D}^{\bullet+}, \text{A}^{\bullet-}]$  represents the corresponding ion pair generated as a result of transfer of an electron from D to A. The ion pair is also often called as radical ion pair when unpaired electrons are generated in the ions, geminate ion pair to emphasize ion pairing, or intimate or contact ion pair to emphasize the close contact between the two components in the ion pair. The constant  $k_1$  represents the rate constant for the spatial separation of the ion pair into individual ions,  $[\text{D}^{\bullet+}]$  and  $[\text{A}^{\bullet-}]$ , the process of which is commonly called charge separation (CS). BET ( $k_{-1}$ ) represents back electron transfer from the ion pair back to the original CT complex with the corresponding rate constant of  $k_{-1}$ , and  $k_2$  represents the rate constant for the product-forming follow-up reaction. BET is also called charge recombination.

The ET process may occur by either thermal or photochemical activation of the corresponding CT complex. When light energy is introduced into the system to induce ET the process is called photoinduced ET (PET). Regardless of the nature of energy, ultrafast laser photolysis has provided experimental proof that the overall efficiency of the energy introduced into the system to carry out the reaction beyond ET up to the follow-up product-forming steps *via* CS depends on the ratio of  $k_1$  to  $k_{-1}$ . Thus, if the BET rate ( $k_{-1}$ ) is substantially faster than the CS rate ( $k_1$ ), a large portion of the energy introduced into the system to generate  $[\text{D}^{\bullet+}, \text{A}^{\bullet-}]$  becomes wasted. This is why great efforts have been directed to developing methods to slow down or to gain control over the energy-wasting BET process (5,6). In particular, in the case of PET, elongation of the lifetime of the charge-separated states (CSSs),  $[\text{D}^{\bullet+}] + [\text{A}^{\bullet-}]$ , is essential to provide the separated ion pair more time or more chance to undergo the follow-up productive pathways, as a means to increase the efficiency and economy of the introduced light energy.

According to the original formulation of Mulliken's CT theory, the ground- and excited-state wave functions (denoted as  $\Psi_G$  and  $\Psi_E$ , respectively) for a D and A complex [D, A] are expressed according to Eqs. (4) and (5):

$$\Psi_G = a\psi_0[\text{A}, \text{D}] + b\psi_1[\text{A}^- - \text{D}^+] + \dots \quad (4)$$

$$\Psi_E = a^*\psi_1[\text{A}^- - \text{D}^+] - b^*\psi_0[\text{A}, \text{D}] + \dots \quad (5)$$

where  $\psi_0[A, D]$  represents the “no-bond” wave function of D and A, and  $\Psi_1[A^- - D^+]$  represents the dative wave function representing ET from D to A (4). The relationships among the coefficients are  $a \gg b$  and  $a^* \gg b^*$ . Thus, the degree of ET from D to A for a CT complex in the ground state is very small ( $a \gg b$ ). Accordingly, there exists only a weak bonding between D and A in the ground state, and the intermolecular distance between D and A is rather long, approaching the van der Waals intermolecular distance. In contrast, in the excited state, the degree of ET is very large ( $a^* \gg b^*$ ) and, as a result, a strong bonding prevails between the two components in the ion pair, and the intermolecular distance between D and A is substantially shorter than the van der Waals intermolecular distance.

It is also often said that a charge is transferred from D to A or A to D on going from the ground state to the excited state or from the excited state to the ground state. Here, the term “charge” stands for either electron or hole. It means that an electron (a negative charge) is transferred from D to A, while a hole (a positive charge) is transferred simultaneously from A to D. In this regard, Mulliken named such intermolecular complexes whose nature of interaction can be described by Eqs. (4) and (5) as CT complexes (4). To be more specific, however, the use of either electron or hole instead of charge is more desirable.

For PET to take place in a CT complex the ground state should absorb the light whose energy corresponds to the difference in the energy between the ground and excited states. Accordingly, CT complexes show new absorption bands that usually appear in the UV and visible region, in addition to the intrinsic (local) absorption bands of D and A. For a CT complex, the local absorption bands of D and A are nearly identical to those of D and A in their isolated forms (before mixing) since D and A are minimally perturbed in the ground state even after complexation [note  $a \gg b$  in Eq. (4)]. Thus, PET takes place in a CT complex upon absorption of light and the resulting ion pair usually undergoes very fast BET leading to the ground, charge-recombined state.

The ET reactions may take place in the gas and solid phases but more often in solution. In such circumstances where ET reactions proceed in solution, each chemical species is surrounded by a set of solvent molecules. The sets of solvent molecules intimately surrounding the D and A or other solute molecules are commonly called solvent cages, denoted by square brackets in Eq. (3). From the understanding that the nature of solvent cages sensitively affect the efficiency and selectivity of ET reactions, considerable effort has been made to elucidate the effect of solvent cages on each process of Eq. (3), particularly the BET process. However, without knowing the exact structures and compositions of the surrounding solvent cages, it is difficult to gain insights into the effect of the solvent cages on each process of Eq. (3). Because of this, major advances in the control of efficiency and selectivity of PET have mostly been achieved from the heterogeneous media by exploiting supramolecular properties of various organized media (6). In particular, zeolites and the related microporous materials have received great attention as versatile organizing media for various PET reactions since they provide well-defined pores with highly versatile yet regular sizes in molecular dimension and shapes (7). In this respect, zeolite cages and pores are very much akin to solvent cages. However, despite the conceptual similarity between the zeolite pores and the solvent cages, there are unique features that only zeolite pores can provide. First, zeolite pores are very rigid and distinctively shaped in contrast to the relatively soft and featureless solvent cages. Second, the rigidity of the molecular pockets provides a unique ability to separate the D-A pairs within well-defined distances, which is obviously not possible in solution. Third, zeolite pores can compartmentalize or entrap highly reactive species that are vulnerable to

association by themselves or to attack by other reactive species in solution, thus offering them the opportunities to serve as unique media to isolate, immobilize, characterize, and utilize the entrapped highly reactive species. Fourth, the negatively charged surfaces of aluminosilicate frameworks provide polar environments, the degree of which can be further modified by varying the number and type of charge-compensating cations *via* conventional ion exchange. Fifth, the pore sizes of zeolites can be finely tuned by ion exchange with cations of various sizes and by controlling the degree of hydration. The above reasons explain why zeolites and the related microporous materials have received great attention as the prototypical spatially organizing media for a variety of photo-induced electron transfer (PET) and photochemical reactions. Furthermore, the zeolite frameworks are not mere compartmentalizing inert solid supports but in fact can actively participate as D depending on the composition of the framework and the type and number of the charge-balancing cations (8–17). By the same context, the charge-balancing cations also frequently serve as either D or A. The ability of the frameworks and charge-balancing cations to participate in the PET reactions makes the zeolites even more versatile media for a variety of PET reactions that take place within and across the zeolite frameworks.

A great deal of novel information about PET reactions has been elucidated during the course of the reactions in and across the zeolite pores due to the aforementioned unique features of zeolites. In return, novel insights into the properties of zeolite frameworks and charge-balancing cations have been gained throughout the studies. This chapter covers interesting features for a variety of PET reactions in and across zeolites that have been explored during the last several decades. The zeolites that frequently appear in this chapter are zeolite Y, zeolite X, zeolite L, mordenite, mazzite, ZSM-5, and zeolite A. For simplicity they are simply termed Y, X, L, M,  $\Omega$ , ZSM-5, and A, respectively. When necessary, the zeolites are also represented as  $M^{n+}Z$  when  $M^{n+}$  represents the charge-balancing cation or the cation of prime concern, and Z represents the type of zeolite.

## II. PHOTOINDUCED ELECTRON TRANSFER BETWEEN INTERCALATED SPECIES

As mentioned earlier (p. 593), the CT absorption band of a CT complex stems from the transition of the complex from the ground state to the excited state by the action (absorption) of light, with the wavelengths corresponding to the CT energy (4). Since the ground and excited states of a CT complex are essentially composed of a pair of D and A and a pair of  $D^+$  and  $A^-$ , respectively [see Eqs. (4) and (5)], the absorption of light by the CT complex at the wavelengths within the CT envelope gives rise to ET from D to A. In other words, PET takes place from D to A within a CT complex upon absorption of light at the CT band. Irradiation of a CT complex at the CT band is also commonly referred to as CT excitation.

A large number of CT complexes remain intact even after repeated, deliberate CT excitation with intense laser beams. This happens when the BET process undergoes very rapidly so that  $k/k_{-1}$  in Eq. (3) reaches zero. In such cases, the light energy absorbed by the system is wasted. Interestingly, however, zeolite matrices have been shown to possess remarkable abilities to retard the BET process, hence to elongate the lifetime of the CSS. Furthermore, the study of the effect of zeolite matrices on the BET process has provided insights into the development of the general methods to increase the lifetime of the CCS applicable to other media.

## A. PET Between Intercalated Species via Charge-Transfer Complexation

Several types of CT complexes between the intercalated species have been assembled in zeolites and their time-resolved BET rates have been measured after laser pulse-induced CT excitation. The intercalated species include all of the species other than the framework, such as charge-balancing cations, neutral guests, and salts. Since the position and the intensity of the CT absorption band and the dynamics of the BET process are sensitively governed by the environment, the zeolite-encapsulated CT complexes also serve as sensitive probes for elucidating novel properties about the zeolite frameworks, charge-balancing cations, nature of interaction between the framework and the cation, and micropolarity. It has also been shown that the CT absorption bands of hydrocarbon–O<sub>2</sub> CT complexes undergo remarkable red shifts to the visible region as a result of the highly polar environment of zeolite pores. This has provided valuable opportunities to produce useful oxygenated hydrocarbons in high selectivity by visible CT excitation. This section summarizes assembly and characterization of several CT complexes in zeolite pores, their dynamic BET processes, and their utilization as useful probes for elucidation of useful informations about zeolites.

### 1. Arene-Pyridinium (Py<sup>+</sup>) CT Complexes

#### a. Assembly and Characterization

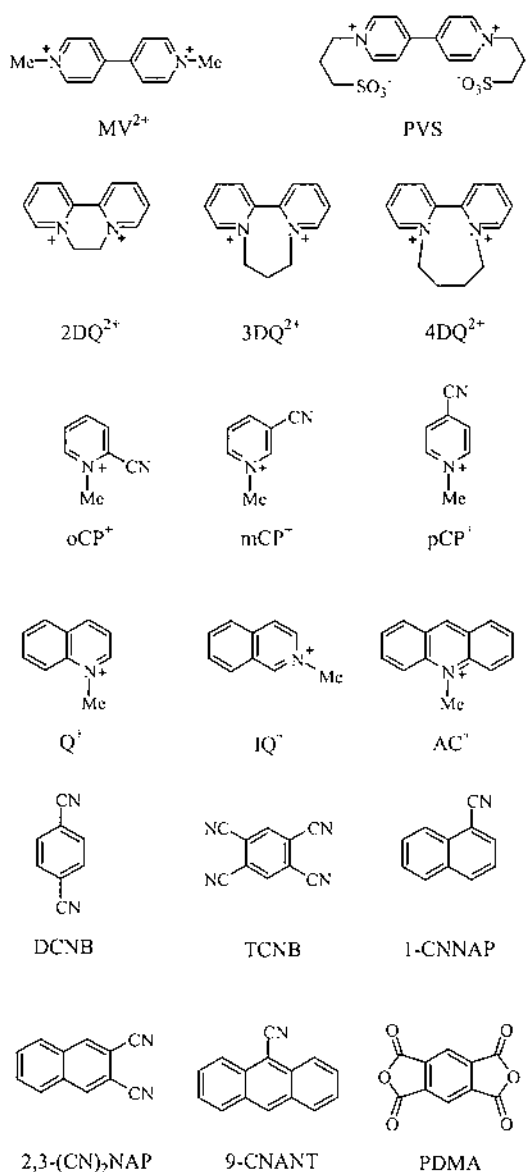
Various pyridinium derivatives that frequently appear in this chapter are listed in Fig. 1. For convenience they are representatively termed as “pyridinium” and designated as Py<sup>+</sup> throughout in this chapter. They have been shown to form CT complexes [Eq. (6)] with various electron donors such as arenes (ArH), halides (X<sup>-</sup>), and anionic metal complexes such as MCl<sub>4</sub><sup>2-</sup> (M = Mn, Fe, Zn).



As a primary step to assemble arene-Py<sup>+</sup> CT complexes in zeolites Py<sup>+</sup> ions are first introduced into zeolites by aqueous ion exchange of charge-balancing cations of zeolites (usually Na<sup>+</sup>) (18). The fact that Py<sup>+</sup> ions are positively charged is beneficial because this ensures their incorporation into the void space of the negatively charged framework. The maximal amount of each Py<sup>+</sup> ion incorporated into several zeolites is given in Table 1. As can be imagined, the maximum increases as the size of the zeolite pore increases and that of the acceptor cation decreases. For Y, which has the largest pores among those listed in Table 1, the incorporated number reaches up to three per supercage for medium-sized acceptors such as mCP<sup>+</sup>, Q<sup>+</sup>, and iQ<sup>+</sup>. In the channel-type zeolites the amount of incorporated acceptor corresponds to about one or less per 7.5-Å channel. Since Py<sup>+</sup> acceptors cannot pass through the aperture of A, the small exchanged amounts represent those that are exchanged onto the external surfaces of the zeolite crystals. In order to secure some empty space available to the subsequently incoming ArH donors, it is desirable to limit the amount of each Py<sup>+</sup> ion to about one per supercage of Y or per 15 Å of each channel of M, L, and Ω. The acceptor-incorporating Y zeolites are denoted as Py<sup>+</sup>(*n*)Y, where the number in the parenthesis represents the average number of the acceptor ion within a supercage of Y. For instance, MV<sup>2+</sup>(1.0)Y stands for zeolite Y incorporating one MV<sup>2+</sup> ion (average) per supercage.

Figure 2 shows a pictorial representation (cartoon) of a methyl viologen (MV<sup>2+</sup>) ion incorporated in a supercage of Y (A) and a channel of L (B, C), respectively. They show that the supercage of Y and the channel of L are spacious enough to accommodate an MV<sup>2+</sup> ion (~13 Å long). To allow access of relatively nonpolar arene donors to the

remaining space, the highly polar pore-filling water molecules should be removed by evacuation at elevated temperatures. Usually the dehydration temperatures should not exceed  $\sim 200^{\circ}\text{C}$ , above which either direct ET from the framework to the acceptor or thermal decomposition of the organic cations begins to take place. The dehydration temperature should be even lower when the loading level of the acceptor ion increases, for reasons to be discussed later (p. 616). Since the temperatures below  $300^{\circ}\text{C}$  are usually not high enough for complete dehydration, it is nearly impossible to obtain rigorously dried  $\text{Py}^+$ -incorporating zeolites. Thus, there are some residual water molecules in the  $\text{Py}^+$ -incorporating zeolites. Nevertheless, the acceptor-incorporating zeolites dehydrated at



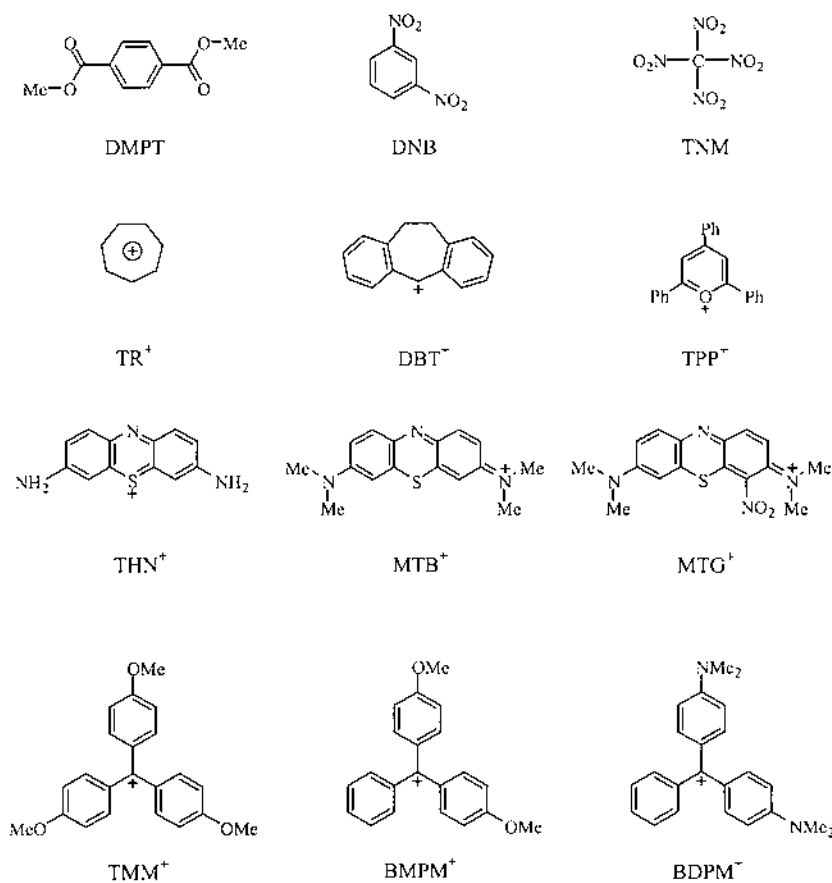


**Fig. 1** Electron acceptors, photosensitizers, and their abbreviations that frequently appear in this chapter.

**Table 1** Maximal Number<sup>a</sup> of Py<sup>+</sup> Acceptors that can be Exchanged into Zeolites<sup>b</sup>

Acceptor	M (6.5 × 7.0) <sup>c</sup>	L (7.1) <sup>c</sup>	Ω (7.4) <sup>c</sup>	Y (7.4) <sup>c</sup>	A (4.2) <sup>c</sup>
pCP <sup>+</sup>	1.2	1.7	0.9	2.4	0.1
oCP <sup>+</sup>	1.2	1.1	1.0	2.3	0.1
mCP <sup>+</sup>	1.2	1.3	1.1	3.1	0.1
MV <sup>2+</sup>	0.9	1.0	0.7	2.1	0.2
DQ <sup>2+</sup>	0.8	0.8	0.6	2.1	0.1
Q <sup>+</sup>	0.6	1.3	0.8	2.9	0.0
IQ <sup>+</sup>	0.4	1.3	0.9	3.1	0.1
Ac <sup>+</sup>	0.2	0.3	1.0	1.9	0.2

<sup>a</sup> Per 7.5-Å channel (M, L, and Ω) or per supercage (Y and A).

<sup>b</sup> From aqueous solutions of halide salts, respectively.

<sup>c</sup> Pore size in angstroms.

Source: Data from Ref. 18.

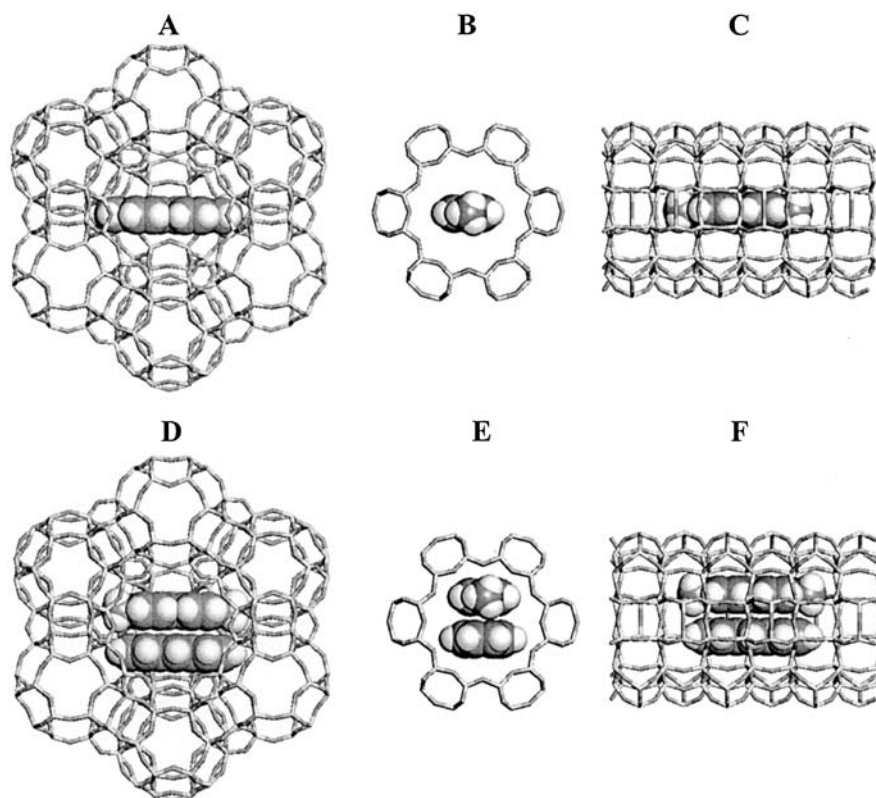


**Fig. 2** Pictorial representation of Y (A) and  $\Omega$  (B, C) incorporating an  $MV^{2+}$  ion or a pair of  $ANT-MV^{2+}$  CT complex drawn in a cofacial arrangement within a supercage of Y (D) and a channel of  $\Omega$  (E, F). (Adapted from Ref. 18a,b.)

moderate temperatures ( $< 200^\circ\text{C}$ ) are usually dry enough to carry out the follow-up incorporation of arene donors.

Incorporation of an arene donor into a dried  $\text{Py}^+$ -exchanged zeolite is usually carried out by adding an arene donor into the acceptor-doped zeolite dispersed in *n*-hexane. The arene donors and the corresponding abbreviations that frequently appear in this chapter are listed in Fig. 3. In fact, the nature of solvent greatly affects the efficiency of donor intercalation. *n*-Hexane is usually the solvent of choice for effective intercalation of arene donors as represented in Fig. 4. Isooctane and *n*-dodecane, the branched and higher aliphatic homologues to *n*-hexane, are less effective for arene intercalation into  $MV^{2+}(1.0)Y$ , whereas they are more effective in  $\text{Na}^+ - Y$ . The solvent with the dielectric constant higher than 2 is generally not effective for incorporation of arene donors. This is understandable since the highly polar zeolite pores prefer intercalation of more polar molecules whether they are solvents or solutes. Interestingly, benzene is not effective for incorporation of arene donors into the zeolite pores despite the fact that the dielectric constants of arene donors and benzene are similar. The reason for this phenomenon may be sought from the fact that the number of benzene molecules is much higher than those of arene donors. By the same token, incorporation of arene donors into zeolites from polar solvents such as tetrahydrofuran and acetonitrile is ineffective. In this context, it is

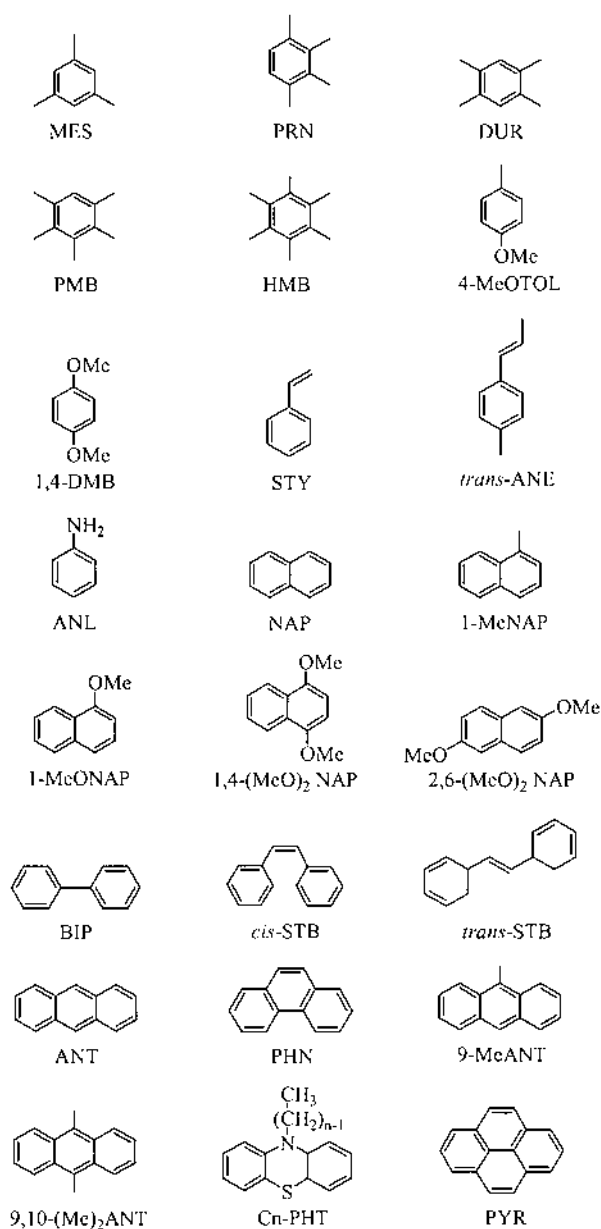


**Fig. 3** Arene donors and their corresponding abbreviations that appear in this chapter.

understandable that the moist, undried, acceptor-doped zeolites do not imbibe arene donors. The above results strongly indicate that removal of solvent molecules from zeolites and incorporation of arene substrates into zeolite pores occur simultaneously.

Intercalation of arene donors into the doped zeolites can also be effected in the complete absence of solvent. For example, the mere addition of liquid arene donors to  $\text{Py}^+$ -exchanged zeolites leads to brilliantly colored zeolites with somewhat greater intensity than those obtained from *n*-hexane solution. The direct exposure of solid arene

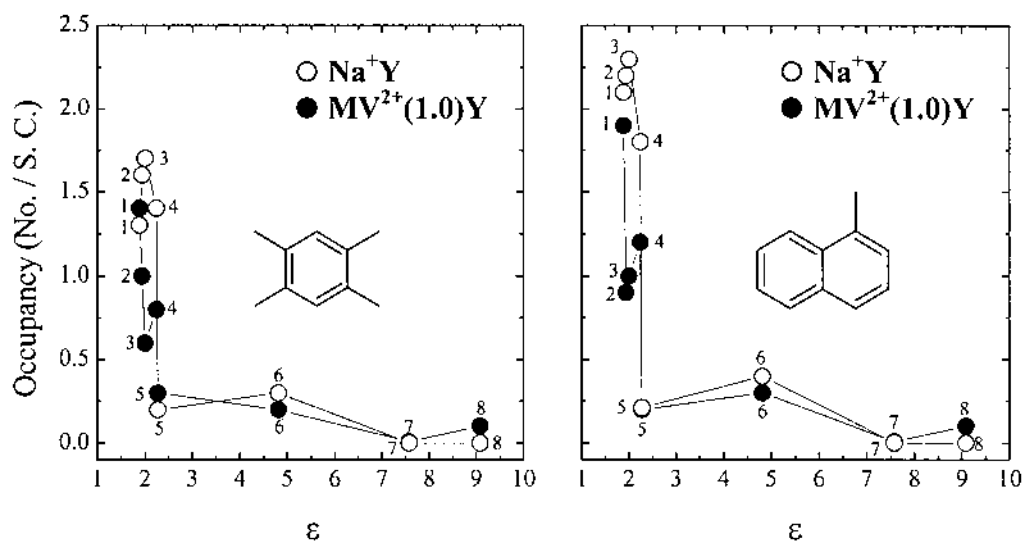


**Fig. 4** Plot of occupancy (number of molecules per supercage) of durene and 1-methylnaphthalene (as indicated) into  $MV^{2+}(1.0)Y$  (●) and  $Na^+Y$  (○), respectively, with respect to the dielectric constant of the solvent employed for arene intercalation: (1) *n*-hexane (1.89), (2) isooctane (1.94), (3) *n*-dodecane (2.01), (4) carbon tetrachloride (2.24), (5) benzene (2.28), (6) chloroform (4.81), (7) tetrahydrofuran (7.58), (8) dichloromethane (9.08). The number in parentheses after each solvent stands for the corresponding dielectric constant. (Data extracted from Ref. 18b).

crystals such as DUR, pentamethylbenzene (PMB), naphthalene (NAP), and anthracene (ANT) to the  $Py^+$ -exchanged zeolites in a closed vessel also leads to characteristic CT coloration. For those arenes that have sufficient vapor pressures at ambient temperatures, their solid-state intercalation into the  $Py^+$ -exchanged zeolites is most effective. Moreover, hexamethylbenzene (HMB), which is normally size excluded by L,  $\Omega$ , and Y in hexane solution, is slowly admitted into the  $Py^+$ -exchanged zeolites at room temperature by the solid-state mixing. This indicates that the solvent is not entirely innocent for the passage of aromatic donors into zeolite pores. Increase in the temperature generally facilitates the incorporation of arene donors into zeolite pores due to contraction of arene donors and enlargement of pore openings as a result of the increase in the rate of thermal vibration of both arene donors and zeolite frameworks. For instance, incorporation of HMB ( $\sigma \cong 8 \text{ \AA}$ ) into L,  $\Omega$ , and Y is significantly enhanced at  $80^\circ\text{C}$ . Consequently, even the aromatic donors with kinetic diameters larger than the zeolite aperture size by up to  $1 \text{ \AA}$  can have access into the pores at elevated temperatures.

The  $Py^+$ -exchanged zeolites are mostly colorless powders, except for the zeolites exchanged with 9-methylacridinium ( $AC^+$ ), which are yellow due to its intrinsic yellow color. The colorless zeolite powders in *n*-hexane slurry usually develop intense color almost instantaneously upon stirring after addition of arene donors, unless passage of the arene donor is denied by the zeolite aperture. The color varies significantly depending on the combination of the arene donor and the acceptor. For instance,  $MV^{2+}(0.8)Y$  immediately turns yellow, orange, and purple upon addition of DUR, 1-methoxynaphthalene (1-MeONAP), and 9-methylanthracene (9-MeANT) into the *n*-hexane slurry of the zeolite. The supernatant solutions remain colorless, and the subsequent quantitative analysis of the supernatant solutions by gas chromatography shows disappearance of

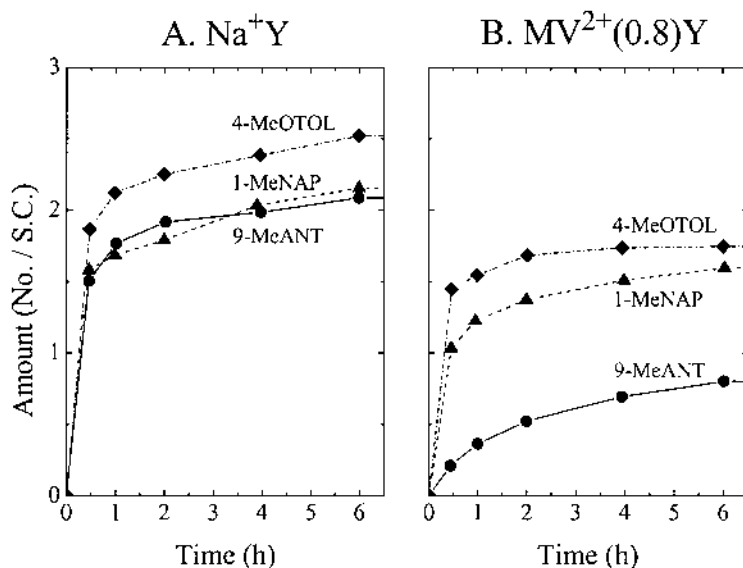


**Fig. 5** Profile of the progressive absorption of 4-MeOTOL ( $\blacklozenge$ ), 1-MeNAP ( $\blacktriangle$ ), and 9-MeANT ( $\bullet$ ) into  $\text{Na}^+\text{Y}$  (A) and  $\text{MV}^{2+}(0.8)\text{Y}$  (B) with time. (Adapted from Ref. 18b.)

arene donors in significant amounts from the solution. Solid-state NMR, UV-vis, and Fourier transform infrared (FTIR) investigation of the colored zeolites also confirm the presence of arene donors within the zeolite hosts.

In most cases, the incorporated amount of arene donors into Y exceeds one molecule per supercage within 30 min. For instance, the incorporated amount of small 4-methoxytoluene (4-MeOTOL) reaches close to two per supercage even into  $\text{MV}^{2+}(0.8)\text{Y}$  within 30 min (Fig. 5). For the relatively large 9-MeANT, its incorporation into  $\text{MV}^{2+}(0.8)\text{Y}$  is much slower and the occupancy reaches one even after 24 h of equilibration. In contrast, the occupancy of 9-MeANT into  $\text{Na}^+\text{Y}$  is comparable with that of 4-MeOTOL into  $\text{Na}^+\text{Y}$ . Thus, for a large arene donor such as 9-MeANT, the preoccupation of the supercage by a large cation such as  $\text{MV}^{2+}$  ion sensitively affects the rate and the amount of incorporation.

The formation of CT complexes is conveniently confirmed by identifying the corresponding CT (new absorption) bands that are absent from the acceptor cations, arene donors, and zeolite matrices in the diffuse reflectance UV-vis spectra. Prototypical CT spectra with  $\text{MV}^{2+}$  ion as the common acceptor are shown in Fig. 6 in the case of four different zeolite structures. The absorption maxima of various arene- $\text{Py}^+$  CT complexes, including the cases where  $\text{Py}^+ = \text{MV}^{2+}$ , are listed in Ref. 18. In accordance with the nature of CT bands, the new absorption band progressively red shifts upon increasing the number of fused rings in the homologous arene series (Fig. 6), i.e., upon decreasing the ionization potential (IP) of the arene donor or upon increasing the donor strengths of the arene donor. The CT nature of new absorption bands is usually confirmed by the linear (Mulliken) relationship (4), as typically shown in Fig. 7, established between the energy of the absorption maximum ( $h\nu_{\text{CT}}$ ) and the difference between the IP of the arene donor [ $\text{Ip}(\text{D})$ ] and the acceptor strength of  $\text{Py}^+$  ions [ $E_{\text{red}}^0(\text{A})$ ] according to the following equation, where  $W$  denotes a constant.

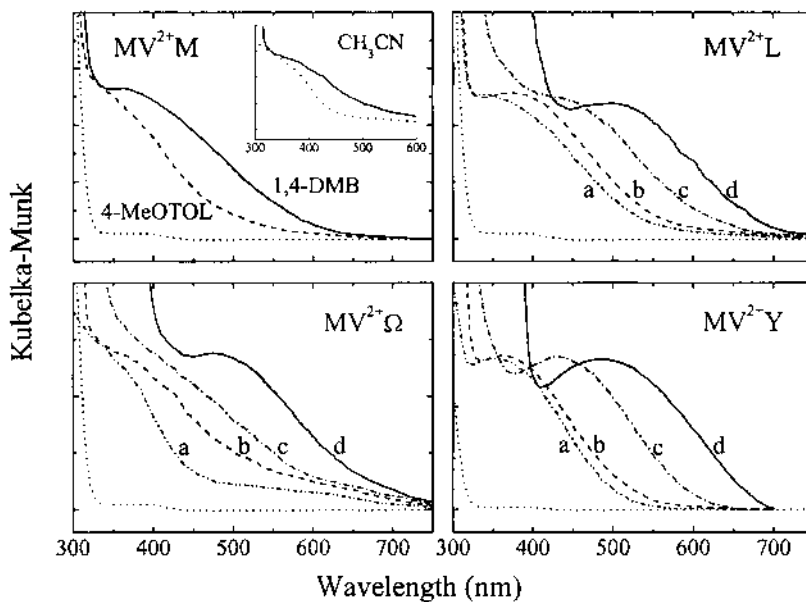


**Fig. 6** Diffuse reflectance spectra of the CT complexes of  $MV^{2+}$  with various aromatic donors with zeolites [DUR (a), PMB (b), 1-MeONAP (c), and ANT (d)]. The inset in the upper left panel presents the corresponding CT spectra in acetonitrile. The untreated  $MV^{2+}$ -exchanged zeolites (...) represent the spectral background. (Adapted from Ref. 18c.)

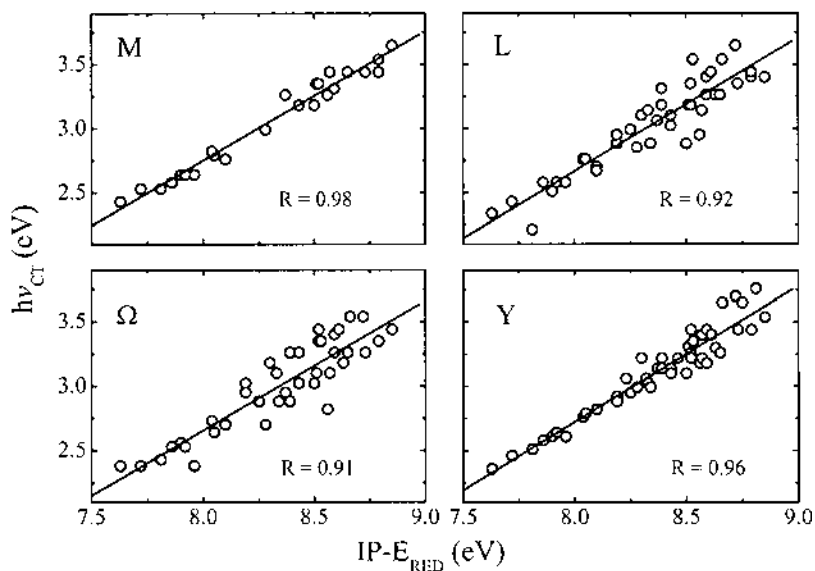


**Fig. 7** Mulliken correlations of the CT bands ( $h\nu_{CT}$ ) of various aromatic complexes with the pyridinium acceptors that are encapsulated in the zeolites (as indicated). The data for each point can be found in Ref. 18c.

$$h\nu_{CT} = I_p(D) - E_{red}^0(A) + W \quad (7)$$

The arene-Py<sup>+</sup> CT complexes are usually very weak intermolecular complexes in solution as judged by their small formation constants, which range from 0.3 to 2.8. Accordingly, isolation of single crystals of arene-Py<sup>+</sup> CT complexes from the mixtures of Py<sup>+</sup> acceptors and arene donors suitable for the analysis by X-ray single-crystal diffraction is usually difficult. Nevertheless, the obtained structure of 2,6-dimethoxynaphthalene [2,6-(MeO)<sub>2</sub>-NAP] and MV<sup>2+</sup> CT complex demonstrates the cofacial interaction between the two flat ring systems as shown in Fig. 8A. On the basis of the structure, a similar face-to-face interaction is inferred as depicted in Fig. 2D, E, and F between MV<sup>2+</sup> and ANT as the typical arene donor. Interestingly, the view of the crystal structure normal to the NAP and MV<sup>2+</sup> planes shows the “crossed” orientation between the two long axes of the ring systems as shown in Fig. 8B. Although the crossed orientation is also possible within the spherical supercages of zeolite Y, such an orientation is not feasible in the channels of L and Ω. Instead, the “collinear” or “parallel” arrangement depicted in Fig. 2F appears to be more reasonable for its structure within the narrow channels of L and Ω. Zeolites can thus provide valuable opportunities to control orientation of CT complexes that are hardly imaginable in solution.

At this stage, there are no available data regarding the formation constants of arene-Py<sup>+</sup> CT complexes in zeolite pores. The only information that is available so far is that the intensity of the CT band for MV<sup>2+</sup> complex of 1,4-dimethoxybenzene (1,4-DMB) or ANT in Y increases with increasing size of the charge-balancing cation from Li<sup>+</sup> to Cs<sup>+</sup>. This seems to be related to the progressive decrease in the pore volume of the supercage with increasing the size of the charge-balancing cation (19).

#### *b. As Visible Probes for Zeolite Properties*

**ZEOLITE SHAPE SELECTIVITY.** The intrazeolite arene-Py<sup>+</sup> CT complexes serve as effective visual probes for demonstration of zeolite shape selectivity (18). For instance, only slim para-disubstituted benzene derivatives such as 4-MeOTOL and 1,4-DMB give intense CT colors in Py<sup>+</sup>M (6.7 × 7.0 Å). Larger arene donors give rise to either very weak or no coloration. In the case of L, Ω, and Y with larger pore openings (> 7.1 Å), clear distinction is observed between the pairs of PMB/HMB, 2,6-(MeO)<sub>2</sub>NAP/1,

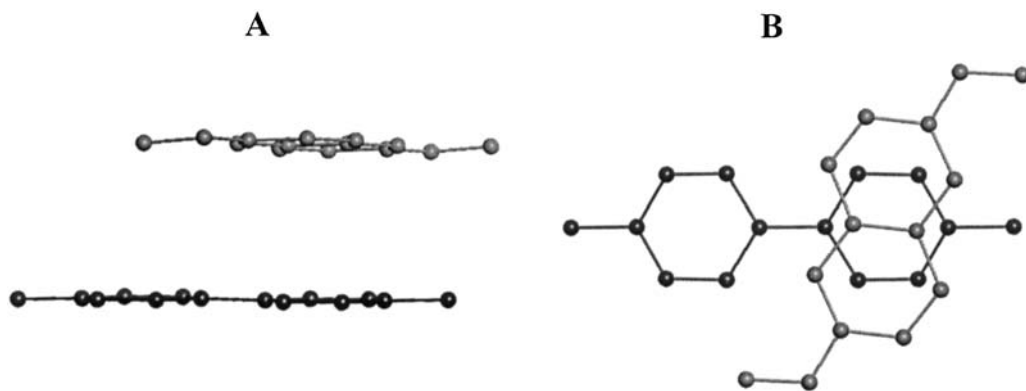
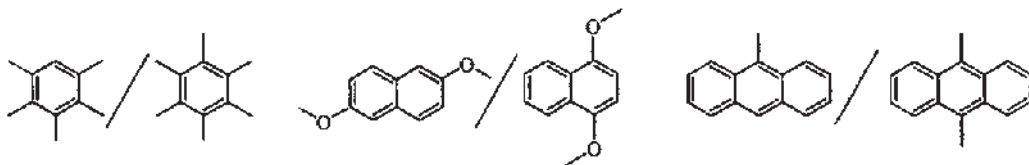


**Fig. 8** Perspective views showing the cofacial arrangement of MV<sup>2+</sup>-2,6-(MeO)<sub>2</sub>NAP complex: (A) side view; (B) top view. (Adapted from Ref. 18a,b.)

4-(MeO)<sub>2</sub>NAP, and 9-MeANT/9,10-(Me)<sub>2</sub>ANT, where the former gives intense CT colors while the latter does not.



Since only those arene donors that enter zeolite pores can develop corresponding CT colors with the preexisting acceptor cations, the mere visual observation of color development is sufficient to examine whether the arene donor can pass the zeolite or not. This result is especially useful for demonstrating the zeolite shape (size) selectivity to undergraduate students.

From the size distinction of the two closely related arenes PMB ( $\sigma=7.15 \text{ \AA}$ ) and HMB ( $\sigma=7.95 \text{ \AA}$ ) by  $\text{Py}^+$ -exchanged L,  $\Omega$ , and Y in hexane slurry, a van der Waals width of about  $8 \text{ \AA}$  is suggested to be sufficient to inhibit an arene from complex formation with acceptors in the zeolites. However, the eventual accommodation of HMB by the zeolites in the absence of solvent, in particular at  $80^\circ\text{C}$ , underscores once again the importance of thermal vibration of both the zeolite framework and the guest molecule in determining the actual size limit of the guest.

The visual observation of CT colors is also effective for the quantitative estimation of arene uptake into  $\text{Py}^+$ -exchanged zeolites (18c). Thus, for the four prototypical zeolites doped with the same amount of  $\text{MV}^{2+}$  as the common acceptor, the quantitative analysis of the uptake of 1,4-DMB (common donor) into the zeolites shows a progressive increase in the amount— $0.36 \text{ (M)}$ ,  $0.60 \text{ ( $\Omega$ )}$ ,  $0.72 \text{ (L)}$ , and  $1.55 \text{ mmol g}^{-1} \text{ (Y)}$ —under the same experimental conditions (concentration of the donor, temperature, equilibration time, etc.). The diffuse reflectance UV-vis spectra in Fig. 9 also show a progressive increase

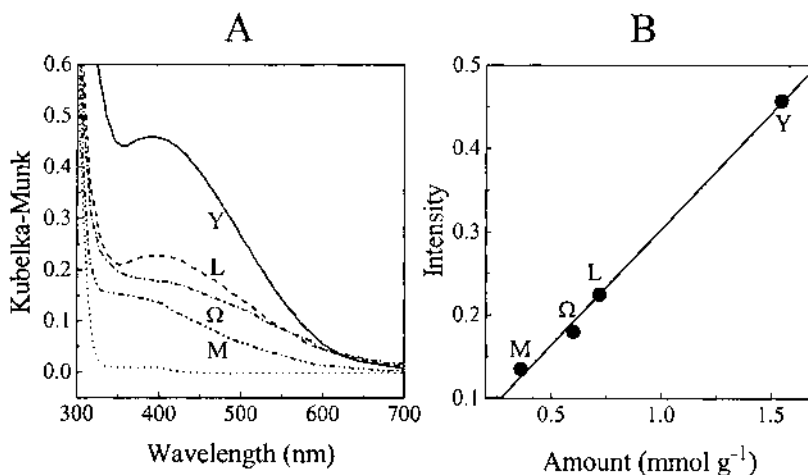


**Fig. 9** Comparison of the relative intensities of the CT bands of 1,4-DMB- $\text{MV}^{2+}$  complex incorporated in M,  $\Omega$ , L, and Y (A). The linear correlation between intercalated amount of 1,4-DMB and the intensities of the CT band (B). (Adapted from Ref. 18c.)

in the intensity of the CT band in the order:  $M < \Omega < L \ll Y$ , consistent with an increase of the incorporated amount. Furthermore, a linear relationship exists between the intensity of the CT band (the visual color intensity) and the incorporated amount as demonstrated in Fig. 9B.

The same trend is observed from other arene donors. Therefore, intrazeolite arene- $\text{Py}^+$  CT complexes serve not only as visual probes for the qualitative test of arene admission into zeolites but also for the quantitative estimation of the admitted amounts. The quantitative response of the intrazeolite arene- $\text{Py}^+$  CT complexes may be useful for monitoring the intrazeolite arene diffusion rate.

**WATER ADSORPTION.** The assembly of arene- $\text{Py}^+$  CT complexes is carried out within the zeolite pores after removal of the zeolitic water molecules. Therefore, the CT complexes are now occupying the crystalline voids that were originally occupied by water. However, there are still some residual spaces available in the zeolite pores even after accommodation of the CT complexes. Refilling the residual void space with water creates a situation in which the CT complexes are surrounded by a thin layer of water, as if dispersing the CT complexes molecularly in water (20). This is an interesting situation that otherwise would not be possible in conventional aqueous solutions since most of arene donors are not soluble in water and the  $\text{Py}^+$  ions are strongly solvated by water, which is also a donor.

To analyze the effect of surrounding water on the physicochemical properties of the CT complexes it is necessary to classify the zeolitic water according to their properties. Although exact classification of the zeolitic water remains to be established, they can be roughly categorized into three types as illustrated in Fig. 10. Type I stands for water molecules that are chemically bound or coordinated to metal cations or protons residing preferentially in small cavities. Removal of this type of water would require relatively higher temperatures often exceeding  $300^\circ\text{C}$ . Type II represents those water molecules that are physically bound to the framework oxide surface, which are effectively liberated at room temperature by evacuation but more effectively by heating the zeolite at moderately elevated temperatures ( $\sim 100^\circ\text{C}$ ). Type III stands for the highly mobile water molecules

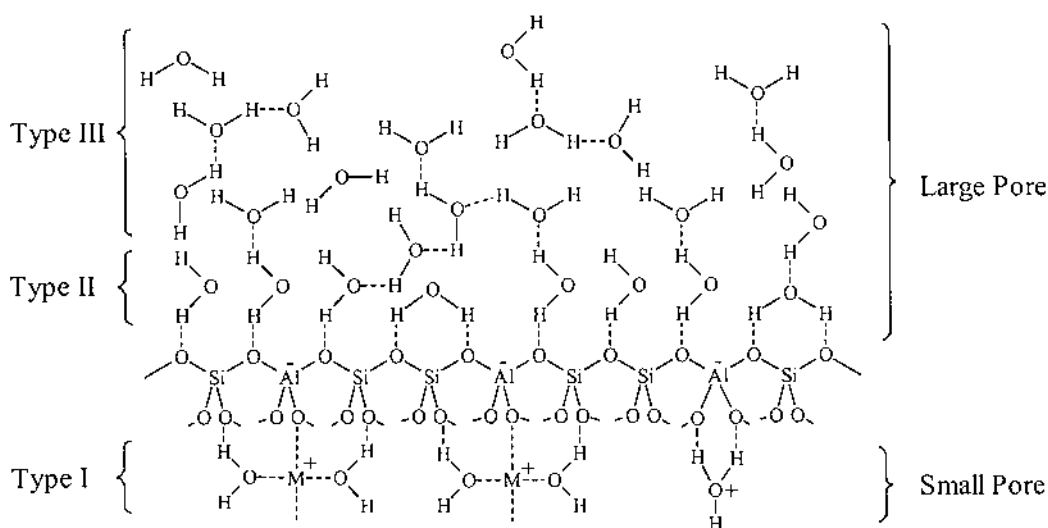


**Fig. 10** Schematic representation of three types of water residing in zeolite pores. (Adapted from Ref. 20.)

clustered near the center of large cavities that can be removed even by gentle evacuation. Among these three types of water, type II waters are most intriguing because they can play a critical role in tuning the size of the zeolite pores for shape selectivity.

Dramatic color changes occur when the intrazeolite arene-Py<sup>+</sup> CT complexes are exposed to water (20). The color changes accompany the corresponding spectral shifts. Interestingly, the degree and direction of spectral shifts, either bathochromic or hypsochromic, depend on the shape and size of zeolite pores and on the presence of the nitrile (-CN) group in the Py<sup>+</sup> acceptor. The following two subsections describe the factors that govern the degree and direction of the moisturization-induced spectral shifts and the corresponding explanations.

**HYPERBARIC EFFECT OF SURFACE-LINING WATER.** For instance, a pure yellow color of 1,4-DMB-pCP<sup>+</sup> CT complex incorporated in dry M gradually turns bright orange upon exposure to moist air (20). Consistent with the color change, the absorption maximum of the CT band red shifts from 360 (dry) to 435 nm (fully moist). The typical moisture-induced gradual bathochromic spectral shift is illustrated in Fig. 11A. In fact, only a small amount of water is enough to induce such spectral change. Thus, moisture uptake of even 2.5% of the total weight of dry zeolite is enough to achieve the lowest energy CT band. The relationship between the spectral shift and the amount of water uptake is shown in Fig. 11B. Deliberate spraying of the dry zeolite with a water aerosol facilitates the moisturizing process.

Similar moisture-induced color changes occur from various arene-Py<sup>+</sup> CT complexes assembled in the channels of M, L, and  $\Omega$ . The color change is reversible and the initial color of the CT complex in the dry zeolite is restored upon evacuation of the moist sample at room temperature. This visual cycle can be repeated numerous times without diminution of color intensities insofar as the arene donor is not lost during evacuation.

The degree of color change and the corresponding degree of bathochromic shift ( $\Delta h\nu_{CT}$ ) of the CT band increase with decreasing the channel size in the order  $M \gg L \cong \Omega$ , whereas moisturization does not affect the spectral shift in the large spherical

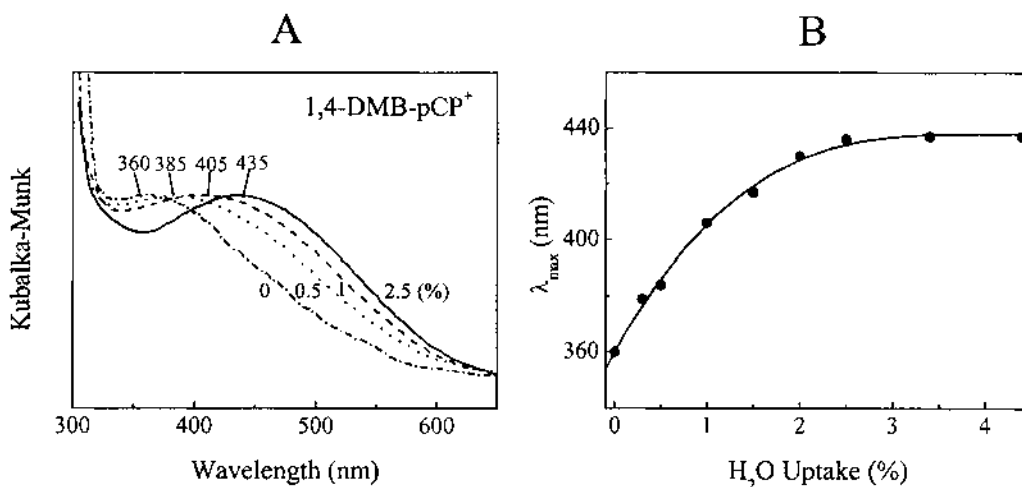


**Fig. 11** Bathochromic shift of the CT band of 1,4-DMB-pCP<sup>+</sup> complex in M upon continued exposure to moist air (A) and the profile of the spectral shift with respect to water uptake (B). (Adapted from Ref. 20.)

**Table 2** Effect of Zeolite Structure on the Bathochromic Shift of the CT Absorption Band of 1,4-DMB-MV<sup>2+</sup> Complex on Moisturization

Zeolite	Cavity (Å)	$\lambda_{CT}$ (nm)		$\Delta h\nu_{CT}(\text{cm}^{-1})$
		Dry	Moist	
M	$7.0 \times 6.7^a$	380	425	2786
L	$7.1^a$	405	425	1162
$\Omega$	$7.4^a$	420	440	1082
Y	$7.4^a, 13^b$	395	395	0

<sup>a</sup> Size of the channel or opening.

<sup>b</sup> Size of the  $\alpha$  cage.

Source: Data from Ref. 20.

supercages of Y. Table 2 lists the actual amount of bathochromic shift of 1,4-DMB-MV<sup>2+</sup> CT complex in the four different zeolites. This trend prevails for a variety of CT complexes of MV<sup>2+</sup> and DQ<sup>2+</sup> with various arene donors encapsulated in zeolites.

In general, the CT absorption bands of many weak  $\pi$ - $\pi$  complexes shift to longer wavelengths upon increasing the pressure on the complexes in solution, in polymeric solid matrices, and in the crystalline state (21). In particular, a series of 1:1 CT complexes of various aromatic donors with typical  $\pi$  acceptors, such as tetracyanoethylene (TCNE), perhalo-substituted benzoquinones (i.e., chloranil and bromanil), and 1,3,5-trinitrobenzene, experience bathochromic shift upon pressurization (22). This phenomenon has been attributed to the decrease in the interannular separation of A and D in response to the mechanical pressure of the medium. Similarly, shortening the interconnecting chains of a series of paracyclophane analog of intramolecular CT complexes causes bathochromic shifts of the CT absorption bands (23).

The principle for the bathochromic shift caused by the decrease of interannular D-A distance is more effectively illustrated by the horizontal displacement (to the left) of the Franck-Condon transition in the potential energy surfaces of weak complexes (21,24) as qualitatively depicted in Fig. 12.

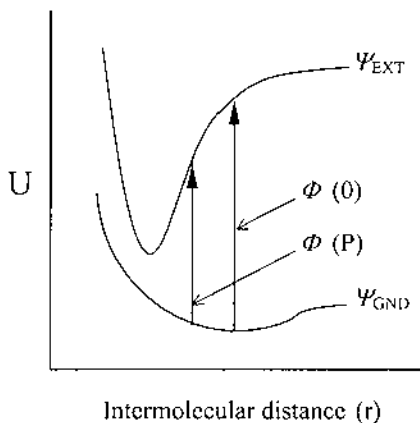


**Fig. 12** Effect of a horizontal displacement (to the left) of the Franck-Condon transition in the potential energy surfaces of weak complexes on the spectral shift. (Adapted from Ref. 20.)

By the same analogy, the moisture-induced bathochromic shifts of the zeolite-encapsulated cofacial arene-Py<sup>+</sup> CT complexes are attributed to the increase in the intrazeolite pressure caused by the reduction in pore volume upon moisturization. This formulation coincides with the marked increase in the magnitude of the bathochromic shift upon decreasing the pore size, i.e.,  $\Omega \cong L \ll M$ , consistent with the increase in the degree of diminution of the internal free space available for the CT complexes upon lining the internal surface with water.

The decrease in the cage volume resulting from water absorption has been experimentally manifested by the decrease in the gas adsorption (25) and by the reduction of mean free path of the coadsorbed xenon gas probed by <sup>129</sup>Xe NMR spectroscopy (26). Such a pore size control by water adsorption has been effectively utilized for catalytic reactions (27).

The water molecules that cause the pressure effects are likely to be those that are hydrogen bonded to the anionic framework oxygen atoms or to the hydroxyl groups introduced during the zeolite washing (i.e., type II in Fig. 10). This formulation is supported by the fact that only 2.5 wt % water, which corresponds to less than 20 mol % of the total water capacity in mordenite, is enough to result in maximal bathochromic shifts. The bulk zeolitic water molecules (type III) that can be readily removed at ambient temperatures by simple evacuation do not appear to exert significant pressure effects on the encapsulated CT complexes, from the fact that the bathochromic shift for the CT complexes encapsulated within the large spherical cavities of Y is negligible.

Although the pressure-induced increase in absorbance and bathochromic shift is a characteristic feature associated with the  $\pi$ - $\pi$  CT complexes, the bandwidths have been shown to be singularly invariant (21). Interestingly, however, the cavity-filling water also gives rise to the decrease in the CT bandwidths. Although additional studies are necessary to elucidate the reason for the above phenomenon, the water molecules seem to put the CT complexes in more uniform environment than in the absence. As mentioned earlier, it is not possible to form arene-Py<sup>+</sup> CT complexes in aqueous media owing to the poor solubility of aromatic donors in water and hydration of the cationic acceptors. However, zeolites provide such unique opportunities to disperse CT complexes molecularly in semiaqueous media. This property might be utilized to carry out those reactions that otherwise would not be feasible in wholly aqueous solutions. In this context, the marked effects of water on reactivity and selectivity in zeolite reactions carried out at mild temperatures (< 100°C) should not be overlooked, particularly when water is produced as a byproduct.

**ACID-BASE INTERACTION OF NITRILE GROUPS WITH CATIONS.** While moisturization gives rise to the same bathochromic shift for the 1,4-DMB complexes of pCP<sup>+</sup> and oCP<sup>+</sup> in the channels of M, L, and  $\Omega$ , it gives rise to hypsochromic shift for the complexes assembled in Y (20). The degree of hypsochromic shift in Y increases as the size of arene donor increases or as the IP of the arene donor decreases, as illustrated in Fig. 13. Consistent with this, while the color change is not so apparent for 1,4-DMB-pCP<sup>+</sup> complex (yellow for dry and moist Y), the color change is substantial for 9-MeANT-pCP<sup>+</sup> complex in Y (purple to orange).

The pore shape-dependent change in the direction of spectral shift arises from the Lewis base-acid interaction between the nitrile group of the cyanopyridinium ion of the acceptor and the acidic sites such as Na<sup>+</sup> ions coordinated to the framework. Consistent with the above conclusion, organic nitriles (R-C≡N) are known to interact with Lewis acids, such as various transition and main group metal ions (28) and even zeolites (29,30).

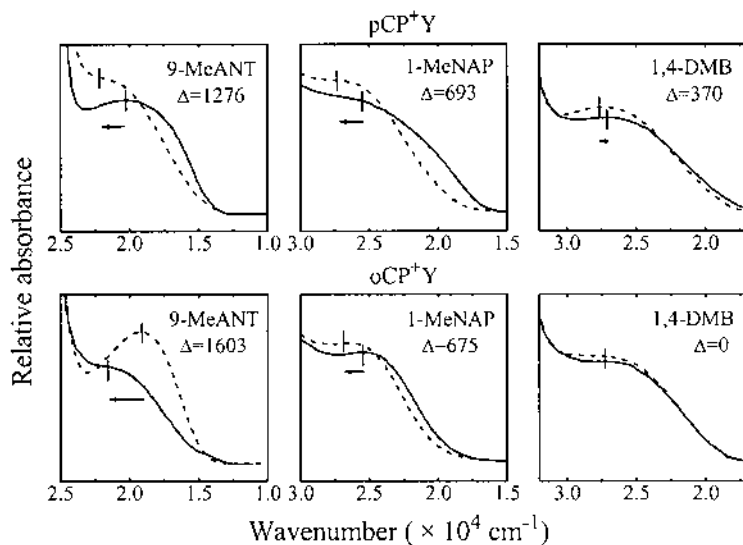


**Fig. 13** Shape selectivity in the hypsochromic shift ( $-\Delta\nu_{CT}$ ) upon moisturization of Y incorporating the isomeric cyanopyridinium complex of pCP<sup>+</sup> (upper) and oCP<sup>+</sup> (lower) with arene donors of decreasing size: 9-MeANT > 1-MeNAP > 1,4-DMB. (Adapted from Ref. 20.)

When a nitrile group is coordinated to a Lewis acidic site, the electron-withdrawing nitrile group becomes more electron deficient and thus withdraws additional electron density from the neighboring substituents. Such an electronic induction effect gives rise to an increase in the acceptor strengths of those nitrile-containing pyridinium acceptors (i.e., pCP<sup>+</sup> and oCP<sup>+</sup>). However, when water is introduced into the supercage, water molecules coordinate the Na<sup>+</sup> ions giving rise to blocking of base–acid interaction between the nitrile group and Na<sup>+</sup> ion. As a result, the acceptor strengths of pCP<sup>+</sup> and oCP<sup>+</sup> are restored to their intrinsic values. Therefore, the moisture-induced hypsochromic shift arises due to the restoration of the acceptor strengths of the cyanopyridinium ions from the unusually high values (dry) to normal ones (wet). Consistent with this, the values of  $\lambda_{CT}$  of the moist samples are closely comparable to those in acetonitrile solution. Such a hypsochromic shift is also induced by anhydrous (gaseous) ammonia and hydrogen cyanide. However, the visible effect of the strong base, ammonia, is not reversible presumably due to the fact that ammonia is not desorbed from the metal cation upon evacuation.

Figure 14 illustrates the striking difference of the behavior of arene-pCP<sup>+</sup> complex in the channel-type zeolites (bathochromic) and cage-type zeolite Y (hypsochromic). Thus, while the spherical cage of 13 Å diameter allows the nitrile group of approximately 9-Å-long pCP<sup>+</sup> cation to point to the charge-balancing sodium ion residing on the surface of the oxide framework the narrow ( $\leq 7.5$  Å) channels of M, L, and  $\Omega$  allow only the collinear orientation of the acceptor cation with the channel direction (*c* axis), which makes it difficult for the acceptor cation to interact with the charge-balancing sodium cations residing on the channel surfaces.

The Fourier transform IR of the pCP<sup>+</sup>-exchanged zeolites in the dry and moist conditions supports the above conclusion. From the ready restoration of the uncoordinated CT bands by water, pCP<sup>+</sup> is regarded as a weaker base to Na<sup>+</sup> than water. It is

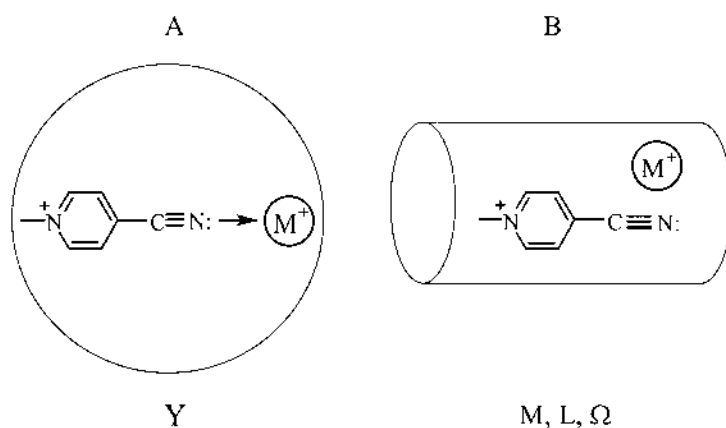


**Fig. 14** Effect of the size and shape of the zeolite pore on the donor–acceptor interaction of pCP<sup>+</sup> with the zeolite surface. (Adapted from Ref. 20.)

also interesting to note that cyanopyridinium acceptors, arenes, and cations (Na<sup>+</sup> ions) form triads.

*c. PET by CT Excitation and Time-Resolved Study of BET*

**LONG-LIVED CHARGE SEPARATION.** CT excitation of the ANT-MV<sup>2+</sup> CT complex (at 532 nm) encapsulated in Y leads to evolution of two well-resolved broad absorption bands that correspond to MV<sup>•+</sup> and ANT<sup>•+</sup> with the absorption maxima at around 620 and 730 nm, respectively, as shown in Fig. 15A (31). Analysis of the decay kinetics of a transient species is usually carried out by plotting the absorption ( $\Delta A$ ) of the transient species at the wavelength on which the transient species shows the maximal absorption ( $\lambda_{\max}$ ) against time as typically shown in Fig. 15B for the case of ANT<sup>•+</sup>. Both transient species (ANT<sup>•+</sup> and MV<sup>•+</sup>) evolve and decay simultaneously with the same first-order rate constant of  $2.9 \times 10^9 \text{ s}^{-1}$ , consistent with PET from ANT to MV<sup>2+</sup> and BET from MV<sup>•+</sup> to ANT<sup>•+</sup> according to Eq. (8):



where  $[\ ]_Y$  denotes the zeolite Y supercage. The BET rate is at least 10 times slower than in acetonitrile solution ( $k > 4 \times 10^{10} \text{ s}^{-1}$ ) (31a). Due to this slower decay rate in zeolite, the spectra of the transient species are relatively intense; accordingly, they are very well resolved when produced in zeolite media rather than in solution.

Photoexcitation of CT complexes of ArH with cyanopyridiniums (oCP<sup>+</sup> and pCP<sup>+</sup>) produces only the transient spectrum of ArH<sup>•+</sup> as typically shown in Fig. 15C,D, since the reduced forms of cyanopyridiniums (neutral pyridyl radicals) do not absorb visible light (from 400 to 800 nm). This procedure may be explored to produce high-quality transient spectra of various aromatic radical cations. The BET rates are usually faster in L than in Y, especially when the pairs of D and A fit tightly within the restricted narrow channels, due to the large size of either D or A or both. For instance, as listed in Table 3, the BET rate for the ANT-DQ<sup>2+</sup> pair is  $22 \times 10^{10} \text{ s}^{-1}$  in dry L, which is about five times faster than that in dry Y ( $4.7 \times 10^{10} \text{ s}^{-1}$ ). However, the rates are similar in both zeolites for the

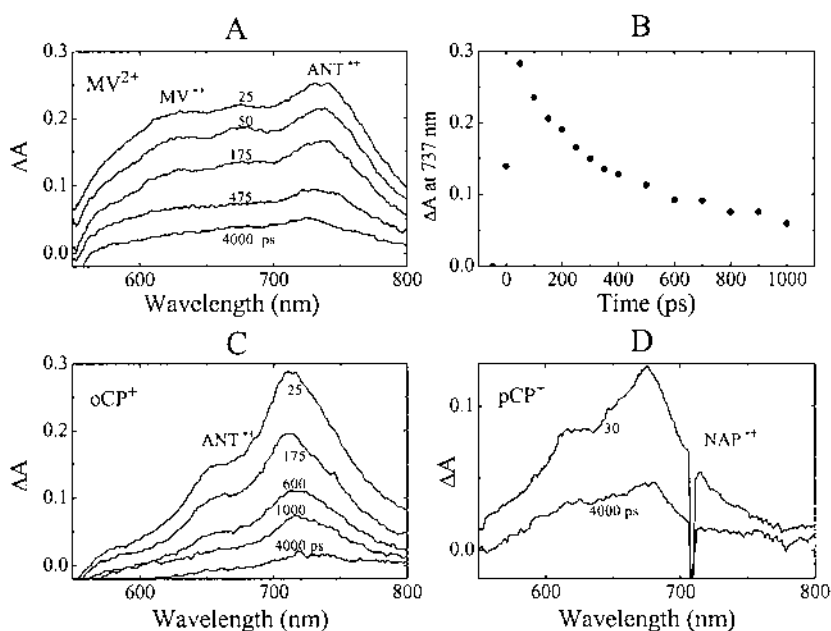


**Fig. 15** Picosecond time-resolved transient spectra of  $\text{ANT}^{\bullet+}$  and  $\text{MV}^{2+}$  generated by laser excitation (532 nm) of  $\text{ANT-MV}^{2+}$  CT complex incorporated in dry Y (A), the decay profile of  $\text{ANT}^{\bullet+}$  monitored at 737 nm from (A) (B), and the corresponding spectra of  $\text{ANT}^{\bullet+}$  (C) and  $\text{NAP}^{\bullet+}$  (D), generated by laser excitation of  $\text{NAP-oCP}^+$  (532 nm) and  $\text{NAP-pCP}^+$  (355 nm) complexes, respectively. (Adapted from Ref. 31b.)

smaller  $\text{NAP-MV}^{2+}$  pair (entry 5). Interestingly, despite the fact that two naphthalene molecules are incorporated in each supercage of  $\text{MV}^{2+}$ (1.0)Y or  $\text{pCP}^+$ (1.0)Y, naphthalene radical dimer ( $\text{NAP}^{\bullet+}$ )<sub>2</sub>, which would absorb at 550 nm, is not observed in Y. Nevertheless, about a fivefold decrease in the decay rate results in the case of  $\text{NAP-pCP}^+$  upon changing the ratio from 1:1 to 2:1.

Most remarkably, the transient absorption spectrum observed on the picosecond time scale does not decay completely back to the baseline even after 4 ns, as shown in Fig. 15A, C, and D. This is in contrast to the fact that the corresponding lifetimes are usually less than 30 ps in acetonitrile solution [see Table 4 (last column)]. The relative amount of residual absorption that persists beyond 4 ns varies depending on the nature of D and A and the type of zeolite. For instance, the amount of  $\text{ArH}^{\bullet+}$  that survives beyond 4 ns (Table 4, entry 5) varies from none ( $\text{ANT-pCP}^+$ ) to 32% (1,4-DMB- $\text{MV}^{2+}$ ). The transient species that survive beyond 4 ns are usually monitored by nano- to microsecond time-scale time-resolved diffuse reflectance setup. Figure 16 shows typical examples of microsecond time-scale time-resolved transient spectra showing BET from  $\text{MV}^{\bullet+}$  to  $\text{ArH}^{\bullet+}$  ( $\text{ANT}^{\bullet+}$  or  $\text{NAP}^{\bullet+}$ ) in dry Y. The fact that transient signals can be detected at microsecond time scale indicates that significant amounts of transient species survive during the period from evolution (< 30 ps) to 1000 ns and beyond. It is worth noting the similarity of the transient spectra in Fig. 15A,D and those in Fig. 16, respectively, despite a large difference in the time frame.

In general, the decay profiles of the transient species in zeolites whose lifetimes extend to microsecond time scales do not follow a simple kinetic law, and in most cases the kinetic

**Table 3** BET Rates in Picosecond Time Scale for Arene-Py<sup>+</sup> CT Complexes Encapsulated in Y and L: Effect of the Pore Size and Moisturization

CT complex	$E^0$ (V) <sup>a</sup>	$\lambda_{\text{max, CT}}$ (nm) <sup>b</sup>	$k^c$ [10 <sup>9</sup> s <sup>-1</sup> ]			
			Dry		Wet	
			Y	L	Y	L
ANT-DQ <sup>2+</sup>	-0.25	505	4.7	22	8.6	41
ANT-MV <sup>2+</sup>	-0.40	490	2.9	6.3	4.7	5.8
ANT-oCP <sup>+</sup>	-0.62	450	1.4	2.9	5.2	6.6
ANT-pCP <sup>+</sup>	-0.64	440	2.8	4.0	5.1	3.4
NAP-MV <sup>2+</sup>	-0.40	390	1.0	0.8	0.8	1.0
NAP-pCP <sup>+</sup> (1:1) <sup>d</sup>	-0.64	360	4.6	1.4	<sup>f</sup>	<sup>f</sup>
(2:1) <sup>e</sup>			1.0		<sup>f</sup>	
1,4-DMB-MV <sup>2+</sup>	-0.40	395	8.7	<sup>g</sup>	16	<sup>g</sup>

<sup>a</sup>  $E^0$  of the acceptor.<sup>b</sup> Absorption maximum of CT band in zeolite Y.<sup>c</sup> Decay rate constant of ion pair.<sup>d</sup> 1:1 complex.<sup>e</sup> 2:1 complex.<sup>f</sup> Sample decomposed in the presence of water.<sup>g</sup> No signal observed.

Source: Data from Ref. 31b.

**Table 4** Half-lives and Residual Absorptions of the Transient Signals in the Nanosecond to Microsecond Time Scale

CT complex	$\tau_{1/2}$ <sup>a</sup> (μs)				R <sup>b</sup> (%)				$\tau$ (ps) CH <sub>3</sub> CN
	Dry		Wet		Dry		Wet		
	Y	L	Y	L	Y	L	Y	L	
ANT-MV <sup>2+</sup>	10	10	25	10	5	0	20	20	19
ANT-PCP <sup>+</sup>	10	130	50	130	0	40	5	40	—
NAP (1:1)-MV <sup>2+</sup>	10	15	> 2000	25	16	20	70	30	30
NAP (2:1)-MV <sup>2+</sup>	10	—	> 2000	—	11	—	66	—	—
NAP (1:1)-pCP <sup>+</sup>	40	30	<sup>c</sup>	80	26	25	<sup>c</sup>	32	25
NAP (2:1)-pCP <sup>+</sup>	10	—	<sup>c</sup>	—	7	—	<sup>c</sup>	—	—
1,4-DMB-MV <sup>2+</sup>	1.6	<sup>d</sup>	> 2000	<sup>d</sup>	32	<sup>d</sup>	60	<sup>d</sup>	—

<sup>a</sup> Half-life of radical cation decay.<sup>b</sup> Relative residual absorption calculated from  $R$  (%) = 100 × [A (200 μs)/A (50 ns)] where A (200 μs) = absorbance at 200 μs, A (50 ns) = absorbance at 50 ns.<sup>c</sup> Sample decomposed in the presence of water.<sup>d</sup> No signal observed.

Source: Data from Ref. 31b.

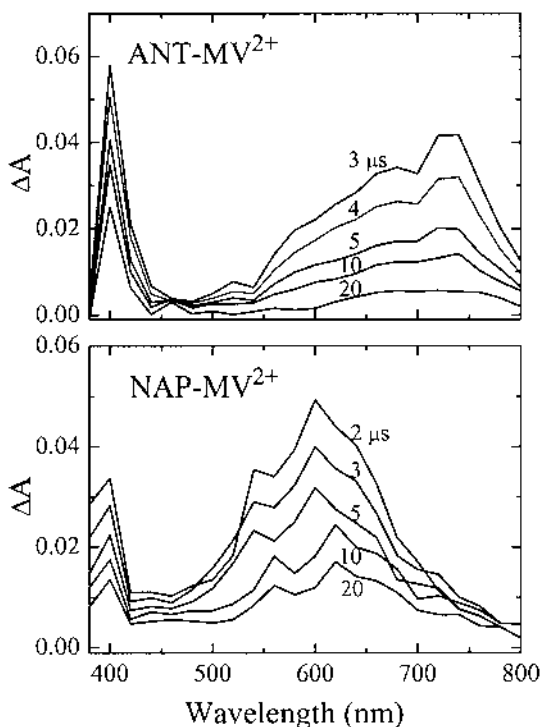


**Fig. 16** Microsecond time-resolved transient spectra upon laser excitation of CT complexes between  $MV^{2+}$  and ANT (top) or NAP (bottom) incorporated into dry Y. (Adapted from Ref. 31b.)

traces can be best fitted by combining multiple first-order decay processes. The kinetic trace for BET from  $MV^{\bullet+}$  to  $NAP^+$  in Y represents a typical example (Fig. 17). Thus, the kinetic trace for the above process is best fitted by two first-order decay processes whose half-lives are 7.7 and 207  $\mu$ s, respectively. Surprisingly, in most cases of BET from reduced  $Py^+$  to  $ArH^+$  the kinetic traces do not decay completely to the baseline but show residual absorptions that persist beyond 1 ms. Because of this complexity in the decay pattern of the microsecond time-resolved absorption spectra, it is usually necessary to report decay half-lives ( $\tau_{1/2}$ ) and the relative residual absorption values,  $R$ , measured after a certain period of time such as at  $t=200 \mu$ s for the above case as listed in Table 4.

Overall, as summarized in Table 5, the combined picosecond and nanosecond kinetic data show that the laser excitation of CT complexes in Y and L generates at least four kinetically distinguishable decay phases of the transients, i.e., one decay process that takes place on the picosecond time scale with lifetimes between 45 ps and 1.2 ns, two processes that take place on the microsecond time scale with half-lives between 1.6 and 130  $\mu$ s, and one very slow process with lifetimes greater than 1 ms. This result clearly demonstrates that CS takes place very rapidly from the ion pair of  $ArH^+$  and one-electron reduced  $Py^+$  acceptor, and the CSSs have extraordinary long lifetimes in zeolites in comparison with that in solution.

Since all of the  $Py^+$  acceptors carry at least a positive charge, the net result of the PET of arene- $Py^+$  CT complexes is a “charge shift” from the acceptor to the neutral donor. Accordingly, the photogenerated ion-radical pairs consist of either two radical cations (+/+ pair) or one radical cation and a neutral radical (+/0 pair). Therefore, it is believed that the Coulombic attraction between the positively charged transient and the

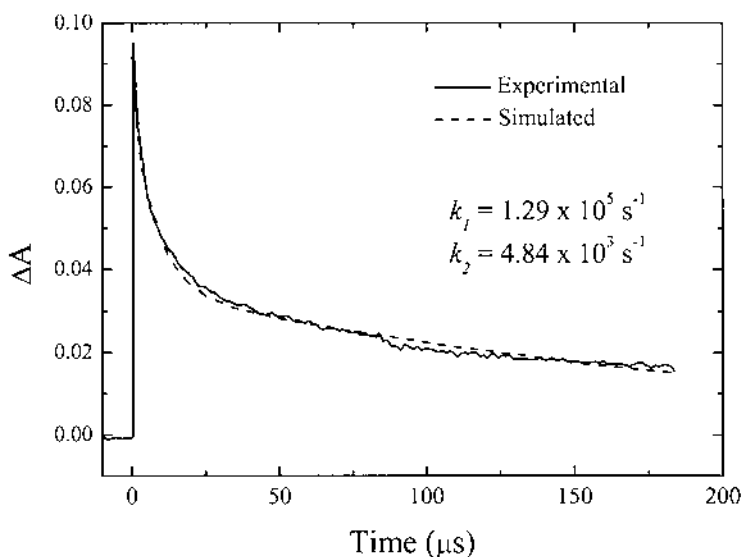


**Fig. 17** Microsecond decay of reduced methyl viologen monitored at 600 nm upon laser excitation of the CT complex between NAP and  $MV^{2+}$  in dry Y. (The dotted line represents biphasic fit leading to  $k_1$  and  $k_2$  for fast and slow first-order. (Adapted from Ref. 31b.)

negatively charged zeolite framework gives rise to the extraordinarily extended lifetimes of the transients, as schematically depicted in Fig. 18 with  $MV^{2+}$  as the typical dicationic acceptor. A similar effect of stabilization of  $+/+$  radical-ion pairs has been observed from NAP- $MV^{2+}$  CT complexes on negatively charged micelle surfaces (32). The multiple decay profiles are attributed to spatial separation of the transient radical ions to a different degree with the help of the negatively charged framework, as formulated in the following scheme:

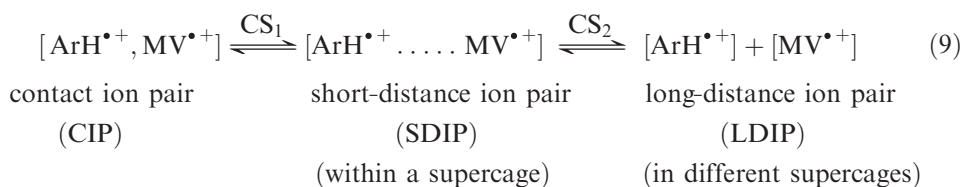


**Table 5** Classification of Ion Pair of  $ANT^{\bullet+}$  and  $MV^{\bullet+}$  in Y by Half-life

Species	Half-life ( $\mu$ s)
I	0.1 ~ 0.6
II	1.6
III	130
IV	> 1000

Source: Data from Ref. 31b.

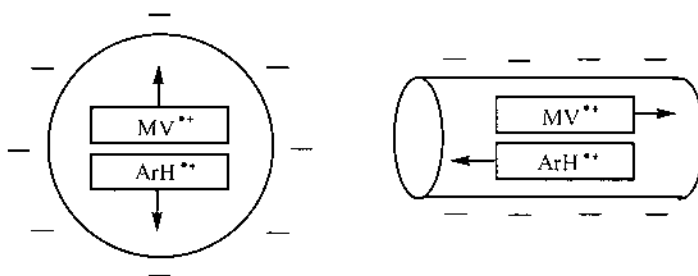
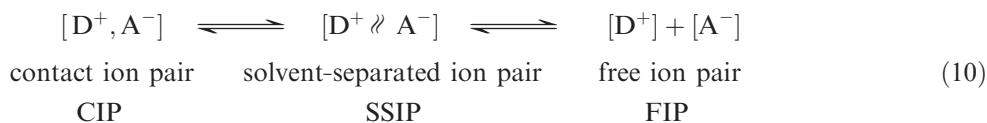


**Fig. 18** Proposed Coulombic attraction between positively charged transient and negatively charged framework leading to long-lived charge-separated state (CSS). (Adapted from Ref. 31b.)

The SDIP in the above formulation may represent the radical-ion pair residing still within a supercage but with each component adhered to the negatively charged framework. The LDIPs then represent those radical ions residing in different supercages. The SDIPs are likely to be those transient ion pairs having lifetimes between 45 ps and 1.2 ns whereas the LDIPs are those with half-lives in the microsecond time scales. Then  $CS_1$  and  $CS_2$  represent the charge separation within a cage and across cages, respectively.

In homogeneous solution, the existence of ion pairs with identical spectra but different lifetimes has been explained in terms of different degrees of solvent interaction, i.e., contact ion pairs (CIP), solvent-separated ion pairs (SSIPs), and free-ion pairs (FIPs).



In zeolite media, the framework surface is likely to play the role of the solvent in controlling the distance between the radical ions.

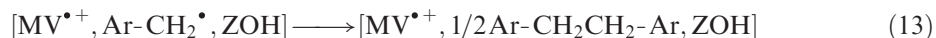
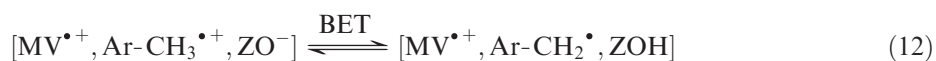
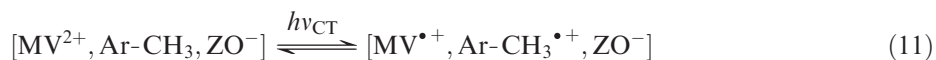
The negatively charged microenvironment of the zeolite may also have an effect on the reduction and oxidation potentials of electron acceptor and donor, respectively. Indeed, Marcus theory predicts that the change in the redox potential of D and/or A affects the BET rate constants (33). However, one has to invoke extremely large change in the redox potential gap between donors and acceptors in order to explain up to 10-fold decreases in rate constants solely by potential changes. Furthermore, the faster decay rates measured in L as compared with Y support the distance-related explanation rather than the potential-related one, since the tighter fit in the channels of L would prevent the primary CIP from being separated. This is not the case in zeolite Y, which leads to faster BET. In compliance with this explanation, increase in the size of D or A gives rise to increase in the BET rate much more pronouncedly in L than in Y since larger guests have tighter fit within the narrower pores. Indeed, the BET rate for ANT-DQ<sup>2+</sup> CT complex composed of a pair of large D and A gives rise to approximately a fivefold increase in L than in Y (see Table 3).

The filling of the residual void space with water greatly affects the kinetic traces of both picosecond and microsecond decay processes. For instance, soaking of the zeolites incorporating ArH-Py<sup>+</sup> complexes with water leads to almost doubling of the BET rate for some CT pairs (Table 3) in the picosecond time scale. Accordingly, this leads to a

decrease of the residual absorbance at 4 ns to about one-third of that in the dry zeolites. In contrast, the half-lives of the microsecond transients and the amounts of very long lived ( $\tau > 1$  ms) transients generally increase in the presence of water (Table 4). The above phenomenon can be interpreted such that the produced amounts of SDIP and LDIP are less and, although the amount is small, the charge recombination of LDIP is very slow in the semiaqueous medium.

The effect of water is unique among the solvents tested. Coadsorbed *n*-hexane, dichloromethane, methanol, acetonitrile, *N,N*-dimethylformamide, propylene carbonate, and even dry ammonia gas are ineffective on all time scales from picoseconds to milliseconds. The unique effect of water may be explained by the readiness of water molecules to enter zeolite cavities and fill up the pores to a degree of bulk solution-like states. Furthermore, a high dipole moment and the strong ability of the molecule to form hydrogen bonds may be responsible for the uniqueness of water. Thus, hydration of the transient species and the lining of the framework surface with water are likely to work together in leading to diminution of the interaction between the zeolite framework and the transient species (radical cations) to such a degree that ET processes occur at conditions and rates similar to those in aqueous homogeneous solutions.

**FRAMEWORK AS PROTON ACCEPTOR.** CT excitation of ArH-MV<sup>2+</sup> CT complexes in the basic zeolite hosts such as, K<sup>+</sup>X, Rb<sup>+</sup>X, and Cs<sup>+</sup>X leads to permanent generation of MV<sup>•+</sup> when the arene donors carry methyl groups directly attached to the aromatic rings (9). For instance, PMB-MV<sup>2+</sup> CT complex turns green in the above basic zeolites upon CT excitation, including exposure to room light, due to the formation of MV<sup>•+</sup>, which is blue, and the remaining CT band, which is yellow (Fig. 19). Other methylated arene donors (Ar-CH<sub>3</sub>) such as mesitylene (MES), DUR, prehnitene (PRN), and 1-MeNAP also give rise to photoinduced permanent generation of MV<sup>•+</sup>. The above phenomenon takes place through deprotonation of Ar-CH<sub>3</sub><sup>•+</sup> by the basic zeolite oxide surfaces (ZO<sup>-</sup>) according to the following scheme;



First, the CT excitation of the Ar-CH<sub>3</sub>-MV<sup>2+</sup> complex converts Ar-CH<sub>3</sub> to the corresponding radical cation, Ar-CH<sub>3</sub><sup>•+</sup> [Eq. (11)]. The radical cations of the methylated arenes are known to readily transfer protons to bases because they are acidic (34). Accordingly, if the framework is basic enough, it can readily deprotonate Ar-CH<sub>3</sub><sup>•+</sup> according to Eq. (12). This process is schematically illustrated in Fig. 20. The generated neutral benzylic radicals would then undergo various other reactions, including radical coupling that leads to formation of a biaryl compound [Eq. (13)]. Overall, MV<sup>•+</sup> persists due to irreversibility of Eq. (13), provided the zeolite is kept free of oxygen. The above scheme also explains why MV<sup>•+</sup> and methyl-free ArH<sup>•+</sup> exist only as transient species despite a long period of CT excitation. For the above scheme to operate, the basicity of the framework should be strong enough to induce the deprotonation step in Eq. (12). In conjunction with this, it is worth mentioning that the MV<sup>2+</sup>-doped M<sup>+</sup>X zeolites with M<sup>+</sup> = K<sup>+</sup>, Rb<sup>+</sup>, and Cs<sup>+</sup> usually generate MV<sup>•+</sup> when they are dehydrated at elevated temperatures (>150°C). This happens when the basic zeolite frameworks play the role of

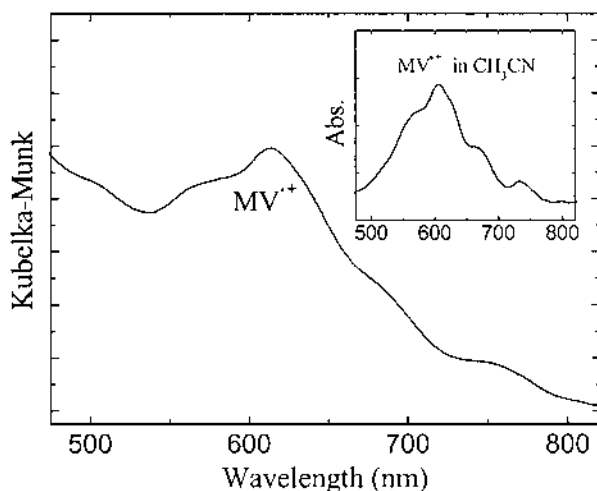


**Fig. 19** Generation of  $MV^{\bullet+}$  from the PMB- $MV^{2+}$  CT complex assembled in the basic  $M^+X$  ( $M^+ = K^+, Rb^+, CS^+$ ) after exposure to room light for several hours or direct irradiation of the CT band ( $\lambda > 400$  nm) using a 500-W mercury lamp for 10 min. The inset shows the authentic spectrum of  $MV^{\bullet+}$  in  $CH_3CN$ . (Adapted from Ref. 9.)

electron donors as discussed later (Sec. III). Therefore, the basic zeolite framework has two functions: a Lewis base and an electron donor.

## 2. Iodide- $Py^+$ CT Complexes

### a. Characteristics

Most of the  $Py^+$  acceptors introduced in the previous section (such as  $MV^{2+}$ ,  $DQ^{2+}$ ,  $Q^+$ , etc.) are colorless when their charge-balancing anions are weak electron donors such as chloride ( $Cl^-$ ), hexafluorophosphate ( $PF_6^-$ ), and trifluoromethanesulfonate ( $CF_3SO_3^-$ ,  $OTf^-$ ). However, they become brilliantly colored when their charge-balancing anions are

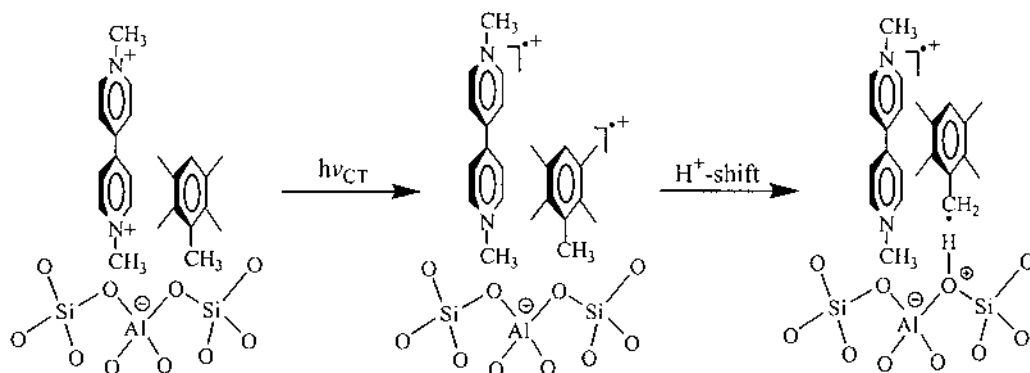
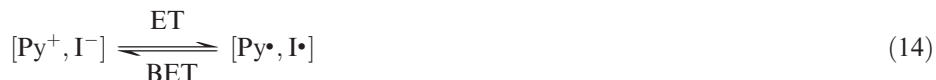


**Fig. 20** Schematic representation showing  $H^+$  abstraction by the basic oxide framework from a radical cation of an arene donor with ring-substituted methyl groups (PMB) that leads to permanent formation of  $MV^{\bullet+}$ . (Adapted from Ref. 7a.)

strong electron donors such as iodide ( $I^-$ ) and anionic metal complexes such as  $ZnCl_4^{2-}$ . Similarly, tropylium ( $TR^+$ ) forms an orange salt with iodide (35). The bright colors are CT colors arising from photoinduced interionic ET from iodide to the organic acceptors such as  $Py^+$ :



Assembly of the CT salts of  $Py^+ - I^-$  in Y is carried out by dipping  $Py^+$ -exchanged Y into the acetonitrile solution of iodide salts, i.e., by occlusion of iodide salts (36). Since iodide has to enter zeolite pores with the corresponding charge-balancing cation, the overall size of the salt is determined by the size of the counteranion when the size of the counteranion is larger than that of iodide as shown in Fig. 21. For instance, when  $Py^+$ -exchanged zeolites are exposed to iodide salts of sodium ( $Na^+$ ), potassium ( $K^+$ ), tetramethylammonium ( $TMA^+$ ), and tetraethylammonium ( $TEA^+$ ) dissolved in acetonitrile, yellow to orange  $Py^+ I^-$  CT salts are formed immediately in the supercages of Y according to the following:



while the supernatant solutions remain colorless. However, when iodide is coupled with the cations with kinetic diameters larger than 8 Å, such as tetra-*n*-butylammonium ( $TBA^+$ ) and tetra-*n*-hexylammonium ( $THA^+$ ), it cannot enter the zeolite and therefore does not induce CT coloration with  $Py^+$  in Y. The above fact clearly demonstrates

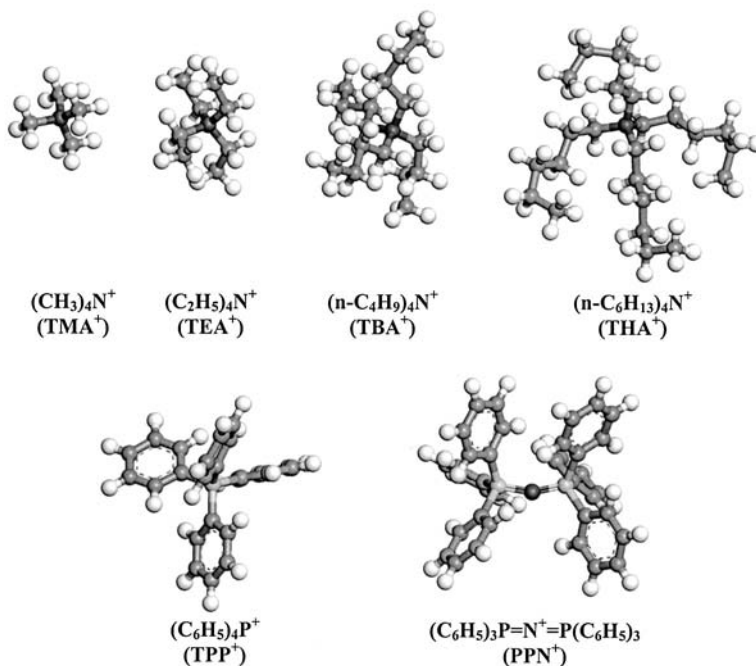
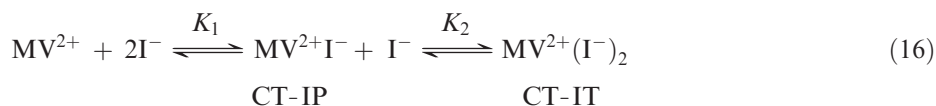


**Fig. 21** Energy-minimized structures and abbreviations of cations that frequently appear in this chapter. Energy minimization was carried out using a commercial program, Materials Studio.

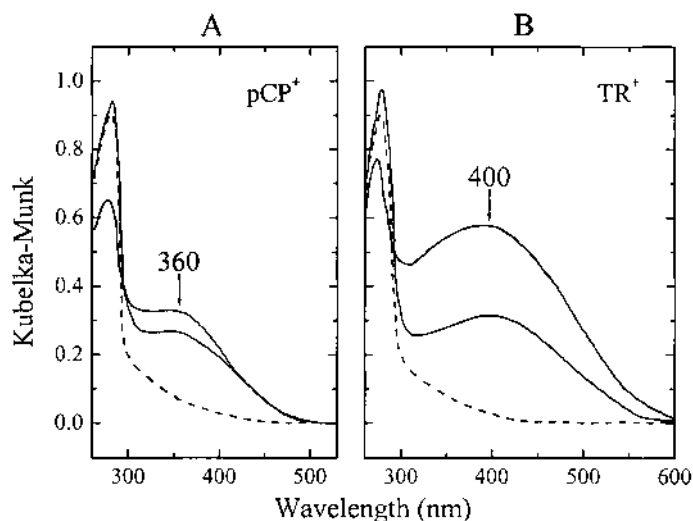
that penetration of iodide into the supercage of Y proceeds via ion pair intercalation or salt occlusion.

Figure 22 shows the diffuse reflectance spectra of the yellow and orange zeolites obtained by occlusion of NaI into pCP<sup>+</sup>Y and TR<sup>+</sup>Y, respectively. Although the intensity of Py<sup>+</sup>I<sup>-</sup> CT salt in zeolite usually increases with increase in the concentration of iodide salt (C<sup>+</sup>I<sup>-</sup>) in solution, the intensity of Py<sup>+</sup>I<sup>-</sup> CT salt does not increase in zeolite in correlation with the added amount of C<sup>+</sup>I<sup>-</sup>, when monovalent Py<sup>+</sup> ions are the acceptor ions, due to leaching of the Py<sup>+</sup> ion from the zeolite matrices by C<sup>+</sup> via ion exchange in organic solution. As a result, the intensity decreases as time elapses whereas the concentration of Py<sup>+</sup>I<sup>-</sup> increases in the supernatant solution.

In the case of bipyridinium acceptor ions such as MV<sup>2+</sup> both CT ion pair [CT-IP, MV<sup>2+</sup>I<sup>-</sup>] and CT ion triplet [CT-IT, MV<sup>2+</sup>(I<sup>-</sup>)<sub>2</sub>] exist due to the following multiple equilibria:



In polar solvents such as water and aqueous acetonitrile, MV<sup>2+</sup>(I<sup>-</sup>)<sub>2</sub> and DQ<sup>2+</sup>(I<sup>-</sup>)<sub>2</sub> extensively dissociate into individual ionic species. Accordingly, a dilute aqueous solution of MV<sup>2+</sup>(I<sup>-</sup>)<sub>2</sub> is usually colorless, and the solution turns pale yellow due to formation of small amounts of CT-IP, even in 1 mM NaI solution, indicating that K<sub>1</sub> is very small. The second association constant K<sub>2</sub> for CT-IT formation in water is even lower, and approaches zero. Therefore, it is not possible to form CT-IT in a polar solvent. In a less polar solvent, such as pure acetonitrile, spectral characterization of both CT-IP and CT-IT is not possible because CT-IP shifts to CT-IT, which precipitates from the solution. In zeolites, however, either CT-IP or CT-IT or both can be selectively generated by merely



**Fig. 22** Diffuse reflectance spectra of the CT salts (A) pCP<sup>+</sup>I<sup>-</sup> and (B) TR<sup>+</sup>I<sup>-</sup> from the intercalation of 7 mM (bottom) and 300 mM (upper) solutions of Na<sup>+</sup>I<sup>-</sup> in acetonitrile into Y exchanged with pCP<sup>+</sup> and TR<sup>+</sup>, respectively. Dashed lines represent the corresponding spectra of untreated pCP<sup>+</sup>(0.7)Y and TR<sup>+</sup>(0.8)Y for comparison. (Adapted from Ref. 36.)

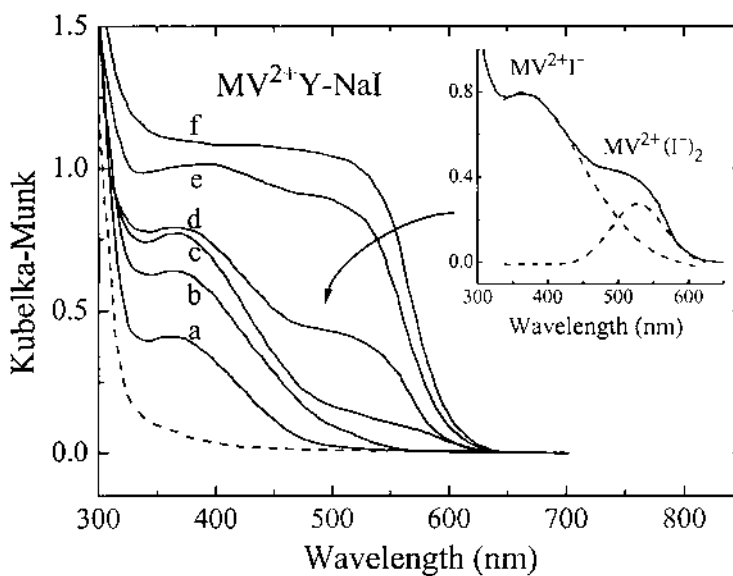


**Fig. 23** Stepwise formation of the ion pair ( $MV^{2+}I^-$ ) and ion triplet [ $MV^{2+}(I^-)_2$ ] identified by their CT spectra obtained from the intercalation of  $Na^+I^-$  from (a) 7, (b) 20, (c) 40, (d) 80, (e) 160, and (f) 320 mM solutions in acetonitrile. The dashed line stands for the diffuse reflectance spectrum of  $MV^{2+}(1.0)Y$ . The inset shows the Gaussian deconvolution of the partially resolved CT envelope (d) into the ion pair and ion triplet components with  $\lambda_{max} = 362$  nm and 528 nm, respectively. (Adapted from Ref. 36.)

varying the amount of iodide incorporation into the  $MV^{2+}$ -exchanged zeolite. For instance, as shown in Fig. 23, CT-IP can be selectively formed in  $MV^{2+}Y$  by exposing the zeolite to the acetonitrile solution of NaI at concentrations below 20 mM. CT-IP is yellow and has the absorption maximum at 362 nm. The red-colored CT-IT can also be generated almost selectively in  $MV^{2+}Y$  by exposing the zeolite to highly concentrated NaI solution (>320 mM). At the intermediate concentrations, both CT-IP and CT-IT are generated. Likewise, the CT-IP and CT-IT from  $DQ^{2+}$  and  $I^-$  can be selectively generated in Y by employing  $DQ^{2+}Y$ .

Although KI is much less soluble in acetonitrile, the heterogeneous mixture of  $MV^{2+}Y$  or  $DQ^{2+}Y$  and KI in acetonitrile leads to formation of even CT-IT, resulting in complete occlusion of KI into Y. However, iodide salts of  $TMA^+$  and  $TEA^+$  cause formation of only CT-IP but not CT-IT, indicating the shape-selective modulation of the multiple ionic equilibria by the size of quaternary ammonium ion. Thus, the above results demonstrate that zeolites can be utilized to differentiate and characterize CT-IP and CT-IT.

*b. As Visual Probes for Zeolite Micropolarity*

Since ionic CT salts have often been exploited as probes for solvent polarity (37,38), the ionic CT salts can also be utilized to delineate the polarity of the supercages of Y. Thus, as shown in Fig. 24, the  $\lambda_{max}(CT)$  of the monoiodide complex of  $MV^{2+}$  ( $MV^{2+}I^-$ ) shifts to a lower energy region with decreasing the polarity of the medium. Such a solvatochromic shift (solvent-dependent color change) of ionic CT salts originates in the decrease of the gap between the energy levels of the ground and excited states as the polarity of the

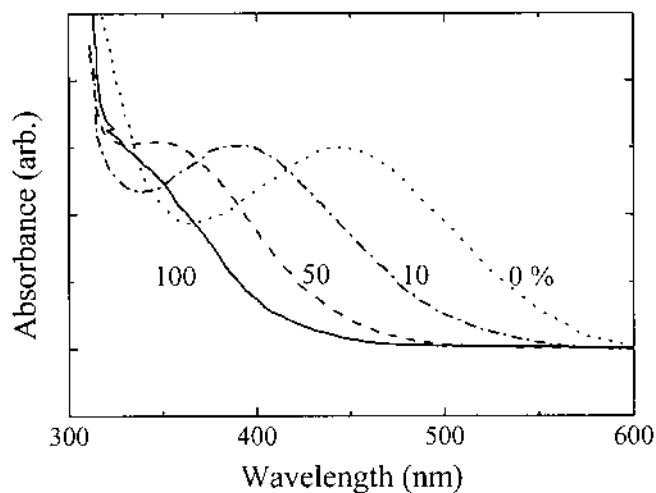


**Fig. 24** Solvatochromic shift of the CT band of  $MV^{2+}(I^-)_2$  in aqueous acetonitrile containing 100%, 50%, 10%, 0%, and no water. (Adapted from Ref. 36.)

medium decreases (35,38,39). From the direct comparison of the yellow CT band of encapsulated CT-IP ( $\lambda_{\text{max}} = 362$  nm) in Y (Fig. 23) with those in solution (Fig. 24), the micropolarity of the zeolite Y supercage may be estimated to be similar to that of 50% aqueous acetonitrile. [A similar result is obtained from an independent study of superoxide ET (40).] The above estimation of the micropolarity of Y should be confirmed by repeating the experiment using the zeolites from which the residual solvent ( $\text{CH}_3\text{CN}$ ) was rigorously removed. Nevertheless, the above results indicate that CT salts can be utilized as the probes for estimation of zeolite micropolarity.

### c. As Visual Probes for NaI Migration

Zeolites have been described as solid electrolytic solvents (41). As demonstrated in the previous section, occlusion of iodide salts into zeolite pores readily takes place from organic solution (acetonitrile). Now a question arises whether the occluded iodide salts are mobile within the zeolite pores as if they were dissolved in polar solvents. Another important question that needs to be addressed is whether the incorporated NaI salt can migrate from one zeolite crystal to another upon mere physical contact. In fact, understanding the phenomenon of salt transfer between zeolite crystals and between zeolite and clay minerals is important for the design and study of zeolites as catalysts and sorbents, since zeolites are often blended with natural clay minerals to produce agglomerates for practical use (42). Delineation of the phenomenon of the intra- and intercrystalline salt transfer is also important since the occluded salts greatly affect the reactivity, selectivity, and stability of the zeolite catalysts.

The mixture of dry  $MV^{2+}Y$  and NaI-intercalating Y rapidly ( $< 30$  min) develops a yellow CT color as a result of formation of  $MV^{2+}-I^-$  upon mere physical contact (43). Similarly, formation of orange  $DQ^{2+}-I^-$  CT-IP occurs from the corresponding zeolites upon solid-state mixing. This phenomenon is attributed to the intercrystalline migration of NaI from the NaI-intercalating crystals of Y to the neighboring crystals of  $MV^{2+}Y$ . In contrast, the finely ground mixture of crystalline NaI salt and  $MV^{2+}Y$  or  $DQ^{2+}Y$  does not lead to CT-IP formation even after standing for 6 months as long as it is kept dry.

From the above contrasting results, it is inferred that the NaI salt intercalated within zeolite exists in a highly mobile molecular form. Addition of small amounts of moisture into the dry mixtures greatly accelerates the intercrystalline salt migration. Increase in the temperature also enhances the process. This result emphasizes again the characteristic aspect of zeolites as solid solvents. Intercrystalline salt migration also occurs between zeolite and synthetic saponite clay.

### 3. Iodide-Alkali-Metal Cation CT Complexes

The donor–acceptor interaction between  $I^-$  and  $Py^+$  is well established in the previous section. Their CT interaction is visually apparent from their CT bands that appear in the visible region. However, as the acceptor strength of the cation decreases the corresponding CT band blue shifts and eventually shifts to the UV region. In principle, alkali metal ions are also electron acceptors, although their acceptor strengths have usually been neglected during ET or acid–base reactions. Nevertheless, the acceptor properties of alkali metal ions have been known for a long time and the direct evidence for that is the observation of iodide-to-alkali metal cation CT bands. Since the acceptor strengths of alkali metal ions are considerably weaker than  $Py^+$  or  $TR^+$ , the corresponding iodide-to-cation CT bands appear in the UV region ( $< 300$  nm).

Before moving directly into the details of this section, it is relevant to review some of the important aspects of iodide and its CT interaction with weak acceptors. In aqueous solution, iodide shows two absorption bands at 5.5 and 6.4 eV (226 and 193 nm, respectively) at 20°C that are much higher in energy than its own ionization potential (3.0 eV) (44). Likewise, iodide gives two absorption bands in other solvents that are considerably higher in energy than its own ionization potential. These absorption bands are known as the charge-transfer-to-solvent (CTTS) bands (44). In molten salts, where cations serve as the sole electron acceptors, iodide gives rise to the related iodide-to-cation charge-transfer (ITC-CT) bands (44a).

The appearance of two bands is ascribed to two different energy states of iodine atom,  $^2P_{1/2}$  and  $^2P_{3/2}$  (44e). The reason for the appearance of two CT bands follows. Thus using the expression for the ground and excited states of a CT complex [Eqs. (4) and (5)], the CT interaction between iodide and an acceptor ( $I^-$ , A) can be described as the following:

$$\Psi_G = a\psi_0(A, I^-) + b\psi_1(A^- - I\bullet) + \dots \quad (17)$$

$$\Psi_E = a^*\psi_1(A^- - I\bullet) - b^*\psi_0(A, I^-) + \dots \quad (18)$$

Since  $a \gg b$  and  $a^* \gg b^*$ ,  $\Psi_G$  is essentially  $a\psi_0(A, I^-)$  whereas  $\Psi_E$  is essentially  $a^*\psi_1(A^- - I\bullet)$ . Therefore, while there is essentially one wave function for the ground state, there are two excited-state wave functions stemming from two different energy states of  $I\bullet$  ( $^2P_{1/2}$  and  $^2P_{3/2}$ ). Figure 25 shows the ITC-CT bands measured for a series of alkali metal ions exchanged in X (45). Two well-resolved ITC-CT bands appear from  $M^+X$  ( $M^+ = K^+$ ,  $Rb^+$ ,  $Cs^+$ ). The absorption maxima for  $M^+X$  are 5.69 ( $Na^+$ ), 5.23 ( $K^+$ ), 5.10 ( $Rb^+$ ), and 4.91 eV ( $Cs^+$ ) for the low-energy band (LEB), and 6.11 ( $K^+$ ), 5.93 ( $Rb^+$ ), and 5.79 eV ( $Cs^+$ ) for the high-energy band (HEB). The energy differences between LEB and HEB are 0.88 ( $K^+$ ), 0.83 ( $Rb^+$ ), and 0.89 ( $Cs^+$ ), i.e., smaller than that in water (0.92 eV). This phenomenon seems to arise due to alteration of the energy difference between  $^2P_{1/2}$  and  $^2P_{3/2}$  of iodine atom as a result of being placed in the highly polar intrazeolite environments.

The ITC-CT band in the above zeolites progressively red shifts with increasing the size of the countercation. On the basis of Mulliken's CT theory (4), the above result clearly shows that the acceptor strengths of alkali metal cations in zeolites increase as the size

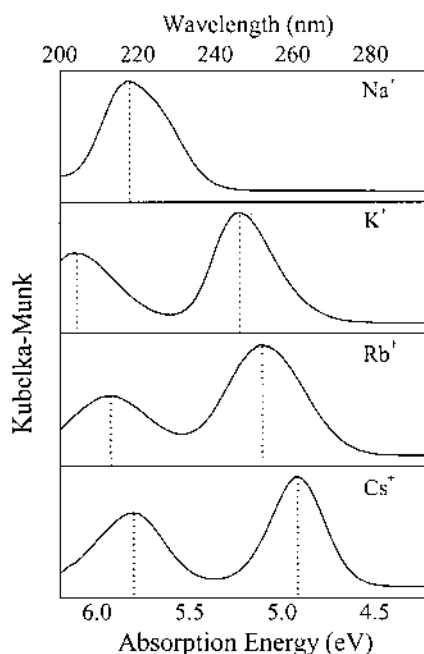


**Fig. 25** Diffuse reflectance UV-vis spectra of iodide in zeolite X exchanged with four different alkali metal ions (as indicated) showing the progressive red shift of the ITC-CT bands with increasing size of the cation. (Adapted from Ref. 45.)

increases, as opposed to the normal behavior of alkali metal cation in solution and in vacuum where space restriction does not apply.

The linear relationship between the electron affinity of  $M^+$  and ITC-CT band shown in Fig. 26A further supports this contrary behavior of the acceptor strength of  $M^+$  in zeolite X. The same trend is observed from  $M^+$  Y zeolites: 5.30 ( $K^+$ ), 5.28 ( $Rb^+$ ), and 5.25 eV ( $Cs^+$ ) for LEB and 6.14 ( $K^+$ ), 6.14 ( $Rb^+$ ), and 6.11 eV ( $Cs^+$ ) for HEB. The degree of cation-dependent shift is much smaller in zeolite Y, due to the presence of smaller number of the site III cations in the supercage ( $\sim 1$  for Y vs.  $\sim 5$  for X).

The size-dependent increase in the acceptor strength of  $M^+$  in zeolites is ascribed to the diminished screening of the cation by the negatively charged framework as depicted in Fig. 27 as the degree of protrusion of the cation toward the center of the supercage increases. In close relation to this, a linear relationship exists between the supercage volume and the absorption energy of the ITC-CT band as shown in Fig. 26B, regardless of the type of zeolite (46). This relationship indicates that the tighter contact between iodide and the cations as a result of the decrease in the pore volume plays a key role for the observed red shift of the ITC-CT band, namely, the actual acceptor strength of the cation. This explains why the sensitivity of the cation-dependent shift of the ITC-CT band is higher in X than in Y.

Overall, the above results reveal that the acceptor strength of a cation in zeolites is more sensitively governed by the degree of protrusion into the pores and the pore volume than by the intrinsic acceptor strength of the cation. The ITC-CT band can also serve as a novel probe for evaluation of actual acceptor strengths of cations in zeolites and cation-dependent pore volume change. The iodide-cation CT interaction is a good complement to the framework-iodine CT interaction (8) described in Sec. III.A.2 (p. 673).

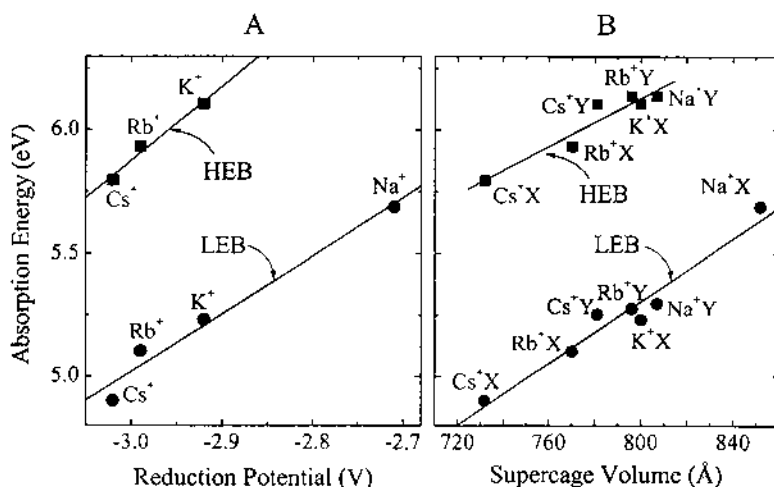


**Fig. 26** Linear relationships between the reduction potential of the cation (as indicated) and the absorption energy of ITC-CT bands in zeolite X (A) and between the supercage volume and the absorption energy of ITC-CT bands in  $M^+X$  and  $M^+Y$  (as indicated) (B), for each high-energy (HEB) and low-energy band (LEB). (Adapted from Ref. 45.)

#### 4. Arene-Arene and Arene-Tetranitromethane Complexes

The highly electron-deficient neutral compounds such as 1,2,4,5-tetracyanobenzene (TCNB) (11,47), *m*-dinitrobenzene (*m*-DNB) (48), and tetranitromethane (TNM) (49) have also been employed as electron acceptors for CT complexation with arene donors. TCNB is conveniently incorporated into dehydrated zeolites by equilibrating it with dichloromethane at room temperature, preferably in a dry box. After washing, the adsorbed solvent is removed by briefly evacuating the TCNB-incorporating zeolite at 50°C. Subsequent introduction of arene donors into the TCNB-incorporating zeolite is achieved by equilibrating the zeolite in *n*-hexane solutions of various aromatic donors. The TCNB molecules previously incorporated into the zeolites do not leach out during donor incorporation due to the poor solubility of the acceptor in *n*-hexane. The zeolite develops distinctive CT colors almost instantaneously upon exposure to various hexane solutions of

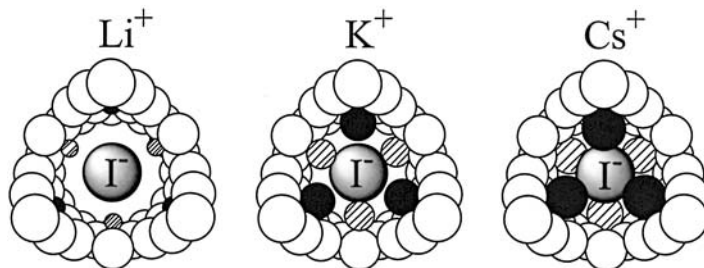


**Fig. 27** Pictorial illustration of the reduction in the available space within the supercage of zeolite X as the size of the cation in sites II (hatched circles) and III (filled circles) increases (as indicated). (Adapted from Ref. 45.)

different arene donors. The diffuse reflectance spectra of some of the arene-TCNB CT bands are shown in Fig. 28A. The Mulliken relation between the CT band ( $h\nu_{CT}$ , in electronvolts) and  $I_p(D)$  is expressed according to the following.

$$h\nu_{CT} = 1.00 I_p(D) - 4.87 \quad (19)$$

The absorption maxima of the CT bands in  $Na^+Y$  are comparable with those in dichloromethane but are slightly blue shifted with respect to those observed in the crystalline state. One of the interesting aspects of arene-TCNB complexes is that they give CT fluorescence, as shown in Fig. 28B. This allows estimation of the energy levels of the CT states by analyzing the peak energies of emission. The result shows that the energy levels are nearly the same in dry  $Na^+Y$  and in solution, unlike arene-cyanopyridinium CT bands.

Moisturization gives rise to a dramatic increase in the intensity of the CT band of most of the arene-TCNB CT complexes. However it does not induce a spectral shift of  $\lambda_{max}(CT)$ , again unlike arene-cyanopyridinium CT complexes. This suggests that the nitrile groups do not interact with the charge-balancing cations, presumably due to steric factors.

The reason for the moisture-induced dramatic increase in the intensity remains to be elucidated. One suggestion is that the CT complexes aggregate and form nano CT crystals upon moisturization (50). The report that moisturization gives rise to aggregation of ANT and biphenyl (BIP) in  $Na^+Y$  or  $Na^+X$  serves as the basis for the above suggestion.

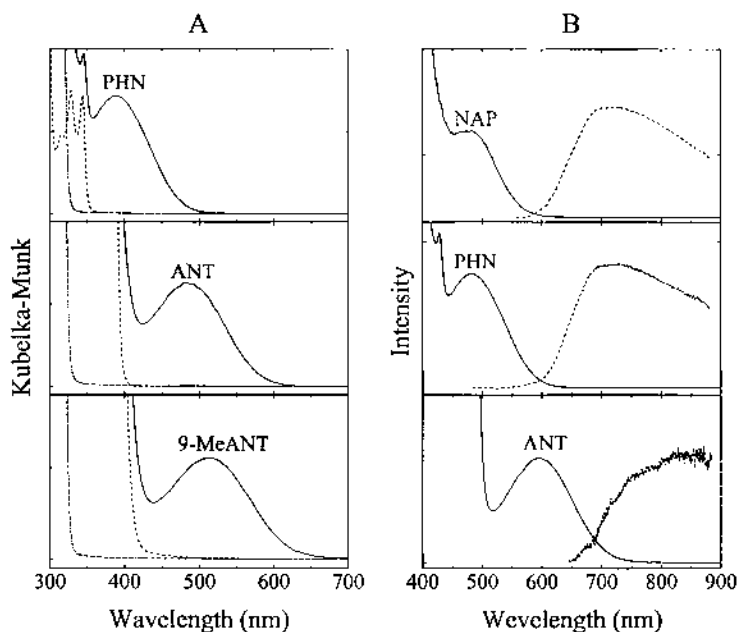


**Fig. 28** (A) Diffuse-reflectance UV-vis spectra of CT complexes of TCNB with PHN, ANT, and 9-MeANT (as indicated) assembled in  $Na^+Y$ . The corresponding spectra of the arene donor (dashed) and TCNB (dashed and dotted) are also included for comparison. (B) Absorption (solid) and corrected (dashed) spectra of CT complexes of TCNB with NAP, PHN, and ANT (as indicated) assembled in  $Na^+Y$ . (Data extracted from Ref. 11.)

However, there are also contradicting reports that ANT and pyrene (PYR) readily dissociate from the dimeric states to the monomeric forms upon moisturization (50c,51). Therefore, further study is necessary to figure out the real causes. For the time being, it is suggested that moisture cuts off the interaction between the framework and the acceptor or the charge-balancing cation and the arene donor, rendering the donor and acceptor interaction more favorable without interference by the framework or the cation. The effect of the charge-balancing cation on the shift of  $\lambda_{\max}(\text{CT})$  is discussed in Sec. III.A.2 (p. 677).

Photoexcitation of NAP-TCNB CT complex in dry  $\text{Na}^+\text{Y}$  at 390 nm with Ti-sapphire laser with 170-fs pulse width results in the transient spectra as shown in Fig. 29 (47a). The spectra consist of two absorption bands due to  $\text{TCNB}^{\bullet-}$  (470 nm) and  $\text{NAP}^{\bullet+}$  (680 nm) (compare with that of Fig. 15D, p. 611). The transient spectra are considerably broader in dehydrated zeolite than in hydrated. This phenomenon seems to be related to the fact that the transient spectra of toluene $^{\bullet+}$  and  $\text{TCNB}^{\bullet-}$  are much broader in frozen toluene or in polymethyl methacrylate matrix, where configurational rearrangement of the CT complexes in various ground and excited states to the more stable states is severely prohibited (52). It is, therefore, inferred that the CT complexes exist in various “locked” states in dry zeolites. Consistent with this interpretation, the sharpness of the transient spectra in hydrated Y is comparable with that in solution.

Both of the transient species decay at the same rate without accompanying any appreciable spectral change. This establishes that the decay process occurs due to BET from  $\text{TCNB}^{\bullet-}$  to  $\text{NAP}^{\bullet+}$  [Eq. (20)].

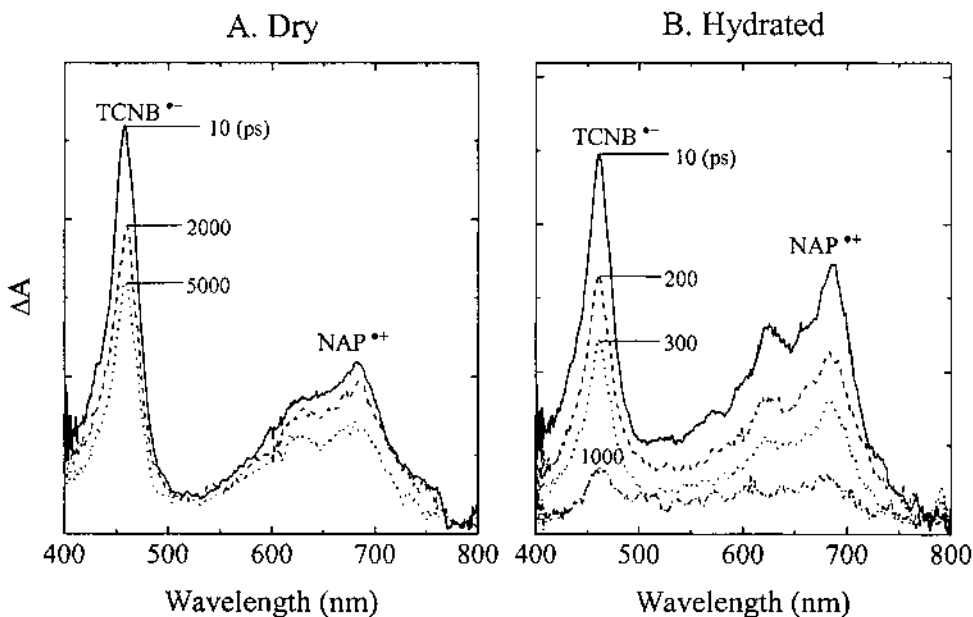


**Fig. 29** Diffuse reflectance transient spectra of  $\text{TCNB}^{\bullet-}$  and  $\text{NAP}^{\bullet+}$  generated by laser excitation (390 nm) of NAP-TCNB CT complex incorporated in dry (A) and in hydrated (B) Y. (Data extracted from Ref. 11.)

The decay processes are mostly biphasic in dry Y, whereas they are monophasic in hydrated samples (Table 6). The decay rate increases by about 10-fold in hydrated Y over that in dry Y, similar to the case of arene-Py<sup>+</sup> CT complexes (see Table 3 on p. 612, and p. 615). Such a marked difference in rates again suggests a strong interaction between the transient species and the zeolite host in the water-free condition.

From the view of the possible Coulombic interaction between the transient species and the negatively charged framework, a repulsion between the negatively charged TCNB<sup>•-</sup> and the framework is expected to accelerate the BET process. However, the interaction between the four nitrile groups of TCNB<sup>•-</sup> and Na<sup>+</sup> ions via acid-base complexation, and therefore the interaction between TCNB<sup>•-</sup> and Na<sup>+</sup>, will become stronger, which may contribute to make the decay process biphasic in dry Na<sup>+</sup>Y.

The assembly of CT complex consisting of aniline (ANL) and *m*-DNB has also been shown in Na<sup>+</sup>Y (48). A broad CT absorption band [ $\lambda_{\max}$  (CT)] appears at around 400 nm. *m*-DNB is first introduced into the supercages of Y by evaporation under vacuum. Homogeneous distribution of the arene donor within the zeolite crystals is achieved by keeping the sample at 300 K for 12 h. ANL is subsequently introduced into *m*-DNB-incorporating Y again by evaporation. Immediate red coloration takes place on the zeolite upon exposure to the vapor of ANL, indicating that the diffusion of ANL into the interiors of the crystals is fast. Neutron powder diffraction analyses of the zeolite Y crystals incorporating perdeuterated ANL-*m*-DNB CT complexes revealed the cofacial interaction between the two arene rings.

Tetranitromethane (TNM) has also been frequently employed as an electron acceptor for CT complexation with various arene donors in solution (53). Coadsorption of TNM and *cis*- or *trans*-stilbene (*cis*-STB or *trans*-STB) into Na<sup>+</sup>X gives rise to formation of the corresponding CT complexes that give CT bands in the 350- to 450-nm region (49). CT excitation (10 ns pulse width) of *trans*-STB-TNM complex at 355 or 420 nm in the atmosphere with a laser pulse with 10-ns width leads to formation of a transient signal at 475 nm due to the adsorption by *trans*-STB<sup>•+</sup>. Photoexcitation of the related *cis*-STB-TNM CT complex shows an additional band at 510 nm assignable to *cis*-STB<sup>•+</sup>. The yield of *cis*-STB<sup>•+</sup> is substantially less than that of *trans*-STB<sup>•+</sup> and decreases with decreasing concentration of STB. Unlike CT excitation, the excitation of the local band of *cis*-STB using 266- or 308-nm laser pulses gives rise to formation of *trans*-STB<sup>•+</sup>, regardless of the presence of TNM. To gain insights into earlier dynamics of the intimate ion pairs, faster kinetic studies are necessary.

**Table 6** BET Rates for Arene-TCNB CT Complexes Encapsulated in Na<sup>+</sup>Y

Arene	Dry		Hydrated	
	$k_{\text{BET}}$	Percentage (%) <sup>a</sup>	$k_{\text{BET}}$	Percentage (%) <sup>a</sup>
NAP	$4.9 \times 10^8$	57	$2.7 \times 10^9$	> 95
	$1.1 \times 10^7$	43		
PHN	$1.8 \times 10^8$	> 95	$1.9 \times 10^9$	
PYR	$1.0 \times 10^9$	83		
	$< 1.0 \times 10^7$	17		
ANT	$1.5 \times 10^9$	69	$1.4 \times 10^{10}$	67
	$9.5 \times 10^7$	31	$1.3 \times 10^8$	33

<sup>a</sup> The decay curves were analyzed with a double-exponential function, and the percentage represents the amount of the fast component.

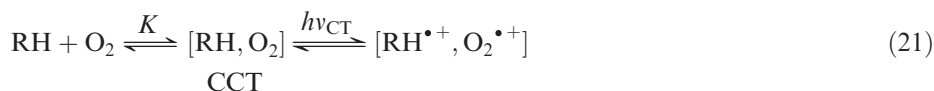
Source: Data from Ref. 11.

## 5. Hydrocarbon–Oxygen CT Complexes

The CT complexes described in the previous sections are useful for elucidating novel informations about zeolites and for providing insights into the design of the systems that leads to long-lived CSS. This section now introduces the formation of CT complexes consisting of hydrocarbon (RH) and O<sub>2</sub> that give CT bands in the visible region (54–60). The corresponding visible CT excitation leads to selective formation of very useful oxygenated products, which otherwise would be difficult to obtain by conventional autooxidation reactions.

The RHs that have been tested are listed in Table 7. Coadsorption of one of the RHs and oxygen onto dry zeolites usually gives a new absorption band whose onset extends to the visible region. The CT nature of the new absorption band is established by the progressive red shift of the onset with decreasing IP of RH. For instance, as shown in Fig. 30, the onset of the diffuse reflectance spectra shifts to longer wavelengths with decreasing IP of the olefin: about 450 nm for *trans*-2-butene (IP = 9.13 eV), 500 nm for 2-methyl-2-butene (IP = 8.67 eV), and 750 nm for 2,3-dimethyl-2-butene (IP = 8.30 eV). The typical applied pressures of olefin and oxygen are 1–10 and 750 Torr, respectively.

In fact, the mixtures of RH and O<sub>2</sub> have been known to form contact charge-transfer (CCT) complexes in gas phase and in solution [Eq. (21)].



Here the CCT complexes mean those CT complexes with very low formation constants

**Table 7** Hydrocarbon Donors Tested for CT Complexation with O<sub>2</sub> in Zeolites and Corresponding Intermediates and Oxygen Adducts Generated by CT Excitation According to Eqs. (22)–(24)

RH						
	(R <sub>1</sub> /R <sub>2</sub> = H/H, H/CH <sub>3</sub> , CH <sub>3</sub> /CH <sub>3</sub> )		(R <sub>1</sub> /R <sub>2</sub> = H/H, H/CH <sub>3</sub> , CH <sub>3</sub> /H)	(R = H, CH <sub>3</sub> , CH <sub>2</sub> CH <sub>3</sub> )	(R <sub>1</sub> /R <sub>2</sub> = H/H, H/CH <sub>3</sub> , CH <sub>3</sub> /CH <sub>3</sub> )	(Ar = C <sub>6</sub> H <sub>5</sub> )
RH <sup>••</sup>						
R•						
ROOH						
Ref.	54	55	56, 57 <sub>i</sub>	57	58	59

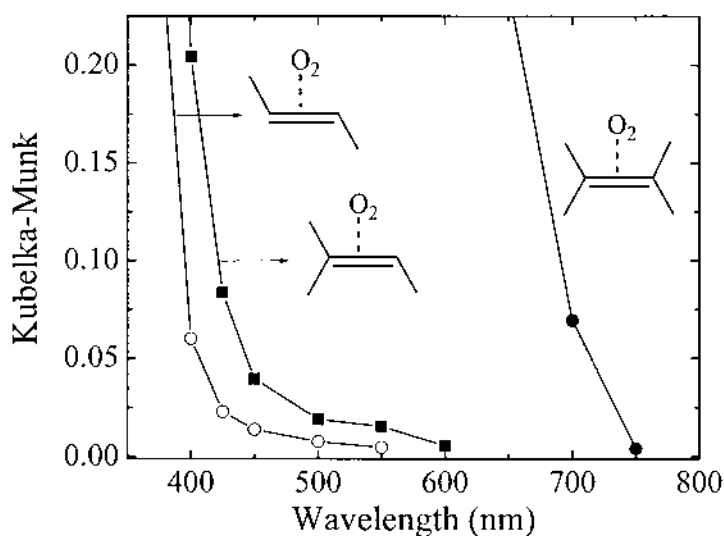


**Fig. 30** The tail absorption of olefin-O<sub>2</sub> complex (as indicated) that extend to the visible region. (Data extracted from Ref. 58.)

(K). Accordingly, their lifetimes in the complexed states are very short. The spectroscopic observations of RH-O<sub>2</sub> CCT complexes have been made in oxygen-saturated organic solutions (61), high-pressure mixtures of RH and O<sub>2</sub> (62) and solid mixtures of RH and O<sub>2</sub> gases (63,64). The degree of red shift for the RH-O<sub>2</sub> CT absorption from the gas phase to solution is usually insignificant (at most a few nanometers) (65), and the shift has been attributed primarily to compression of the complex in the condensed phase (66). The shift from a nonpolar to a polar organic solvent has also little effect on the RH-O<sub>2</sub> CT absorption band (61,67). The red shifts arising from transition from O<sub>2</sub>-saturated solution of RH to a solid RH-O<sub>2</sub> matrix are only about 10 nm (63,64).

Upon comparing with the above, the observed red shifts of about 12,000 cm<sup>-1</sup> (1.5 eV) of the onsets of the olefin-O<sub>2</sub> CT spectra in Na<sup>+</sup>Y relative to the corresponding absorptions in the conventional media are truly remarkable. The observed shifts are at least an order of magnitude larger than those that can be achieved by varying the solvent polarity. The strong electrostatic fields of the zeolite pores are attributed to be responsible for the remarkable red shifts since they can effectively stabilize the charge-transferred excited state of alkene-O<sub>2</sub> CT complex, as schematically depicted in Fig. 31. In support of this, the electrostatic field within zeolite pores has been estimated to be one to several volts per angstrom at a distance of 2–4 Å from an Na<sup>+</sup> ion (41,68). The measurements of the intensity of the electric field-induced IR absorptions of homonuclear diatomic molecules (N<sub>2</sub>, O<sub>2</sub>) and methane, and ESR studies (69) also give the similar magnitude of electric fields in zeolites.

The RH-O<sub>2</sub> absorption band undergoes a more pronounced red shift in Ba<sup>2+</sup>Y as demonstrated in Fig. 32. Thus, the onset of diffuse reflectance spectra of *trans*-2-butene-O<sub>2</sub> in Ba<sup>+</sup>Y is between 500 and 550 nm, which corresponds to a further red shift by about

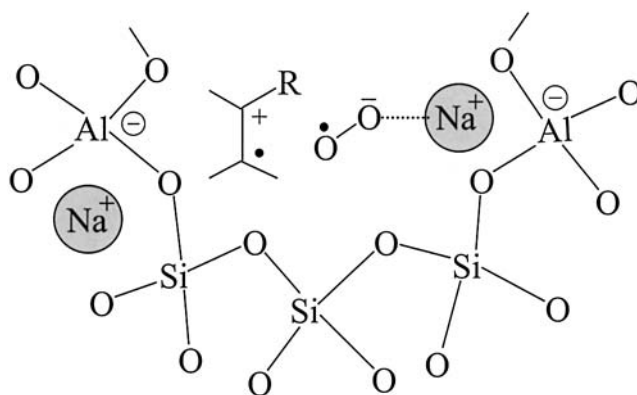


**Fig. 31** Possible orientation of the electron-transferred state of an olefin- $O_2$  CT complex between the negatively charged framework and the cation leading to remarkable stabilization of the excited state. (Adapted from Ref. 7a.)

100 nm, with respect to the corresponding onset in  $Na^+Y$  (~450 nm, vide supra). Isobutane (54b) and toluene (56a) also show similar tail absorptions that extend to visible region when mixed with  $O_2$  in  $Ba^{2+}Y$ . The more pronounced red shift is attributed to an increase in the charge density arising from employing a divalent cation, which gives rise to increase in the electric field. The use  $Ba^{2+}$  is more effective than that of  $Ca^{2+}$  since the large  $Ba^{2+}$  ions cannot enter the sodalite units and hexagonal prisms, and as a result, all of the exchanged  $Ba^{2+}$  ions reside in the supercage (70). There are, however, some concerns

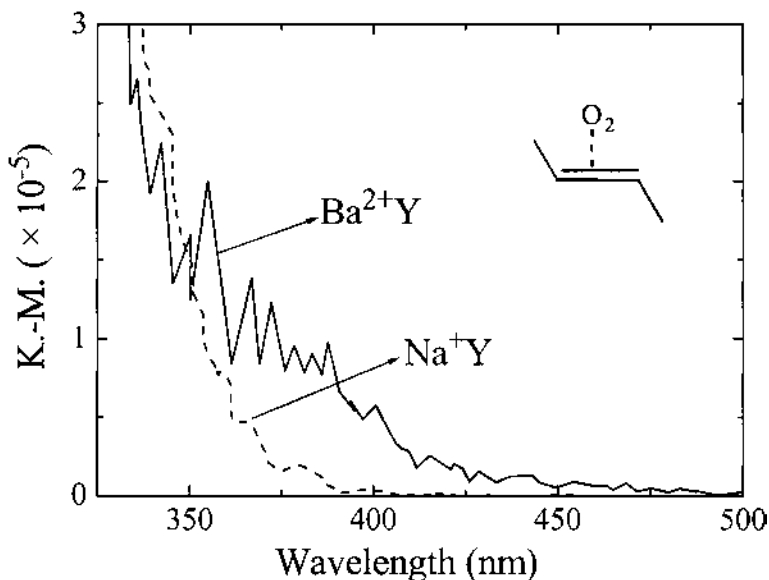


**Fig. 32** Effect of  $Ba^{2+}$  on the *trans*-2-butene- $O_2$  CT band. (Data extracted from Ref. 56d,e.)

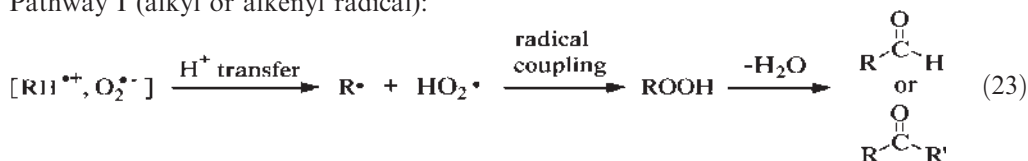
in assigning the tail absorptions to RH-O<sub>2</sub> CT bands from the absence of absorption maxima even in Ba<sup>2+</sup>Y and from the nonlinear relationship between the onset of the adsorption and the IP of RH.

CT excitation of intrazeolite RH-O<sub>2</sub> CT complexes by visible light leads to selective formation of various oxygenated products (54–60). Analyses of the products and intermediates suggest that the reactions undergo via PET from RH to O<sub>2</sub> according to Eq. (22).

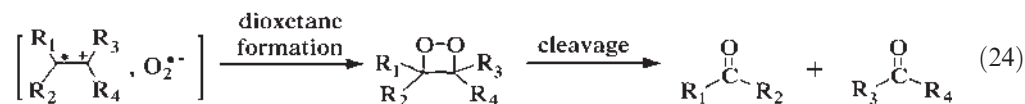


The proposed radical cations of RH (RH<sup>•+</sup>) are listed in Table 7. The resulting ion pairs undergo either pathway I [Eq. (23)] or both pathway I and pathway II [Eq. (24)] depending on the type of RH.

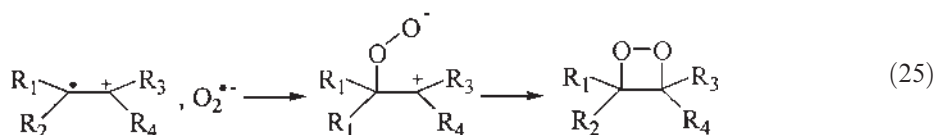
Pathway I (alkyl or alkenyl radical):



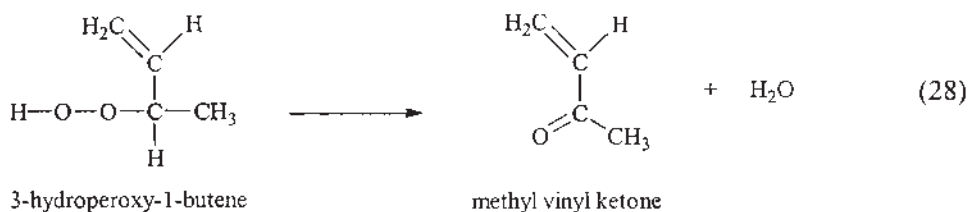
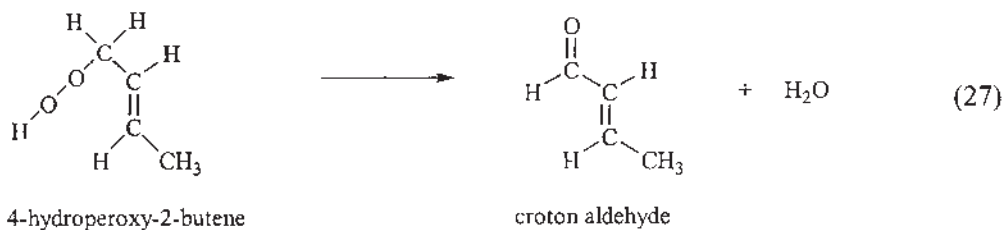
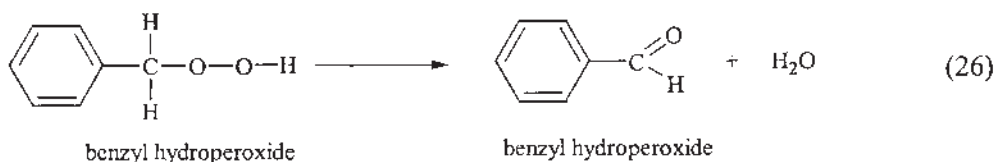
Pathway II (alkenyl radical):



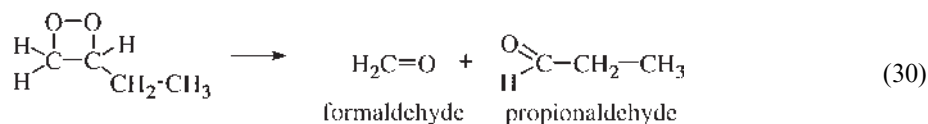
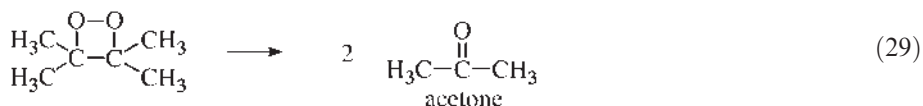
The ion pairs generated from saturated hydrocarbons only undergo proton shift from RH<sup>•+</sup> to superoxide (O<sub>2</sub><sup>•-</sup>) followed by radical coupling between alkyl radical (R<sup>•</sup>) and hydroperoxy radical (HO<sub>2</sub><sup>•</sup>), leading to exclusive formation of alkyl hydroperoxide (ROOH). The ion pairs generated from unsaturated hydrocarbons (alkenyl radical cation and superoxide) follow both pathways. Thus, they can also undergo dioxetane formation (pathway II) via direct radical coupling between alkenyl radical cation and O<sub>2</sub><sup>•-</sup> according to Eq. (25) in addition to proton shift that leads to formation of alkenyl hydroperoxide (pathway I).



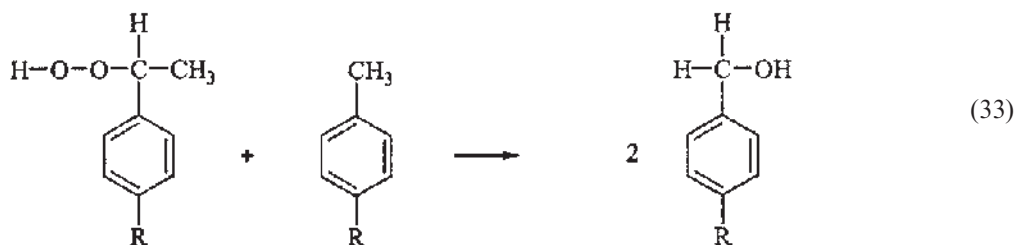
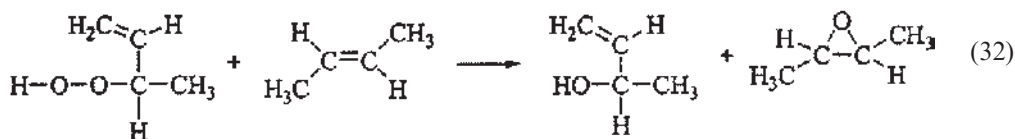
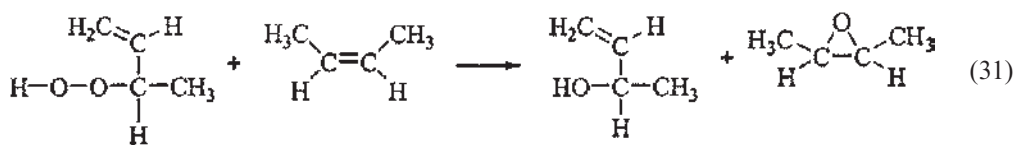
When the produced alkyl or alkenyl hydroperoxides are unstable they readily undergo dehydration leading to formation of either corresponding aldehydes or ketones depending on the structure of the hydrocarbon backbone [Eqs. (26)–(28)].



The produced dioxetanes undergo cleavage and eventually lead to formation of a variety of saturated aldehydes and ketones, some of which are described below.



Because oxygen atom transfer can occur from alkyl or alkenyl hydroperoxides to parent reactants, complications also arise in pathway I. For instance, 3-hydroperoxy-1-butene epoxidizes excess reactants (alkenes) such as *cis*- and *trans*-2-butene in a stereo-selective way [Eqs. (31) and (32)]. The benzyl hydroperoxides also undergo oxygen atom transfer to the parent compound [Eq. (33)]. Thus, the subsequent oxygen atom transfer reactions furnish further diversity to the oxygenated products.



The photoyield increases with increasing the strength of the electric field at the cation site (56b). For instance, as shown in Fig. 33, the photoyield of benzaldehyde from the mixture of toluene and O<sub>2</sub> increases on going from X to Y and Na<sup>+</sup> to Ba<sup>2+</sup>, consistent with the increase in the strength of electric field. This result indicates that stabilization of ion pair [RH<sup>•+</sup>, O<sub>2</sub><sup>•-</sup>] is one of the rate-determining steps for product formation. It was revealed that the presence of Brønsted acid sites in the zeolite hosts leads to production of

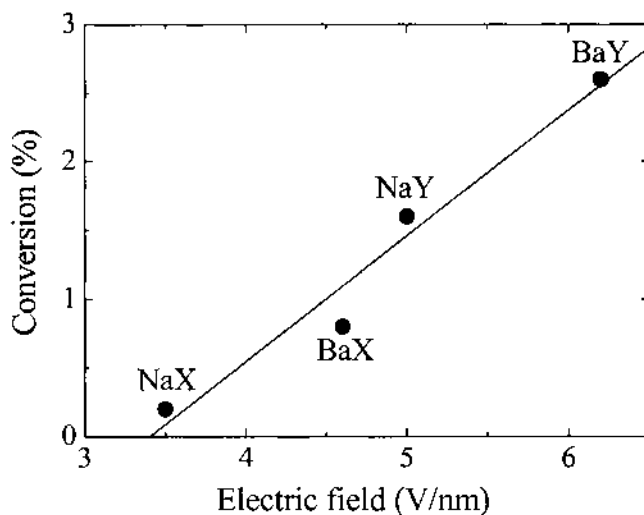
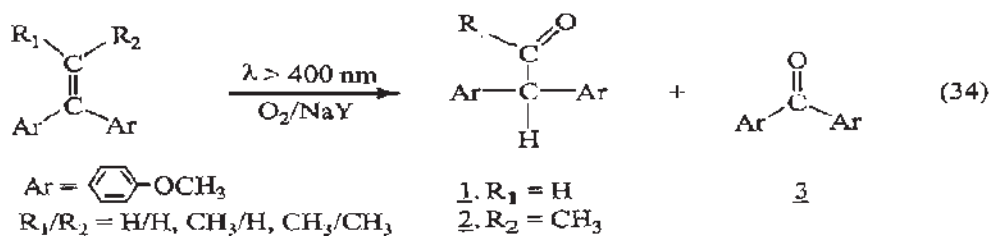


**Fig. 33** Correlation between the strength of electric field within zeolite and the photoyield of benzaldehyde from the visible ( $\lambda > 400$  nm) excitation of toluene–O<sub>2</sub> CT complex encapsulated in zeolites. (Data extracted from Ref. 56b.)

a variety of acid-catalyzed secondary products. In this respect, to achieve high reactivity and selectivity, the content of Brønsted acid site should be minimized while maximizing the electric field at the cation site, which is obviously difficult.

Interestingly, in the case of 1,1-diarylethylene, the visible irradiation ( $\lambda > 400$  nm) of the compounds in  $\text{Na}^+\text{Y}$  in the presence of  $\text{O}_2$  yields 1,1-diarylmethyl aldehyde ( $\text{R}_1 = \text{H}$ , 1) or 1,1-diarylpropane-2-one ( $\text{R}_1 = \text{CH}_3$ , 2) as well as diarylketone (3), as shown in Eq. (34) (60).



While pathway II [Eq. (34)] seems to be responsible for the formation of diarylketone (3), the mechanism for formation of 1 and 2 is not clear. The unusual products are likely to be formed via hydrogen atom abstraction from the solvent (*n*-hexane) by the generated radical cation of the parent olefin followed by subsequent reaction of the aralkyl carbonium ion with the superoxide anion ( $\text{O}_2^{\bullet-}$ ), which is usually the least favored pathway in solution.

## B. ET Between Intercalated Species by Photosensitization

### 1. ET from Photosensitized Arenes to Alkali-Metal Cations

As discussed in Secs. II.A.1.b (p. 608) and II.A.3 (p. 622) alkali metal ions are very weak electron acceptors. Accordingly, in many PET reactions in zeolites, they usually behave as inert charge-balancing agents for the negatively charged frameworks. In contrast, clusters of alkali metal ions, in particular four sodium ions ( $4 \text{Na}^+$ ) residing in the sodalite units of faujasite-type zeolites, act as relatively strong electron acceptors or electron trapping sites. Thus, they often temporarily accommodate electrons ejected from photoexcited arene and alkene donors; as a result, CS exists between the photo-oxidized organic donors and the reduced form of tetranuclear sodium ionic cluster, which is usually expressed as  $\text{Na}_4^{3+}$ .

For instance, photoexcitation of ANT or PYR incorporated within dehydrated  $\text{Na}^+\text{Y}$  or  $\text{Na}^+\text{X}$  by 333 nm leads to photoexcited singlet state of the arene,  $^1\text{*ANT}$  or  $^1\text{*PYR}$ , which subsequently undergoes ET to a group of four sodium ions residing in sodalite units (71). As a result,  $\text{ANT}^{\bullet+}$  or  $\text{PYR}^{\bullet+}$  and  $\text{Na}_4^{3+}$  appear as transient species (Fig. 34), and BET from  $\text{Na}_4^{3+}$  to the arene radical cation ( $\text{ArH}^{\bullet+}$ ) takes place as time elapses. The tetranuclear sodium ionic cluster is usually characterized by a broad absorption band with  $\lambda_{\text{max}}$  at around 550 nm and a 13-line ESR spectrum with the *g* value of about 2.00. The details about alkali metal ionic clusters are described separately in Sec. II.B.4 (p. 657).

A linear relationship exists between the laser intensity and the yield of  $\text{PYR}^{\bullet+}$  in  $\text{Na}^+\text{X}$  with the laser power of up to  $8 \text{ mJ/cm}^2$ . This initially suggests that the PET process is monophotonic, i.e., the PET is a single-photon process. However, the result from an independent oxygen quenching study of  $\text{PYR}^{\bullet+}$  suggests that an independent biphotonic (two-photon) PET process also exists. In other words, both one-photon and two-photon

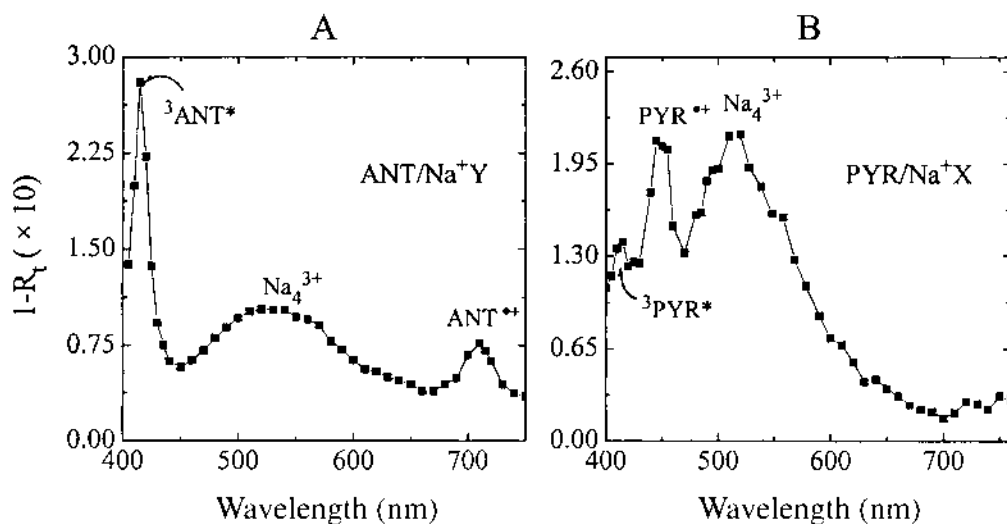


**Fig. 34** Diffuse-reflectance transient spectra of dehydrated ANT-impregnated Na<sup>+</sup>Y (A) and PYR-impregnated Na<sup>+</sup>X (B) immediately after laser excitation with a nitrogen laser (337 nm).  $1-R_t$  in the  $y$  axis represents  $(J_0 - J_t)/J_0$ , where  $J_0$  is the initial reflectance light from the sample before the laser pulse and  $J_t$  is the reflected light at time  $t$  after laser excitation. The value  $1-R_t$  is a linear function of the amount of transient present. (Adapted from Ref. 10a.)

absorptions lead to PET from PYR to 4 Na<sup>+</sup>. From the fact that only biphotonic processes are allowed to induce PET from arenes adsorbed on silica gel or alumina to the solid support (72) and from the consideration that polar environment results in lowering of the ionization energy from that of the gas phase value, the highly polar nature of the zeolite cage is attributed to be responsible for the occurrence of the monophotonic PET process. Alternatively, the CT interaction between the incorporated arene donor and the electron-acceptor site may be responsible for the monophotonic PET.

The simultaneous appearance of the triplet excited state of each arene (<sup>3</sup>\*ANT and <sup>3</sup>\*PYR, respectively) in each spectrum of Fig. 34 indicates that the singlet excited state (<sup>1</sup>\*ANT or <sup>1</sup>\*PYR) also undergoes intersystem crossing to the triplet state.

For the PET from photoexcited arene donors (\*ArH) to four Na<sup>+</sup> ions to be effective, the zeolite host should be dry and the degree of loading of arene donors should be very low, such as less than one arene per 10 supercages. At high loading levels of arenes, PET also readily takes place between the incorporated arenes as discussed in more detail in Sec. II.B.2 (p. 640). From the lack of direct contacts between the arene donors in supercages and the four Na<sup>+</sup> ions in sodalite units, a stepwise ET from \*ArH to the conduction band of the zeolite framework and subsequently to four sodium ions is suggested, as schematically illustrated in Fig. 35.

In contrast, the arene donors adsorbed on the external surface of NaA do not induce such PET. This may result presumably due to the existence of the externally adsorbed arene donors in the crystalline form. Alternatively, the reduction potential of a group of four sodium ions may significantly shift to the negative direction due to increased basicity (electron donor property) of the framework of A, since framework basicity sensitively affects the acceptor strength of the charge-balancing cation, as discussed in Sec. III (p. 663).

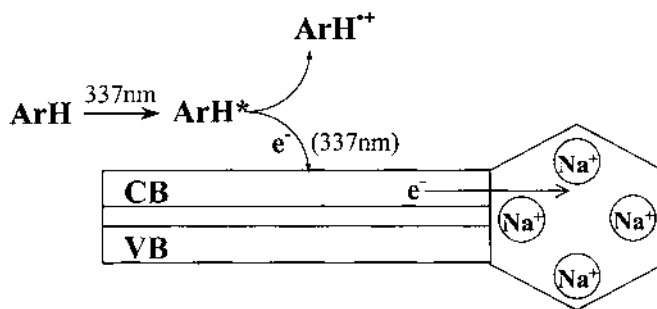


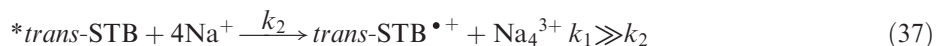
**Fig. 35** Proposed scheme for sequential PET from an arene donor (ArH) to the conduction band (CB) of the zeolite framework followed by thermal ET to four Na<sup>+</sup> ions residing in a sodalite unit.

NAP and BIP were also proposed to undergo PET to groups of two and three sodium ions (2 Na<sup>+</sup> and 3 Na<sup>+</sup>) even in hydrated Na<sup>+</sup>X and Na<sup>+</sup>Y at very low loading levels of the arenes (less than two arene donors per 100 supercages) (73). In the case of NAP, increase in the loading level leads to formation of a dimer cation, (NAP)<sub>2</sub><sup>•+</sup>, which is likely to proceed by the association of NAP<sup>•+</sup> and NAP residing in the same or in the neighboring supercages [Eq. (35)].



The dimer radical cation is characterized by a broad featureless absorption band with  $\lambda_{\text{max}}$  at 590 and 1100 nm. The lower energy band (1100 nm) originates from CT transition from the neutral NAP to NAP<sup>•+</sup>. Interestingly, the lifetime of (NAP)<sub>2</sub><sup>•+</sup> is significantly longer (~100 ms) in the supercages of X or Y than in solution, presumably due to the confinement effect of the cages. From this respect, the zeolite cages can be likened to low-temperature glassy matrices, tethered polymer systems, and supersonic jets in which various cluster ions have longer lifetimes.

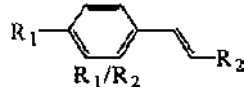
Photoexcitation (266 or 308 nm) of either *cis*- or *trans*-STB in Na<sup>+</sup>X leads to formation of only *trans*-STB<sup>•+</sup> and Na<sub>4</sub><sup>3+</sup> (49). This suggests that *cis*-to-*trans* isomerization of photoexcited *cis*-STB (*\*cis*-STB) [Eq. (36)] takes place much faster than ionization of *\*cis*-STB [Eq. (37)]. When the zeolite is not rigorously dry the formation of only *trans*-STB<sup>•+</sup> takes place but not Na<sub>4</sub><sup>3+</sup> (74).



Again, the yields of both *trans*-STB<sup>•+</sup> and Na<sub>4</sub><sup>3+</sup> are substantially higher in dry Na<sup>+</sup>X, and oxygen (O<sub>2</sub>) accelerates the decay of Na<sub>4</sub><sup>3+</sup>. Interestingly, photoexcitation (532 nm) of Na<sub>4</sub><sup>3+</sup> by a second laser pulse after a 1- to 2- $\mu$ s delay from the first laser shot leads to efficient bleaching of the transient species. However, bleaching dose not lead to formation of radical anion of the parent arene donor via electron trapping or to decay of *trans*-STB<sup>•+</sup> via charge recombination with the ejected electron. This suggests that photoexcitation of Na<sub>4</sub><sup>3+</sup> results in redistribution of the trapped electrons to other unknown electron-accepting sites in zeolite frameworks.

Photoexcitation (266 nm) of a series of STY derivatives listed in Table 8 in Na<sup>+</sup>Y also leads to formation of the corresponding radical cation and Na<sub>4</sub><sup>3+</sup> [Eq. (38)] (75).

**Table 8** Comparison of the First-Order Decay Rate Constants<sup>a</sup> of Some Radical Cations of STY Derivatives in Na<sup>+</sup>Y and in Acetonitrile

	NaY <sup>b</sup>		CH <sub>3</sub> CN <sup>c</sup>
	Fast	Slow	
H/H	4.5	0.5	~50000
CH <sub>3</sub> /H	2.6	0.4	300
OCH <sub>3</sub> /H	1.4	0.1	1.3
OCH <sub>3</sub> /CH <sub>3</sub>	0.05	0.05	0.04

<sup>a</sup> In 10<sup>6</sup> s<sup>-1</sup>.

<sup>b</sup> Data from Ref. 75.

<sup>c</sup> Data from Ref. 76.



(R<sub>1</sub>/R<sub>2</sub>) = (H/H), (CH<sub>3</sub>/H), (OCH<sub>3</sub>/H), (OCH<sub>3</sub>/CH<sub>3</sub>)

BET of the above proceeds in a biphasic manner, and the analyzed BET rate constants ( $k_{\text{BET}}$ ) for the fast and slow parts are listed in Table 8 in comparison with the corresponding rate constants measured in solution (CH<sub>3</sub>CN). As noted, the decay rates for the radical cation of (H/H) and (CH<sub>3</sub>/H) are about four and two orders of magnitude slower in Na<sup>+</sup>Y than in CH<sub>3</sub>CN, respectively, while those of (OCH<sub>3</sub>/H) and (OCH<sub>3</sub>/CH<sub>3</sub>) are nearly the same. This indicates that the stabilizing effect of the zeolite cage is far more effective for those radical cations that are less stable in solution. This result again demonstrates the stabilizing effect of zeolite cages for those highly reactive species in solution.

Cyanoarene sensitizers such as 1-CNNAP, 2,3-(CN)<sub>2</sub>NAP, and 9-CNANT also generate the corresponding radical cations and Na<sub>4</sub><sup>3+</sup> upon laser excitation (266 nm or 355 nm) in Na<sup>+</sup>X (77). For instance, photoexcitation of 2,3-(CN)<sub>2</sub>NAP with 266 nm leads to simultaneous formation of 2,3-(CN)<sub>2</sub>NAP<sup>•+</sup> and Na<sub>4</sub><sup>3+</sup> at 380 and 560 nm, respectively, as shown in Fig. 36A. As noted, the presence of 2,3-(CN)<sub>2</sub>NAP<sup>•+</sup> is not so apparent due to its weaker absorption than that of Na<sub>4</sub><sup>3+</sup>. However, use of chlorinated solvents such as dichloromethane leads to significant suppression of the absorption of Na<sub>4</sub><sup>3+</sup> presumably due to ET from Na<sub>4</sub><sup>3+</sup> to chlorinated solvents [Eq. (39)].



Figure 36B further demonstrates that the decay of Na<sub>4</sub><sup>3+</sup> (absorption of 560 nm) is faster when PET from 2,3-(CN)<sub>2</sub>NAP to 4 Na<sup>+</sup> is carried out using 15% dichloromethane/*n*-hexane mixture than using pure *n*-hexane. Therefore, the use of chlorinated solvents seems to be useful for obtaining clearer transient spectra of arene radical cations with small molar extinction coefficients, which otherwise would be obscured by the intense

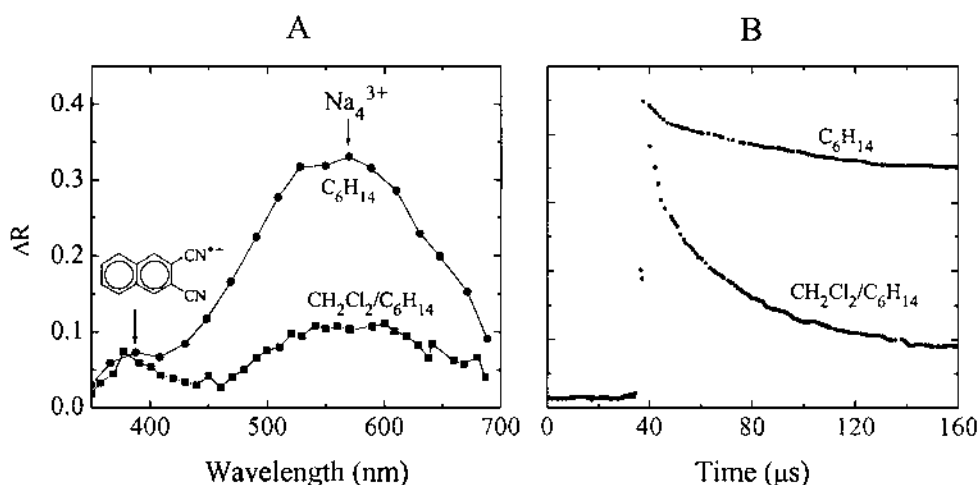


**Fig. 36** (A) Transient spectra measured after 266 nm excitation of samples of 2,3-dicyanonaphthalene (10  $\mu\text{mol/g}$ ) in  $\text{Na}^+\text{X}$  prepared using hexane (●) or 15% dichloromethane/hexane (■) as solvent. (B) Normalized decay traces measured at 560 nm under conditions of A. (Adapted from Ref. 77.)

spectrum of  $\text{Na}_4^{3+}$ . The use of hydrated zeolites as the hosts may be an alternative way to suppress the formation of  $\text{Na}_4^{3+}$  (73). However, oxygen ( $\text{O}_2$ ) is more often the reagent of the choice since it can also conveniently remove  $\text{Na}_4^{3+}$  according to the following reaction:



For instance, as shown in Fig. 37, a clear spectrum of the radical cation of *trans*-anethole (*trans*-ANE $^+$ ) can be generated in  $\text{Na}^+\text{X}$  by 266-nm irradiation of the sample saturated with  $\text{O}_2$ .

1,1-Diarylethylenes also undergo photoionization-accompanying generation of  $\text{Na}_4^{3+}$  in  $\text{Na}^+\text{Y}$  upon direct irradiation at 254 nm (60). In fact, the most preferred reaction of the radical cations of 1,1-diarylethylenes in solution is addition to the parent olefin. Interestingly, however, formation of 1,1-diarylethanes via hydrogen abstraction from the solvent (*n*-hexane) by the radical cation of 1,1-diarylethylenes is the exclusive pathway in zeolite despite the fact that this is the least favored in solution. Another interesting point is that presence of  $\text{O}_2$  is a prerequisite for the radical cations of 1,1-diarylethylenes to undergo hydrogen abstraction. Equation (40) may be responsible for providing the generated 1,1-diarylethylene longer chances to undergo relatively slower hydrogen abstraction processes.

While teaming up is indispensable for alkali metal ions to behave as practical electron-accepting centers, even a single cation can serve as the acceptor when the cation has reasonably high acceptor strength. Indeed, upon irradiation at 320 nm, PET from a series of *N*-alkyl phenothiazine (Cn-PHT) to transition metal cations such as  $\text{Cu}^{2+}$ ,  $\text{Fe}^{3+}$ ,  $\text{Cr}^{3+}$ ,  $\text{Ni}^{2+}$ , and  $\text{Mn}^{2+}$  readily takes place in zeolites and the related microporous and mesoporous materials [Eq. (41)] (78).

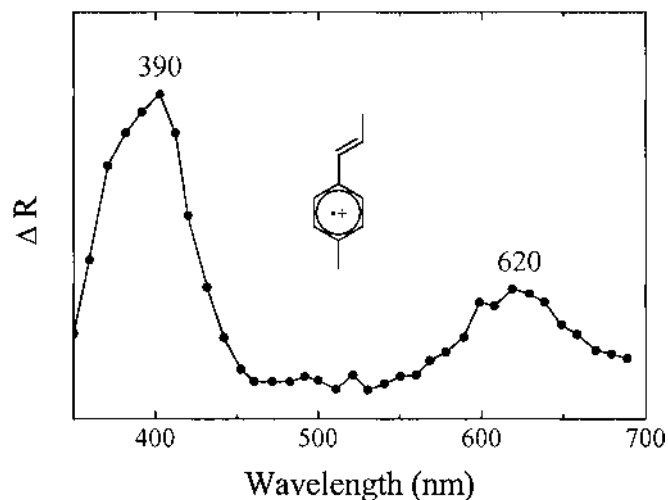
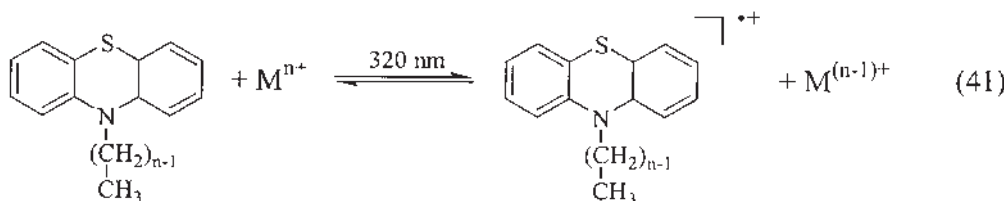


**Fig. 37** Transient spectrum of radical cation of *trans*-anethole (*trans*-ANE) obtained by 266 nm excitation of O<sub>2</sub>-saturated compound in Na<sup>+</sup>X after 20 μs delay showing the full suppression of the absorption by Na<sub>4</sub><sup>3+</sup> at approximately the 550 nm region.



$n = 1, 3, 6, 10, 16$

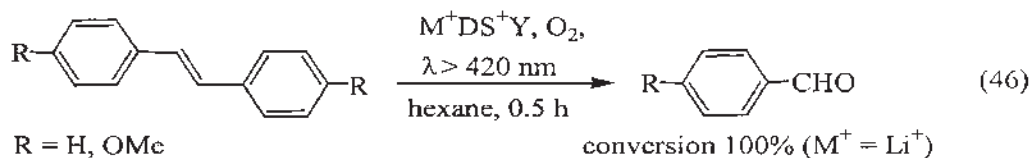
$\text{M}^{n+} = \text{Cu}^{2+}, \text{Fe}^{3+}, \text{Cr}^{3+}, \text{Ni}^{2+}$  and  $\text{Mn}^{2+}$

As can be expected, the photoyield increases with increasing acceptor strength and concentration of the transition metal cation. The photoyield also increases with increasing alkyl chain length consistent with the increase in the donor strength of C<sub>n</sub>-PHT with increasing chain length. In the cases where strong acceptor cations such as Cu<sup>2+</sup> and Fe<sup>3+</sup> are employed, thermal ET also takes place from C<sub>n</sub>-PHT to the transition metal ions. Even for a weak acceptor such as Ni<sup>2+</sup>, thermal ET becomes significant when the concentration of the cation increases (78b). This indicates that the thermal ET process is governed by thermodynamic equilibrium.

While Na<sup>+</sup> ions serve as electron acceptors in alkali-metal cation exchanged zeolites, the transition metal cations imbedded within the frameworks of mesoporous materials also serve as electron acceptors. For instance, PET from C<sub>n</sub>-PHT to the transition metal in MUHM-3 (M = Cu, Ni, Cr, and Mn), MSBA-15 (M = V, Ti), and MAPO-5, and 11 (M = V, Ti) occurs readily (79,81). ET also takes place from the photoexcited 5,10,15,20-tetraphenyl-21H,23H-porphine manganese(III) to Ti<sup>4+</sup> in the framework of TiMCM-41 (81).



pylium ( $\text{DBT}^+$ ), and triarylmethyl cation have been incorporated into zeolites and mesoporous silica and their photosensitized ET activities have been tested (85). Among these  $\text{THN}^+$ ,  $\text{MTB}^+$ , and  $\text{MTG}^+$  can be incorporated into zeolites by simple aqueous ion exchange. The Y incorporating a dye sensitizer ( $\text{DS}^+\text{Y}$ ) can selectively oxidize *trans*-STB and its derivative into aldehydes when irradiated in the presence of oxygen [Eq. (46)].



The proposed scheme for the above reaction follows [Eqs. (47)–(50)].



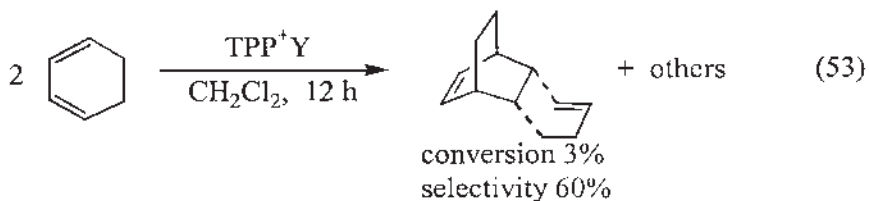
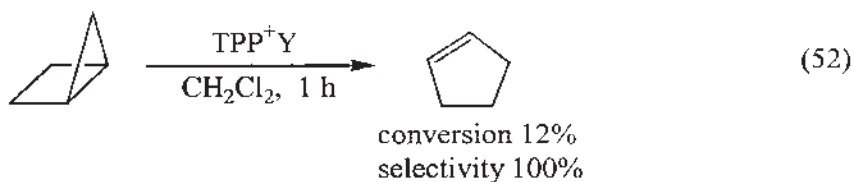
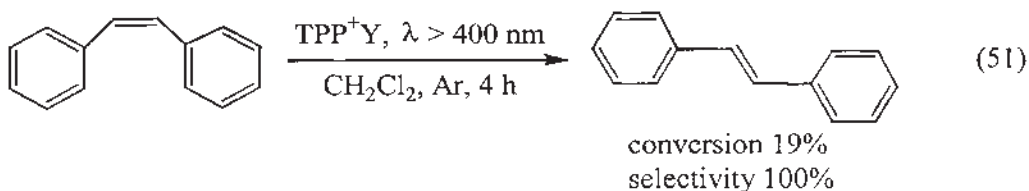
The reaction proceeds much more effectively in zeolite than in hexane solution. Thus, while the conversion reaches 100% within 0.5 h irradiation in zeolite, it reaches only 50% even after 6 h irradiation in hexane. The high efficiency in zeolite seems to stem from high local concentration of substrate near  $\text{DS}^+$  in zeolite rather than in solution since zeolites have a much higher affinity for arenes and olefins than hexane. The zeolite should be kept dry in the above reaction system to prevent the dyes from aggregating within zeolite pores (86) since the aggregated dyes undergo efficient self-quenching in the excited singlet state (87). The zeolitic water will also prevent inclusion of the substrates into the pores and quench the singlet oxygen.

Interestingly, the yield progressively decreases upon increasing the size of charge-balancing alkali metal cation from  $\text{Li}^+$  to  $\text{Cs}^+$ , i.e., in the order:  $\text{Li}^+ > \text{Na}^+ > \text{K}^+ > \text{Rb}^+ > \text{Cs}^+$ . The decrease in the supercage volume, which hampers close contact between  $\text{DS}^+$  and the substrate, might be responsible for the above trend. Alternatively, the increase in the degree of ET from the framework to  ${}^1\text{DS}^+$  seems to be more responsible for the progressive decrease in the yield consistent with the increase in the donor strength of the framework (see Sec. IIIA, p. 666).

#### b. Triarylpopylium and Triarylmethyl cation as the Photosensitizers

Incorporation of  $\text{TPP}^+$  is carried out by direct synthesis of the sensitizer in zeolite by applying the so-called ship-in-a-bottle strategy (88). Encapsulation of this large sensitizer cation in Y is carried out by acid-catalyzed reaction of chalcone and acetophenone in isoctane at  $110^\circ\text{C}$ . The zeolite-encapsulated  $\text{TPP}^+$  shows moderate activities as an ET

photosensitizer toward isomerization of *cis*-STB to *trans*-STB (88), bicyclo[2,1,0]pentane (housane) to cyclopentene (89), and cyclodimerization of 1,3-cyclohexadiene to [4+2] endo dimer (90) [Eqs. (51)–(53)].



The above reactions proceed by ET from the substrate (SUB) to the photoexcited TPP<sup>+</sup> (\*TPP<sup>+</sup>) according to the following equation:



Unlike oxidation of *trans*-STB [Eq. (46)], the conversions of the above isomerization reactions are significantly lower in the heterogeneous systems than in solution. The poor yields seem to arise from the employment of dichloromethane as the solvent, which disfavors inclusion of hydrocarbon substrates into the interior of Y. In this respect, reexamination of the above reactions seems to be necessary by employing nonpolar hydrocarbon solvents such as *n*-hexane and *n*-octane.

In the case of *cis*-to-*trans* isomerization of STB, addition of azulene ( $E=0.95$  V vs. SCE) into the heterogeneous mixture to quench the out-of-cage fraction of the photosensitized *cis*-STB leads to a decrease of the initial yield to 60% of that in the absence of azulene. However, the resulting yield is still considerably higher than that obtained in the homogeneous solution in the presence of azulene. The smaller degree of quenching by azulene in TPP<sup>+</sup>Y than in solution is attributed to slower diffusion of *cis*-STB<sup>•+</sup> in zeolite since this radical cation has to balance the negative framework charge. The above result further indicates that CS occurs to a considerable extent inside the

supercages of Y. Interestingly, unlike in homogeneous solution, the isomerization reaction is not perturbed by the presence of oxygen and no byproducts are formed from oxidative cleavage. This is attributed to the “cage effect” of zeolite. The *cis-to-trans* isomerization of STB is more efficient when TPP<sup>+</sup> is encapsulated within the large channels (~20 Å) of MCM-41 (91).

In the case of photosensitized dimerization of 1,3-cyclohexadiene, the high selectivity to [4+2] endo dimer confirms that the reaction proceeds by Eq. (52) (90). The selectivity decreases when DBT<sup>+</sup> is employed instead of TPP<sup>+</sup> in ZSM-5 (90). Interestingly, while DBT<sup>+</sup> is readily attacked by H<sub>2</sub>O in solution, it survives for a much longer period in hydrated Y (~15 days). Moreover, it remains intact for several months in the narrow channels of ZSM-5. This phenomenon is attributed to the “tight fit” of the cation within the channels. Thus, the lack of space for the transition state seems to help preserve DBT<sup>+</sup> from the nucleophilic attack by water.

Similarly, nucleophilic addition of water to TPP<sup>+</sup> takes place very rapidly in solution and this leads to formation of 1,3,5-triphenylpent-2-en-1,5-dione (PDO). For instance, TPP<sup>+</sup>BF<sub>4</sub><sup>-</sup> becomes completely hydrolyzed in a few hours when suspended in water although the salt is sparingly soluble in it. However, TPP<sup>+</sup>BF<sub>4</sub><sup>-</sup> survives long enough in an aqueous acetonitrile (50%) for the laser flash photolysis studies to be carried out. Under these conditions, the triplet excited state of TPP<sup>+</sup> (<sup>3</sup>\*TPP<sup>+</sup>) is the only transient species that is observed, but there is no evidence for the formation of TPP (92). This indicates that PET from H<sub>2</sub>O to TPP<sup>+</sup> does not occur in solution despite the fact that this process is predicted to be exergonic based on the Rehm-Weller equation (93) and despite the wide use of TPP<sup>+</sup> as ET photosensitizer (94).

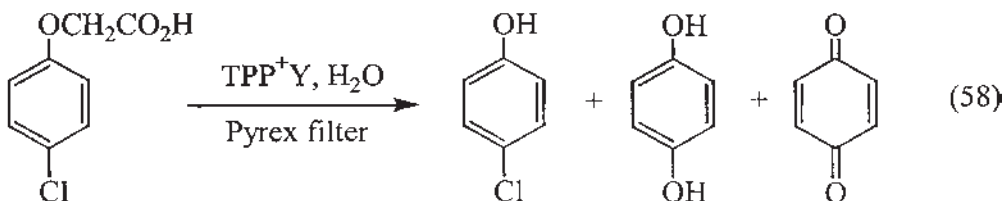
Surprisingly, cleavage of TPP<sup>+</sup> to PDO is totally (>3000 h) suppressed inside the supercages of Y, and PET occurs readily from H<sub>2</sub>O to TPP<sup>+</sup> upon irradiation at 355 nm [Eqs. (55) and (56)] (92). Furthermore, the zeolite-entrapped TPP<sup>+</sup> also remains intact from the attack by the powerful oxidizing hydroxyl radical HO•, which is generated by cleavage of H<sub>2</sub>O<sup>•+</sup> [Eqs. (55)–(57)].



Again, the tight fit of the bulky TPP<sup>+</sup> ion inside the rigid supercage seems to be responsible for keeping the ion safely from the attack by both H<sub>2</sub>O and HO•, which requires severe structural change of TPP<sup>+</sup>. The photoinduced generation of hydroxy radicals was confirmed by spin trapping with 5,5-dimethyl-1-pyrroline *N*-oxide (DMPO) and by time-resolved spectroscopy using benzene and MV<sup>2+</sup> as probes. The framework structure of the zeolite is not damaged by the hydroxy radical.

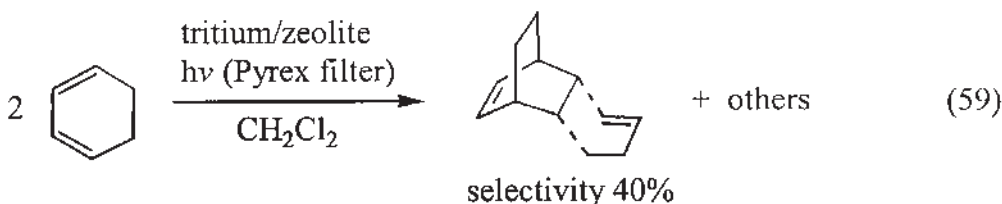
TPP<sup>+</sup>Y also shows high activity for removal of pollutants dissolved in water (93). For instance, the efficiency of TPP<sup>+</sup>Y is much higher than TiO<sub>2</sub> or TPP<sup>+</sup>-adsorbing SiO<sub>2</sub> (TPP<sup>+</sup>-SiO<sub>2</sub>) in oxidizing 4-chlorophenoxyacetic acid (CPA) from the aqueous solution

upon visible irradiation (Pyrex filter). CPA is often used as a model compound for other more widely used chlorinated herbicides.



The higher efficiency of  $\text{TPP}^+\text{Y}$  over  $\text{TPP}^+\text{-SiO}_2$  is ascribed to the ability of Y to absorb highly polar CPA into the supercages, which leads to a large increase in the local concentration of CPA near  $\text{TPP}^+$ . The catalytic oxidation of CPA by  $\text{TPP}^+\text{Y}$  seems to proceed via formation of  $\text{H}_2\text{O}_2$  as a result of oxidation of  $\text{H}_2\text{O}$  with  $^*\text{TPP}^+$  [Eq. (56)]. The detailed mechanism remains to be elucidated.

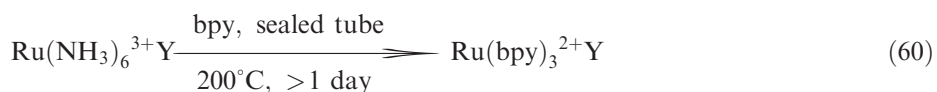
A series of substituted triarylmethyl cations (trityl cations or tritium) such as tris(4-methoxyphenyl)methyl cation ( $\text{TMM}^+$ , malachite green), bis(4-methoxyphenyl)phenylmethyl cation ( $\text{BMPM}^+$ ), and bis(4-dimethylaminophenyl)phenylmethyl cation ( $\text{BDPM}^+$ ) has also been prepared in Y, beta, and MCM-41 (95). They are also effective photosensitizers for dimerization of 1,3-hexadiene to give [4+2] endo dimer in high selectivity.



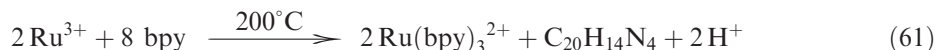
The trityl cations are synthesized from the reaction of benzaldehyde or a ring-substituted derivative and *N,N*-dimethylaniline or anisole.

### c. $\text{Ru}(\text{bpy})_3^{2+}$ as the Photosensitizer

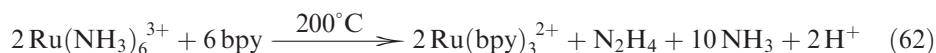
**SYNTHESIS AND CHARACTERIZATION.** Synthesis of  $\text{Ru}(\text{bpy})_3^{2+}$  (bpy = 2,2'-bipyridine) in the supercages of Y (96) and the subsequent PET from the excited triplet state of the  $\text{Ru}(\text{II})$ -complex ( $^*\text{Ru}(\text{bpy})_3^{2+}$ ) to the acceptors placed in the neighboring cages have been extensively studied. The intrazeolite synthesis of  $\text{Ru}(\text{bpy})_3^{2+}$  is usually carried out by heating the mixture of  $\text{Ru}(\text{NH}_3)_6^{3+}$ -exchanged Y and bpy at  $200^\circ\text{C}$  for a day or longer in a tube sealed under vacuum [Eq. (60)] (97–99).



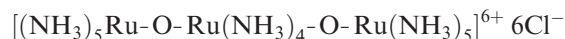
When amine is not coordinated to the  $\text{Ru}^{3+}$  species exchanged into zeolite, the added bpy serves as the reducing agent (96c). Accordingly, for production of  $\text{Ru}(\text{bpy})_3^{2+}$ , excess bpy should be introduced into the reactor with a Ru/bpy ratio of 1:4 [Eq. (61)].



When amine is coordinated to  $\text{Ru}^{3+}$  as in the case of  $\text{Ru}(\text{NH}_3)_6^{3+}$  the complexed amine acts as the reductant for reduction of  $\text{Ru}^{3+}$  to  $\text{Ru}^{2+}$ . Therefore, the required mole ratio of  $\text{Ru}^{3+}$  bpy can be lowered to 1:3 but more preferentially to 1:3.5. The following equations represent the two proposed stoichiometries:



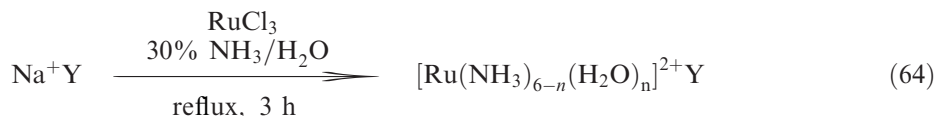
The balanced equations show that  $\text{H}^+$  is generated. Ion exchange of  $\text{Ru}(\text{NH}_3)_6^{3+}$  into Y is usually carried out under inert gas atmosphere to prevent irreversible formation of ruthenium red, whose absorption maxima appear at 245, 375, 532, and 758 nm (100). The pH of the aqueous solution is usually adjusted to 4–5 prior to ion exchange of  $\text{Na}^+$  with  $\text{Ru}(\text{NH}_3)_6^{3+}$ , also to help prevent formation of ruthenium red.



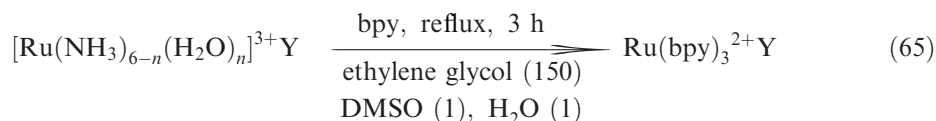
ruthenium red

Zeolite Y may be calcined at  $500^\circ\text{C}$  overnight to remove hydrocarbon impurities in the zeolite prior to ion exchange with  $\text{Ru}(\text{NH}_3)_6^{3+}$ . The excess unreacted bpy is removed by Soxhlet extraction with ethanol for 3–4 weeks. The  $\text{Ru}(\text{bpy})_3^{2+}$  complexes assembled on the external surfaces are removed by washing the zeolite with the aqueous solution of NaCl.

Instead of expensive  $\text{Ru}(\text{NH}_3)_6^{3+}$ , cheaper  $\text{RuCl}_3$  can be directly employed as the Ru source for  $\text{Ru}(\text{bpy})_3^{2+}$  (101). In this case, aqueous ammonia solution is employed and the in situ generated  $\text{Ru}(\text{NH}_3)_{6-n}(\text{H}_2\text{O})_n^{2+}$  ( $n = 0-6$ ) complexes are incorporated into Y.



During the reaction, the black aqueous solution of  $\text{RuCl}_3$  turns reddish pink indicating the reduction of Ru(III) to Ru(II). Subsequent complexation of Ru(II) with bpy is carried out by refluxing the mixture of Ru(II)-Y and bpy for 3 h in the mixture of ethylene glycol (b.p.  $196^\circ\text{C}$ ), DMSO, and  $\text{H}_2\text{O}$  in the volume ratio of 150:1:1.



This procedure seems to be superior to the sealed-tube dry-powder method from the respects of the reaction time, reproducibility, and homogeneous distribution of  $\text{Ru}(\text{bpy})_3^{2+}$  in the zeolite particles.

The assembled  $\text{Ru}(\text{bpy})_3^{2+}$  can be easily identified by comparing the characteristic resonance Raman (97) and diffuse reflectance UV-vis spectra with the authentic ones. The UV-vis absorption spectrum of the complex in zeolite gives two bands at  $\sim 280$  and  $\sim 450$  nm, which arise due to  $\pi \rightarrow \pi^*$  and  $d(t_2) \rightarrow \pi^*$  MLCT transitions, respectively (Fig. 38). The color of the complex is orange-red due to the MLCT band. The positions and intensities of these bands for hydrated zeolite are similar to that of an aqueous solution. The assembled  $\text{Ru}(\text{bpy})_3^{2+}$  is more convincingly identified by isolation from the zeolite hosts by dissolving the framework with HF (99) or  $\text{H}_2\text{SO}_4$  (101). The isolated  $\text{Ru}(\text{bpy})_3^{2+}$  ions are then identified spectrophotometrically (102) or by high-performance liquid chromatography analysis (101). The use of  $\text{H}_2\text{SO}_4$  gives slightly higher yield of  $\text{Ru}(\text{bpy})_3^{2+}$  than HF. When the surfaces of the Y crystals with  $\sim 100$ -nm sizes are tethered with octadecyl groups through siloxyl

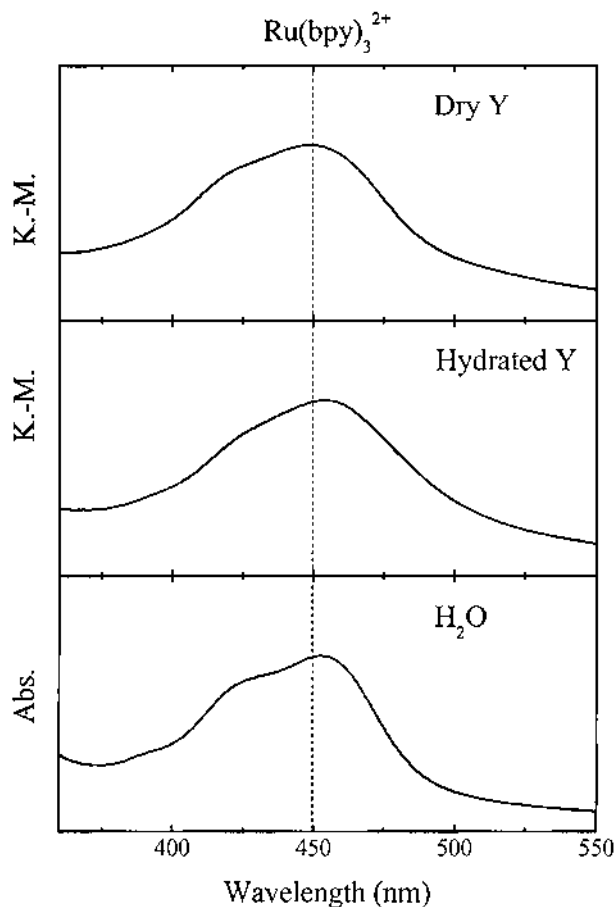
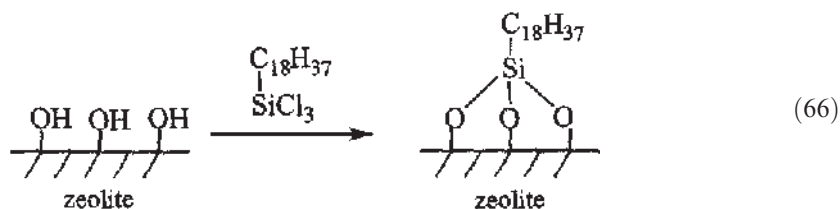


**Fig. 38** UV-vis spectrum of  $\text{Ru}(\text{bpy})_3^{2+}$  in dry (top) and hydrated (middle), and in aqueous solution. (Adapted from Ref. 103.)

linkages [Eq. (66)], the nanosized zeolite crystals can be homogeneously dispersed in toluene (103).



The toluene solution dispersed with the octadecyl-tethering nanocrystalline Ru(bpy)<sub>3</sub><sup>2+</sup>Y is so highly transparent that even transmission spectroscopic techniques can be applied for monitoring and assay of the Ru(II) complex. In particular, at the dispersion level below 1 mg ml<sup>-1</sup> scattering by the colloidal particles is sufficiently low such that all of the entrapped Ru(bpy)<sub>3</sub><sup>2+</sup> in the zeolite is sampled by optical spectroscopy.

Almost all of the Ru species in the zeolite are transformed into Ru(bpy)<sub>3</sub><sup>2+</sup> when the loading level is below one complex per two supercages (50%). At higher loading levels, formation of byproducts such as [Ru(bpy)<sub>n</sub>(NH<sub>3</sub>)<sub>6-2n</sub>]<sup>2+</sup> is usually indispensable due to the increase in the difficulty of bpy transport. By repeated treatment with bpy, the maximal loading level of pure Ru(bpy)<sub>3</sub><sup>2+</sup> can be reached to ~65%. Up to this loading level, a homogeneous distribution of Ru(bpy)<sub>3</sub><sup>2+</sup> is realized within the crystals of Y (99). At higher loading levels, population of Ru(bpy)<sub>3</sub><sup>2+</sup> is highest at the outer most supercages and it decreases upon going into the interior. Interestingly, the Ru complexes encapsulated within Y are thermally stable up to 350°C.

Care must be taken during assembly of Ru(bpy)<sub>3</sub><sup>2+</sup> in X since crystallinity of X is severely lost when the routine procedure for assembly of Ru(bpy)<sub>3</sub><sup>2+</sup> in Y is employed without modification (104). First, acidification of the aqueous solution for ion exchange with Ru(NH<sub>3</sub>)<sub>6</sub><sup>3+</sup> should be avoided since X is not stable in the acidic medium. Instead, it is desirable to handle the solution at low temperature and under inert gas atmosphere during ion exchange to prevent formation of ruthenium red. The best result can be achieved by use of divalent hexamine Ru(II), Ru(NH<sub>3</sub>)<sub>6</sub><sup>2+</sup>. In this case, all of the procedures, including aqueous ion exchange, should be carried out under inert atmosphere since the Ru(II) complex is highly air sensitive (104).

Various other related Ru(II) complexes have also been assembled in Y as shown in Fig. 39 (105–111). The available full names for the Ru(II) complexes and the corresponding absorption and emission maxima are listed in Tables 9 and 10, respectively.

The diaquo bisbipyridyl Ru(II) complex, Ru(bpy)<sub>2</sub>(H<sub>2</sub>O)<sub>2</sub><sup>2+</sup>, is prepared by reacting Ru(NH<sub>3</sub>)<sub>6</sub><sup>2+</sup>Y with bpy at 90°C for 20 h in a sealed-tube reactor (96c,102,106,107) or by refluxing [Ru(NH<sub>3</sub>)<sub>6-n</sub>(H<sub>2</sub>O)<sub>n</sub>]<sup>2+</sup>Y (*n* = 0–6) in ethanol (b.p. 78°C) in the presence of bpy for 3 h (101). Various Ru(bpy)<sub>2</sub>L<sub>2</sub><sup>2+</sup>-type complexes (L = bidentate ligand related to bpy) are derived from the Ru(bpy)<sub>2</sub>(H<sub>2</sub>O)<sub>2</sub><sup>2+</sup> in Y (105,108,110,111). Ru(bpy)<sub>2</sub>(bpz)<sup>2+</sup> is especially useful to prepare the binuclear Ru(II) complex, Ru(bpy)<sub>2</sub>bpz-Ru(NH<sub>3</sub>)<sub>5</sub>, which occupies two neighboring supercages of Y, with each Ru(II) center occupying each supercage. Subsequent treatment of Ru(bpy)<sub>2</sub>bpz-Ru(NH<sub>3</sub>)<sub>5</sub> with other bidentate ligands leads to formation of two different types of Ru(II) complexes in the neighboring supercages (109,112).

**CHARACTERISTIC FEATURES.** Ru(bpy)<sub>3</sub><sup>2+</sup> gives emission upon photoexcitation of the MLCT band arising from decay of <sup>3</sup>MLCT state (102). The emission maxima appear at

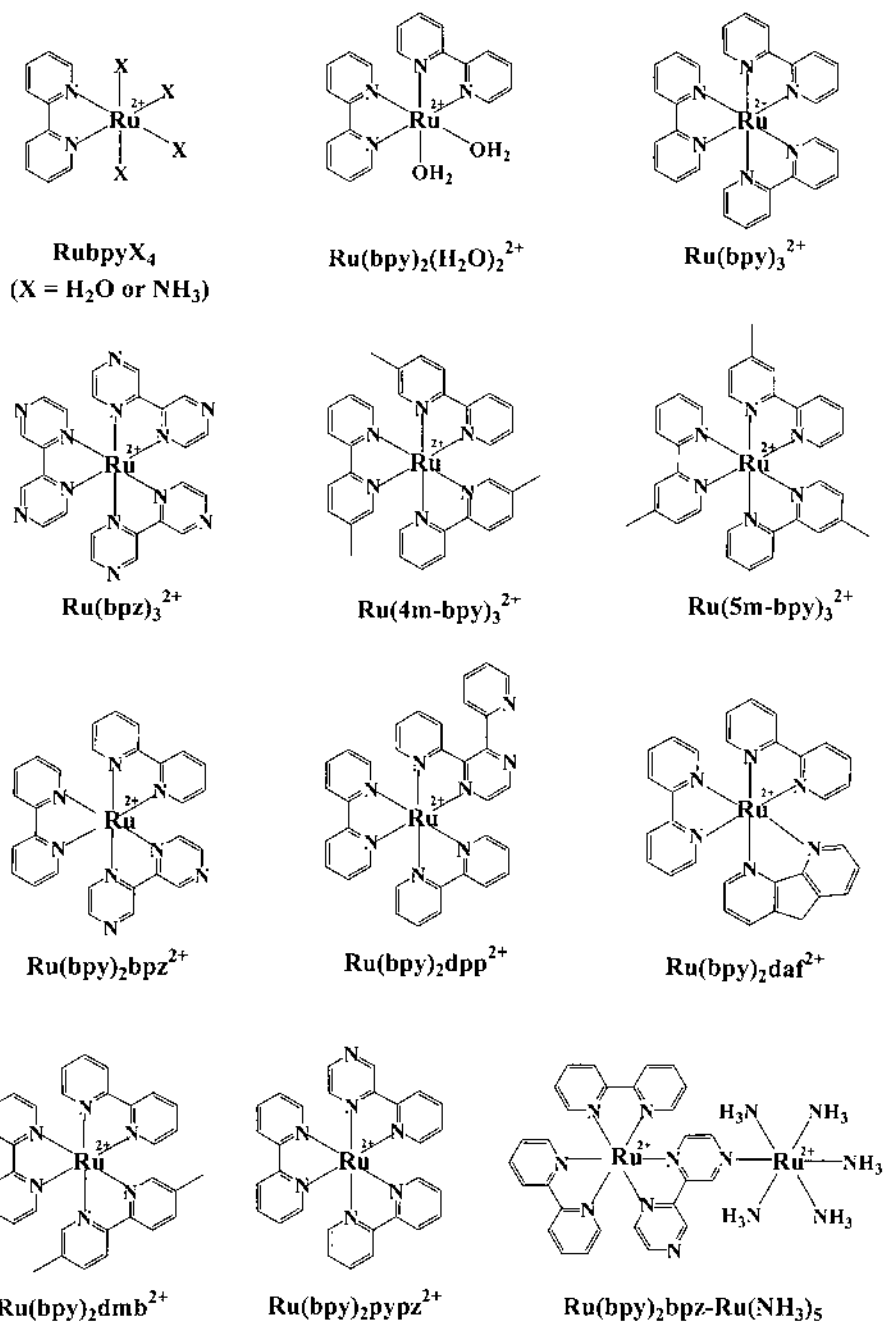


Fig. 39 Various Ru(II) complexes assembled in Y.

**Table 9** Type of Zeolite-Encapsulated Ru(II) Complexes

Formula	Name	Ref.
Rubpy X <sub>4</sub> <sup>2+</sup> <sup>a</sup>	—	105
Ru(bpy) <sub>2</sub> (H <sub>2</sub> O) <sub>2</sub> <sup>2+</sup>	Bis(2,2'-bipyridine) diaquo ruthenium(II)	96c, 102, 106, 107
Ru(bpy) <sub>3</sub> <sup>2+</sup>	Tris(2,2'-bipyridine) ruthenium(II)	108
Ru(bpz) <sub>3</sub> <sup>2+</sup>	Tris(2,2'-bipyrazine) ruthenium(II)	108
Ru(4m-bpy) <sub>3</sub> <sup>2+</sup>	Tris(4-methyl-2,2'-bipyridine) ruthenium(II)	108
Ru(5m-bpy) <sub>3</sub> <sup>2+</sup>	Tris(5-methyl-2,2'-bipyridine) ruthenium(II)	109
Ru(bpy) <sub>2</sub> bpz <sup>2+</sup>	Bis(2,2'-bipyridine)-2,2'-bipyrazine ruthenium(II)	108
Ru(bpy) <sub>2</sub> daf <sup>2+</sup>	Bis(2,2'-bipyridine)-4,5-diazafluorene ruthenium(II)	110
Ru(bpy) <sub>2</sub> dmb <sup>+</sup>	Bis(2,2'-bipyridine)-4,4'-dimethyl-2,2'-bipyridine ruthenium(II)	108
Ru(bpy) <sub>2</sub> pypz <sup>2+</sup>	Bis(2,2'-bipyridine)-2-(2-pyridyl) pyrazine ruthenium(II)	111
Ru(bpy) <sub>2</sub> dpp <sup>2+</sup>	Bis(2,2'-bipyridine)-2,3-bis(2-pyridyl) pyrazine ruthenium(II)	105
Ru(bpy) <sub>2</sub> bpz-Ru(NH <sub>3</sub> ) <sub>5</sub>	—	109

<sup>a</sup> X = H<sub>2</sub>O or NH<sub>3</sub>.

612, 621, and 586 nm in aqueous solution, hydrated Y, and dry Y, respectively (Fig. 40). Thus, while the emission maximum ( $\lambda_{\text{max}}$ ) of Ru(bpy)<sub>3</sub><sup>2+</sup> in hydrated Y is similar to that in aqueous solution, the emission maximum blue shifts substantially (35 nm) in dehydrated (at 350 °C) Y. Since resonance Raman studies show that dehydration has a minimal effect on the structure of Ru(bpy)<sub>3</sub><sup>2+</sup> in the ground state (97), the marked blue shift is attributed to the increase in the rigidity of Ru(bpy)<sub>3</sub><sup>2+</sup> in the excited state as a result of increase in the

**Table 10** Absorption and Emission Data ( $\lambda_{\text{max}}$ ) of Ru(II) Complexes Assembled in Y

Compound	Absorption <sup>a</sup>		Emission <sup>b</sup>		Ref.
	Y	H <sub>2</sub> O	Y	H <sub>2</sub> O	
Rubpy X <sub>4</sub> <sup>2+</sup> <sup>c</sup>	—	295, 367, 523	—	—	105
Ru(bpy) <sub>2</sub> (H <sub>2</sub> O) <sub>2</sub> <sup>2+</sup>	292, 342, 488	290, 346, 487	673 <sup>d</sup>	664 <sup>d</sup>	96c, 102, 106, 107
Ru(bpy) <sub>3</sub> <sup>2+</sup>	286, 432, 456	287, 426, 452	618 <sup>d</sup>	609 <sup>d</sup>	108
Ru(bpz) <sub>3</sub> <sup>2+</sup>	292, 446	295, 443	598 <sup>d</sup>	600 <sup>d</sup>	108
Ru(4m-bpy) <sub>3</sub> <sup>2+</sup>	292, 430, 462	286, 426, 456	630 <sup>d</sup>	615 <sup>d</sup>	108
Ru(5m-bpy) <sub>3</sub> <sup>2+</sup>	446	—	605 <sup>d</sup>	—	109
Ru(bpy) <sub>2</sub> bpz <sup>2+</sup>	282, 410, 480	282, 406, 485	674 <sup>d</sup>	705 <sup>d</sup>	108
Ru(bpy) <sub>2</sub> daf <sup>2+</sup>	289, 457	286, 450	620 <sup>d</sup>	610 <sup>d</sup>	110
Ru(bpy) <sub>2</sub> dmb <sup>2+</sup>	288, 429, 464	287, 428, 456	623 <sup>d</sup>	618 <sup>d</sup>	108
Ru(bpy) <sub>2</sub> pypz <sup>2+</sup>	286, 449	—	656 <sup>e</sup>	672 <sup>e</sup>	111
Ru(bpy) <sub>2</sub> dpp <sup>2+</sup>	284, 430, 474	282, 424, 476	700 <sup>f</sup>	684 <sup>f</sup>	105
Ru(bpy) <sub>2</sub> bpz-Ru(NH <sub>3</sub> ) <sub>5</sub>	417, 481, 617, 673	254, 283, 412, 482, 620, 664	673 <sup>d</sup>	664 <sup>d</sup>	109

<sup>a</sup>  $\lambda_{\text{max}}$ , in nm.

<sup>b</sup> Excitation wavelength in nm.

<sup>c</sup> X = NH<sub>3</sub> or H<sub>2</sub>O.

<sup>d</sup>  $\lambda_{\text{ext}}$  = 457.9 nm.

<sup>e</sup>  $\lambda_{\text{ext}}$  = 488 nm.

<sup>f</sup>  $\lambda_{\text{ext}}$  = 354.7 nm.

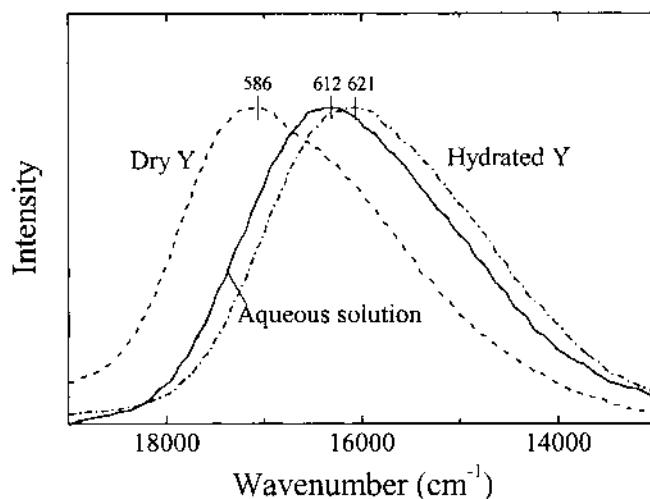


**Fig. 40** Normalized emission spectra of  $\text{Ru}(\text{bpy})_3^{2+}$  in dry Y, aqueous solution, and in hydrated Y (as indicated,  $\lambda_{\text{ext}} = 457.9$  nm). (Adapted from Ref. 102.)

interaction between  $\text{Ru}(\text{bpy})_3^{2+}$  and the zeolite framework, which hampers relaxation of the  $^3\text{MLCT}$  state from the higher energy level to a more stable one. In support of the above interpretation, emission energy of  $^*\text{Ru}(\text{bpy})_3^{2+}$  increases on going from a fluid to a rigid medium by lowering the temperature (113). Replacement of  $\text{Na}^+$  ions in  $\text{Ru}(\text{bpy})_3^{2+}$ -incorporating Y with tetraethylammonium ion ( $\text{TEA}^+$ ) also leads to substantial blue shift of the emission maximum from 626 nm (hydrated  $\text{Na}^+$  Y) to 605 nm (hydrated  $\text{TEA}^+$  Y) as well as a 2.7-fold increase in the emission intensity. Since both  $\text{Ru}(\text{bpy})_3^{2+}$  and  $\text{TEA}^+$  ions cannot be accommodated in a supercage, the result is also attributed to the decrease in the amount of water in the zeolite system as a result of incorporation of large hydrophobic organic cations (114).

The emission intensity of  $^*\text{Ru}(\text{bpy})_3^{2+}$  decreases upon increasing the population of the Ru(II) complex in zeolite (98). For instance, a 2.5-fold decrease is observed in the emission intensity upon increasing the population of  $\text{Ru}(\text{bpy})_3^{2+}$  in Y from 1 per 66.7 to 1 per 1.9 supercages. This arises from the intermolecular interaction between the  $\text{Ru}(\text{bpy})_3^{2+}$  complexes encapsulated in the adjacent supercages. The nonradiative decay processes, such as nonradiative interaction between the ground and excited states and triplet-triplet annihilation between the excited states via ET, seem to be responsible for the faster decay of the excited states leading to a decrease in the emission intensity (98).

**INTERCAGE ET.** ET takes place from  $\text{Ru}(\text{bpy})_3^{2+}$  to  $\text{MV}^{2+}$  in the adjacent cages upon selective photoexcitation of the complex at 413.1 or 457.9 nm (115). This is a typical example of intercage ET since both  $\text{Ru}(\text{bpy})_3^{2+}$  and  $\text{MV}^{2+}$  cannot be placed in a single supercage. Interestingly, the blue color of  $\text{MV}^{\bullet+}$  persists for 1 h under anaerobic and rigorously dry conditions thereby indicating very long-lived CS between  $\text{MV}^{\bullet+}$  and  $\text{Ru}(\text{bpy})_3^{3+}$ .

Time-resolved resonance Raman spectrum (Fig. 41) shows the appearance of the characteristic bands arising from  $^*\text{Ru}(\text{bpy})_3^{2+}$  and  $\text{MV}^{\bullet+}$  together with those of  $\text{Ru}(\text{bpy})_3^{2+}$  in the ground state. This indicates that ET proceeds from  $^*\text{Ru}(\text{bpy})_3^{2+}$  to

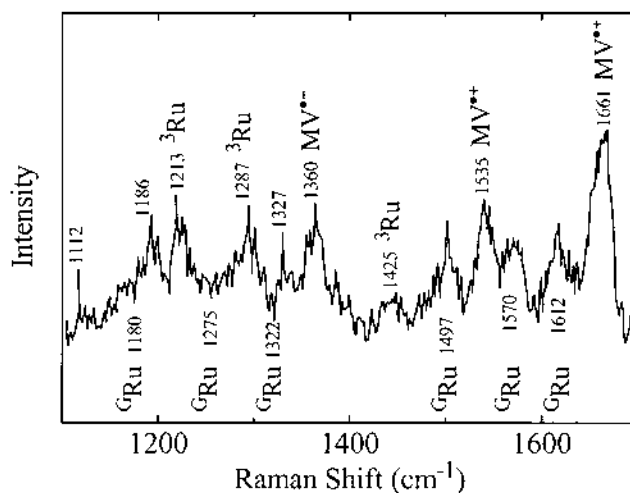
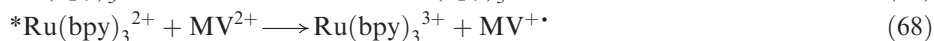
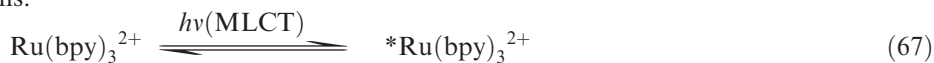


**Fig. 41** Time-resolved resonance Raman spectrum (335 nm, 15 ns) of hydrated  $\text{Ru}(\text{bpy})_3^{2+} - \text{MV}^{2+}(1.0)\text{Y}$ . (Adapted from Ref. 115.)

$\text{MV}^{2+}$ . However, the simultaneous generation of  $\text{Ru}(\text{bpy})_3^{3+}$  is not apparent in Fig. 41 despite that there is a weak signal at  $1112 \text{ cm}^{-1}$  that is characteristic of  $\text{Ru}(\text{bpy})_3^{3+}$  (115). One reason for the failure to observe Raman signals of  $\text{Ru}(\text{bpy})_3^{3+}$  is due to the severe overlap between the signals of  $\text{Ru}(\text{bpy})_3^{2+}$  and  $\text{Ru}(\text{bpy})_3^{3+}$ . Other attempts, such as UV-vis, XPS, and EPR studies, also failed to provide evidence for the simultaneous formation of  $\text{Ru}(\text{bpy})_3^{3+}$ . However, monitoring the growth and decay of  $\text{MV}^{*+}$  and  $\text{Ru}(\text{bpy})_3^{2+}$ , respectively, as a function of time (Fig. 42) provides indirect evidence for the following equations:



The observation of two isosbestic points at  $\sim 400$  and  $\sim 500$  nm further supports the equilibrium between the two absorbing species. However, the system gets more complicated in the dehydrated Y since the framework can reduce  $\text{Ru}(\text{bpy})_3^{3+}$  to  $\text{Ru}(\text{bpy})_3^{2+}$  leaving a hole center in the framework when the zeolite is dry as discussed in detail in Sec. IV.C (p. 705).

The forward ET from the photoexcited complex  ${}^*\text{Ru}(\text{bpy})_3^{2+}$  to  $\text{MV}^{2+}$  is most likely to undergo via direct contact between the donor and acceptor at the supercage window. The fact that the excited electron resides on the  $\pi^*$  orbital of the surrounding bpy ligand, as a result of MLCT transition, will help promote the ET. The Stern-Volmer plot of lifetime of  ${}^*\text{Ru}(\text{bpy})_3^{2+}$  with respect to the concentration of  $\text{MV}^{2+}$  in hydrated Y (Fig. 43) shows that the quenching process [Eq. (68)] has a small dynamic component but is primarily static in nature. This indicates that the mobility of  $\text{MV}^{2+}$  is limited within the pores.

The BET from  $\text{MV}^{*+}$  to  $\text{Ru}(\text{bpy})_3^{3+}$  occurs in the Marcus inverted region (116). For instance, when a series of  $\text{DQ}^{2+}$ , namely,  $2\text{DQ}^{2+}$  ( $E^0 = -0.37 \text{ V}$ ),  $3\text{DQ}^{2+}$  ( $E^0 = -0.55 \text{ V}$ ), and  $4\text{DQ}^{2+}$  ( $E^0 = -0.65 \text{ V}$ , vs. NHE), are introduced into the  $\text{Ru}(\text{bpy})_3^{2+} -$

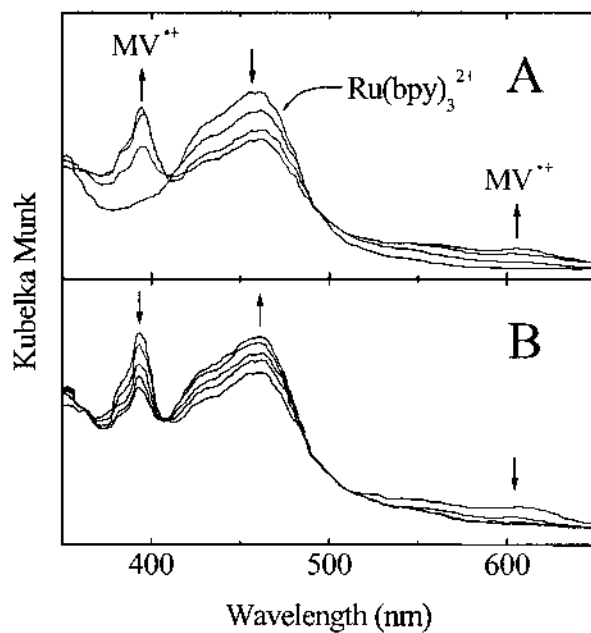


**Fig. 42** Spectral change of the diffuse reflectance spectra of hydrated  $\text{Ru}(\text{bpy})_3^{2+}$ - $\text{MV}^{2+}$ -zeolite Y during irradiation (A) and in the dark after irradiation for 30 min (B). The range of wavelength is 420–630 nm and the interval is 10 min.

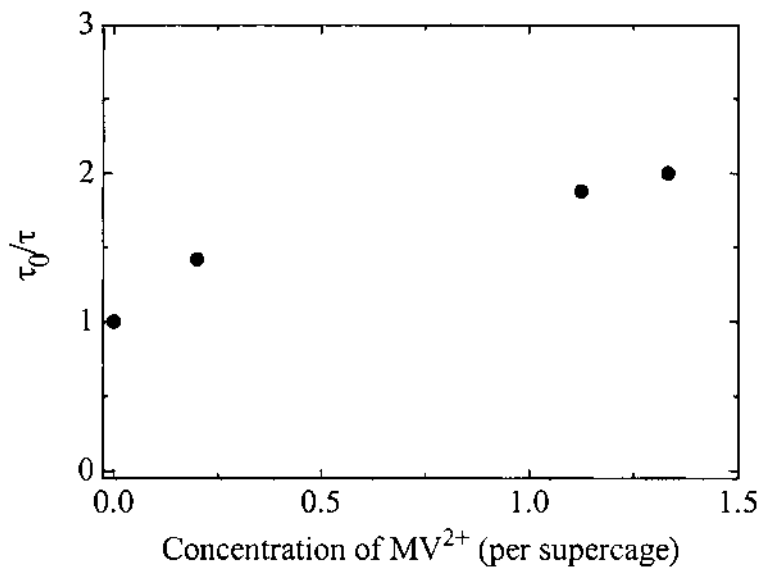
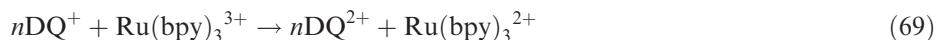


**Fig. 43** Stern-Volmer plot of the lifetime of  $^*\text{Ru}(\text{bpy})_3^{2+}$  vs.  $\text{MV}^{2+}$  concentration in zeolite. (Adapted from Ref. 115.)

incorporating Y, the observed BET rates for Eq. (69) are  $4.0 \times 10^4$  ( $n = 2$ ),  $1.1 \times 10^4$  ( $n = 3$ ), and  $0.7 \times 10^4 \text{ s}^{-1}$  ( $n = 4$ ) for the zeolites with the loading levels of  $n\text{DQ}^{2+}$  of 1 per 15 ( $n = 2$ ) or 1 per 10 supercages ( $n = 3, 4$ ), and  $2.5 \times 10^5$  ( $n = 2$ ),  $1.8 \times 10^5$  ( $n = 3$ ), and  $1.2 \times 10^5 \text{ s}^{-1}$  ( $n = 4$ ) for the zeolites with the loading level of 1.6 ( $n = 2$ ), 1.4 ( $n = 3$ ), and 1.2 per supercage ( $n = 4$ ).



Thus, as noted, the BET rate decreases as the thermodynamic driving force for the ET increases in the order  $2\text{DQ}^{\bullet+} < 3\text{DQ}^{\bullet+} < 4\text{DQ}^{\bullet+}$ . In zeolites with higher loadings of  $n\text{DQ}^{2+}$  efficient charge propagation occurs during both forward and reverse ET through the densely packed diquats.

Along with electron migration, the corresponding positive charge should reposition to maintain the charge balance inside the zeolite system (115). This is accomplished by migration of  $\text{Na}^+$  through the intrazeolite void space as schematically illustrated in Fig. 44. The importance of migration of counteranion along with electron migration is evident from the slower rates of generation and decay of  $\text{MV}^{\bullet+}$  upon changing the counteranion from  $\text{Na}^+$  to  $\text{Li}^+$  (Fig. 45). It is well known that  $\text{Li}^+$  has a lower diffusion coefficient ( $1.302 \times 10^{-5} \text{ cm}^2 \text{ s}^{-1}$ ) than  $\text{Na}^+$  ( $1.484 \times 10^{-5} \text{ cm}^2 \text{ s}^{-1}$ ) in a 1 M chloride solution (117).

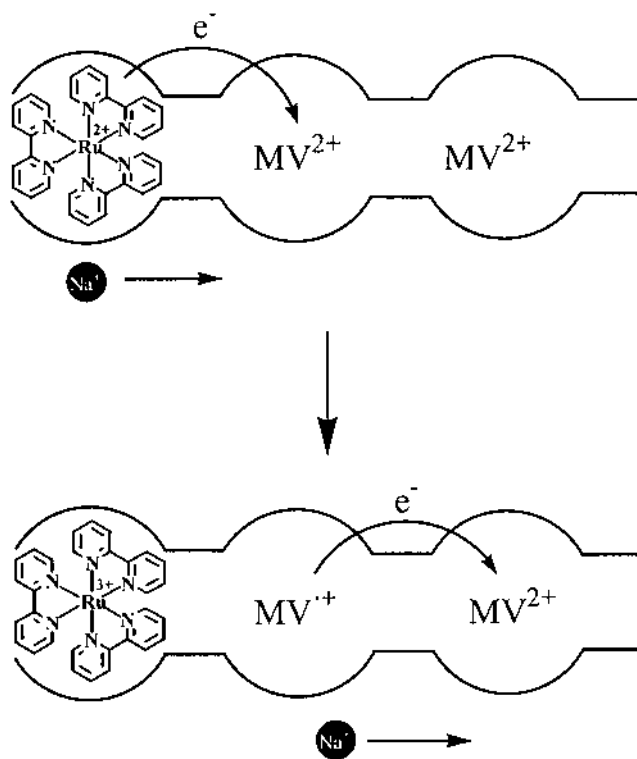


**Fig. 44** A schematic illustration showing simultaneous movement of counteranion toward the direction electron is advancing.

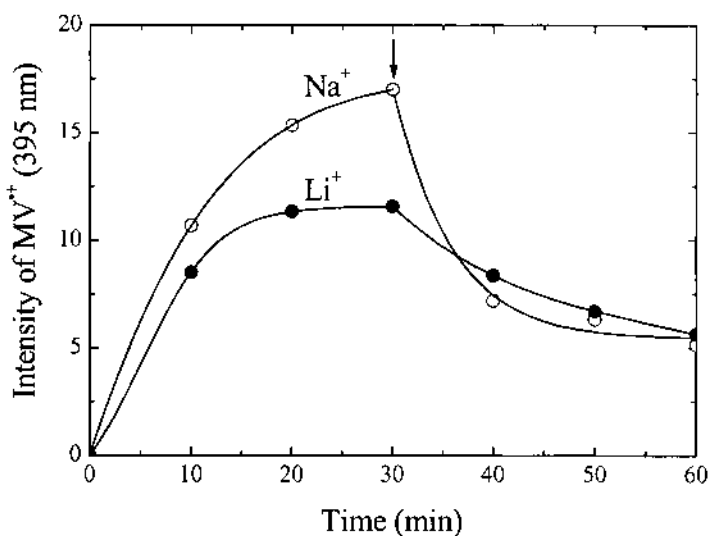
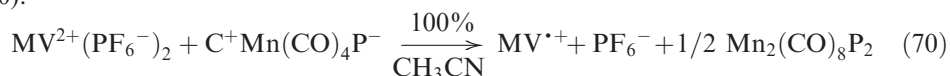
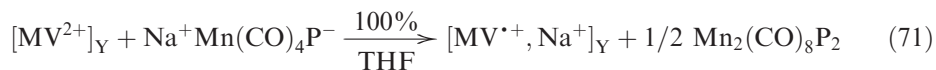


**Fig. 45** Growth upon photolysis (first 30 min) and decay (second 30 min) of  $MV^{\bullet+}$  in the dark as measured by the signal at 395 nm in the diffuse reflectance spectra of (a)  $Ru(bpy)_3^{2+}-MV^{2+}-Na^+Y$  and (b)  $Ru(bpy)_3^{2+}-MV^{2+}-Li^+Y$  under identical experimental and instrumental conditions. The point at which photolysis was discontinued is shown by an arrow. (Loadings: one Ru complex per 25 supercages and two  $MV^{2+}$  per supercage). (Adapted from Ref. 115.)

The important role of counteraction for propagation of ET is also verified from the interfacial ET between the size-excluded donor placed outside the zeolite crystals and the acceptors distributed within the entire zeolite crystal (118). For instance,  $C^+[Mn(CO)_4P]^-$  [ $C^+ = Na^+$ ,  $TEA^+$ , and  $PPN^+$ ,  $P = P(OPh)_3$ ] reduces  $MV^{2+}$  to  $MV^{\bullet+}$  according to Eq. (70).



The above reaction proceeds instantaneously and quantitatively in acetonitrile regardless of the type of the charge-balancing cation,  $C^+$ . When  $Na^+Mn(CO)_4P^-$  is introduced into a tetrahydrofuran (THF) solution suspended with  $MV^{2+}(1.0)Y$ , all of the  $MV^{2+}$  ions are immediately ( $< 10$  min) reduced to  $MV^{\bullet+}$  while generating the stoichiometric amount of  $Mn_2(CO)_8P_2$ , despite the fact that the donor  $Mn(CO)_4P^-$  cannot pass through the 7.4-Å window of Y [Eq. (71)]. Simultaneously, all of the  $Na^+$  ions migrate from the solution to the zeolite pores.



The above result establishes an example that electron donor does not have to enter the supercage in order to transfer an electron to the acceptor placed within the supercage. The ET is most likely to proceed through the contact of Mn donor and  $MV^{2+}$  at the supercage window, but the possibility of electron tunneling from the Mn donor to  $MV^{2+}$

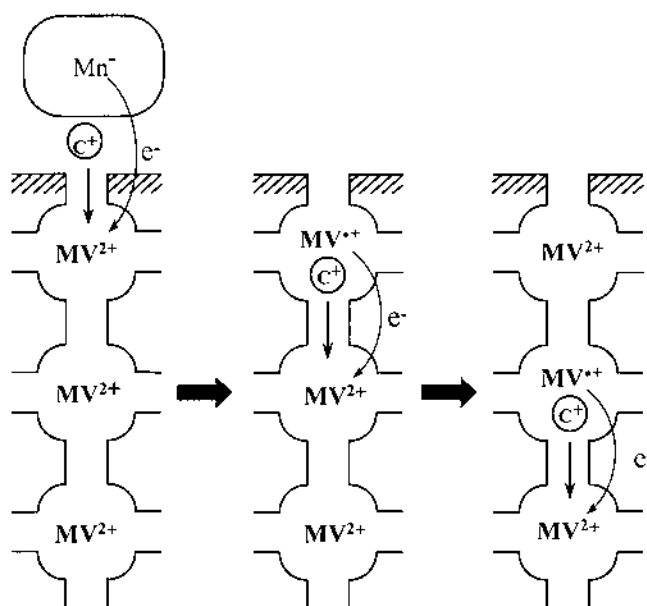
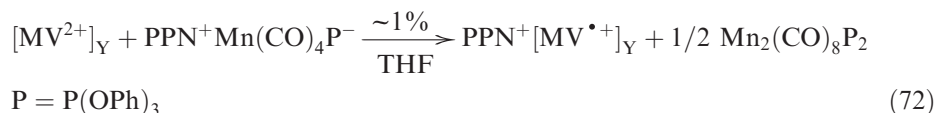


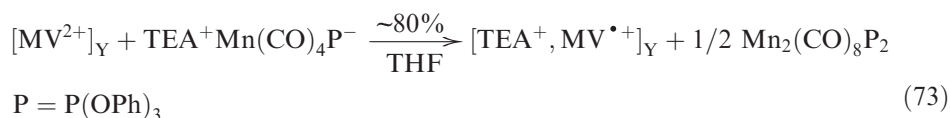
**Fig. 46** Electron conduction mechanism for the propagation of  $MV^{\bullet+}$  through zeolite supercages, showing the accompanying transport of the counteranion  $C^+$ . (Adapted from Ref. 118.)

through the framework (like electrodes) should not be discarded. The above result also shows that electron propagation from the  $MV^{\bullet+}$  ion placed at the outermost supercage to the  $MV^{2+}$  ions residing in the inner supercages should accompany migration of charge-balancing cation as illustrated in Fig. 46.

Consistent with the above, with the size-excluded  $PPN^+$  as the counteranion, the reaction takes place only with those  $MV^{2+}$  ions placed at the outermost supercages, even after 24 h. As a result, only  $\sim 1\%$  of Mn donor (with respect to the amount of  $MV^{2+}$  in Y) is consumed, in accordance with the amount of  $MV^{2+}$  ion residing at the outermost supercages.



With the intermediate-sized  $TEA^+$  as the cation, which can pass through the supercage windows but is much bulkier than  $Na^+$ , ET proceeds very rapidly in the beginning (within 10 min) until the conversion reaches approximately 50% but slows down considerably after 50% conversion, and finally stops at around 80% conversion (Fig. 47).



The above phenomena clearly demonstrate that ET accompanies migration of counteranion and the nature of counteranion governs the degree and kinetics of the ET. The

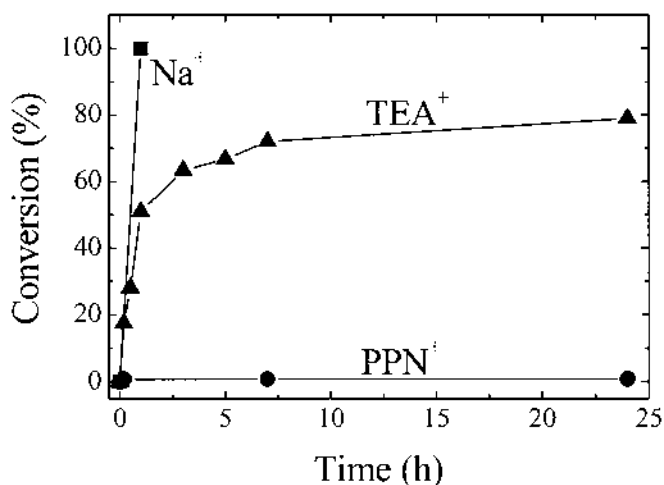
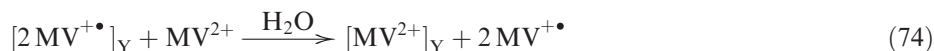


**Fig. 47** Rate profiles for ET from size-excluded  $\text{Mn}(\text{CO})_4\text{P}(\text{OPh})_3^-$  to  $\text{MV}^{2+}$  in Y showing the effect of the counteraction  $\text{C}^+$  (as indicated). (Adapted from Ref. 118.)

related cation-dependent ET from the electrode to the zeolite-encapsulated substrates has been observed during the studies of zeolite-modified electrodes (119,120). In this regard, the carbonylmanganate donor  $\text{Mn}(\text{CO})_4\text{P}^-$  [ $\text{P} = \text{P}(\text{OPh})_3$ ] can be likened to a cathode.

$^*\text{Ru}(\text{bpy})_3^{2+}$  also can act as the electron acceptor in the presence of strong electron donors such as *N,N,N',N'*-tetramethyl-1,4-phenylenediamine (TMPD, Wurster's reagent) and 10-phenylphenothiazine present in the neighboring supercages of X (121). This is another example of intercage PET. However, care must be taken in interpreting the ET quenching of the luminescence of  $^*\text{Ru}(\text{bpy})_3^{2+}$  in dehydrated zeolites since the framework can also act as the electron donor, as discussed in detail in the next section (p. 663). Likewise, in dehydrated Y, the intercage ET from  $^*\text{Ru}(\text{bpy})_3^{2+}$  to  $\text{MV}^{2+}$  or  $\text{DQ}^{2+}$  may simultaneously proceed using the framework as the relay. Thus, ET takes place initially from  $^*\text{Ru}(\text{bpy})_3^{2+}$  to the conduction band of the zeolite framework followed by ET from the conduction band to  $\text{MV}^{2+}$ . The facile PET from arene donors to groups of alkali metal cations discussed in Sec. II (p. 634) supports the possibility of this pathway.

The  $\text{MV}^{\bullet+}$  produced by photoexcitation of  $\text{Ru}(\text{bpy})_3^{2+}$  in hydrated Y can be isolated by ion exchange of the radical cation with  $\text{MV}^{2+}$  ions in aqueous solution [Eq. (74)] (122).



This result demonstrates that irradiation can yield to permanent CS by coupling with ion exchange, when BET is slow. ET quenching of emission from  $^*\text{Ru}(\text{bpy})_3^{2+}$  by  $2\text{DQ}^{2+}$  is another example of intercage PET (114).

Silver ion-exchanged zeolite Y ( $\text{Ag}^+\text{Y}$ , one  $\text{Ag}^+$  per 10 supercages) turns yellowish brown upon treatment with  $\text{NaBH}_4$  at  $4^\circ\text{C}$  under  $\text{N}_2$  (123). The diffuse reflectance UV-vis spectrum of the yellowish brown zeolite shows an absorption band with the maximum at 406 nm. The colored species have been assigned to the mixture of hexanuclear silver ionic cluster  $\text{Ag}_6^{4+}$  residing inside the zeolite and some metallic cluster particles,  $\text{Ag}_x$ , with the size of 10–15 nm residing on the external surface. Excitation of the silver particles at 406.7 nm leads to emission with the maximum at 495 nm. Photoexcitation (406.7 nm) of the

clusters in the presence of  $MV^{2+}$  ions leads to formation of  $MV^{•+}$ , which persists for several hours under anaerobic conditions indicating long-lived CS. The presence of  $MV^{2+}$  also leads to concomitant decrease in the emission intensity of the 495-nm band. The above result represents an example of PET from silver ionic clusters or silver nanoparticles to  $MV^{2+}$ , which demonstrates the potential of silver ionic clusters or silver nanoparticles as strong photosensitized donors.

#### 4. Alkali Metal Ionic Clusters

The ability to generate and host the well-defined alkali metal ionic clusters is one of the characteristic features of zeolite (124). As described in Sec. II.B.1 (p. 634), groups of alkali metal ions have frequently served as popular electron-trapping sites in zeolites. In this regard, understanding the nature and characteristics of intrazeolite alkali metal ionic clusters is necessary for the full account of PET in zeolites.

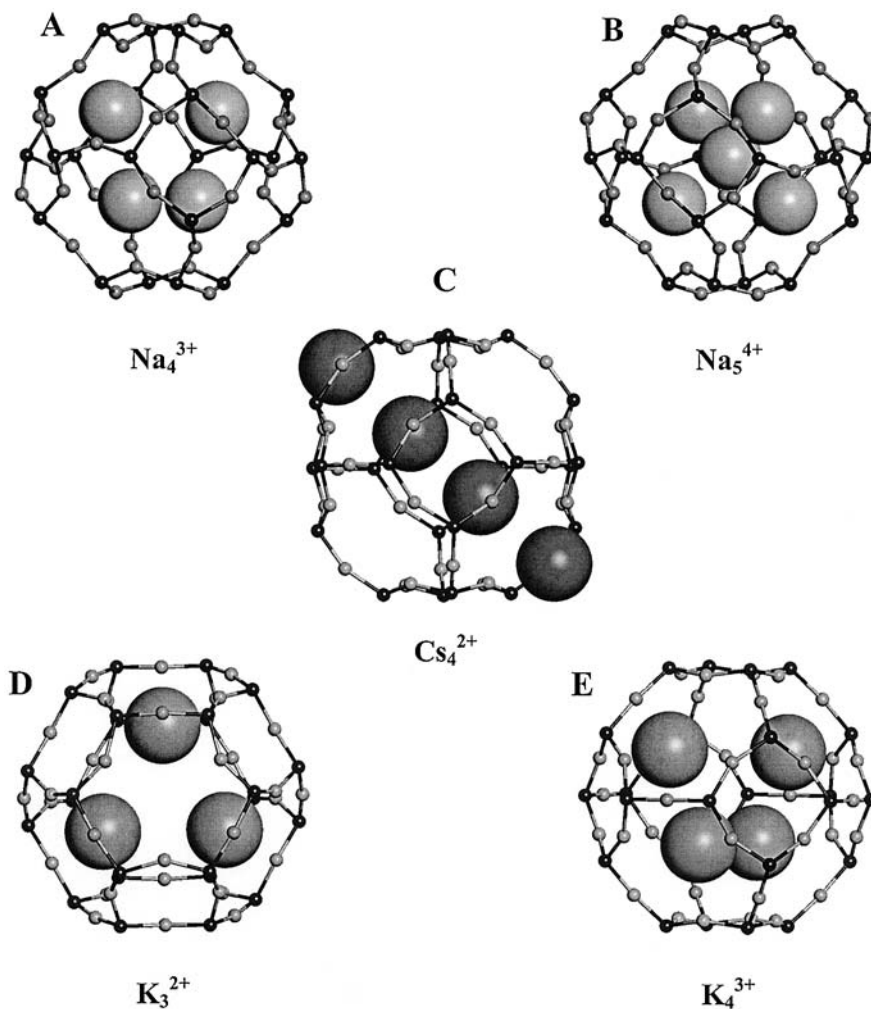


**Fig. 48** Structures of alkali metal cations in sodalite units. A:  $Na_4^{3+}$  (Ref. 128), B:  $Na_5^{4+}$  (Ref. 129), C:  $Cs_4^{2+}$  (Refs. 130, 131), D:  $K_3^{2+}$  (Ref. 132), E:  $K_4^{3+}$  (Ref. 133).

The alkali metal ionic cluster discovered first is tetranuclear sodium ionic cluster, namely,  $\text{Na}_4^{3+}$ . Kasai made the first discovery of  $\text{Na}_4^{3+}$  in 1965 while investigating electron trapping sites in zeolites for the electrons that are excited from the valence band to the conduction band of the framework (125). His view about the nature of relationship between the aluminum center and the charge-balancing cation was that of electron acceptor and ionized donor, respectively. He discovered that white powder of dehydrated  $\text{Na}^+\text{Y}$  turns pink upon irradiation with  $\gamma$  or X rays under vacuum and the pink hue disappears upon heating at  $200^\circ\text{C}$  or upon exposure to oxygen. Analysis of the pink zeolite with ESR revealed the presence of 13 isotropic ESR lines at  $g = 1.999 \pm 0.001$  with hyperfine constant ( $A_{\text{iso}}$ ) of 32.3 G. Since the nuclear spin of Na ( $I_{\text{Na}}$ ) is 3/2, the isotropic 13-line ESR signal was assigned as the tetranuclear sodium ionic cluster, in which an electron is delocalized among the four sodium ions.

The tetranuclear sodium ionic cluster was initially proposed to be residing in a supercage but later discovered to be residing in the sodalite unit. The pink zeolite sample showed a broad absorption band with  $\lambda_{\text{max}}$  at around 500 nm. In this respect,  $\text{Na}_4^{3+}$  has been regarded as a kind of color center or F center in  $\text{Na}^+\text{Y}$ . Soon after the discovery of Kasai, Rabo and coworkers found that evaporation of metallic sodium into  $\text{Na}^+\text{Y}$  also gives rise to the formation of  $\text{Na}_4^{3+}$  by facile ionization of the incoming Na atom into  $\text{Na}^+$  and  $e^-$  (126). Barrer and Cole demonstrated that the same sodium ionic cluster can be generated within the mineral sodalite by sodium evaporation (127). This finding led to firm establishment that  $\text{Na}_4^{3+}$  exists in the sodalite unit as depicted in Fig. 48A. Various other alkali metal ionic clusters, such as  $\text{Na}_2^+$ ,  $\text{Na}_3^{2+}$ ,  $\text{Na}_5^{4+}$ ,  $\text{Na}_6^{5+}$ ,  $\text{K}_3^{2+}$ , and  $\text{K}_4^{3+}$ , have been produced as listed in Table 11 (71a, 125–127, 134–161). Along this line, Heo and Seff discovered the linear tetranuclear cesium ionic cluster residing in the fully  $\text{Cs}^+$ -exchanged A (131). This was originally assigned as  $\text{Cs}_4^{3+}$  but later identified as the diamagnetic cluster  $\text{Cs}_4^{2+}$  ( $s = 0$ ) by careful measurements of the magnetic susceptibility (130).

Including the two methods described above nine other methods have also been developed for production of alkali metal ionic clusters, as summarized in Table 11. In addition to the  $\gamma$ - or X-ray irradiation, high-energy electron beam, far UV (185, 193, and 248 nm), and electrons ejected from a Tesla coil have also been found effective for

**Table 11** Classification of the Electron Source and Method for Generation of Ionic Clusters, and the Type of Ionic Clusters

Electron source	Method	Classification code	Type of ionic cluster	Ref.
Framework	$\gamma$ -, X-ray	I	$\text{Na}_2^+$ , $\text{Na}_3^{2+}$ , $\text{Na}_4^{3+}$ , $\text{K}_3^{2+}$ , $\text{K}_4^{3+}$	125, 134–139
	High-energy electron beam	II	$\text{Na}_2^+$ , $\text{Na}_3^{2+}$ , $\text{Na}_4^{3+}$ , $\text{K}_3^{2+}$ , $\text{K}_4^{3+}$	137–139
	Far-UV (193, 248 nm)	III	$\text{Na}_2^+$ , $\text{Na}_3^{2+}$ , $\text{Na}_4^{3+}$ , $\text{K}_3^{2+}$ , $\text{K}_4^{3+}$	139–141
	Tesla coil	IV	$\text{Na}_4^{3+}$	142
Arene donor	UV	V	$\text{Na}_4^{3+}$	71a, 143
Alkali metal (M)	Evaporation	VI	$\text{Na}_4^{3+}$ , $\text{Na}_5^{4+}$ , $\text{Na}_6^{5+}$ , $\text{K}_3^{2+}$ , $\text{K}_4^{3+}$ , $\text{Cs}_4^{2+}$	126, 127, 130, 131, 144–154
	Decomposition of $\text{MN}_3$	VII	$\text{Na}_4^{3+}$ , $\text{Na}_6^{5+}$ , $\text{K}_3^{2+}$ , $\text{K}_4^{3+}$	154–158
Solvated electron	Solid-state mixing	VIII	$\text{Na}_4^{3+}$ , $\text{Na}_6^{5+}$ , $\text{K}_3^{2+}$ , $\text{K}_4^{3+}$	159
	M/amine	IX	$\text{Na}_3^{2+}$ , $\text{Na}_4^{3+}$ , $\text{K}_3^{2+}$ , $\text{K}_4^{3+}$	160
	M/crown ether	X	$\text{Na}_4^{3+}$ , $\text{Na}_6^{5+}$ , $\text{K}_3^{2+}$ , $\text{K}_4^{3+}$	159
	Organometal	<i>n</i> -BuLi, PhLi	XI	$\text{Na}_4^{3+}$

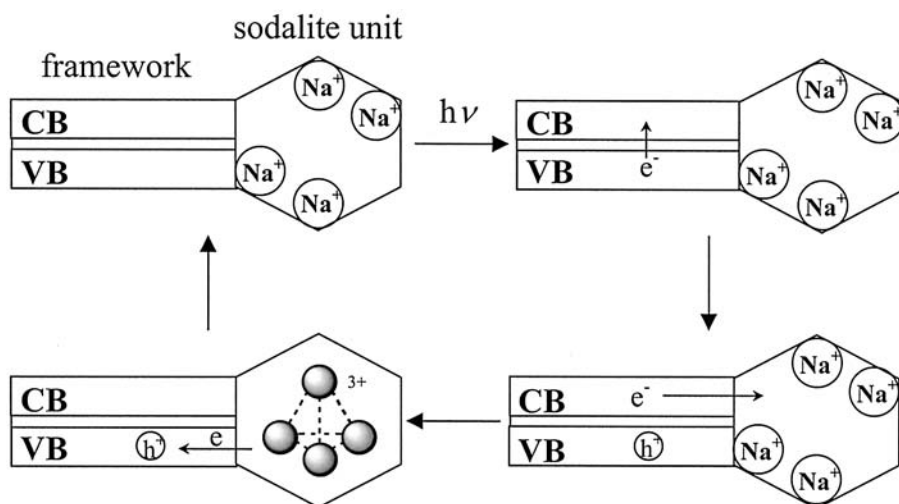


**Fig. 49** A schematic representation illustrating the formation of  $\text{Na}_4^{3+}$  by high-energy radiation.

production of ionic clusters. This phenomenon is ascribed to electron ejection from the valence band of zeolite framework to the conduction band as a result of high-energy radiation (HER) and subsequent ET from the conduction band to four sodium ions residing in sodalite unit, as illustrated in Fig. 49 for the case  $\text{Na}_4^{3+}$ . Consistent with this scheme, the ionic clusters generated by physical methods are stable only at 77 K but they usually disappear upon warming to room temperature due to facile BET from the ionic cluster to the hole center in the framework. As for the electron source, the photoexcited arene donors can also serve as described in Sec. II.B.1 (p. 634).

Thermal decomposition of the impregnated alkali metal azides ( $\text{MN}_3$ ) is an alternative way to introduce alkali metal atoms into zeolites (154–158). Interestingly, direct solid-state mixing of dry  $\text{Na}^+\text{Y}$  or  $\text{K}^+\text{Y}$  with metallic sodium or potassium at room temperature also leads to effective formation of  $\text{Na}_4^{3+}$  or  $\text{K}_4^{3+}$  in the corresponding zeolite (159). Since vapor pressures of the alkali metals at room temperature are negligible, the above intriguing phenomenon arises as a result of facile (spontaneous) dissolution of alkali metals into zeolites, followed by ionization of the dissolved atom into  $\text{M}^+$  and  $\text{e}^-$ , as illustrated in Fig. 50. The dissolution of alkali metals into zeolites may alternatively proceed by initial interfacial ET from the bulk potassium metal to the group of four sodium ions located within the outermost sodalite unit at the edge of the zeolite crystal followed by transfer of potassium ion from the metallic bulk to the zeolite framework to maintain charge balance, perhaps through the larger supercage window. The electron and the potassium ion then advance to the interior of the zeolite crystal while interfacial ET and cation transport newly occur at the metal–zeolite interface. This formulation is very much alike with simultaneous transport of electron and cation as depicted in Fig. 46.

The above phenomenon indicates that the amount of overall energy released as a result of formation of  $\text{Na}_4^{3+}$  and  $\text{K}_4^{3+}$  and accommodation of charge-balancing alkali metal cations in the polar zeolite matrix is large enough to compensate for the energy required for atomization of bulk alkali metal into atoms and subsequent ionization of the atoms. In relation to the above, the energy required to transform a free sodium atom and

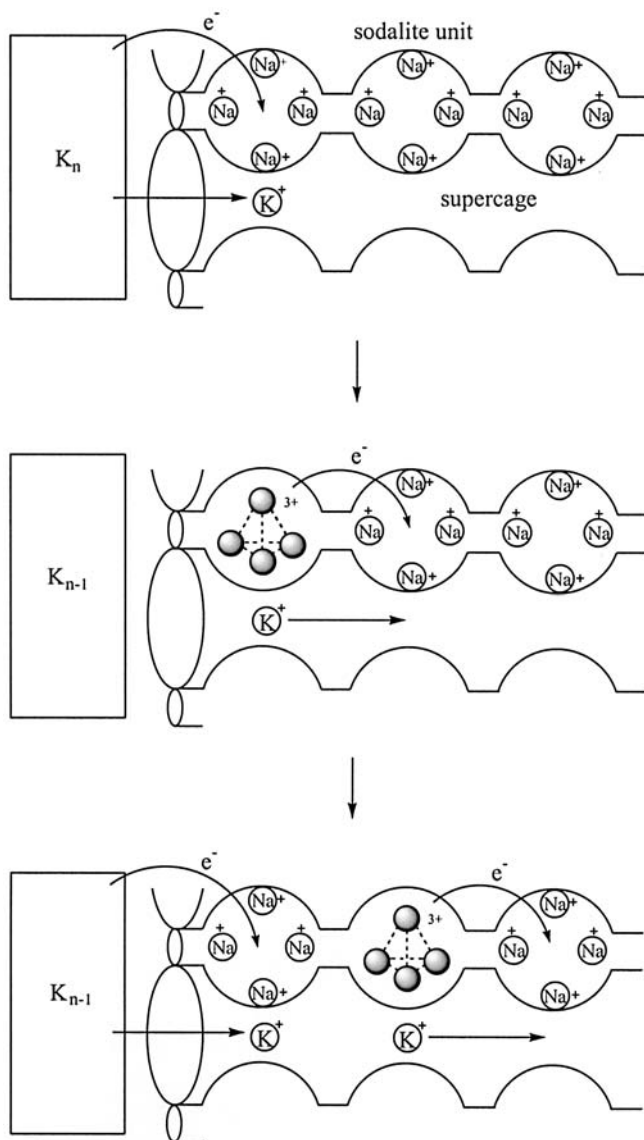


**Fig. 50** Schematic representation showing the interfacial electron transfer from potassium metal to four sodium ions in the sodalite unit accompanied by counteraction transport and the intercege electron hopping to allow subsequent interfacial electron transfer at the periphery of the zeolite crystal. (Adapted from Ref. 7a.)

four sodium ions residing in the sodalite unit to a sodium ion and  $Na_4^{3+}$  in zeolite was estimated to be  $-1.84$  eV (162). The phenomenon of spontaneous dissolution of potassium metal into zeolites further reveals that the electron trapped by four sodium ions in a sodalite unit also readily migrates at room temperature to other groups of four sodium ions residing in the neighboring sodalite units. The overall phenomenon of spontaneous dissolution of alkali metals into zeolite matrices, ionization of atoms into cations and

electrons, and the subsequent trapping of electrons by groups of alkali metal ions is very much likened to dissolution of alkali metals in liquid ammonia [Eq. (75)] (163).



Generation of alkali metal ionic clusters can also be achieved by treating the dry zeolite with solvated electrons prepared in ethereal solvents such as THF and diethyl ether (159) or in liquid ammonia (160). Both alkali metal (160a) and metallic europium (160b) are effective for generation of solvated electrons in liquid ammonia.

Irradiation of fully hydrated  $\text{Na}^+\text{X}$  and  $\text{Na}^+\text{Y}$  with  $\gamma$  ray (138) or pulsed electron beam (164) at room temperature leads to formation of hydrated electrons (electrons solvated by water) which absorb at 620 nm. The absorption band is blue shifted by 0.28 eV relative to that of the hydrated electrons in bulk liquid water. The absorption band progressively red shifts with decreasing the water content in the supercage, and when the water content decreases to  $\sim 32$  water molecules per pseudocell (a supercage plus a sodalite cage), the electron surrounded by water molecules migrates to four sodium ions in the sodalite unit. It was also revealed that the presence of water in the zeolite accelerates the charge recombination between the hole center in the framework and the electron residing in the ionic clusters (141).

The alkali metal ionic clusters can also be generated by exposing dry zeolites to the solutions of organolithium compounds such as *n*-BuLi and PhLi (161). Interestingly, while *n*-BuLi spontaneously generates a large amount of  $\text{Na}_4^{3+}$  in Y upon contact with dehydrated  $\text{Na}^+\text{Y}$ , PhLi requires irradiation at the wavelengths longer than 350 nm in order to generate  $\text{Na}_4^{3+}$ , consistent with the order of the electron donating ability of the two alkyllithium compounds, *n*-BuLi > PhLi.

Among the alkali metal ionic clusters listed in Table 11, the most extensively studied is  $\text{Na}_4^{3+}$ . The absorption maximum of  $\text{Na}_4^{3+}$  in  $\text{Na}^+\text{Y}$  usually appears at  $\sim 500$  nm (see Table 12), as typically shown in Fig. 51A. The absorption maximum significantly red shifts on going from  $\text{Na}^+\text{Y}$  ( $\sim 500$  nm) to  $\text{Na}^+\text{X}$  ( $\sim 550$  nm), to  $\text{Na}^+\text{A}$  (570 nm), and to  $\text{Na}^+\text{SOD}$  (560–628 nm). The corresponding absorption maximum of  $\text{K}_4^{3+}$  appears at  $\sim 560$  nm in Y and 575 nm in X (see Table 13), as typically shown in Fig. 51B.

A typical ESR spectrum of  $\text{Na}_4^{3+}$  in  $\text{Na}^+\text{Y}$  is shown in Fig. 51C. As listed in Table 12, The  $A_{\text{iso}}$  value ranges from 22.8 to 40 G. The highest  $A_{\text{iso}}$  value is observed from  $\text{Na}^+\text{GaY}$  (40G). The  $g$  value ranges from 1.9926 to 2.0057. Figure 51D shows a typical ESR spectrum of  $\text{K}_4^{3+}$  in  $\text{K}^+\text{Y}$ . The corresponding  $g$  values,  $A_{\text{iso}}$ , and  $\lambda_{\text{max}}$  are listed in Table 13.

The ESR spectrum of  $\text{Na}_4^{3+}$  often accompanies a strong singlet in the middle of the characteristic 13-line spectrum. Figure 52 shows a gradual change of the ESR spectrum of  $\text{Na}^+\text{Y}$  as the amount of evaporated sodium atom increases. The nature of the singlet was initially attributed to the metallic sodium nanoclusters encapsulated in  $\alpha$  cages. However, careful magnetic resonance and structural studies elucidated that the singlet ESR line originates from the interaction of neighboring  $\text{Na}_4^{3+}$  centers (128,165). The electrons in  $\text{Na}_4^{3+}$  centers occupying adjacent sodalite cages are sufficiently close to one another that their wave functions overlap and they couple through quantum mechanical exchange forces. As a result, even for just two interacting centers, individual hyperfine lines can hardly be resolved. When four to eight  $\text{Na}_4^{3+}$  centers interact, the hyperfine structure vanishes and the ESR envelope becomes a smooth symmetrical line. Figure 53 shows a schematic representation of an array of interacting  $\text{Na}_4^{3+}$  centers. The measured

**Table 12** The Type of Zeolite Host, Method, and Temperature to Generate  $\text{Na}_4^{3+}$  and the Corresponding Absorption and ESR Data

Zeolite	Method	Temp. (K)	$\lambda_{\text{max}}$ (nm)	$g$ value	$A_{\text{iso}}$ (G)	Ref.	
$\text{Na}^+$ Sod	II	298	560	—	—	137	
	III	—	560	—	—	139	
	VI	298	—	—	—	127	
	VI	298	628	—	—	152	
Li, Cl-Sod	VI	298	—	2.0020	31.5	151	
		14	—	2.0020	30.5		
Na, Cl-Sod	VI	298	—	2.0020	31.5	151	
		14	—	2.0020	30.4		
K, Cl-Sod	VI	298	—	2.0020	31.3	151	
		14	—	2.0020	29.6		
Cs, Cl-Sod	VI	298	—	2.0020	31.3	151	
		14	—	2.0020	30.0		
Na, Br-Sod	VI	298	—	2.0020	28.5	151	
		14	—	2.0020	27.0		
Na, I-Sod	VI	298	—	2.0020	24.8	151	
		14	—	2.0020	24.1		
K, I-Sod	VI	298	—	2.0020	24.6	151	
		14	—	2.0020	22.8		
$\text{Na}^+$ A	II	343	570	—	—	137	
	III	—	—	—	—	139	
$\text{Na}^+$ X	I	77	—	1.9990	28.0	135	
	I	196	—	1.9983	27.5	135	
	II	77	550	1.9990	27.5	137	
	III	—	550	—	—	139	
	III	—	530	—	—	141	
	IV	77	—	2.000	26.0	142	
	V	—	550	—	—	71a	
	IX	298	—	2.0010	29.2	160	
	XI	298	—	2.0031	29.0	161	
	$\text{Na}^+$ X(1.4) <sup>a</sup>	I	77	546	—	—	136
	$\text{Na}^+$ Y	I	298	500	1.9990	32.3	125
I		77	—	1.9990	30.0	135	
I		196	—	1.9990	30.0	135	
I		295	—	1.9992	32.5	135	
II		—	500	1.9990	30.0	137	
III		—	500	—	—	139	
IV		77	495	2.0020	35.0	142	
V		—	550	—	—	71a	
VI		—	—	1.9990	32.3	126	
VI		120	—	1.9990	—	146	
VI		120	—	1.9990	32.1	147	
VI		—	497	1.9926	35.0	154	
VII		298	—	2.0012	32.5	155	
VII		—	—	2.0030	33.5	156	
VIII		298	495	2.0042	36.3	159	
IX		298	—	2.0030	33.3	160	
X		298	—	2.0057	35.0	159	
XI		298	—	2.0010	35.0	161	
$\text{Na}^+$ Y(1.8) <sup>a</sup>		I	77	514	—	—	136
$\text{Na}^+$ Y(2.2) <sup>a</sup>	I	77	508	—	—	136	
$\text{Na}^+$ Y(2.5) <sup>a</sup>	I	77	505	—	—	136	
	I	298	—	1.9990	30.0	136	
$\text{Li}^+_{44}\text{Na}^+_{12}\text{Y}$	IX	298	—	2.0025	37.5	160	
$\text{Na}^+$ GaY <sup>b</sup>	III	—	525	—	—	140	
	VII	298	—	2.0020	40.0	153	

<sup>a</sup> Number in the parentheses represents the Si/Al ratio.

<sup>b</sup>  $\text{Na}^+$ -exchanged gallosilicate with faujasite structure.

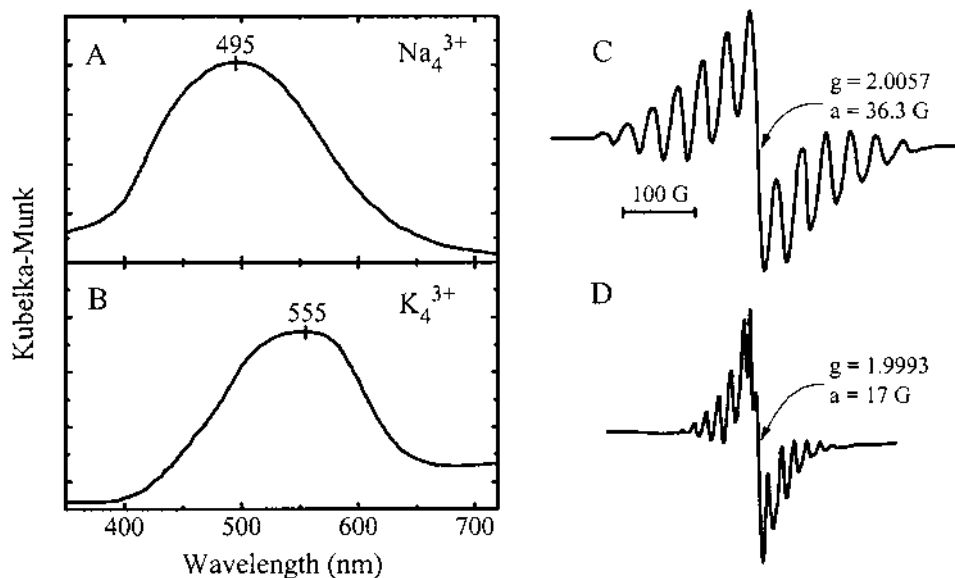


**Fig. 51** Typical absorption spectra of Na<sub>4</sub><sup>3+</sup> (A) and K<sub>4</sub><sup>3+</sup> (B) and the corresponding ESR spectra of Na<sub>4</sub><sup>3+</sup> (C) and K<sub>4</sub><sup>3+</sup> (D). (Adapted from Ref. 159.)

intercluster distance is 5.36 Å, which is short enough to explain the loss of the hyperfine structure at modest metal loadings (128).

At higher loadings of alkali metals it is inevitable for the extra metal atoms to aggregate inside the α cages of the zeolites. Even in such cases, the metal clusters exist in the highly ionized forms rather than in the neutral forms, since ionization of occluded species is a generic property of zeolite. Thus, the extra alkali metal ions exist in the form of extended clusters that spread continuously throughout the zeolite cages, cavities, and channels. At high concentrations of electron, even sodide (Na<sup>-</sup>) is generated as well as sodium atom (Na<sup>•</sup>) according to the following proposed stoichiometry (166):



The ionic clusters are potentially useful for many applications. For instance, the very large periodic array of closely spaced alkali metal cations (167), or “cationic continuum” (131), exhibits an electronic conductivity. Interesting optical and magnetic (ferromagnetism) properties have been observed from K-loaded K<sup>+</sup>A (168), and Na<sub>6</sub><sup>5+</sup>-containing X catalyzes isomerization of cyclopropane to propene (169).

### III. PET FROM FRAMEWORK TO INTERCALATED SPECIES

The CT interactions and PET between various intercalated species have been demonstrated in the previous sections. There, zeolite frameworks have been regarded as rigid and inert hosts for supramolecular assembly of donors and/or acceptors for CT complexation and PET.

Now the question is whether the zeolite framework, being a class of negatively charged inorganic polymer, is indeed inert and merely serves as an inert compartmentalizing host to the encapsulated species. In principle, any material can behave as a donor or

**Table 13** Type of Zeolite Host, Method, and Temperature to Generate Various Alkali Metal Ionic Clusters and Corresponding Absorption and ESR Data

Ionic cluster	Zeolite	Method	Temp. (K)	$\lambda_{\text{max}}$ (nm)	g value	$A_{\text{iso}}$ (G)	Ref.		
$\text{Na}_2^+$	$\text{Na}^+\text{A}$	I	77	—	2.0050	72.0	135		
		II	77	> 750	2.0050	72.0	137		
		III	—	—	—	—	139		
		III	—	> 750	—	—	141		
	$\text{Li}^+_7\text{Na}^+_5\text{A}$	I	77	—	—	1.9983	100.0	135	
		$\text{Na}^+\text{ZK-4}$	II	—	—	—	—	138	
		$\text{Na}^+\text{M}$	III	—	680	—	—	140	
$\text{Na}_3^{2+}$	$\text{Li}^+_{46}\text{Na}^+_{34}\text{X}$	I	77	—	2.0063	85.0	135		
		$\text{Na}^+\text{SOD}$	I	77	—	1.9988	30.0	135	
		I	196	—	—	1.9987	33.0	135	
		II	173	700	—	1.9987	31.5	137	
		III	—	660	—	—	—	139	
	$\text{Li}^+_7\text{Na}^+_5\text{A}$	I	196	—	—	2.0003	65.0	135	
		$\text{Na}^+\text{A}$	I	196	—	2.0026	39.5	135	
			II	196	680	2.0026	39.5	137	
			III	—	—	—	—	139	
			III	—	680	—	—	141	
		$\text{Na}^+\text{ZK-4}$	II	—	—	—	—	138	
			$\text{Na}^+\text{M}$	III	—	540	—	—	140
			$\text{Na}^+\text{X}$	III	—	650	—	—	139
	$\text{Na}_5^{4+}$	$\text{Na}^+\text{X}$	III	—	680	—	—	141	
VI			—	—	—	—	149		
$\text{Na}_6^{5+}$	$\text{Na}^+\text{X}$	VI	—	—	1.9990	—	126		
		VI	298	—	2.0022	25.0	149		
		VI	298	—	2.0011	25.9	154		
		VII	298	—	2.0013	25.5	154		
		VII	298	—	2.0013	25.9	155		
		VIII	298	—	2.0010	27.0	159		
$\text{K}_3^{2+}$	$\text{K}^+\text{A}$	VI	77	—	1.9992	12.8	141		
		$\text{K}^+\text{X}$	I	77	775	1.9983	12.5	140	
		I	196	—	—	1.9983	12.8	135	
		III	—	720	—	—	140		
		VI	77	—	—	1.9992	12.8	141	
		VI	298	—	—	1.9994	13.0	154	
		VII	298	—	—	1.9997	12.8	154	
		VII	298	—	—	1.9990	16.6	155	
		VIII	298	—	—	1.9990	16.0	159	
		$\text{K}_4^{3+}$	$\text{K}^+\text{L}$	III	—	700	—	—	140
$\text{K}^+\text{X}$	III		—	575	—	—	140		
$\text{K}^+\text{Y}$	VI		120	—	—	1.9950	—	146	
	VI		120	—	—	1.9960	16.4	147	
	VI		—	565	—	1.9975	15.6	154	
	VII		298	—	—	1.9990	12.8	155	
	VIII		298	555	—	1.9993	17.0	159	

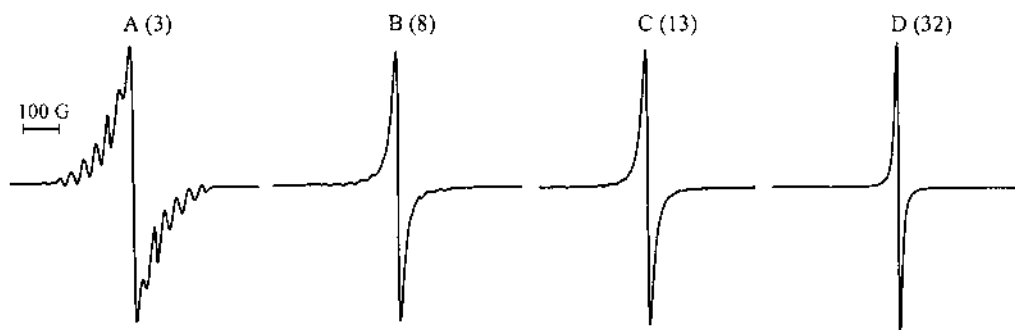


**Fig. 52** The ESR spectra of  $\text{Na}^+\text{Y}$  containing 3(A), 8(B), 13(C), and 32(D) extra sodium atoms per unit cell. (Data extracted from Refs. 124a and 165.)

an acceptor depending on the relative electron density of the interacting counterpart. The zeolite framework is not an exception. Indeed, a great number of experimental results have verified that the zeolite framework is by no means inert but rather actively participates as the electron donor for a variety of intercalated compounds (8–17). For instance, it is well established that exposure of electron acceptor compounds such as tetracyanoethylene (17a,b), 1,3,5-trinitrobenzene (16a,b,17a), *m*-dinitrobenzene (17a), and *o*-chloranil (17c) to dry zeolites gives rise to formation of the corresponding radical anion in zeolites even at room temperature. Formation of the radical anion of sulfur

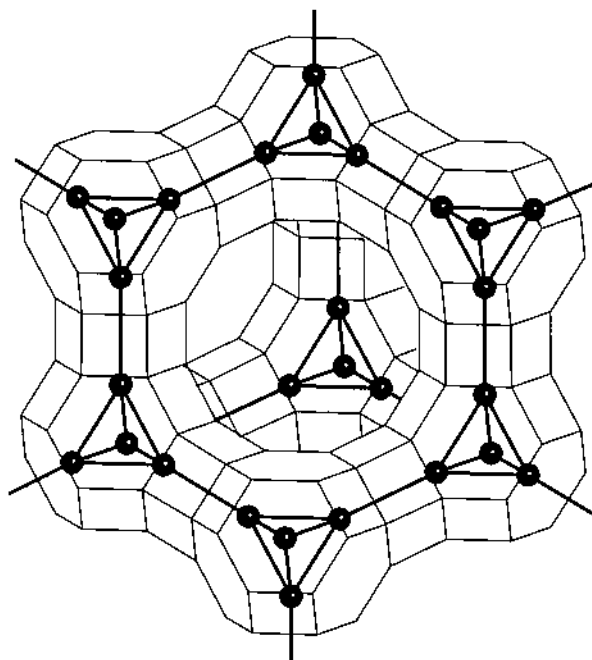


**Fig. 53** Representation of an array of interacting  $\text{Na}_4^{3+}$  clusters. (Adapted from Ref. 124a.)

dioxide ( $\text{SO}_2^{\bullet-}$ ) (16b,17b) also readily occurs at elevated temperatures ( $\sim 200^\circ\text{C}$ ). Thus, the donor property of zeolites has been well established. Instead, poorly defined defect sites have often been attributed as the source of electron. Now the following examples provide firm evidence that zeolite frameworks are the true sources of electron to the encapsulated acceptor molecules.

## A. CT Interaction of the Framework with Intercalated Species

### 1. Framework- $\text{MV}^{2+}$ CT Interaction and PET from Framework to $\text{MV}^{2+}$

It has been well established that “the zeolite basicity increases with increasing the aluminum content and/or the size of the charge-balancing cation for a series of alkali metal ions. (8–12,170–177). The meaning of zeolite basicity is rather vague; it should be more clearly specified as the framework basicity since the negatively charged framework actually exerts the basic property and the charge-balancing cation actually exerts the acidic property. As discussed in the introduction of this chapter, basicity is synonymous with donor strength. Therefore, it can be now said that the donor strength of the framework increases with increasing aluminum content and/or the size of the charge-balancing cation for a series of alkali metal ions.

The reason for the increase in the framework donor strength upon increasing aluminum content is rather clear since the increase in aluminum content results in the increase in negative charge density on the framework. However, the effect of the latter on the donor strength of the framework has remained unclear. As an attempt to understand this, a CT interaction between the cation and the framework has been proposed by Mortier (170) Jhon (177) and their coworkers on the basis of theoretical studies. In the mean time, Mortier and coworkers successfully applied the concept of Sanderson’s electronegativity equalization principle to the zeolite system and developed a formulation that can derive the Sanderson’s partial charge of the framework oxygen ( $\delta_{\text{O}}$ ) from the values of Sanderson’s intermediate electronegativity of zeolite ( $S_{\text{Z}}$ ) and Sanderson’s electronegativity of oxygen ( $S_{\text{O}}$ ) according to the following equation:

$$\delta_{\text{O}} = (S_{\text{Z}} - S_{\text{O}})/2.08S_{\text{O}}^{1/2} \quad (77)$$

$S_{\text{Z}}$  is expressed by the geometrical mean of the Sanderson’s electronegativities of all framework elements and cations according to the following equation:

$$S_{\text{Z}} = (S_{\text{M}}^p S_{\text{Si}}^q S_{\text{Al}}^r S_{\text{O}}^t)^{1/(p+q+r+t)} \quad (78)$$

where,  $S_{\text{M}}$ ,  $S_{\text{Si}}$ ,  $S_{\text{Al}}$ , and  $S_{\text{O}}$  represent Sanderson’s electronegativities of the alkali metal cation, silicon, aluminum, and oxygen, respectively, and  $p$ ,  $q$ ,  $r$ , and  $t$  respectively represent the number of the corresponding element in a unit cell. There are numerous examples that verify the linear correlation between  $\delta_{\text{O}}$  and the framework donor strength. Therefore, nowadays it has become a routine practice to employ  $\delta_{\text{O}}$  as the criterion for the framework donor strength. However, despite the great success in taking the type of cation into the account of  $\delta_{\text{O}}$ , Sanderson’s principle does not explain the nature of interaction between the cation and the framework.

The direct experimental proof for the nature of interaction between the framework and the cation being CT interaction was provided by employment of  $\text{MV}^{2+}$  as the probe cation (9). For instance, the diffuse reflectance UV-vis spectra of a series of dried  $\text{MV}^{2+}$ - $\text{M}^+\text{Y}$  and  $\text{MV}^{2+}$ - $\text{M}^+\text{X}$  samples show absorption bands in the 220- to 320-nm region, as shown in Fig. 54A. The exchanged amount of  $\text{MV}^{2+}$  in the above zeolites is one per unit

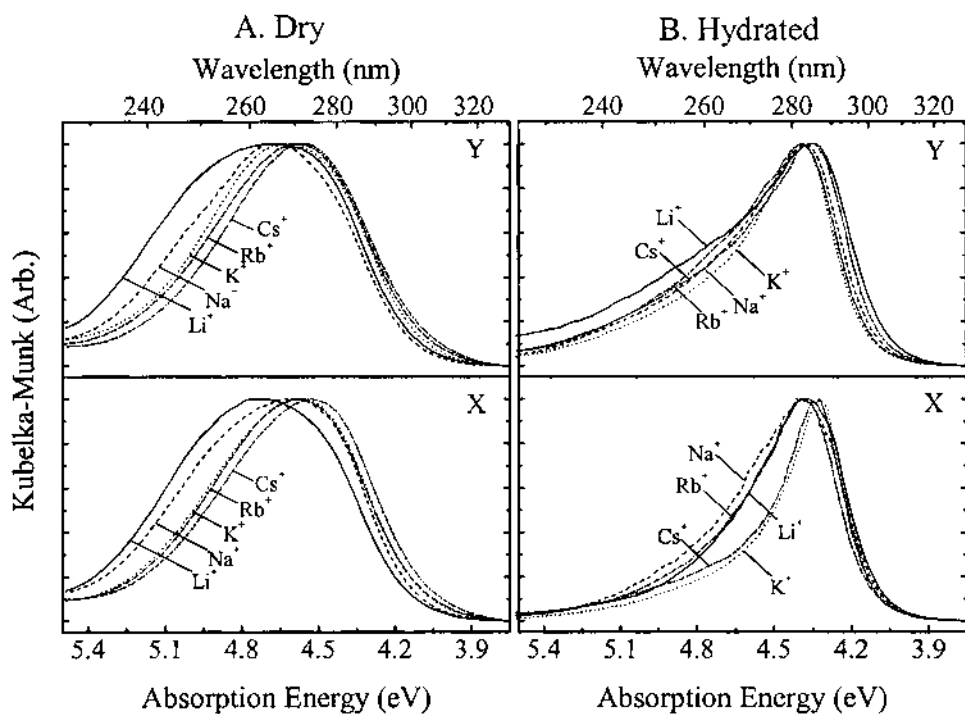


**Fig. 54** (A) Diffuse reflectance UV-vis spectra of the dehydrated  $MV^{2+}-M^+Y$  (top) and  $MV^{2+}-M^+X$  (bottom). (B) Diffuse reflectance UV-vis spectra of the fully hydrated  $MV^{2+}-M^+Y$  (top) and  $MV^{2+}-M^+X$  (bottom). (Adapted from Ref. 9.)

cell, and  $M^+$  stands for alkali metal cations with compositions as listed in Table 14. Thus,  $M^+$  represents the major cation and  $MV^{2+}$  the minor probe cation.

The absorption band progressively red shifts upon increasing the size of  $M^+$ . Concomitantly, the bandwidth of each spectrum progressively decreases upon increasing size of  $M^+$ , with the order being  $Li^+ > Na^+ > K^+ > Rb^+ > Cs^+$ . In marked contrast, the fully hydrated samples give nearly the same cation-independent absorption bands, as shown in Fig. 54B. Such a marked difference in the behavior of the absorption band arises due to the presence and disappearance of CT interaction between framework and  $MV^{2+}$  in the dry and hydrated zeolites, respectively.

Decomposition of the spectra using multiple Gaussian bands reveals that each absorption band is composed of three bands; a long, weak tail band and two full Gaussian bands as typically shown for  $MV^{2+}-M^+Y$  in Fig. 55A. The weak tail band arises due to the residual absorption of the zeolite framework. Of the two Gaussian bands, the progressively moving, higher energy band (dashed curve) is the framework-to- $MV^{2+}$  CT band. The CT nature of this band is verified from the linear relationship between the absorption band and  $\delta_0$ , as shown in Fig. 55B. The stationary, lower energy band is the local (intrinsic) band of  $MV^{2+}$  in Y. Therefore, only the local band appears in the hydrated zeolites.

The CT band is always much broader (fwhm =  $\sim 0.68$  eV) and more intense than the local band (fwhm =  $\sim 0.43$  eV) and the envelope of the broad CT band always covers the local band. Accordingly, the selective excitation of only the local band without simulta-

**Table 14** Chemical Compositions of the Alkali Metal–Exchanged Zeolites X and Y Used to Study CT Interaction Between  $MV^{2+}$  and Corresponding Sanderson’s Partial Electron Density on the Framework Oxygen ( $\delta_o$ )<sup>a</sup>

Zeolite	Unit cell composition	$\delta_o$
$Li^+Y$	$Li_{37}Na_{16}Al_{53}Si_{139}O_{384}$	-0.247
$Na^+Y$	$Na_{53}Al_{53}Si_{139}O_{384}$	-0.265
$K^+Y$	$K_{49}Na_4Al_{53}Si_{139}O_{384}$	-0.276
$Rb^+Y$	$Rb_{35}K_{13}Na_2H_3Al_{53}Si_{139}O_{384}$	-0.284
$Cs^+Y$	$Cs_{37}K_{14}Na_2Al_{53}Si_{139}O_{384}$	-0.304
$Li^+X$	$Li_{68}Na_{16}Al_{84}Si_{108}O_{384}$	-0.287
$Na^+X$	$Na_{84}Al_{84}Si_{108}O_{384}$	-0.316
$K^+X$	$K_{75}Na_9Al_{84}Si_{108}O_{384}$	-0.331
$Rb^+X$	$Rb_{51}K_{21}Na_5H_7Al_{84}Si_{108}O_{384}$	-0.338
$Cs^+X$	$Cs_{46}K_{26}Na_6H_6Al_{84}Si_{108}O_{384}$	-0.352

Source: Data from Ref. 9.

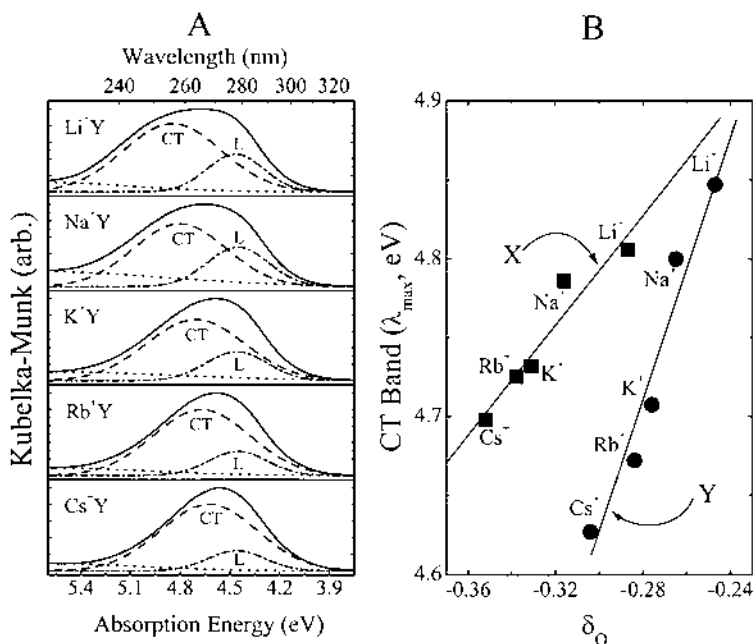


**Fig. 55** (A) Decomposed spectra of the dehydrated  $MV^{2+}-M^+Y$  for five different alkali metal cations (as indicated), showing the residual absorption of the zeolite framework (dotted line); the broad CT band (dashed line); and the narrower, local band of  $MV^{2+}$  (L) (dashed and dotted line). (B) Mulliken’s linear relationship between the CT band and the calculated Sanderson’s (average) partial charge of the framework oxygen of  $M^+Y$  and  $M^+X$  (as indicated). (Adapted from Ref. 9.)

neous excitation of the CT band is not possible. In contrast, selective excitation of the CT band is possible by irradiation at the wavelengths shorter than  $\sim 250$  nm.

The larger slope observed for Y than X in Fig. 55B indicates that the degree of red shift of the CT band upon increasing framework donor strength is much more sensitive for Y than X for a common acceptor,  $MV^{2+}$ . This phenomenon seems to arise as a result of the increase in the number of alkali metal cation in the supercage of X, which interferes with the CT interaction between  $MV^{2+}$  and the negatively charged framework. For instance, the excess cations will hamper the closer contact between  $MV^{2+}$  and the framework and alter the orientation of  $MV^{2+}$  with respect to the available basic site. Consistent with this interpretation, CT bands have been shown to blue shift upon increasing the intermolecular distance (23,24) or the steric hindrance between the donor-acceptor pairs (178).

Alternatively, congestion of the supercage with  $M^+$  in X may push  $MV^{2+}$  to the less basic sites of the framework since basic sites are known to be inhomogeneous (170f,174c). No matter what the reasons are, the above result suggests that the cation-dependent donor strengths of the frameworks cannot be judged merely on the basis of their chemical compositions. Rather, the actual donor strength of the framework exerting to an acceptor is governed by the multiple factors, such as framework structure, Si/Al ratio, size and number of the cation, nature of the available basic sites in the framework, and shape and size of the acceptor (179). A similar conclusion is derived from the CT interaction of iodine with the zeolite framework as discussed in Sec. III.A.2 (p. 673).

The disappearance of the CT band upon hydration of  $MV^{2+}-M^+X$  and  $MV^{2+}-M^+Y$  in Fig. 54B arises from the loss of direct interaction between  $MV^{2+}$  and the zeolite framework by the intervening water, which preferentially adheres to the polar oxide surfaces of zeolites. However, unlike  $MV^{2+}$ -exchanged X and Y, even the fully hydrated  $MV^{2+}$ -adopted ZSM-5 shows a distinguished shoulder band at around 260 nm, as shown in Fig. 56A. This arises since water cannot eliminate the  $MV^{2+}$ -framework CT interaction in ZSM-5 as it does in X and Y due to tighter fit of the bulky  $MV^{2+}$  ion within the narrower zeolite pores ( $\sim 5.5$  Å) and the hydrophobic nature of the silica-rich zeolite.

Interestingly, the local band of  $MV^{2+}$  appears at 290 nm in ZSM-5, which corresponds to a red shift by 10 and 20 nm with respect to the  $\lambda_{max}$  in  $Na^+X$  (280 nm) and  $Na^+Y$  (270 nm), respectively. Thus, the progressive red shift is related to the progressive decrease in pore size (14,180). This phenomenon is attributed to the progressive deviation of the planarity of the rings and the increase in the degree of molecular orbital distortions as a result of the increase in the degree of confinement in a restricted space. This induces a larger degree of separation between the CT and local band, which makes the CT band look more apparent in ZSM-5 than in Y, even before mathematical deconvolution (Fig. 56B).

The framework-to- $MV^{2+}$  CT complexation is not surprising in view of the fact that  $MV^{2+}$  forms CT complexes with various counteranions in the solid state (181). The most widely studied anions are halides ( $X^- = Cl^-, Br^-, I^-$ ) and some anionic metal complexes such as  $Cu_2Cl_6^{2-}$ ,  $MnCl_4^{2-}$ ,  $FeCl_4^{2-}$ , and  $ZnCl_4^{2-}$ . For instance, the colors of halide salt of  $MV^{2+}$  is colorless ( $Cl^-$ ), yellow ( $Br^-$ ), and red ( $I^-$ ) in the solid state. Although CT interaction between  $MV^{2+}$  and  $Cl^-$  is not visually apparent in the colorless  $MVCl_2$  salt, the diffuse reflectance spectrum of the crystal clearly shows the corresponding CT band at 377 nm in addition to the local band of  $MV^{2+}$  at 260 nm (181a). Likewise, the CT interaction between  $MV^{2+}$  and its counteranions prevails in all of the  $MV^{2+}$  salts,

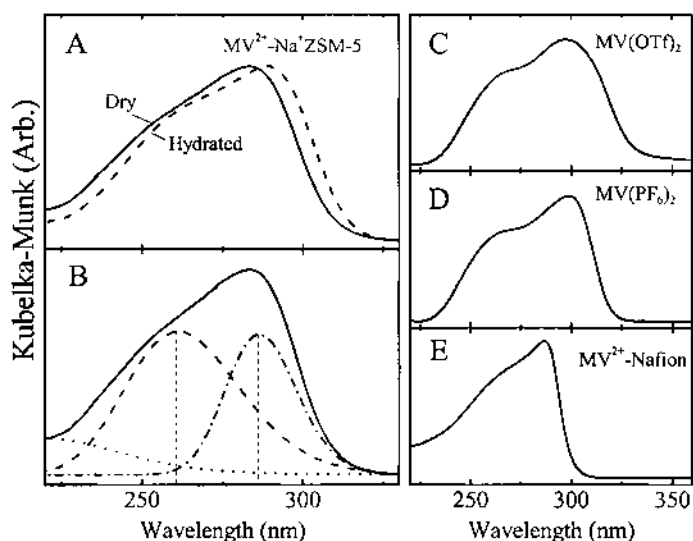
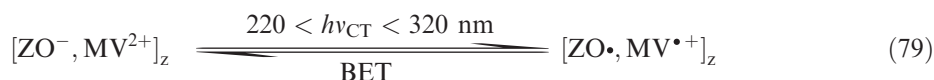


**Fig. 56** (A) Diffuse reflectance UV-vis spectra of the  $MV^{2+}\text{-Na}^+\text{ZSM-5}$  in the dry (solid line) and the hydrated (dashed line) state, showing the presence of BHEB at around 250 nm even before decomposition. (B) Decomposition of the spectrum of the dry sample showing the corresponding CT and local bands in ZSM-5. (C–E) Diffuse reflectance spectra of the  $MV^2$  salts with three different anions (as indicated). (Adapted from Ref. 9.)

regardless of the type and the donor strength of the anion. For instance, as shown in Fig. 56C, and D, respectively, even  $MV^{2+}(\text{CF}_3\text{SO}_3^-)_2$  [ $MV(\text{OTf})_2$ ] and  $MV^{2+}(\text{PF}_6^-)_2$  show additional absorption bands at around 300 nm in the solid states in addition to the local band of  $MV^{2+}$  at around 260 nm despite the fact that these anions are normally believed to be highly inert. Moreover, the diffuse reflectance spectrum of  $MV^{2+}$  with Nafion (a polymer with perfluorinated polyethylene backbone and tethered vinyl ether- $\text{CF}_2\text{-CF}_2\text{-SO}_3^-$  units) as the counteranion also reveals an additional band at around 280 nm as well as the local band of  $MV^{2+}$  at around 260 nm (Fig. 56E). These additional bands should be assigned as the corresponding CT bands arising from the CT interaction between  $MV^{2+}$  and the counteranions from the analogy of halide salts. Likewise, from the view that zeolite framework is merely a class of polyvalent anions like Nafion, it is not difficult to accept the CT interaction between  $MV^{2+}$  and the zeolite framework as an example of the general CT interaction between  $MV^{2+}$  and its counteranion.

The finding of framework-to- $MV^{2+}$  CT interaction also establishes that PET occurs from the framework to  $MV^{2+}$  upon absorption of light at the wavelengths between  $\sim 220$  and  $\sim 320$  nm [Eq. (79)]:



where  $[_z]$ ,  $\text{ZO}^-$ ,  $\text{ZO}\cdot$  respectively denote zeolite pore, the zeolite framework, and the one-electron oxidized form of the framework. In dry  $MV^{2+}$ -exchanged zeolites, irradiation of the samples at wavelengths between  $\sim 250$  and  $\sim 320$  inevitably leads to simultaneous excitation of the local band of  $MV^{2+}$  [Eq. (80)] to the singlet excited state,  $*MV^{2+}$ , as well

as the CT transition [Eq. (81)]. The framework and  $*MV^{2+}$  then undergo ET according to Eq. (82).



Equation (81) is highly feasible since  $*MV^{2+}$  is a strong oxidant ( $E^0 = 3.34$  V vs. NHE) and the  $E^0$  of  $Na^+Y$  can be as low as 1.26 V (vs. NHE) as discussed in Sec IV.C (p. 706).

In fully hydrated X and Y, selective excitation of  $MV^{2+}$  is possible due to disappearance of the framework- $MV^{2+}$  CT band. In ZSM-5, however, excitation of both bands is inevitable even in the hydrated state although selective excitation of the CT band is still possible by irradiating the wavelengths shorter than  $\sim 260$  nm. Overall, PET from the zeolite framework to  $MV^{2+}$  takes place by two independent pathways as described in Fig. 57. Indeed, irradiation of partially hydrated  $MV^{2+}$ -exchanged X and Y at 77 K at the wavelengths covering 257 nm gives rise to formation of  $MV^{\bullet+}$  (182a). Since the partially hydrated samples contain both the CT and the local band the above formation of  $MV^{\bullet+}$  is likely to occur by both pathways shown in Fig. 57. The yield of  $MV^{\bullet+}$  decreases sharply (to  $\sim 10\%$ ) upon full hydration of the zeolite. This is related to elimination of CT-excitation pathway by hydration, indicating that the CT excitation pathway is more efficient than the local excitation pathway for PET to occur.

Excitation of partially hydrated  $MV^{2+}$ -exchanged Y, ZSM-5, and MCM-41 at 266 nm also leads to formation of  $MV^{\bullet+}$  (14). In this case PET is also likely to undergo by both pathways, but mostly by CT-excitation pathway. It has been observed that BET slows down as donor strength of the framework increases. During the course of irradiation a transient absorption with the maximum at 490 nm appears, which can be assigned to the dimer of  $MV^{\bullet+}$  [ $(MV^{\bullet+})_2$ ]. In fact, the dimer appears at  $\sim 530$  nm in hydrated Y, especially when the zeolite is fully hydrated (182b).

With regard to the nature of the electron-donating sites, the framework oxygen atoms are believed to serve as the donor sites, especially the ones that are directly

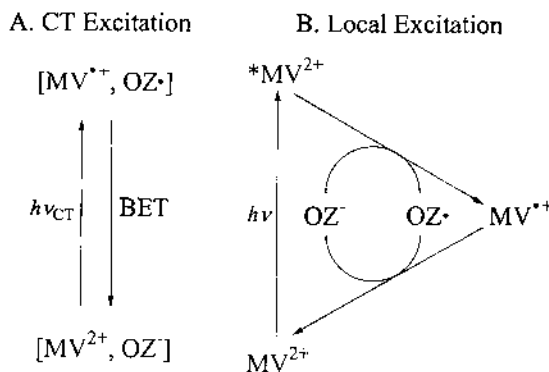
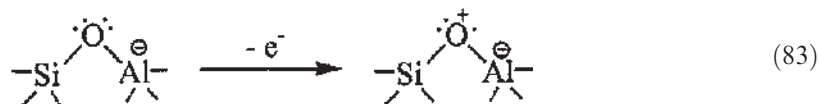


**Fig. 57** Two different pathways that lead to PET from the zeolite framework ( $OZ^-$ ) to  $MV^{2+}$ ; excitation of framework-to- $MV^{2+}$  CT band (A) and local band of  $MV^{2+}$  (B).

coordinated to Al atoms (14). The linear relationship established in Fig. 55B seems to support this idea. On the basis of this model the following equation is proposed:



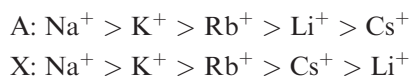
However, considering the polymeric nature of the framework, it is more likely that the electrons are liberated from the valence band of the framework. One might think that the electrons originate from the defect sites. However, the nature of the defect sites is not yet fully understood. Furthermore, the amount of  $MV^{2+}$  is too large to relate the yield of  $MV^{2+}$  to the defect sites of the lattices.

From the standpoint of the framework,  $MV^{2+}$  is a mere charge-balancing cation. Therefore, establishment of the CT interaction between the two components is very important in the sense that it provides a direct clue that the nature of interaction between the framework and other charge-balancing cation is also CT, regardless of the acceptor strength of the cation. This can serve as the most reasonable theoretical basis in accounting for the increase of the donor strength of the framework with increasing size of the alkali metal cation. Thus, in the ground state, the amount of electron density transferred from the framework to the cation decreases as the size of the cation increases, i.e., as the acceptor strength decreases.

Although Mulliken's CT theory implies that the net amount of electron density transferred from D to A is very small in the ground state, many examples have demonstrated that the actual amount of electron density being transferred from D to A is quite substantial even in the ground state. For instance, in the case of  $\text{ArH-NO}^+$  CT complexes the stretching frequency of  $\text{NO}^+$  decreases as the donor strength of ArH increases (183). Since the least unoccupied orbital (LUMO) of  $\text{NO}^+$  is an antibonding orbital, addition of an extra electron to the molecule leads to weakening of the bonding, i.e., to a decrease of the stretching frequency. Thus, it is clear that a substantial amount of electron density is indeed transferred from D to a cationic acceptor ( $\text{NO}^+$ ) even in the ground state. The CT interaction between a donor to iodine ( $\text{I}_2$ ) described in the next section is another excellent example that demonstrates the actual transfer of a substantial amount of electron density from D to A in the ground state.

As a result, even if the acceptor strength of an individual charge-balancing cation is very weak, if there are a large number of charge-balancing cations around the framework, the total amount of electron density that is actually transferred from the framework to the large number of cations will be substantial. This explains why the framework donor strength increases as the size of the alkali metal cation increases or the acceptor strength of the cation decreases. This principle applies for other cations as well.

Such a donor-acceptor interaction between framework and cation may also be applied to interpret the phenomenon in which A and X with low Si/Al ratios ( $A = 1$ ,  $X = 1.2$ ) have a preference for cations with stronger acceptor strengths, as in the following order:



while Y with a higher Si/Al ratio (2.8) shows a strong preference for cations with weaker acceptor strengths, as in the following order (184):



In the above series of alkali metal cations,  $\text{Li}^+$  is exceptional owing to its very thick hydration shell. Thus, it can be said that frameworks with strong donor strengths (A and X) prefer strong acceptor cations to reduce the framework electron density, whereas frameworks with weak donor strengths (Y) prefer weak acceptor cations to minimize the amount of electron density being transferred from the framework to the cation, even during aqueous ion exchange.

## 2. Framework-I<sub>2</sub> CT Interaction

Iodine has been known as a prototypical solvatochromic compound for more than a century. Thus, it is violet in carbon tetrachloride as in the vapor, red in benzene, various shades of brown in alcohols and ethers, and pale yellow in water (185). The dramatic color change arises due to the CT interaction between the solvent and iodine (3,4,186–188). As illustrated in Fig. 58, the visible absorption of iodine corresponds to the electronic transition from  $\pi^*$  (HOMO) to  $\sigma^*$  (LUMO), where the energy level of the latter is subject to an increase in the electron-rich solvents due to the EDA interaction between the solvent and iodine (188). Accordingly, the higher the donor strength of the solvent, the more the energy level of  $\sigma^*$  increases, resulting in a higher degree of hypsochromic shift of the visible iodine band. Thus, the hypsochromic shift is a direct measure of the transfer of electron density from the donor to iodine.

Figure 59A illustrates the negative linear relationship between the observed visible iodine bands ( $\lambda_{\text{max}}$  in electronvolts) and the ionization potentials of a series of aromatic solvents. Other homologous series of solvents also show the negative linear relationship. They range from the relatively weak donors such as alkyl halides to the strong donors such as ethers, sulfides, and amines, both in solution and in the vapor state. The visible bands of iodine adsorbed on various zeolites also show the same trend of hypsochromic shift upon increasing the donor strengths of the frameworks. Thus, as shown in Fig. 60 (A, B, and C)

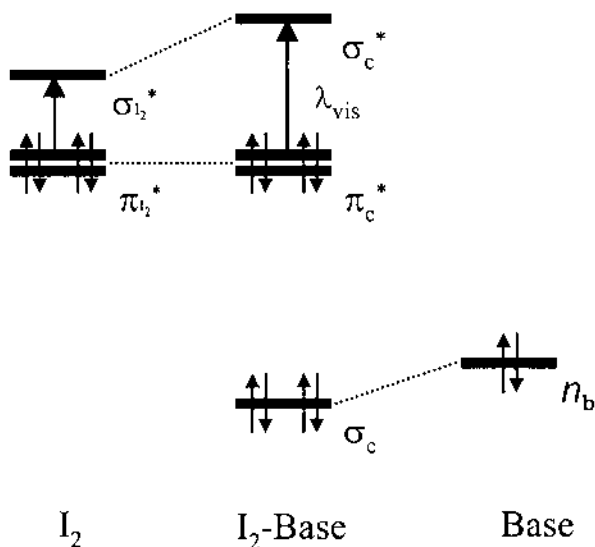


**Fig. 58** The MO energy diagram showing the effect of the CT interaction of iodine with a donor on the visible iodine band.

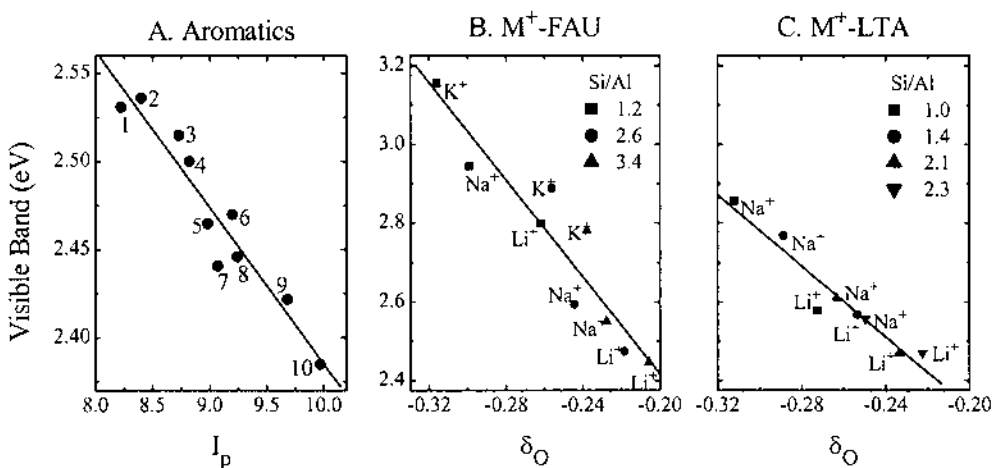


**Fig. 59** The negative linear relationship between the donor strength of the solvent and the visible iodine band (1: methoxybenzene, 2: 1,3,5-trimethyl benzene, 3: iodobenzene, 4: toluene, 5: bromobenzene 6: benzene, 7: chlorobenzene, 8: fluorobenzene, 9: trifluoromethyl benzene, 10: hexafluorobenzene) (A). Negative linear correlations between the visible bands of iodine (in electronvolts) adsorbed on a series of alkali metal-exchanged faujasite-type zeolite (B) and LTA (C) with different Si/Al ratios (as indicated) and their calculated partial charge on the zeolite framework oxygen. (Adapted from Ref. 8.)

the visible iodine band blue shifts upon increasing aluminum content in the framework (Si/Al: 1.2 > 2.6 > 3.4) for a same type of zeolite structure (faujasite) and upon increasing electropositivity of the countercation ( $K^+ > Na^+ > Li^+$ ). Consistent with the spectral shift, the resulting iodine color also blue shifts upon increasing donor strength of the framework. For instance, the color of iodine changes from pink ( $Li^+$ ) to orange-red ( $Na^+$ ) and to yellow-orange ( $K^+$ ) in Y. This trend prevails over a variety of zeolites with different framework structures, Si/Al ratios, and counteranions. For instance, even among a series of ZSM-5 with relatively high Si/Al ratios, the visible iodine band progressively red shifts in accordance with the exact order of the Si/Al ratio, although the increment diminishes progressively (Fig. 60D). As in the case of solution (Figure 59A), plot of the visible iodine band ( $\lambda_{max}$  in electronvolts) with respect to  $\delta_O$  gives a negative linear relationship, as demonstrated in Fig. 59B and C. This establishes the CT interaction between iodine and the zeolite framework. This phenomenon also serves as an experimental basis on which to exploit iodine as a visible probe to evaluate zeolite donor strength (basicity).

The X-ray crystallographic analysis further supports the CT interaction between iodine and the framework oxygen (189a). As shown in Fig. 61, the iodine-to-oxygen distance is 3.29 Å (which is smaller than the normal van der Waals distance between the two atoms), and the interiodine distance increases to 2.79 Å upon adsorption onto the framework oxygen from 2.67 Å in the free gaseous state. The configuration of I-I-O atoms being linear coincides with the nature of LUMO of iodine molecule being  $\sigma^*$ , and the increase of the interiodine distance upon interaction with the framework oxygen also coincides with the theory that the electron-accepting orbital is indeed  $\sigma^*$ , as illustrated in Fig. 58. The actual increase of the interiodine distance further confirms the transfer of a certain degree of electron density from the zeolite framework to iodine in the ground state.

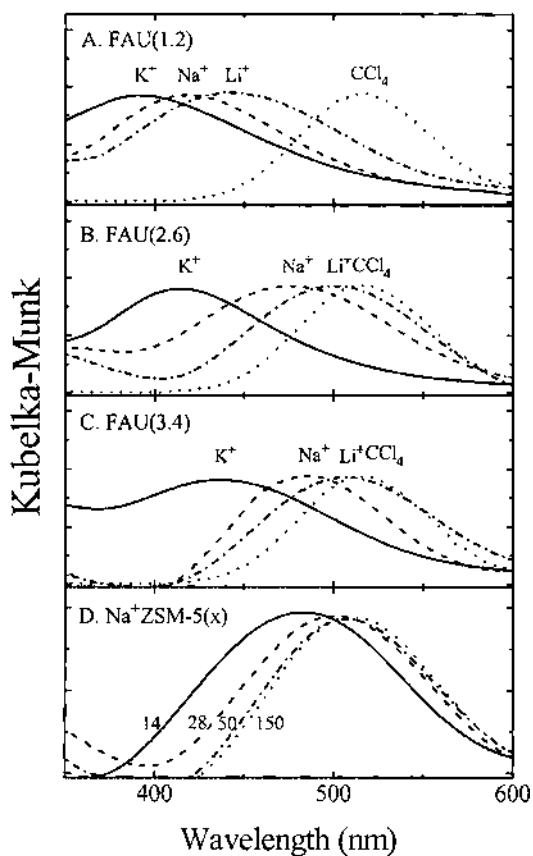


**Fig. 60** Diffuse reflectance spectra (visible region) of iodine adsorbed on a series of faujasite zeolites (a, b, c) and  $\text{Na}^+$ ZSM-5 (d) with different cation and Si/Al ratio (as indicated). For comparison, the absorption band of iodine in  $\text{CCl}_4$  is shown in the dotted line. (Adapted from Ref. 9.)

Accordingly, the electron density retained in the framework decreases as the number of adsorbed iodine increases. This leads to a progressive red shift of the visible iodine band upon increasing the amount of adsorbed iodine. For instance, as shown in Fig. 62, the absorption red shifts from 414 to 447 nm upon increasing the amount of adsorbed iodine from 0.04 to 0.81 molecule per supercage.

The above phenomenon can be interpreted in terms of an inductive electronic effect. The inductive effect has long been known for small molecules. For instance, attachment of an electron-withdrawing group within a molecule leads to depletion of electron density (to a varying degree) from all of the atoms in the molecule. Likewise, if the zeolite framework is viewed as a large, three-dimensionally linked polymeric molecule, the adsorbed iodine depletes the electron density from the whole framework. In other words, the adsorbed iodine depletes the electron density from the valence band of the framework. Consistent with this interpretation, the visible iodine band does not split into two resolved bands even in the zeolites with mixed cations. Rather, the visible iodine band shifts in response to the change in  $\delta_0$ , which represents the average donor strength of the framework. In close relation to this, Barrer and Wasilewski (189b) observed a sharp decrease in the isosteric

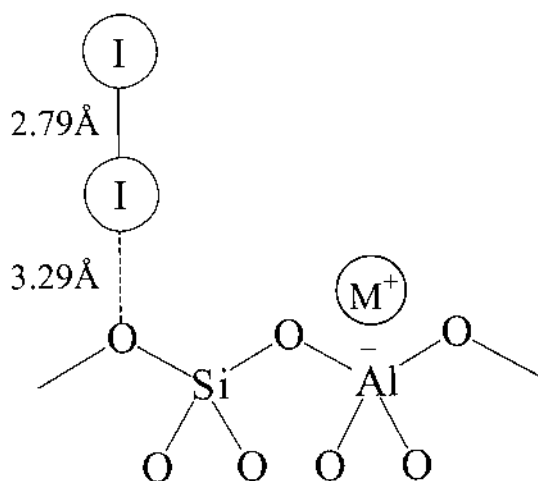


**Fig. 61** Perpendicular interaction of iodine with zeolite framework oxygen revealed by X-ray diffraction analysis. (Adapted from Ref. 189a.)

heat of adsorption upon increasing the adsorbed amount of iodine during the initial stage of iodine occlusion (surface coverage of less than 10–20%, and the adsorbed amounts less than 100–200 mg/g of zeolite). Such a phenomenon looks to be a general feature for a multiple CT interaction between a large, polymeric molecule with multiple electron-donating sites and many small electron acceptor molecules.

The fact that the correlation slopes being different in the two different zeolite structures demonstrated in Fig. 59B and C reflects that the efficiency of CT interaction between iodine and framework varies depending on the structure of the zeolite. From the

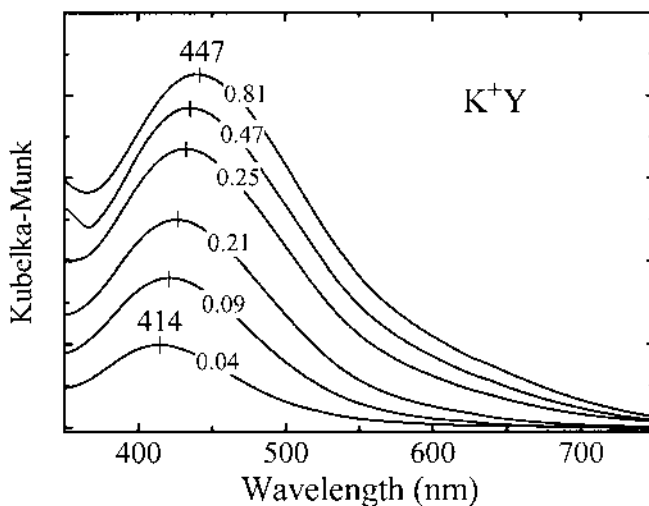


**Fig. 62** Progressive red shift of the visible iodine band upon increasing the amount of adsorption on  $K^+Y$ , a: 0.04, b: 0.09, c: 0.21, d: 0.25, e: 0.47 and f: 0.81 molecule per supercage.

larger slope in the more spacious supercages of Y than in A, a more favorable CT interaction between the large iodine molecule and the framework of Y is inferred. The sensitivity of the CT interaction between  $MV^{2+}$  and the framework also decreases sharply upon decreasing the pore volume, i.e., upon changing the zeolite from Y to X as described in the previous section (see Fig. 55, p. 668). Thus, unlike in solution where the steric hindrance is not imposed by the solvent, the CT efficiency is sensitively governed by the pore volume of the zeolite. This indicates that the basicity of the framework is governed not only by the chemical composition of the framework but also by the pore size.

Iodine can also probe the dehydration process in zeolites, since the visible band of iodine progressively blue shifts upon increasing the degree of dehydration. This occurs due to the increase in the donor–acceptor interaction between the framework and iodine as a result of water loss. In the case of  $NH_4^+$ -exchanged zeolites, the visible iodine band red shifts with increasing degree of deamination. This is quite conceivable since coordination of  $H^+$  with  $NH_3$  will pacify the electron-withdrawing property of  $H^+$  from the framework.

In close relation to the previous observation of CT interaction between the framework and  $MV^{2+}$  or  $I_2$ , the diffuse reflectance UV-vis spectra of TCNB and pyromellitic dianhydride (PMDA) in zeolites show the bands that can be assigned as the CT bands arising from the CT interaction between the zeolite framework and the acceptor (12). For instance, as shown in Fig. 63A, the diffuse reflectance spectrum of TCNB in ultrastable Y (USY) gives three adsorption maxima at about 294, 304, and 314 nm. Among these, it is apparent that the 314-nm band progressively red shifts with increasing donor strength of the framework, i.e., upon changing of zeolite host from USY to  $Na^+Y$  and to  $Cs^+Na^+Y$ . Although more rigorous analysis is yet necessary, the above result clearly suggests that the lowest energy band is the framework-to-TCNB CT band. Likewise, the diffuse reflectance UV-vis spectra of PMDA in the three zeolites reveal that the lowest energy band is the corresponding framework-to-PMDA CT band (Fig. 63B). These results further under-

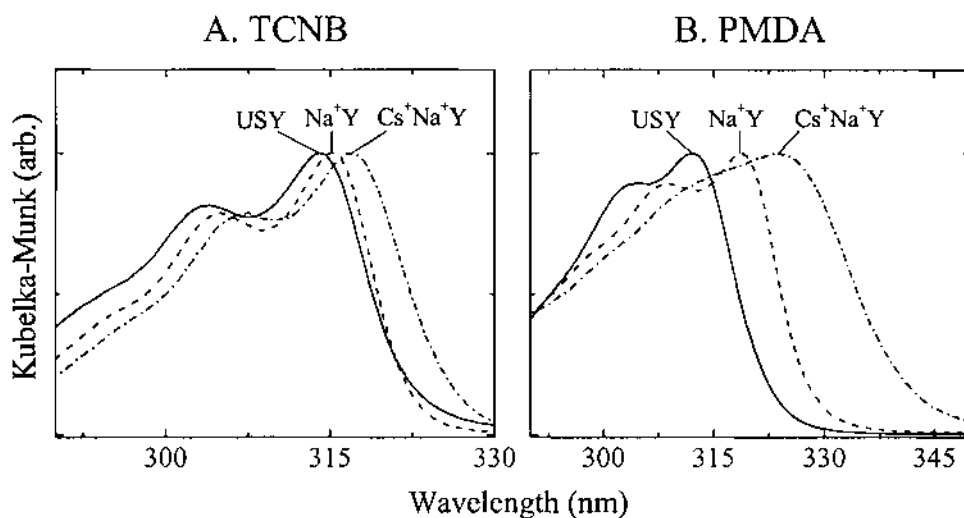
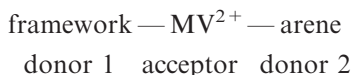


**Fig. 63** Diffuse reflectance UV-vis spectra of USY,  $Na^+Y$ ,  $Cs^+Na^+Y$  (as indicated) incorporating TCNB (A) and PMDA (B).

score the generality of the framework–acceptor CT interaction, regardless of the type of acceptor.

### 3. Framework–Acceptor–Guest Donor Triad (D–A–D') Interaction

Since  $MV^{2+}$  forms a CT complex with the framework as described in the previous section, the intrazeolite  $MV^{2+}$ -arene CT complexes discussed previously (Section III.A.1) should more strictly be formulated as a triad (donor–acceptor–donor) interaction of  $MV^{2+}$  with both the framework (donor 1) and the arene (donor 2) as depicted in Fig. 64A.



Indeed, the resultant  $MV^{2+}$ -arene CT color progressively blue shifts in dry Y upon increasing the size of  $M^+$  on going from  $Li^+$  to  $Cs^+$ . For instance, the colors of  $MV^{2+}$ -ANT complex in  $M^+Y$  are plum ( $Li^+$ ), pink ( $Na^+$ ), brownish pink ( $K^+$ ), brown ( $Rb^+$ ), and brownish yellow ( $Cs^+$ ). Consistent with the gradual color change, the diffuse reflectance UV-vis spectrum progressively blue shifts as demonstrated in Fig. 65A for three typical arene donors in Y. In marked contrast, all the  $MV^{2+}$ -arene CT bands are nearly identical irrespective of  $M^+$ , as shown in Fig. 65B, in hydrated zeolites. This indicates that  $MV^{2+}$  ion has a direct contact with the framework while maintaining the face-to-face interaction with the arene donor.

From the fact that a substantial amount of electron density is actually transferred from D to A in the ground state, the above phenomenon is ascribed to progressive weakening of the acceptor strength of  $MV^{2+}$  as a result of progressive increase in the degree of ET from the framework to the bipyridinium acceptor in the ground state, in response to the increase in the donor strength of the framework upon increasing the size of  $M^+$ . Consistent with this, a negative linear relationship is demonstrated between the framework- $MV^{2+}$  and the arene- $MV^{2+}$  CT bands as shown in Fig. 66. This relationship is a clear indication that arene,  $MV^{2+}$ , and the framework are all linearly interlinked, namely, by a triad interaction.

Likewise, TCNB forms triads with the framework and the guest arene donors, as depicted in Fig. 64B (11,47). Indeed, the absorption maximum of the arene-TCNB CT band blue shifts in dry  $M^+Y$  as the size of  $M^+$  increases as shown in Fig. 67, with a deviation with  $Cs^+$ . The deviation arising from  $Cs^+$  is ascribed to the steric effect of the cation which hampers the optimum positioning of TCNB with both an arene donor and

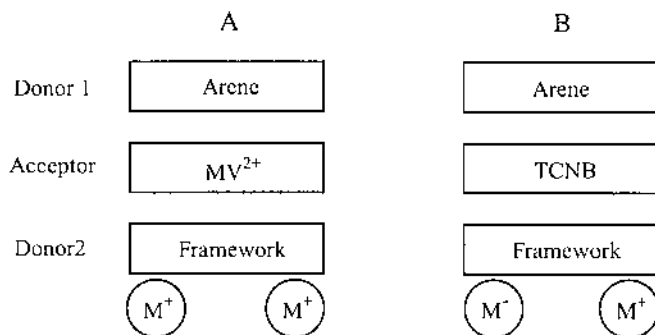


**Fig. 64** Possible  $\pi$ - $\pi$  type of triad interaction of  $MV^{2+}$  (A) and TCNB (B) with both an arene donor and the framework.

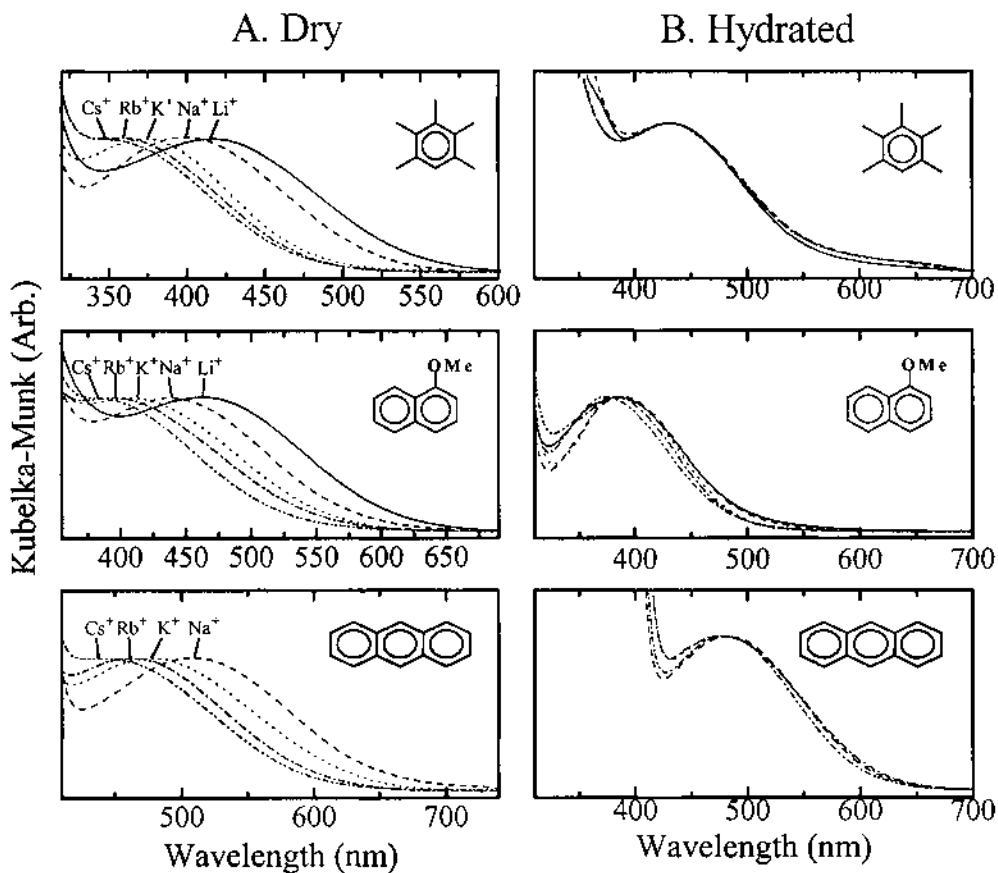


**Fig. 65** The CT bands of the  $MV^{2+}$  complexes with three different arene donors (as indicated) in dry (A) and hydrated (B) Y, with different alkali metal counteranions (as indicated).

the framework in the limited space of the supercage of Y. The difference in the behaviors of arene- $MV^{2+}$  and arene-TCNB with  $Cs^+$  as the counteranion can be ascribed to the fact that TCNB demands wider area due to the four nitrile groups, than the long but narrow  $MV^{2+}$ , as compared in Fig. 68.

One might attribute the cation-induced shift of arene-TCNB CT band to coordination of one of the nitrile groups of the acceptor to a charge-balancing cation, as depicted in Fig. 69, as in the case of arene- $pCP^+$  CT complex in dry Y (p. 608). Such a  $\sigma$ -type interaction between the nitrile group and  $M^+$  will give rise to a red shift of the CT band. However, knowing that the acceptor strength of cation increases with increasing size in the supercage (see p. 622), the resulting arene-TCNB CT band will experience red shift as the size of the cation increases if the shift arises from the cation-nitrile  $\sigma$ -type interaction. Obviously what is observed is the reverse. Therefore, in the case of TCNB, the coordination of nitrile groups to alkali metal cations seems to be unfavorable, unlike  $pCP^+$  or  $oCP^+$  presumably due to steric reasons.

The spectral shift of the arene-TCNB CT band does not arise from the change in the polarity of the supercage as changing the cation, since the absorption maxima of neutral CT complexes usually do not shift significantly with a change in the solvent polarity. This

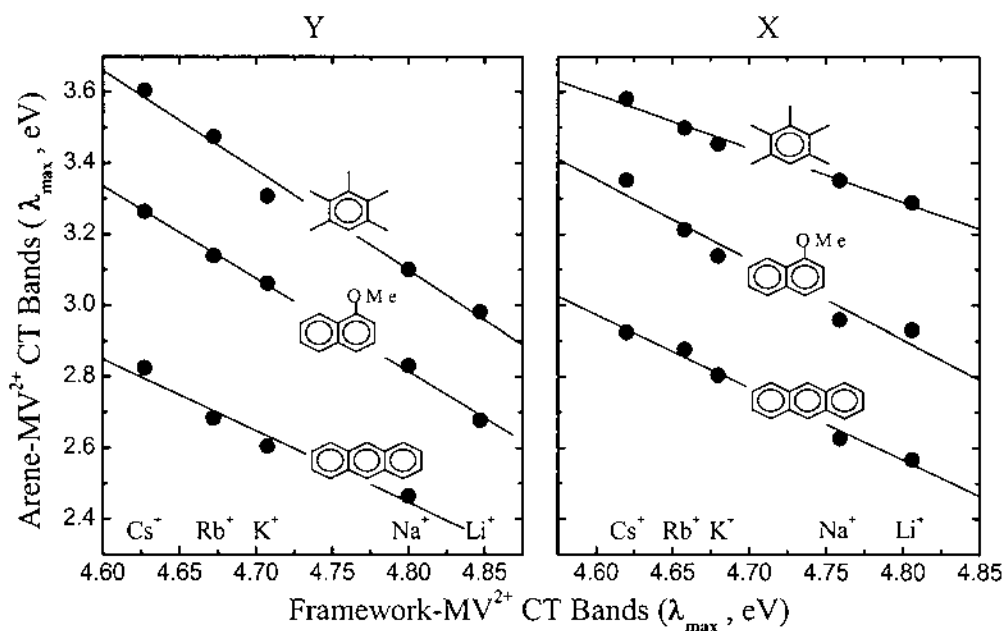


**Fig. 66** Negative linear relationship established between the framework-MV<sup>2+</sup> and arene-MV<sup>2+</sup> CT bands for three prototypical arene donors (as indicated) in Y (left) and X (right).

is because the solvent reorganization energy increases while the excited state energy decreases upon increasing the solvent polarity. Indeed, as listed in Table 15, the arene-TCNB CT band remains almost invariant despite variation of the medium polarity. It is also interesting to note that the CT band from the least basic Li<sup>+</sup> Y is most similar to the one observed in solution and crystal. This indicates that the other CT bands experience unusual blue shifts, again due to the increase in the degree of ET from the framework to TCNB.

Although the negative linear relationship between  $\delta_o$  and the CT energy is not perfect due to deviation of Cs<sup>+</sup> Y, the Stokes shift of the CT fluorescence shows a good linear correlation with respect to  $\delta_o$  as shown in Fig. 70 (47). The Stokes shift is a measure of the structural rearrangement in the Frank-Condon excited state of the complexes, i.e., a larger Stokes shift results from the complex which undergoes a larger geometrical rearrangement to relax to the lowest (fluorescent) excited state. In solution, the Stokes shift increases with increasing solvent polarity because of a larger stabilization of the excited CT state in polar media (190,193). In zeolites too, this phenomenon can also be interpreted by the increase in the degree of stabilization of the CT excited state with increasing size of M<sup>+</sup>, since the donor-acceptor interaction between TCNB<sup>•-</sup> and M<sup>+</sup> is expected to increase as the size of M<sup>+</sup> increases, i.e., as the acceptor strength of M<sup>+</sup> increases (45).

## B. ET from the Framework to Photosensitized Acceptor

### 1. Photoexcitation of the Acceptor

Several examples have been demonstrated in which ET takes place from the framework to photoexcited acceptors. The acceptors range from an arene (PYR) to well-known acceptors such as TCNB, 1,4-dicyanobenzene (1,4-DCNB), PMDA, dimethylterephthalate (DMTP), MV<sup>2+</sup>, and *o*-chloranil.

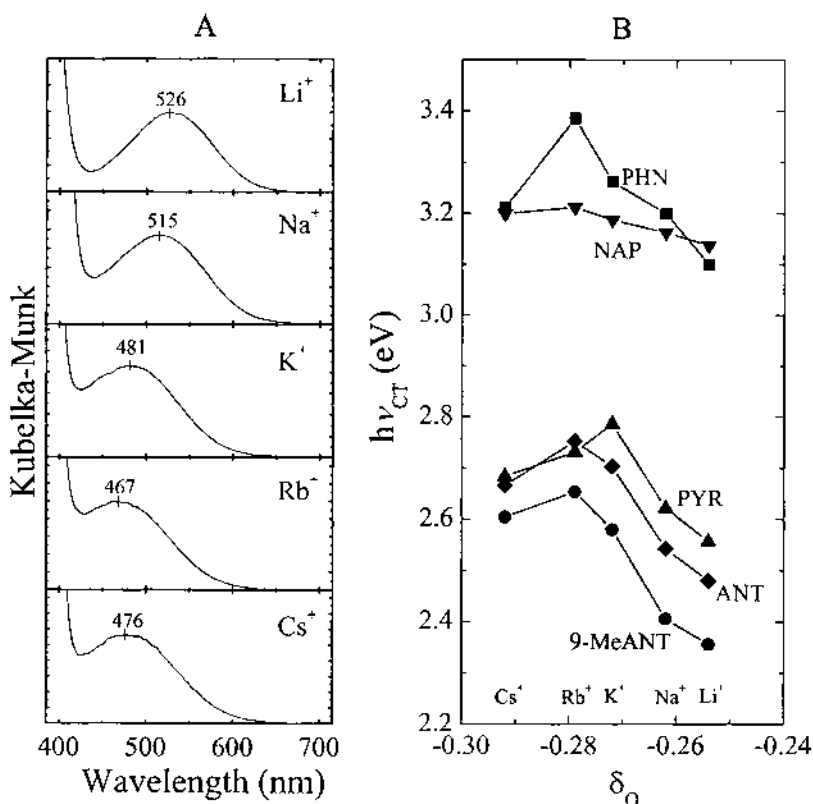


**Fig. 67** (A) Absorption spectra of 9-MeANT-TCNB CT complexes in alkali metal ion-exchanged zeolite Y. (B) Relationship between the peak energy of CT absorption and mean charge on oxygen,  $\delta_O$  calculated according to the Sanderson's electronegativity equalization principle.

For instance,  $\text{PYR}^{\bullet-}$  is readily generated upon excitation of PYR placed in Y at 337 nm (10,71b,143,162b,c). This happens via ET from the framework to PYR in the singlet excited state ( $^1\text{*PYR}$ ) by a single-photon excitation [Eq. (84)]:



The possibility of ET between  $^1\text{*PYR}$  and PYR [Eq. (44)] is eliminated because the above reaction undergoes even at the PYR loading of less than one per  $\sim 200$  supercages. The above result, therefore, represents a case in which the zeolite framework serves as the electron donor for production of  $\text{PYR}^{\bullet-}$ .

Figure 71 provides direct evidence that the zeolite framework is the source of electron. Thus, the photoyield increases as the negative charge density on the framework oxygen ( $\delta_O$ ) increases. The data listed in Table 16 further show that  $^1\text{*PYR}$  (but not  $^3\text{*PYR}$ ) is the one that actually receives an electron from the framework. Thus, while the yield of  $\text{PYR}^{\bullet-}$  increases with increasing  $\delta_O$  of the framework, the quantum yield and the lifetime of  $^3\text{*PYR}$  have no correlation with  $\delta_O$ . The formation of  $\text{PYR}^{\bullet+}$  indicates that ET from  $^1\text{*PYR}$  to 4  $\text{Na}^+$  also takes place simultaneously under the given experimental condition as discussed in Sec. II.B.1 (p. 634). However, the yield of  $\text{PYR}^{\bullet+}$  is independent of  $\delta_O$ , and the decay rate of  $\text{PYR}^{\bullet+}$  does not correlate with that of  $\text{PYR}^{\bullet-}$ . This further

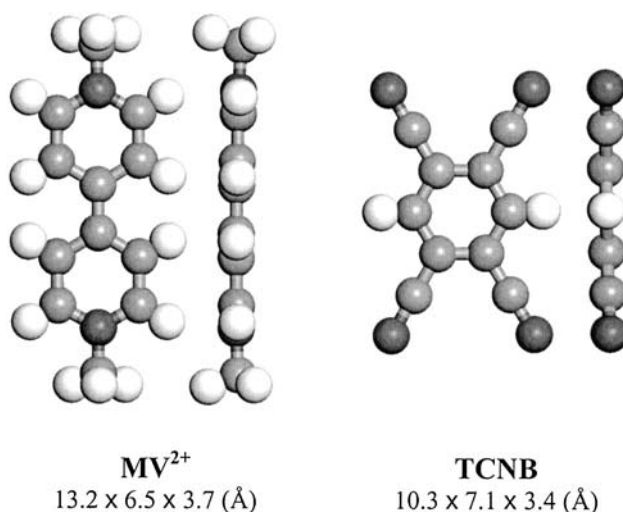


**Fig. 68** The ball and stick models of MV<sup>2+</sup> and TCNB.

confirms that PYR<sup>\*-</sup> does not arise from ET between PYR and <sup>1</sup>\*PYR [Eq. (44)] as opposed to the case where PYR loading is high (84). This fact indicates that there are two different sites in zeolites with opposite functionalities: electron donating and electron accepting (10,71, 143,164).

Photoexcitation of TCNB in Y at 266 nm also leads to ET from the framework (ZO<sup>-</sup>) to <sup>n</sup>\*TCNB ( $n=1$  or 3) (12).

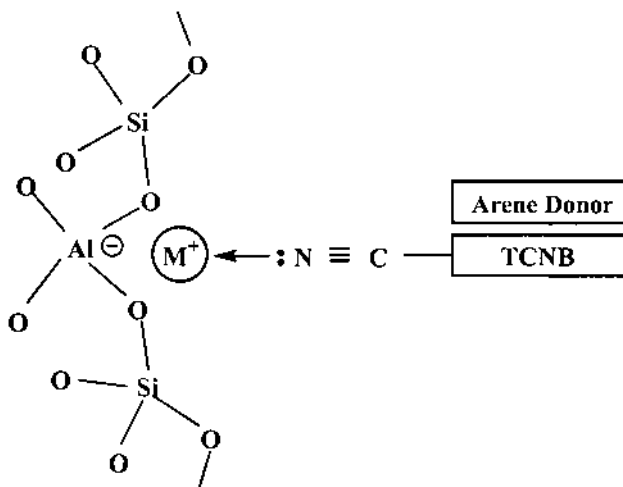
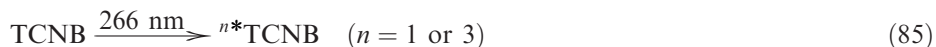


**Fig. 69** Possible acid–base interaction of the nitrile groups of TCNB with the cations ( $\sigma$ -type) while simultaneously interacting with an arene donor ( $\pi$ -type).

**Table 15** Absorption Peak Energy ( $\text{cm}^{-1}$ ) of Arene-TCNB CT Complexes with Different Donors in Various Media

Donor	$\text{C}_6\text{H}_6^{\text{a}}$	$\text{CHCl}_3^{\text{b}}$	Crystal <sup>c</sup>	$\text{LiY}^{\text{d}}$
NAP	25,100	25,000	25,000	25,300
PHN	24,900	25,000	23,800	25,400
PYR	20,700	20,100	—	20,600
ANT	20,100	19,700	19,600	19,700

<sup>a</sup> From Ref. 190.

<sup>b</sup> From Ref. 191.

<sup>c</sup> From Ref. 192.

<sup>d</sup> From Ref. 47.

In dry zeolites, the absorption signal of  $\text{TCNB}^{\bullet-}$  is very long lived (i.e., weeks). In partially (2%) hydrated zeolites, however, the decay of the signal becomes fast (i.e., microseconds) enough for comparison of the effect of the Si/Al ratio and the nature of charge-balancing cation on the decay rate. In the partially hydrated zeolites, formation of  $\text{TCNB}^{\bullet-}$  proceeds by two steps: a fast rise within the duration of the laser pulse (8 ns) and a slow rise in the microsecond time scale. The slow part of  $\text{TCNB}^{\bullet-}$  formation is accompanied by the decay of  $^3\text{*TCNB}$ . This indicates that ET simultaneously takes place from  $\text{ZO}^-$  to  $^3\text{*TCNB}$ . From this, the fast rise of  $\text{TCNB}^{\bullet-}$  is concluded to occur by ET from  $\text{ZO}^-$  to  $^1\text{*TCNB}$ .

Whereas the transient signal of  $\text{TCNB}^{\bullet-}$  is not observed in partially hydrated ultrastable Y (USY), the signal intensity is substantial in  $\text{Na}^+\text{Y}$  and more intense in

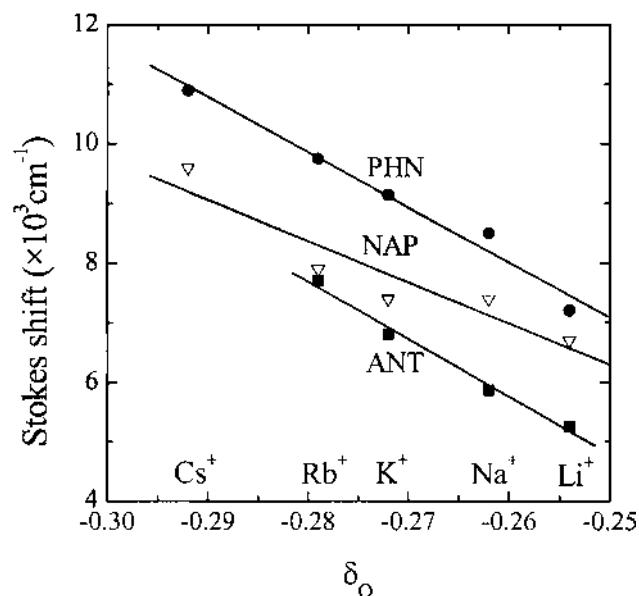


**Fig. 70** Negative linear relationship between the Stokes shift and the mean charge on oxygen,  $\delta_{\text{O}}$  for TCNB- PHN (●), TCNB-NAP (▽), and TCNB-ANT (■) CT complexes. (Adapted from Ref. 47.)

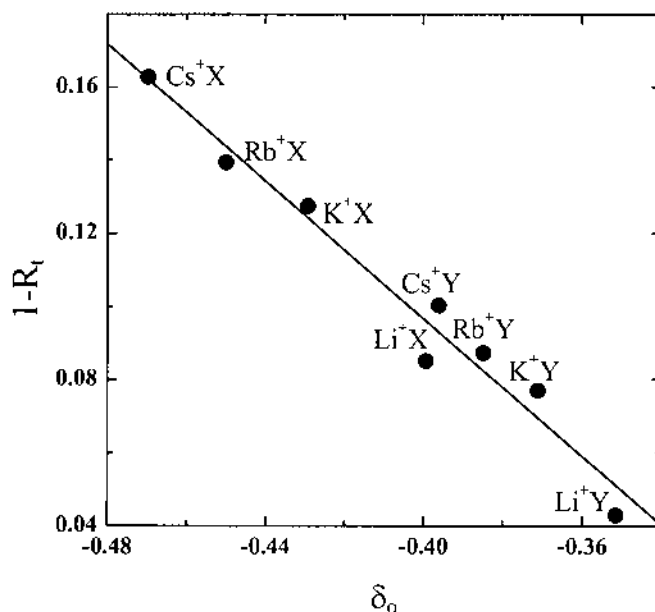


**Fig. 71** Plot of the yield of  $\text{PYR}^{*-}$  against the partial charge on framework oxygen of  $\text{Li}^+$ ,  $\text{K}^+$ ,  $\text{Rb}^+$ , and  $\text{Cs}^+$  zeolite X and Y. (Adapted from Ref. 10.)

$\text{Cs}^+\text{Na}^+\text{Y}$  (61%  $\text{Cs}^+$ ). This trend also serves as direct evidence that the zeolite framework serves as the electron donor. A linear relationship is established between the laser power and the signal intensity of  $\text{TCNB}^{*-}$ , indicating that the above PET occurs via a single-photon process.

Consistent with the intensity of  $\text{TCNB}^{*-}$ , the decay rate of fluorescence increases in the order  $\text{Cs}^+\text{Na}^+\text{Y} < \text{Na}^+\text{Y} < \text{USY}$ . In  $\text{Cs}^+\text{Na}^+\text{Y}$ , the heavy-atom effect is not important for the fluorescence quenching since the relative yield of  $^3\text{TCNB}$  does not enhance even in the  $\text{Cs}^+$ -exchanged zeolite as compared to that in  $\text{Na}^+\text{Y}$ . This indicates that  $\text{TCNB}$  preferentially adsorbs on the basic sites of the framework and the molecule is

**Table 16** Cation-Dependent Variation of Apparent Yield, Quantum Yield, and Lifetime of Some Selected Species of  $\text{PYR}^a$

Zeolite	$-\delta_o$	Yield			Quantum yield ( $\times 10^{-2}$ )				Lifetime (ns)
		$\text{PYR}^{*-}$	$\text{PYR}^{*+}$	$\text{PYR}^{*-}/\text{PYR}^{*+}$	$^1\text{PYR}$	$^3\text{PYR}$	$\text{PYR}^{*+}$	$\text{PYR}^{*-}$	$^1\text{PYR}$
LiY	0.35	0.044	0.074	0.59	40	0.38	0.48	0.18	
KY	0.37	0.077	0.075	1.03	11	0.34	0.48	0.32	
RbY	0.39	0.088	0.076	1.16	7	0.46	0.49	0.37	
CsY	0.40	0.101	0.086	1.17		1.26	0.55	0.42	
LiX	0.40	0.085	0.150	0.57	61	0.93	0.96	0.35	86
KX	0.43	0.127	0.137	0.93	41	0.82	0.88	0.53	44
RbX	0.45	0.140	0.137	1.02	11	0.93	0.88	0.58	9
CsX	0.47	0.163	0.147	1.11		1.47	0.94	0.68	2

<sup>a</sup> Pyrene loading:  $2.8 \times 10^{-6}$  m/g, 337 nm excitation.  
Source: Data from Ref. 10a.

positioned away from  $\text{Cs}^+$ . Considering that  $\text{Cs}^+$  is a strong acceptor in zeolite (45) (see p. 622), it is conceivable that TCNE, another strong acceptor, wants to position away from  $\text{Cs}^+$ .

Likewise, 1,4-DCNB, PDMA, and DMTP become anion radicals in the above three zeolites upon photoexcitation at 266 nm (12). The yields of the anion radicals increase in the order  $\text{USY} < \text{Na}^+ \text{Y} < \text{Cs}^+ \text{Na}^+ \text{Y}$ , again indicating that the frameworks serve as the electron donors. Attempts to estimate the oxidation potential of the zeolite framework were made by applying the Rehm-Weller equation (194) [Eq. (87)] to the zeolite system:

$$\Delta G = E_{1/2}^{\text{Ox}}(\text{D}) - E_{1/2}^{\text{Red}}(\text{A}) - \Delta^* E_{\text{A}} \quad (87)$$

where  $\Delta G$ ,  $E_{1/2}^{\text{Ox}}(\text{D})$ ,  $E_{1/2}^{\text{Red}}(\text{A})$ , and  $\Delta^* E_{\text{A}}$  represent the Gibbs free energy change, oxidation potential of the donor, reduction potential of the acceptor, and the energy level of the acceptor in the excited state (either singlet or triplet), respectively. For the cases where PET readily takes place from the framework to the photoexcited acceptor, Eq. (87) can be expressed as the followings.

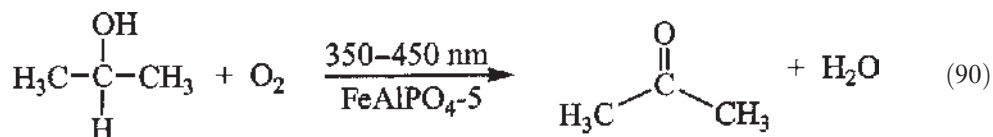
$$E_{1/2}^{\text{Ox}}(\text{ZO}^-) - E_{1/2}^{\text{Red}}(\text{A}) - \Delta^* E_{\text{A}} < 0 \quad (88)$$

$$E_{1/2}^{\text{Ox}}(\text{ZO}^-) < E_{1/2}^{\text{Red}}(\text{A}) + \Delta^* E_{\text{A}} \quad (89)$$

where  $E_{1/2}^{\text{Ox}}(\text{ZO}^-)$  denotes the oxidation potential of the zeolite framework.

Interestingly, from the ready formation of  $\text{PYR}^{\bullet-}$  in dry Y, as described in the beginning of this section, it is deduced that  $E_{1/2}^{\text{Ox}}(\text{ZO}^-)$  can be as low as 1.52 V (vs. NHE) using the following values of PYR:  $E_{1/2}^{\text{Red}} = -1.82$  V (vs. NHE) and  $\Delta^* E_{\text{A}} = 3.34$  eV. On the basis of this result, the donor strength of the framework can be comparable with those of thianthrene ( $E_{1/2}^{\text{Ox}} = 1.52$  V), PYR ( $E_{\text{p}}^{\text{Ox}} = 1.49$  V), and 8,9-diphenylanthracene ( $E_{1/2}^{\text{Ox}} = 1.54$  V) (195). This explains why  $\text{PYR}^{\bullet-}$  can be generated from  $^1\text{PYR}$  either in the presence or absence of available PYR molecules [compare Eqs. (44) and (84)]. Later study shows that  $E_{1/2}^{\text{Ox}}(\text{ZO}^-)$  can be decreased further down to 1.26 V (vs. NHE).

In conjunction with PET from the framework to guest acceptors an interesting photocatalyzed oxidation of alcohols with molecular oxygen is demonstrated, in which photoexcitation of LMCT from the framework oxygen to a transition metal center in  $\text{MeAlPO}_4\text{-5}$ , plays a crucial role (15). Thus, upon excitation of  $\text{FeAlPO}_4\text{-5}$  at 350–450 nm in the presence of methanol or 2-propanol the corresponding oxidized products are readily formed. For instance, with propanol as the substrate the overall reaction proceeds according to the following equation:



The proposed mechanism for the above reaction is shown in Fig. 72. Thus, upon excitation of the LMCT band of O- $\text{Fe}^{\text{III}}$ -O system ET takes place from the framework oxygen to  $\text{Fe}(\text{III})$  center (step A). The  $\text{Fe}(\text{II})$  center then transfers an electron to molecular oxygen ( $\text{O}_2$ ) upon contact (step B). Subsequently, the hole center removes an electron from alcohol, leading to formation of its radical cation and to restoration of the initial form of  $\text{FeAlPO}_4\text{-5}$  (step C). Thus, the above reaction involves three different types of ET. Most of

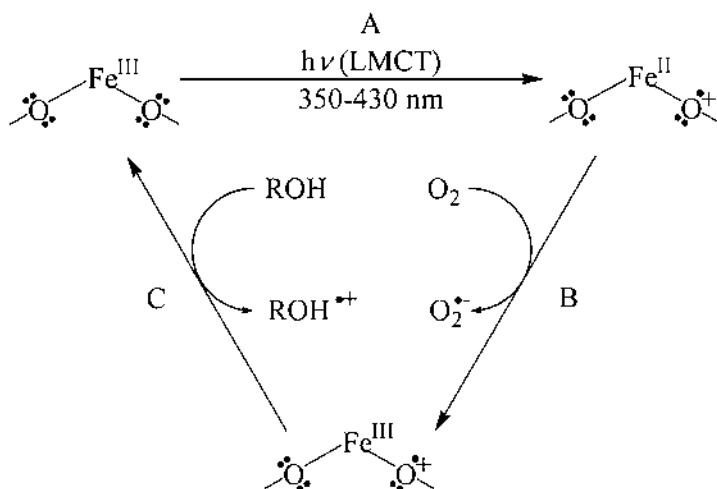
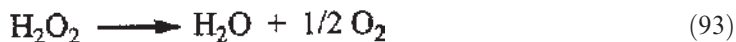
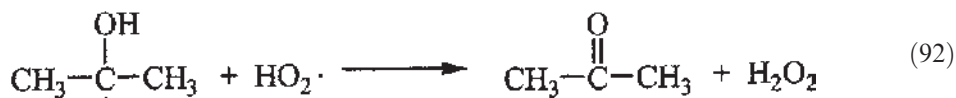
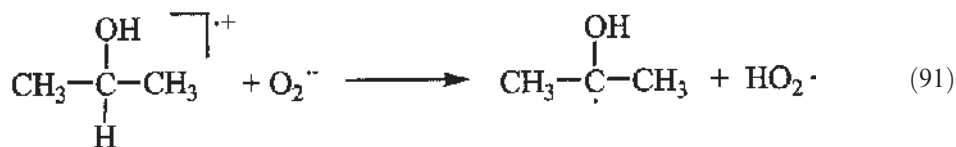


**Fig. 72** Proposed scheme for the photo-oxidation of alcohol with oxygen over FeAlPO<sub>4</sub>-5.

all, the reaction scheme demonstrates a two-way ET both from the framework to the guest and from the guest to the framework. In this regard, the above reaction is one of the ideal systems that demonstrate the importance of the zeolite-based PET for practical applications.

The generated radical cation of alcohol and superoxide undergo proton transfer to give hydroxy alkyl radical and hydroperoxy radical, which subsequently undergo hydrogen atom transfer to give formaldehyde or acetone and hydrogen peroxide. For instance, with 2-propanol as the reactant the following reactions take place.



The finding that O<sub>2</sub> is reduced efficiently by transient Fe<sup>2+</sup> in the framework suggests that its reduction potential lies at least 0.5 V more negative than that of the conduction band of dense-phase Fe<sub>2</sub>O<sub>3</sub> particles. This may open up the demanding photoreductions not accessible by photochemistry at iron oxide semiconductor materials.

## 2. Excitation of the Framework by High-Energy Radiation

As briefly described in the section of alkali-metal ionic clusters (p. 657), it has been long known that zeolite framework ejects electrons upon exposure to high-energy radiation

(HER) such as  $\gamma$  ray, X ray, electron beams, and high-energy UV ( $< 250$  nm, such as 185, 193, and 248 nm).



The scheme for the above phenomenon is described in Fig. 49 (p. 659). The generated electrons then undergo reduction of either group of alkali metal ions or acceptors such as  $\text{MV}^{2+}$ ,  $\text{DQ}^{2+}$ , and  $\text{O}_2$  (14,142,164), as schematically illustrated in Fig. 73. When the acceptor strength of a guest acceptor is stronger than a group of four sodium ions, ET preferentially occurs to the guest acceptor. Namely, processes I and II compete depending on the acceptor strengths of the guest acceptor (A) and four  $\text{Na}^+$ .

For instance, when  $\text{MV}^{2+}$ -exchanged zeolites are exposed to X rays in the high-vacuum chamber of an X-ray photoelectron spectrometer, the sample turns blue due to generation of  $\text{MV}^{\bullet+}$  (14). The color bleaches during the course of several hours as a result of charge recombination between the hole center and  $\text{MV}^{\bullet+}$ . As for the source of electron beams, pulsed electron beams generated from the pulse radiolysis setups are often the choice for accurate control of the electron dosage and time resolution (138). Alternatively, a Tesla coil can also be applied as a cheap yet convenient source of electron beams for demonstration of HER-induced generation of electrons from the framework to students (142).

For instance, exposure of the glass tube containing dry  $\text{Na}^+$ Y powder under a static vacuum (removed from the vacuum system) to the electron beams generated from a laboratory Tesla coil leads to pink coloration over the surfaces of the zeolite powders due to formation of  $\text{Na}_4^{3+}$ . Although the pink color bleaches within a few minutes at room temperature, the color persists for several days without loss of intensity at 77 K. Similarly,  $\text{MV}^{2+}$  or  $2\text{DQ}^{2+}$ -exchanged dry  $\text{Na}^+$ Y turns blue or green due to formation of  $\text{MV}^{\bullet+}$  or  $2\text{DQ}^{\bullet+}$ , respectively. In this case,  $\text{Na}_4^{3+}$  ions are not generated because  $\text{MV}^{2+}$  or  $2\text{DQ}^{2+}$  ions are stronger electron acceptors than four  $\text{Na}^+$ . The comparison of the decay profiles

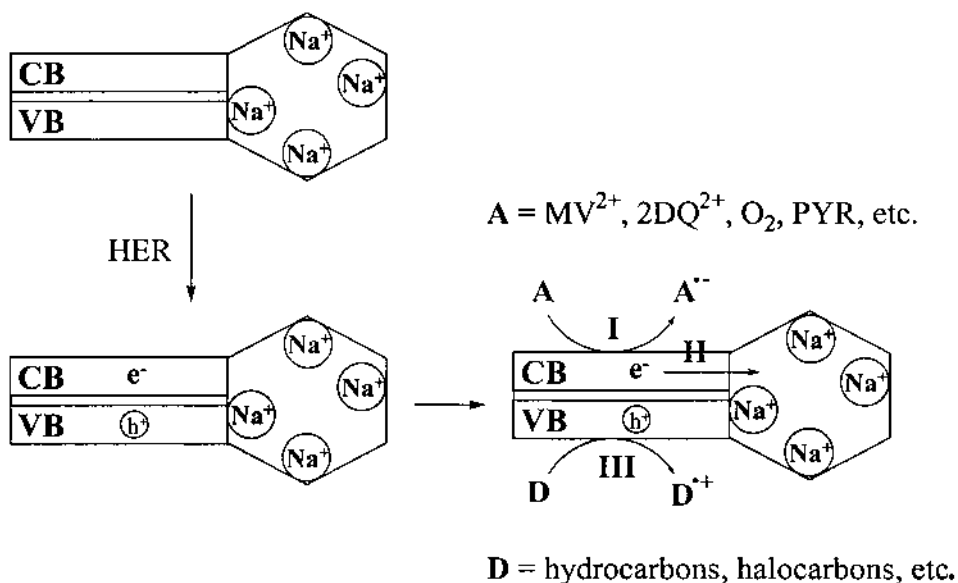


**Fig. 73** Schematic illustration showing the dual role (as D and A) of zeolite framework upon high-energy radiation (HER).

(Fig. 74A) shows that the decay of  $MV^{\bullet+}$  is faster than that of  $2DQ^{\bullet+}$  consistent with the fact that the acceptor strength of  $2DQ^{2+}$  is higher than that of  $MV^{2+}$ . Furthermore, for a series of  $MV^{2+}$ -exchanged X and Y with different alkali metal ions ( $Li^+$ ,  $Na^+$ , and  $K^+$ ) the decay rate of  $MV^{\bullet+}$  slows down as the donor strength of the framework increases. Thus, although the experimental setup is not applicable for accurate comparison of the decay profiles, it is good enough to demonstrate HER-induced generation of electrons and the effect of the cation and the Si/Al ratio on the donor strength of the framework.

So far, attention has been directed to transfer of radiolytically generated electrons to electron acceptors. However, it should also be kept in mind that ET from guest electron donors (D) to hole centers in the framework also readily occurs and this has been utilized to generate various organic radical cations for ESR studies (196,197). For instance, various radical cations of alkanes, olefins, acetylene, and halocarbons have been generated within various zeolite matrices at 77 K by applying the above methodology.



The resulting radical cations usually undergo various reactions such as proton transfer, elimination, and rearrangement upon increasing the temperature of the matrices. In this regard, zeolite matrices are highly beneficial since the framework structures of zeolites retain their rigidity even at high temperatures unlike the conventional matrices composed of halocarbons and rare gases. In other words, zeolite matrices allow study of radical cations over a much wider temperature range. Zeolite matrices also permit more

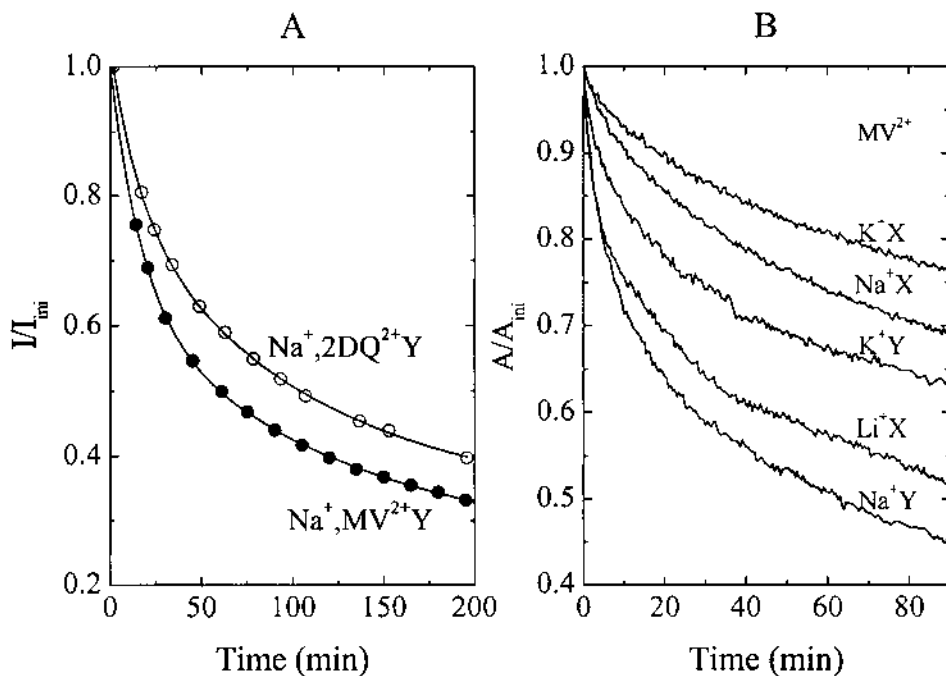


**Fig. 74** (A) Comparison of the decay rates of  $2DQ^{\bullet+}$  (○) and  $MV^{\bullet+}$  (●) in  $Na^+Y$  generated by a Tesla coil monitored by ESR signals. (B) Decay profiles of  $MV^{\bullet+}$  generated in  $K^+X$ ,  $Na^+X$ ,  $Li^+X$ ,  $K^+Y$ , and  $Na^+Y$  (as indicated) monitored by diffuse reflectance UV-vis spectra. (Adapted from Ref. 142.)

variation of experimental conditions in addition to temperature, such as polarity and volume of the nanoreactions. As a result, the novel features of zeolite matrices allow greater diversity to the chemistry of radical cations.

#### IV. PET ACROSS ZEOLITE–SOLUTION INTERFACE

##### A. Strategies to Achieve Long-Lived Charge Separation

Charge separation (CS), i.e., the spatial separation of the electron-transferred donor–acceptor pair, is crucial for ensuing biological reactions and its control is an essential element in the development of artificial photosynthetic systems designed to harness solar energy (5,6). Thus, the efficiency and economy of light-harvesting systems strongly depend on the ability to control CS. As described in the previous sections, zeolites have been employed as versatile organizing media for artificial supramolecular assembly of various D and A pairs and the studies of PET between the D–A pairs have provided insight into the factors that govern the charge-separated states (CSSs). This section summarizes various elegant ideas that have been designed to achieve long-lived CSS across the zeolite–solution interface.

ET readily takes place from  $^*Ru(bpy)_3^{2+}$  placed on the external surfaces of Y and L to  $MV^{2+}$  ions placed within the pores (Fig. 75) (198). Thus, upon irradiation of the deoxygenated, aqueous suspensions of the  $Ru(bpy)_3^{2+}$ – $MV^{2+}$  zeolites at 532 nm by Nd:YAG Q-switched laser (11-ns pulses, 15–25 mJ per pulse), two positive peaks at 400 and 600 nm and a negative peak at 450 nm appear in the diffuse-reflectance transient absorption spectroscopic image due to formation of  $MV^{+}$  and bleaching of  $Ru(bpy)_3^{2+}$ , respectively (Fig. 76A). The  $Ru(bpy)_3^{2+}$  does not luminesce due to ET quenching of  $Ru(bpy)_3^{2+}$  by the internal  $MV^{2+}$  ions. Stern-Volmer plots show good linearities in Y and L, indicating that the ET quenching is dynamic (Fig. 76B). Thus, the quenching rate is controlled by diffusion of  $MV^{2+}$  through zeolite pores. In the case of mordenite with smaller channels the Stern-Volmer plots become nonlinear. This indicates that the type of zeolite structure sensitively affects the charge-recombination kinetics. Table 17 compares bimolecular quenching rate constants and diffusion coefficients of  $MV^{2+}$  in L and Y

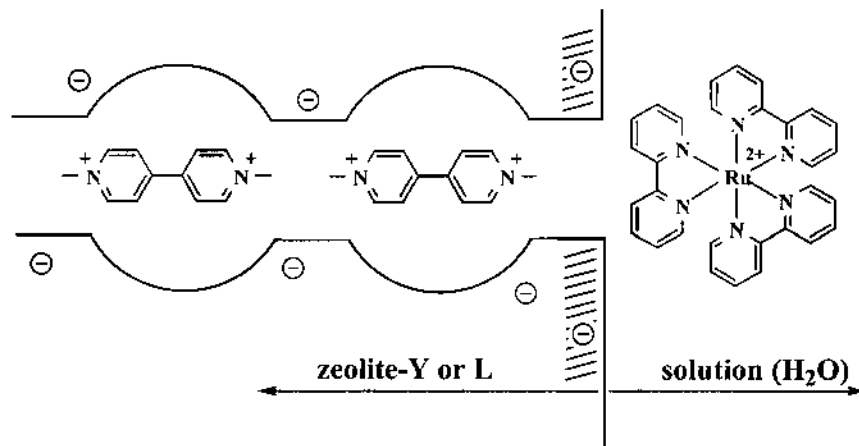


**Fig. 75** Spatial arrangement of  $MV^{2+}$  and  $Ru(bpy)_3^{2+}$  in zeolite and water, respectively. (Adapted from Ref. 7a.)

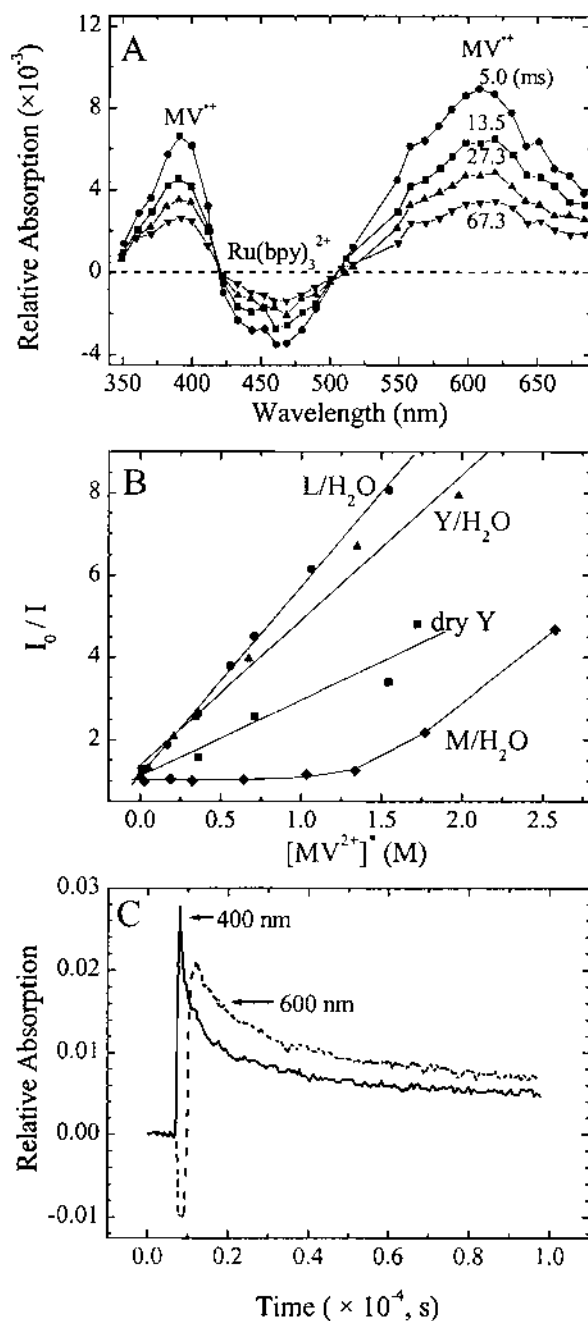


**Fig. 76** (A) Transient diffuse reflectance spectra of Ru(bpy)<sub>3</sub><sup>2+</sup>/MV<sup>2+</sup>/zeolite L (loading levels of Ru(bpy)<sub>3</sub><sup>2+</sup> and MV<sup>2+</sup> are  $1.0 \times 10^{-5}$  and  $3.0 \times 10^{-4}$  mol g<sup>-1</sup>, respectively) recorded after laser excitation (as indicated). (B) Stern-Volmer plots for quenching of Ru(bpy)<sub>3</sub><sup>2+</sup> by MV<sup>2+</sup> in aqueous suspensions of zeolite L, Y, and M and in a powder sample of zeolite Y dried in vacuum (as indicated). (C) Decay of signals at 400 (solid line) and 600 nm (dashed line).

**Table 17** Bimolecular Quenching Rate Constants of Ru(bpy)<sub>3</sub><sup>2+</sup> and Diffusion Coefficients of MV<sup>2+</sup> in Zeolite L, Y, and Other Microenvironments<sup>a</sup>

	$k_{SV}(M^{-1})$	$k_q(M^{-1}s^{-1})$	$D_{MV^{2+}}(cm^2s^{-1})$
L <sup>b</sup>	4.2	$9.1 \times 10^6$	$1.3 \times 10^{-7f}$
Y <sup>b</sup>	4.6 (1.8)	$7.9 \times 10^6, (3.1 \times 10^6)$	$7.9 \times 10^{-7f}, (4.4 \times 10^{-8})$
Hectorite <sup>c</sup>		$1.1 \times 10^6$	
ZrPS <sup>d</sup>	9.8	$1.2 \times 10^7$	$1.6 \times 10^{-8}$
Aq. soln. <sup>e</sup>		$5 \times 10^8$	

<sup>a</sup> Values in parentheses refer to powdered zeolite Y samples air dried in vacuo at 400°C.

<sup>b</sup> Data from Ref. 198.

<sup>c</sup> Data from Ref. 199.

<sup>d</sup> Data from Ref. 200.

<sup>e</sup> Data from Ref. 201.

<sup>f</sup> Average pore radii of zeolite Y and L were taken to be 5 Å.

together with those in related microenvironments (199–201). The fact that quenching rate constants  $k_q$  in both zeolites are lower than those obtained in aqueous solutions (202) indicates that the contact between \*Ru(bpy)<sub>3</sub><sup>2+</sup> and MV<sup>2+</sup> is more localized and the diffusion of MV<sup>2+</sup> through the zeolite pores is restricted.

Thus, organization of D and A on and in zeolite media leads to long-lived CSSs. Although lifetimes of transient signals vary depending on the type of zeolite and the amounts of loading of Ru(bpy)<sub>3</sub><sup>2+</sup> and MV<sup>2+</sup>, they are generally longer than 100 ms. In both cases, the time scale for charge recombination is shorter than those observed in fully dehydrated Y (*vide supra*) (102). The lower value of  $k_q$  in the partially dried Y suggests that the pore-filling water has an important role in enhancing the mobility of ions within zeolite pores. Quantum yields for CS efficiencies for Ru(bpy)<sub>3</sub><sup>3+</sup> and MV<sup>•+</sup> in these zeolites are 6–9%.

As have routinely been observed in zeolite media, the decay curves of the above systems do not follow first- or second-order kinetics (Fig. 76C), indicating complicated BET processes between Ru(bpy)<sub>3</sub><sup>3+</sup> and MV<sup>•+</sup>. Time-resolved emission experiments show that decays of \*Ru(bpy)<sub>3</sub><sup>2+</sup> emission also do not follow single-exponential kinetics. This contrasts with the equal-concentration second-order kinetics (201,203) in homogeneous solutions, and the single exponential decay of \*Ru(bpy)<sub>3</sub><sup>2+</sup> emission from the MV<sup>2+</sup>-free, Ru(bpy)<sub>3</sub><sup>2+</sup>-exchanged zeolites. The latter indicates that the heterogeneity of adsorption sites available to Ru(bpy)<sub>3</sub><sup>2+</sup> on these zeolite surfaces does not affect the photophysics. Accordingly, the nonlinearity in the decay kinetics of \*Ru(bpy)<sub>3</sub><sup>2+</sup> in the Ru(bpy)<sub>3</sub><sup>2+</sup>- and MV<sup>2+</sup>-doped zeolite systems should be attributed to the restricted diffusional motion of MV<sup>2+</sup> in zeolite pores.

PET from a size-excluded photosensitizer to an acceptor inside the channels of L takes place much more readily when an electron relay is tethered to the photosensitizer and the electron relay is intercalated into the channel (204). For instance, when 2DQ<sup>2+</sup>-tethering Ru(5,5'-Me<sub>2</sub>bpy)<sub>3</sub><sup>2+</sup> and benzyl viologen (BV<sup>2+</sup>) are spatially organized onto L as depicted in Fig. 77, photoexcitation of the Ru complex at 532 nm using a 10-ns pulsed laser gives rise to formation of BV<sup>•+</sup> and bleaching of the absorption of the Ru complex. The formation of the Ru(III)-BV<sup>•+</sup> CSS occurs within 100 ns, which is the shortest time scale under which the experiment was carried out. Control experiments from the BV<sup>2+</sup>-exchanged L exchanged with 2DQ<sup>2+</sup>-free Ru(5,5'-Me<sub>2</sub>bpy)<sub>3</sub><sup>2+</sup> show only modest quenching of the MLCT state by BV<sup>2+</sup>, indicating that the direct ET from \*Ru(5,5'-Me<sub>2</sub>bpy)<sub>3</sub><sup>2+</sup>

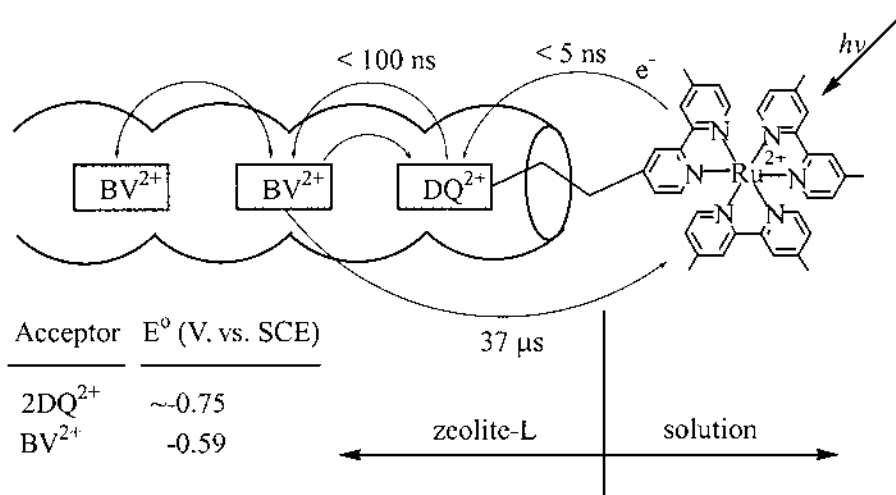


**Fig. 77** Spatial arrangement of  $BV^{2+}$  and the  $DQ^{2+}$ -tethering Ru(II) complex in and on L.

to intrazeolite  $BV^{2+}$  is much less efficient. Thus, Ru(III)- $BV^{+}$  CSS takes place via intermolecular ET from  $2DQ^{+}$  to  $BV^{2+}$ .

Close contact between  $2DQ^{2+}$  and  $BV^{2+}$  is a must for fast and efficient ET. Consistent with the increase in the efficiency of PET the quantum yield reaches  $\sim 17\%$ , which is significantly higher than the simpler, previous system shown in Fig. 75. Interestingly, the lifetime of Ru(III)- $BV^{+}$  CSS is about  $37\ \mu\text{s}$  and it decays via first-order exponential kinetics. The spatial separation of the Ru(II) complex and  $BV^{2+}$  is responsible for elongation of the lifetime of the Ru(III)- $BV^{+}$  CSS.

For the electron relay to be effective, the acceptor strength of the relay should be weaker than that of the final acceptor but strong enough to accept electron from the photoexcited donor. In the above system the estimated acceptor strengths of  $2DQ^{2+}$  and  $BV^{2+}$  are about  $-0.51$  and  $-0.35$  V (vs. NHE), respectively, in aqueous zeolite. The rather small potential difference between  $2DQ^{2+/+}$  and  $BV^{2+/+}$  couples suggests that BET from  $BV^{+}$  to Ru(III) via  $2DQ^{2+/+}$  is also possible. Emission study on L shows that ET from  $*Ru(5,5'-Me_2bpy)_3^{2+}$  to the tethered intrazeolite  $2DQ^{2+}$  occurs within 5 ns.

Upon increasing the length of spacer the rate of forward ET from the size-excluded photosensitizer to the zeolite-intercalated electron acceptor decreases (205). Thus, in a system schematically depicted in Fig. 78, the rate constant for  $*Ru(II)$  to  $MV^{2+}$  decreases by approximately one natural log unit per methylene added to the spacer and the distance dependence is apparently greater for L and M but less for Y, as shown in Fig. 79A. The forward ET is monitored by observing the decay of the  $*Ru(II)$  at 360 nm. The time scale of the ET quenching in homogeneous solutions is tens of picoseconds to hundreds of nanoseconds depending on the length of the spacer and its conformation (206).

For the shortest spacer chains ( $M_2$  and  $A_2$ ) MLCT lifetimes are shorter than 30 ns, which is the detection limit of the instrumental setup, on zeolite surfaces. For longer chains ( $M_3$ – $M_8$ ), forward ET occurs 1–2 orders of magnitude more slowly on zeolite surfaces than it does in homogeneous solutions. The retardation is primarily attributed to the loss of conformational flexibility of the diad ions, as a result of immobilization on the zeolite surface, as opposed to free ions that can explore many different conformations on the time

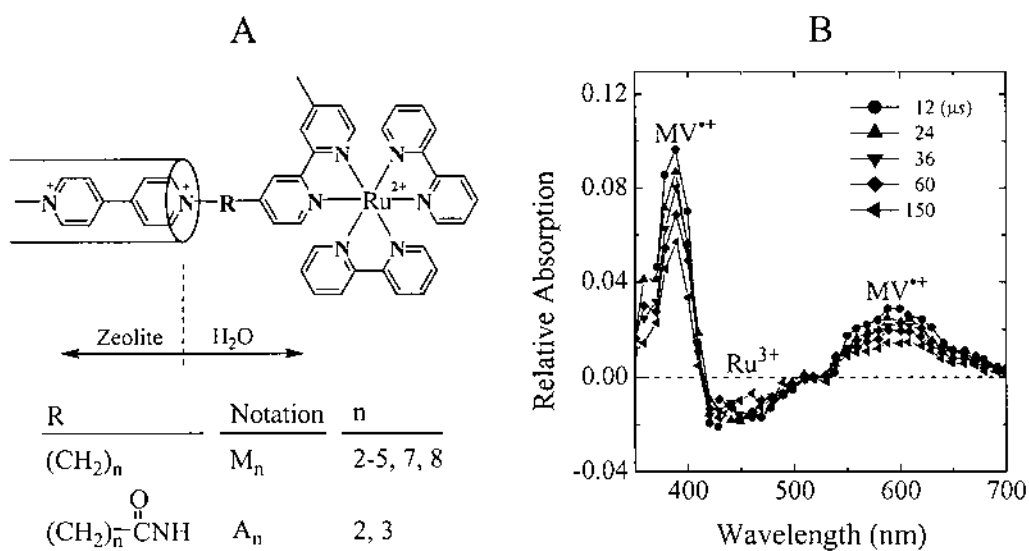


**Fig. 78** Spatial arrangement of  $\text{MV}^{2+}\text{-R-RuL}_3^{2+}$  diad complexes on zeolite surface (A), and transient UV-visible diffuse reflectance spectra for  $\text{H}_3\text{M}$  on mordenite, recorded 12–15  $\mu\text{s}$  after 532-nm laser excitation (B).

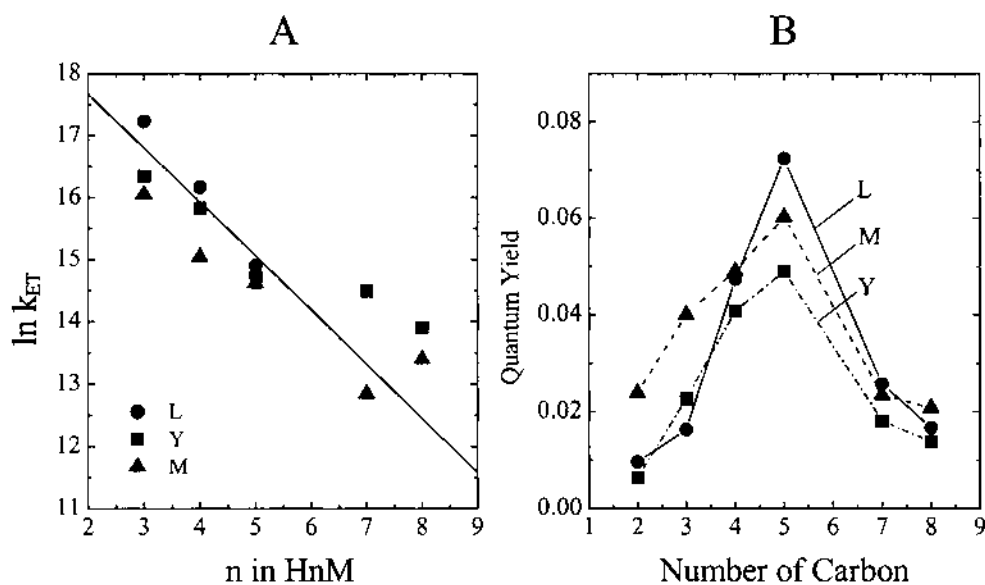


**Fig. 79** Plot of  $\ln k_{\text{ET}}$  vs.  $n$  for forward ET in  $\text{H}_n\text{M}$  diads on zeolites. The slope of the solid line is 0.86 (A). Transient quantum yields for formation of CSS in  $\text{MV}^{2+}\text{-Ru}$  complex diads on three different zeolites (as indicated) in aqueous suspensions (B).

scale of ET reactions in solution by use of the flexible aliphatic spacers. The reduction of the thermodynamic driving force for the weakly exoergic forward ET, as a result of ion exchange of the diads onto the zeolite surface, also seems to cause the retardation (207).

Unlike in homogeneous solutions, the diad ions give long-lived CSSs on the zeolite surfaces. Thus, while the time scale for the BET from  $MV^{\bullet+}$  to Ru(III) is tens to hundreds of microseconds for  $M_n$  and  $A_n$ , that of  $M_5$  in homogeneous solutions is less than 10 ns. Again, the BET process is kinetically complex in contrast to the forward ET, which follows simple first-order kinetics. There is a rapid initial decay of the CSS, followed by a longer lived CSS that decays over a time scale of hundreds of microseconds.

Interestingly, the quantum yield for formation of the long-lived CSS increases progressively with increasing the chain length ( $n$ ), but reaches a maximum at  $n=5$  and decreases as the chain length further increases, as illustrated in Fig. 79B. The decrease of the quantum yield for longer spacers can be understood from the decrease of the forward ET rates. However, the lower quantum yields for the shorter spacers are rather surprising. The lateral ET between Ru(III) and Ru(II) and/or between  $MV^{\bullet+}$  and  $MV^{2+}$  juxtaposed on the zeolite surface seems to be responsible for this phenomenon. The fact that the CS quantum yield is low (1~7%) for all chain lengths indicates that the rate of BET within the D-A diads is in all cases faster than the lateral ET rate.

Introduction of a secondary, size-excluded electron donor that can selectively reduce Ru(III) to Ru(II) into the above system can lead to CS between the oxidized form of the newly introduced secondary donor and  $MV^{\bullet+}$  in zeolites (205). For instance, addition of promethazine cation ( $PMZ^+$ ) as a secondary donor into the acetonitrile suspension of M exchanged with  $M_2$  leads to CS between  $PMZ^{2+}$  and  $MV^{\bullet+}$  upon photosensitization (532 nm) of the Ru(II) complex (Fig. 80A). This happens as a result of sequential ET from  $*Ru(II)$  to  $MV^{\bullet+}$  (step I) and  $PMZ^+$  to Ru(III) (step II). This reaction is thermodynamically feasible since  $E^0$  value of  $PMZ^+$  (+1.18 V vs. NHE in  $CH_3CN$ ) lies between those of Ru(III) (+1.23 V) and  $*Ru(II)$  (+0.77 V). Thus,  $PMZ^+$  can selectively reduce Ru(III) but not Ru(II).

Despite the increase in the spatial separation between the oxidized donor and reduced acceptor as a result of introduction of  $PMZ^+$  and the inability of the direct contact between the  $MV^{\bullet+}$  in zeolite and  $PMZ^{2+}$  in solution, the photoefficiency of  $PMZ^{2+}$ -Ru(II)- $MV^{\bullet+}$  is nearly the same as that of Ru(III)- $MV^{\bullet+}$ . Interestingly, BET from  $MV^{\bullet+}$  to  $PMZ^{2+}$  (step III) follows second-order kinetics, unlike BET from  $MV^{\bullet+}$  to Ru(III). Second-order kinetics implies that  $PMZ^{2+}$  escapes from the zeolite surface before BET takes place. Since BET from  $MV^{\bullet+}$  to  $PMZ^{2+}$  is not likely to occur via the Ru(II) center, electron conduction from  $MV^{\bullet+}$  to  $PMZ^{2+}$  through zeolite framework or other media should be imagined to account for the second-order kinetics. It is also interesting to note that the driving force for BET from  $MV^{\bullet+}$  to  $PMZ^{2+}$  becomes smaller than that from  $MV^{\bullet+}$  to Ru(III) as shown in Fig. 80B. In light of this, coupled with the impossibility of direct contact between  $MV^{\bullet+}$  and  $PMZ^{2+}$ , the BET rate is supposed to decrease upon introduction of  $PMZ^+$  as the secondary electron donor, unless the BET takes place in the Marcus inverted region.

In such a situation where photosensitizer is encapsulated in zeolite and the electron acceptor is placed outside the zeolite (in solution) the electron transport from the photosensitized donor to the electron acceptor also becomes much more facile by incorporating an appropriate electron relay between donor and acceptor (208). For instance, in the supramolecular system depicted in Fig. 81A, the presence of *N,N'*-tetramethylene-2,2'-bipyridinium ( $4DQ^{2+}$ ) in each empty supercage of  $Ru(bpy)_3^{2+}Y$  leads to ~10-fold increase in the yield of the radical anion of propyl viologen sulfonate

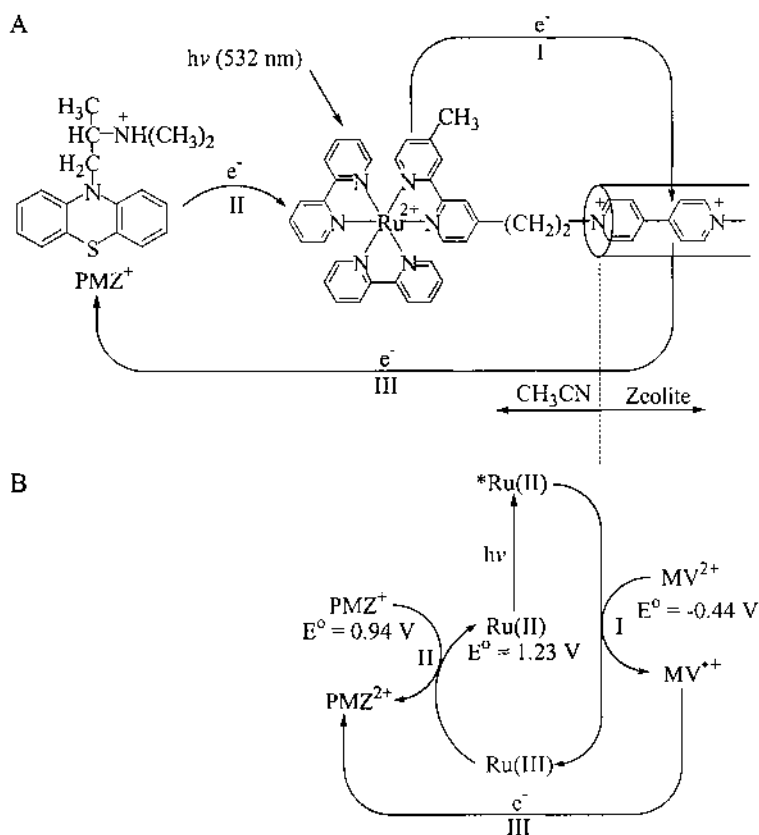


**Fig. 80** Spatial arrangement of PMZ<sup>+</sup>, Ru(II) complex, and MV<sup>2+</sup> at the interface of zeolite and solution (A), and the scheme of the electron flow (B).

(PVS<sup>•-</sup>) upon photoexcitation (420–680 nm, 200 mW) of the Ru complex under anaerobic conditions, with respect to the yield produced from the 4DQ<sup>2+</sup>-free system (Fig. 82). This phenomenon is likened to the increase in the CSS between the externally placed photosensitizer and the zeolite-encapsulated electron acceptor as a result of intercalating an electron relay tethered to the photosensitizer into the zeolite pores, as demonstrated earlier (see Fig. 77, p. 692).

Figure 81B illustrates the vectorial ET from \*Ru(bpy)<sub>3</sub><sup>2+</sup> to PVS mediated by 4DQ<sup>2+</sup>. Interestingly, when 4DQ<sup>2+</sup> is replaced by MV<sup>2+</sup> the photoefficiency decreases substantially as shown in Fig. 82. From the comparison of the reduction potentials (E<sup>0</sup>) of 4DQ<sup>2+</sup> (-0.65) and MV<sup>2+</sup> (-0.44 V vs. NHE) the dramatic difference between 4DQ<sup>2+</sup> and MV<sup>2+</sup> seems to emphasize that the reduction potential of the electron relay should lie between that of the photosensitized donor and the ultimate electron acceptor. Even with 4DQ<sup>2+</sup> as the relay, the nature of the driving force for charge hopping (electron propagation) between the neighboring 4DQ<sup>2+</sup> ions is not yet clear. From the large increase in the photoefficiency with 4DQ<sup>2+</sup> as the electron relay it is inferred that the activation barrier for the thermoneutral electron self-exchange between the neighboring supercages is low. The inefficiency of MV<sup>2+</sup> as the electron relay may arise presumably due to higher activation barrier of MV<sup>2+</sup> for electron self-exchange between the relays in the

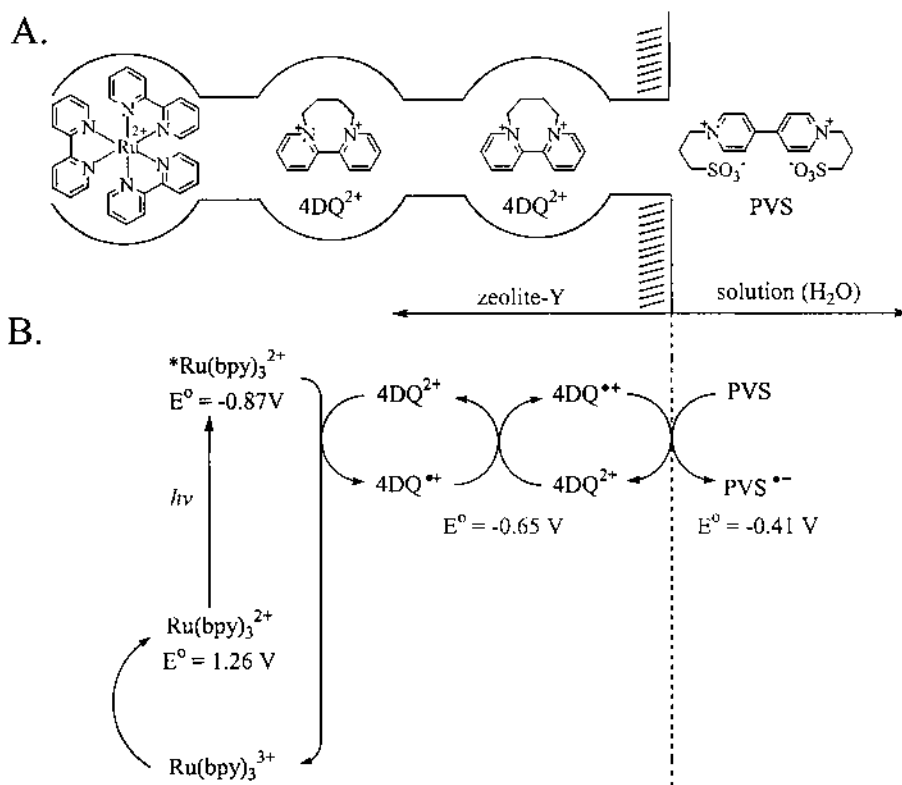


**Fig. 81** Spatial arrangement of  $\text{Ru}(\text{bpy})_3^{2+}$ ,  $4\text{DQ}^{2+}$ , and PVS in Y and in solution, respectively (A) and the scheme of electron flow (B).

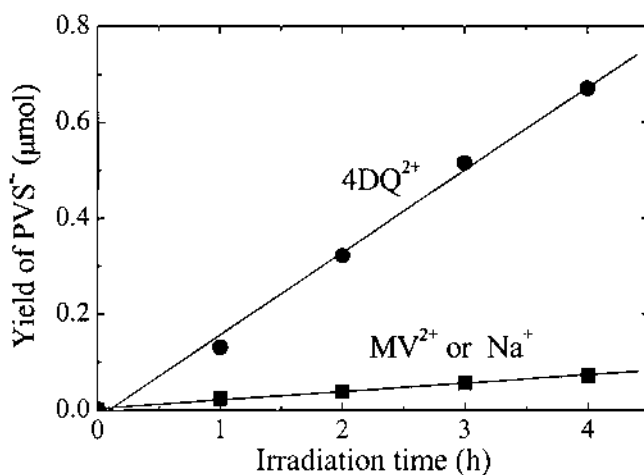


**Fig. 82** Relay-dependent growth of viologen radical as a function of photolysis time (as indicated). 200 mW of 420- to 680-nm radiation is incident on a 20-mg pellet of  $\text{Ru}(\text{bpy})_3^{2+}$ -Y suspended in 3 ml of 0.01M PVS solution in a 1-anaerobic cuvette.

neighboring supercages. The estimated quantum yield for the CSS with 4DQ<sup>2+</sup> as the relay is only  $5 \times 10^{-4}$ , which suggests that further work is necessary to improve the photoefficiency.

The efficiency of CS further increases by a factor of 2 by employing nanocrystals of X (250 nm) rather than conventional micrometer-sized crystals of Y, since nanocrystals offer higher surface-to-volume ratios under identical photoexcitation conditions (104). Interestingly, the efficiency of CS is also governed by the crystallinity of the zeolite framework, and it turns out that the yield of CS increases with increasing crystallinity of the zeolite framework. Therefore, care must be taken, as discussed earlier (p. 647), to avoid damaging the framework of X during the ship-in-a-bottle synthesis of Ru(bpy)<sub>3</sub><sup>2+</sup> in the nanocrystalline zeolite.

The TiO<sub>2</sub> nanowires prepared within the interior of Y also act as the electron relay between the encapsulated photosensitized electron donor and the size-excluded donor placed on the exterior of Y (101). For instance, in the supramolecular system schematically depicted in Fig. 83, the rate of quenching of the \*Ru(bpy)<sub>3</sub><sup>2+</sup> increases as the amount of TiO<sub>2</sub> loading increases for a fixed concentration of Co(Ph<sub>2</sub>PHN)<sub>3</sub><sup>3+</sup> in the supernatant solution. From the fact that TiO<sub>2</sub> also quenches \*Ru(bpy)<sub>3</sub><sup>2+</sup> (209) the above phenomenon can primarily be attributed to the increase in the amount of quencher. However, the calculated quenching rate is higher than the sum of the calculated quenching rate by each component, TiO<sub>2</sub> or Co(Ph<sub>2</sub>PHN)<sub>3</sub><sup>3+</sup>, indicating that the combination shows a synergistic effect on the quenching rate. The synergy effect can therefore be attributed to the dual role of TiO<sub>2</sub> as the electron acceptor and relay.

The emission maximum of Ru(bpy)<sub>3</sub><sup>2+</sup> gradually shifts to red on going from aqueous solution (610) to fully hydrated Y (630) and to fully hydrated TiO<sub>2</sub>-incorporating Y (645 nm). The observed red shift is invoked as indirect evidence for the interaction between Ru(bpy)<sub>3</sub><sup>2+</sup> and TiO<sub>2</sub>. However, the effect of proton, which inevitably exchanged into Y during TiO<sub>2</sub> preparation, on the spectral shift is yet to be elucidated.

Some electron relays require photoexcitation to perform its role. For instance, in the system schematically depicted in Fig. 84A, the charge-balancing Fe<sup>2+</sup> ions serve as electron donors to 7,7,8,8-tetracyanoquinodimethane (TCNQ) in the supernatant solution (acetonitrile) (210). The ion-exchanged 9-methylacridinium (AC<sup>+</sup>) plays the role of photosensitized electron relay, as illustrated in Fig. 84B. Thus, upon irradiating AC<sup>+</sup> using a Pyrex-filtered Hg lamp, AC<sup>+</sup> reaches the excited state and the excited AC<sup>+</sup> (\*AC<sup>+</sup>) receives an electron from a surrounding Fe<sup>2+</sup> ion. Subsequently, the generated acryl radical (AC•) transfers an electron to TCNQ at the interface while becoming AC<sup>+</sup>. Overall, the reaction of the above system can be described according to Eq. (96).



The yield of TCNQ<sup>•-</sup> reaches about 13% with respect to the amount of Fe<sup>2+</sup> in the zeolite after 21 h irradiation. The initial rate of formation of TCNQ<sup>•-</sup> increases with increasing Fe<sup>2+</sup> loading in the zeolite. The estimated initial rates of TCNQ<sup>•-</sup> formation are  $\sim 1.5 \times 10^{-8}$  to  $3.0 \times 10^{-8}$  mol L<sup>-1</sup> s<sup>-1</sup> for the Fe<sup>2+</sup> loading of  $1.9 \times 10^{-5}$ – $8.2 \times 10^{-5}$  mol g<sup>-1</sup>. The measured BET from independently prepared TCNQ<sup>•-</sup> ( $1.5 \times 10^{-5}$  mol L<sup>-1</sup>) to Fe<sup>3+</sup>-exchanged Y (loading of  $7.5 \times 10^{-6}$  mol g<sup>-6</sup> mol g<sup>-1</sup>) is  $1.5 \times 10^{-10}$  mol L<sup>-1</sup> s<sup>-1</sup>. Comparison of the two sets of rates shows that forward ET is about two orders of magnitude faster than BET from TCNQ<sup>•-</sup> to Fe<sup>3+</sup>. However, care must be taken in assessing the rates since simultaneous introduction of proton is inevitable during the ion exchange of Fe<sup>3+</sup> into zeolite and this may lead to loss of crystallinity of Y. Furthermore,

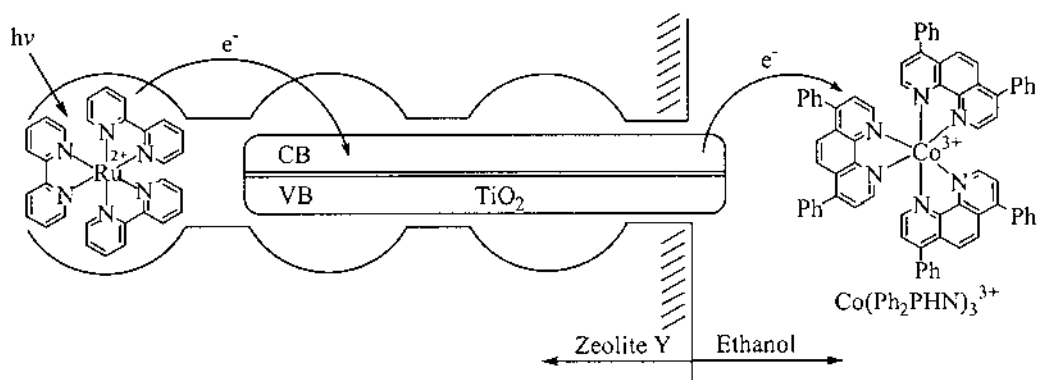
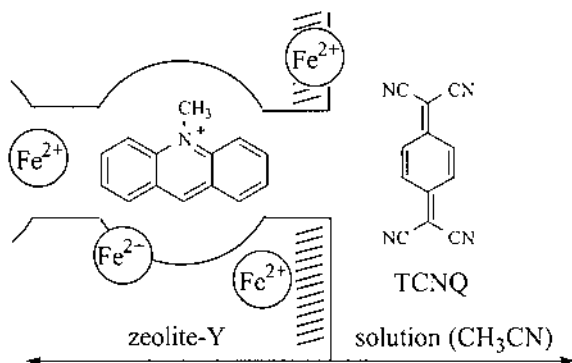


**Fig. 83** Spatial arrangement of  $\text{Ru}(\text{bpy})_3^{2+}$ ,  $\text{TiO}_2$ , and  $\text{Co}(\text{Ph}_2\text{PHN})_3^{3+}$  in Y and in solution, respectively.

A.



B.

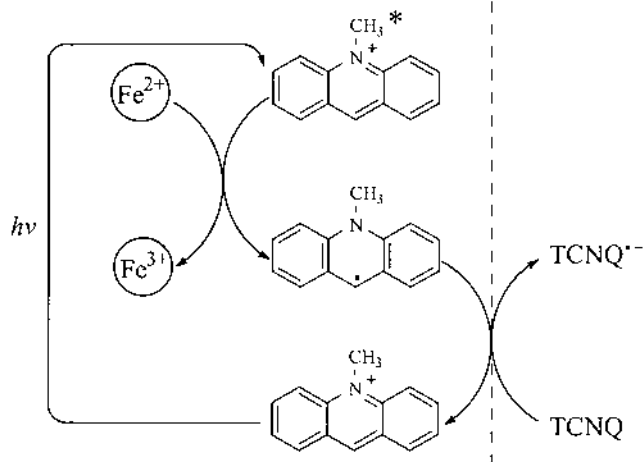


**Fig. 84** (A) Spatial arrangement of  $\text{Fe}^{2+}$ ,  $\text{Ac}^+$ , and TCNQ in Y and in solution, respectively. (B) Schematic representation showing the role of  $\text{Ac}^+$  for photoinduced electron relay from  $\text{Fe}^{2+}$  in zeolite to TCNQ in solution.

the portion of thermal ET from  $\text{Fe}^{2+}$  ions in zeolites and the zeolite framework itself to TCNQ should not be neglected. Nevertheless the above system demonstrates an interesting example about photosensitized electron relay.

From the previous demonstrations it becomes clear that employment of either electron relay (Figs. 77, 81, 83, and 84) or secondary electron donor (Fig. 80) into the organized D-A systems contributes to the increase in the photoefficiency of CSSs. Now the question is, what happens when the two strategies are combined? It turns out that the combination of the two strategies gives rise to further increase in the photoefficiency (112). Thus, in the D-A system depicted in Fig. 85A, selective photoexcitation (473 nm) of  $\text{Ru}(\text{bpy})_2\text{bpz}^{2+}$  leads to a fourfold increase in the yield of  $\text{PVS}^{\bullet-}$  in comparison with the

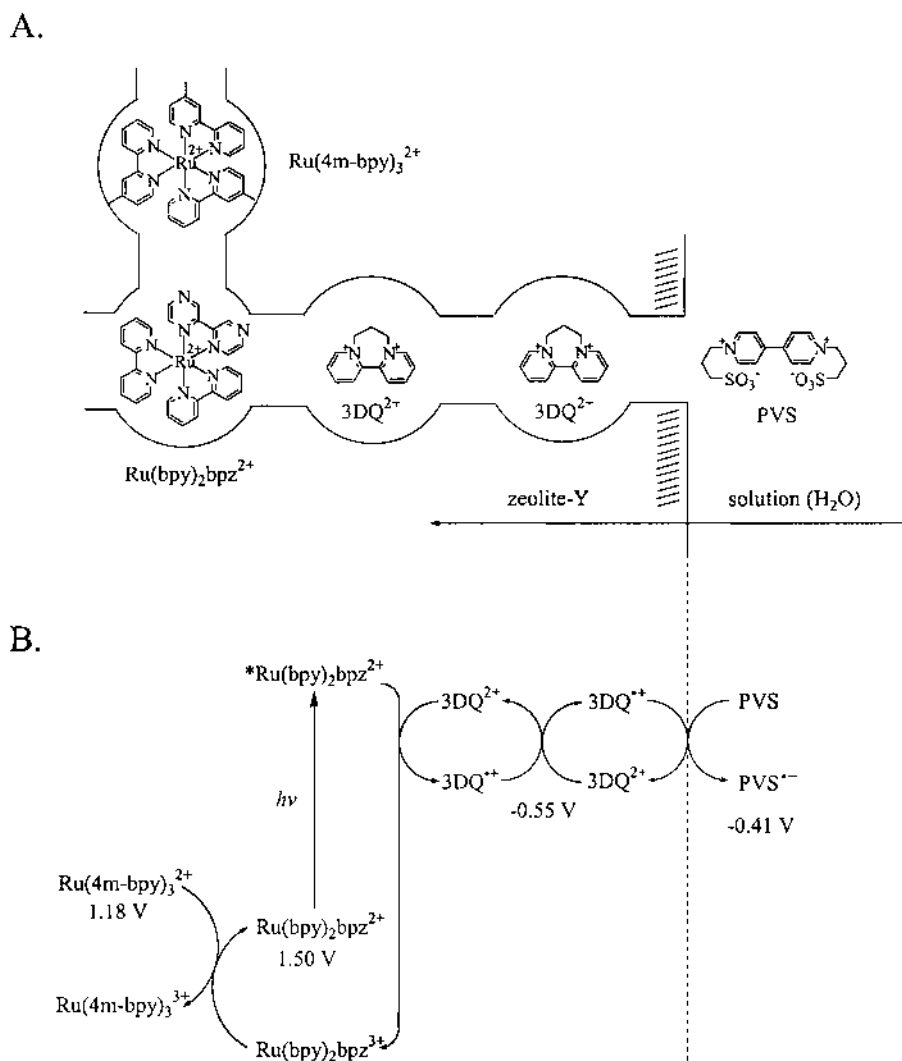


**Fig. 85** (A) Spatial arrangement of  $\text{Ru}(4\text{m-bpy})_3^{2+}$ ,  $\text{Ru}(\text{bpy})_2(\text{bpz})^{2+}$ ,  $3\text{DQ}^{2+}$  in Y and PVS in solution. (B) Schematic illustration of electron flow showing the effect of the adjacent  $\text{Ru}(4\text{m-bpy})_3^{2+}$  complex on the improvement of charge separation.

yields obtained from the Y encapsulating only  $\text{Ru}(\text{bpy})_2\text{bpz}^{2+}$  or  $\text{Ru}(4\text{m-bpy})_3^{2+}$  and the physical mixture of the two zeolites-Y (Fig. 86A).

The schematic illustration of the role of  $\text{Ru}(4\text{m-bpy})_3^{2+}$  is shown in Fig. 85B. Thus, the photoexcited  $\text{Ru}(\text{bpy})_2\text{bpz}^{2+}$  [ $^*\text{Ru}(\text{bpy})_2\text{bpz}^{2+}$ ] transfers an electron to the electron relay,  $3\text{DQ}^{2+}$ , and becomes  $\text{Ru}(\text{bpy})_2\text{bpz}^{3+}$ . The electron acquired by  $3\text{DQ}^{2+}$  then propagates eventually to the  $3\text{DQ}^{2+}$  situated at the outermost supercage through multiple thermoneutral, electron self-exchange reactions. The reduced  $3\text{DQ}^{2+}$  in the outermost supercage then transfers electron to PVS in the supernatant solution. The electron flow up to this part is the same with that shown in Fig. 81. The difference comes from the immediate reduction of  $\text{Ru}(\text{bpy})_2\text{bpz}^{3+}$  back to  $\text{Ru}(\text{bpy})_2\text{bpz}^{2+}$  by  $\text{Ru}(4\text{m-bpy})_3^{2+}$  in the adjacent supercage. The intercage ET from  $\text{Ru}(4\text{m-bpy})_3^{2+}$  to  $\text{Ru}(\text{bpy})_2\text{bpz}^{3+}$  is feasible since the former ( $E_0 = 1.18$  V) is a better donor than  $\text{Ru}(\text{bpy})_2\text{bpz}^{2+}$  ( $E_0 = 1.50$  V).

As a result of regeneration of  $\text{Ru}(\text{bpy})_2\text{bpz}^{2+}$ ,  $\text{Ru}(4\text{m-bpy})_3^{3+}$  now becomes the ultimate electron acceptor from  $\text{PVS}^{\bullet-}$  in the supernatant solution. The driving force for the BET from  $\text{PVS}^{\bullet-}$  to a Ru(III) complex diminishes from 1.91 to 1.59 V, and this leads to decrease in the BET rate unless the BET takes place in the Marcus inverted region. The above system is different from that of Fig. 80 in the sense that the secondary electron donor is situated right next to the primary donor, making itself always ready for ET, whereas the secondary donor in Fig. 80 is not always available. This may be why the above system gives rise to a large increase in the yield of CSS while the system in Fig. 80 does not. This fact emphasizes the importance of the readiness of the secondary donor by being situated next to the primary donor. In this sense Y is a very useful and interesting host that allows spatial organization of two different donors right next to each other.

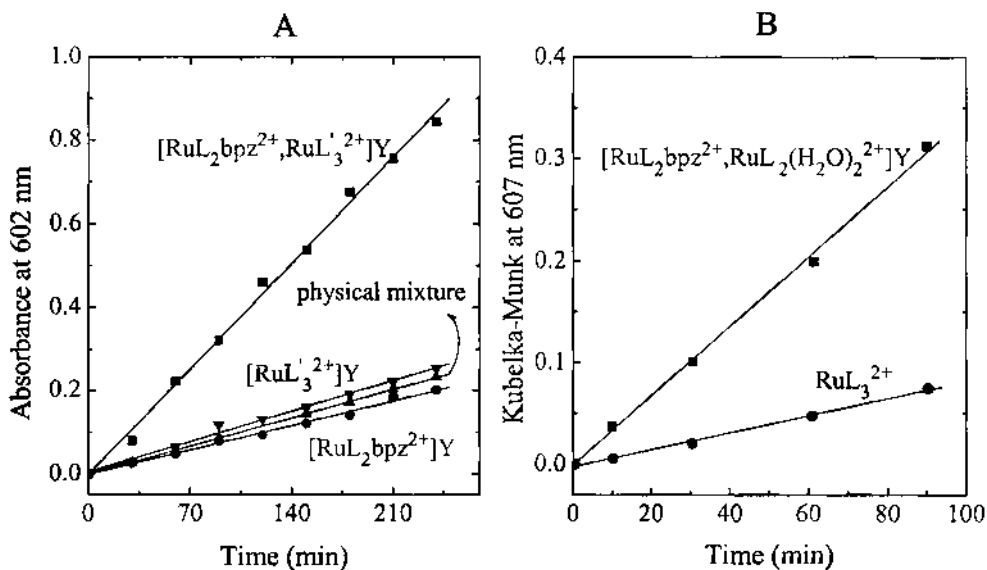
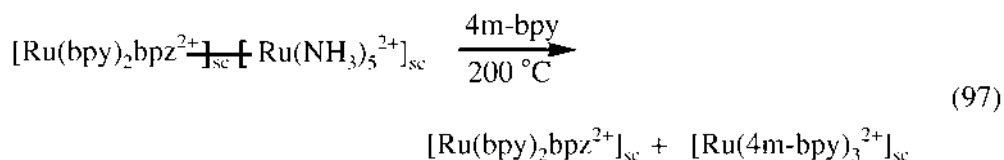


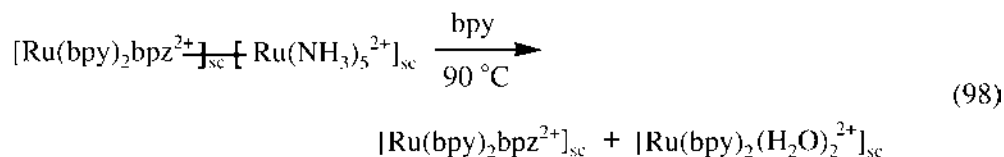
**Fig. 86** (A) Growth of PVS as a function of time for the adjacent cage dyad assemblies of  $\text{RuL}_2\text{bpz}^{2+}$  and  $\text{RuL}'_3{}^{2+}$  in ( $L = \text{bpy}$ ,  $L' = 4\text{m-bpy}$ ). The control experiments are labeled as such. (B) Growth of  $\text{MV}^{+}$  as a function of photolysis time for the adjacent cage assembly,  $Z\text{-}[\text{RuL}_2(\text{bpz})\cdot\text{RuL}_2(\text{H}_2\text{O})_2]^{4+}$  ( $L = \text{bpy}$ ), and for the isolated system,  $Z\text{-}\text{RuL}_3{}^{2+}$ . In both cases, the relative concentration of the complex are identical (1 complex per  $\sim 30$  cages).

Encapsulation of two different Ru(II) complexes in the adjacent supercages is carried out by the elegant method briefly described in the following (109). First, Ru(bpy)<sub>2</sub>bpz<sup>2+</sup> is assembled in Y. Next, a large excess of Ru(NH<sub>3</sub>)<sub>5</sub>H<sub>2</sub>O is introduced into the Ru(bpy)<sub>2</sub>bpz<sup>2+</sup>-encapsulating Y to generate Ru(bpy)<sub>2</sub>bpz-Ru(NH<sub>3</sub>)<sub>5</sub> with each Ru(II) complex placed in one of the two neighboring supercages and with bpz as the linker for the two Ru(II) centers. The formation of the dinuclear Ru(II) complex is characterized by appearance of new bands at 617 and 673 nm. Finally, 4m-bpy is introduced into the Y encapsulating the binuclear Ru(II) complex according to Eq. (97) to generate two different Ru(II) complexes in the neighboring supercages, by rupturing of the peripheral N<sub>bpz</sub>-Ru(NH<sub>3</sub>)<sub>5</sub> bond of the binuclear complex.



The rupture of the peripheral bond and the formation of Ru(4m-bpy)<sub>3</sub><sup>2+</sup> is characterized by the disappearance of the bands at 617 and 673 nm accompanied by the appearance of a new band at 446 nm.

The same strategy can be extended to prepare Y encapsulating Ru(bpy)<sub>2</sub>bpz<sup>2+</sup> and Ru(bpy)<sub>2</sub>(H<sub>2</sub>O)<sub>2</sub><sup>2+</sup> in the adjacent supercages according to Eq. (98) (107).



A novel D'-D-A triad system can be assembled in Y by introducing MV<sup>2+</sup> into the above zeolite. The photoyield of MV<sup>•+</sup> obtained from Ru(bpy)<sub>2</sub>bpz<sup>2+</sup>-Ru(bpy)<sub>2</sub>(H<sub>2</sub>O)<sub>2</sub><sup>2+</sup>-MV<sup>2+</sup>Y system is four times higher than that obtained from Ru(bpy)<sub>3</sub>-MV<sup>2+</sup>Y system as compared in Fig. 86B. Unlike the Ru(bpy)<sub>2</sub>bpz<sup>2+</sup>-Ru(4m-bpy)<sub>3</sub><sup>2+</sup>Y/PVS system, the diffuse-reflectance UV-vis spectra of Ru(bpy)<sub>2</sub>bpz<sup>2+</sup>-Ru(bpy)<sub>2</sub>(H<sub>2</sub>O)<sub>2</sub><sup>2+</sup>-MV<sup>2+</sup>Y system show bleaching of the absorption of Ru(bpy)<sub>2</sub>(H<sub>2</sub>O)<sub>2</sub><sup>2+</sup> (~480 nm) upon laser irradiation (100 mW) of the system at 457.9 nm, indicating that Ru(bpy)<sub>2</sub>(H<sub>2</sub>O)<sub>2</sub><sup>2+</sup> is oxidized (Fig. 87).

## B. Reduction of Ru(bpy)<sub>3</sub><sup>3+</sup> by Water

Unlike Ru(bpy)<sub>2</sub>(H<sub>2</sub>O)<sub>2</sub><sup>3+</sup>, Ru(bpy)<sub>3</sub><sup>3+</sup> is stable only in highly acidic aqueous solutions such as 1 M H<sub>2</sub>SO<sub>4</sub>, and it is reduced back to Ru(bpy)<sub>3</sub><sup>2+</sup> by water when pH is higher than ~2. This is conceivable from the higher E<sup>0</sup> value of Ru(bpy)<sub>3</sub><sup>2+</sup> (1.26 V in 1 M H<sub>2</sub>SO<sub>4</sub> vs. NHE) (211) than that of water (1.23 V for 2H<sub>2</sub>O ⇌ O<sub>2</sub> + 4H<sup>+</sup> + 4e<sup>-</sup>) (212). Likewise, the Ru(bpy)<sub>3</sub><sup>3+</sup> generated in Y is also slowly reduced back to Ru(bpy)<sub>3</sub><sup>2+</sup> by water, unless the corresponding PET reactions are carried out in acidic aqueous media or there exist secondary electron donors with higher donor strengths than water, such as PMZ<sup>+</sup> (E<sup>0</sup><sub>(+/2+)</sub> = 0.94 V), Ru(4m-bpy)<sub>3</sub><sup>2+</sup> (E<sup>0</sup><sub>(2+/3+)</sub> = 1.18 V), and Ru(bpy)<sub>2</sub>(H<sub>2</sub>O)<sub>2</sub><sup>2+</sup> (E<sup>0</sup><sub>(2+/3+)</sub> = 0.63 V), right next to Ru(bpy)<sub>3</sub><sup>3+</sup>. However, the reduction of Ru(bpy)<sub>3</sub><sup>3+</sup>

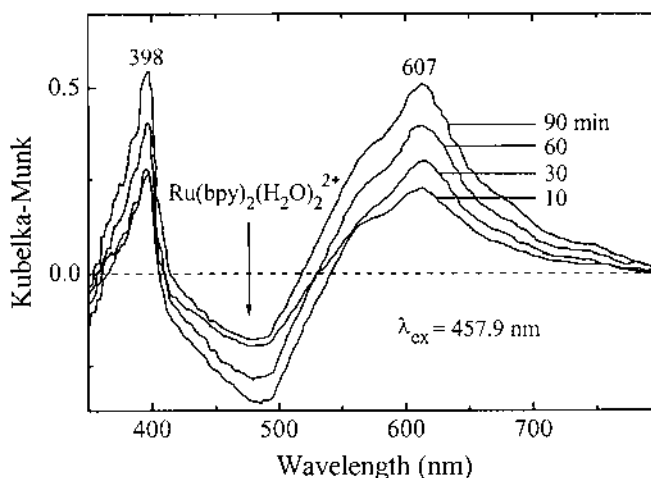


**Fig. 87** The diffuse reflectance spectra showing the bleach of  $\text{Ru}(\text{bpy})_2(\text{H}_2\text{O})_2^{2+}$  (at  $\sim 450$  nm) and the growth of  $\text{MV}^{+}$  (398 and 607 nm;  $\lambda_{\text{ex}} = 457.9$  nm).

by water is slower in Y than in water owing to the absence of multimetal-centered degradation reactions, which are typically observed in solution (213). Nevertheless, the rate of reduction follows first-order kinetics, as shown in Fig. 88, and it increases as the pH increases.

Although the thermal reduction of  $\text{Ru}(\text{bpy})_3^{3+}$  by water is slow, irradiation of the zeolite containing  $\text{Ru}(\text{bpy})_3^{3+}$  in the visible region (420–650 nm) leads to a significant increase in the rate (214). For instance, while it takes several days to reduce  $\text{Ru}(\text{bpy})_3^{3+}$  by water in the dark, it takes only a few hours when irradiated. Therefore, under the conditions whereby PET from zeolite-encapsulated  $\text{Ru}(\text{bpy})_3^{2+}$  to an acceptor is carried out in aqueous media, the rate of reduction of the generated  $\text{Ru}(\text{bpy})_3^{3+}$  by water

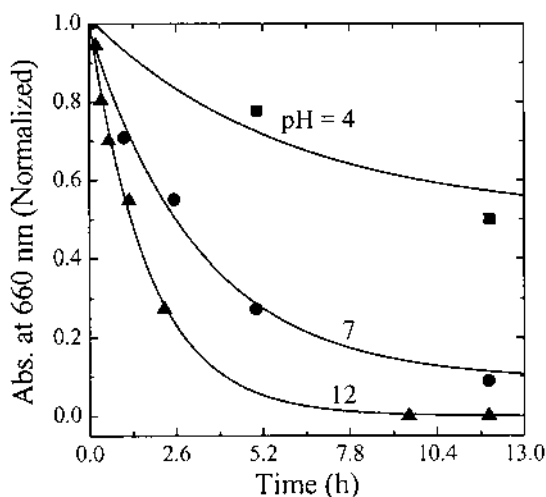


**Fig. 88** Decay of the LMCT band (660 nm) intensity of  $\text{Ru}(\text{bpy})_3^{3+}$ -Y at various pH values (as indicated).

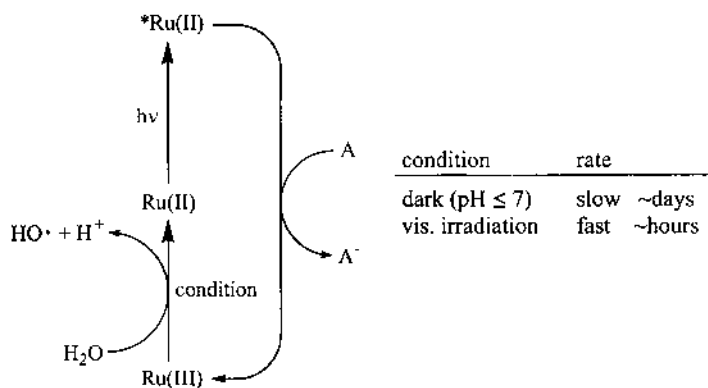


**Fig. 89** Schematic illustration of the mechanism of ET from water to acceptor (A) and the condition for the rate.

becomes significant under the irradiating conditions and the restored  $\text{Ru}(\text{bpy})_3^{2+}$  is likely to be recycled as the photosensitized donor (Fig. 89). In such cases, water is the ultimate electron donor to the acceptor and  $\text{Ru}(\text{bpy})_3^{2+}$  acts as the photosensitized electron relay, or photocatalyst, as schematically illustrated in Fig. 90.

This explains why the intensity of the negative absorption of  $\text{Ru}(\text{bpy})_3^{2+}$  is usually smaller than that of the positive absorption of  $\text{A}^-$  in most transient absorption spectra even if the molar extinction coefficient ( $\epsilon$ ) of  $\text{Ru}(\text{bpy})_3^{2+}$  is higher than that of  $\text{A}^-$ . For instance, in the case of Fig. 78B, the intensity of the negative absorption of  $\text{Ru}(\text{bpy})_3^{2+}$  is much smaller than that of the positive absorption of  $\text{MV}^{\bullet+}$  despite that  $\epsilon$  of  $\text{Ru}(\text{bpy})_3^{2+}$  is  $13,800 \text{ M}^{-1}\text{cm}^{-1}$  at 450 nm, which is larger than that of  $\text{MV}^{\bullet+}$  ( $\epsilon = 12,690$  at 605 nm).

The disparity between the two intensities becomes greater as the lifetime of the CSS increases. Accordingly, in a system such as that shown in Fig. 81, which leads to very long-lived CSSs without employing secondary electron donor, detection of  $\text{Ru}(\text{bpy})_3^{3+}$  becomes difficult if the system was exposed to light for a long period, as in the case of steady-state irradiation. In light of the above discussion, the persistence (> 90 min) of the negative absorption of  $\text{Ru}(\text{bpy})_2(\text{H}_2\text{O})_2^{2+}$  in Fig. 87 after laser excitation is understandable since the  $E^0$  value of the Ru(II) complex (0.63 V) is much lower than that of water.

In fact, reduction of  $\text{Ru}(\text{bpy})_3^{3+}$  by water has received considerable attention as a possible means to generate  $\text{O}_2$  in an effort to employ  $\text{Ru}(\text{bpy})_3^{2+}$  as the photocatalyst to split water into  $\text{H}_2$  and  $\text{O}_2$  [Eq. (99)] (215).

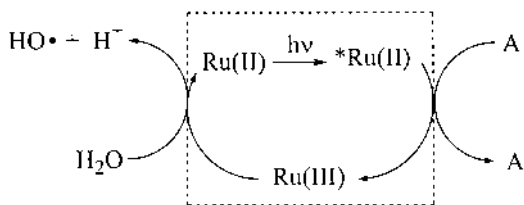
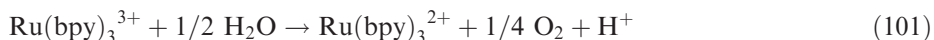
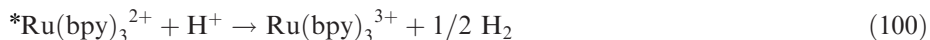
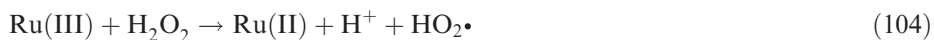
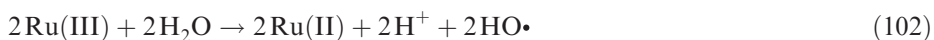


**Fig. 90** Schematic illustration emphasizing the photocatalytic role of the Ru(II) complex.

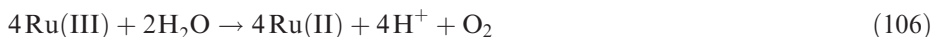
The ideal half-cell reactions proceed according to the followings.



The above half-cell reactions have been confirmed to occur, although the overall goal of water splitting remains elusive due to the multielectron processes involved, unfavorable energetics of intermediates, and mismatch of the reaction rates within the two half-cell reactions (216–220). Of the two above half-cell reactions the reduction of  $\text{Ru}(\text{bpy})_3^{3+}$  by water [Eq. (101)] involves  $4e^-$  processes that can be broken down to the following equations:



Overall,



Equation (102) has been proposed to proceed according to the scheme shown in Fig. 91 (213). This scheme explains why visible irradiation promotes the reduction of  $\text{Ru}(\text{bpy})_3^{3+}$  with water. Thus, the photoexcitation of the 650-nm band, which is a ligand-to-metal charge-transfer (LMCT) band, leads to promotion of the intramolecular ET from bpy ligands to the  $\text{Ru}(\text{III})$  center, which in turn leads to an increase in the electrophilicity of the

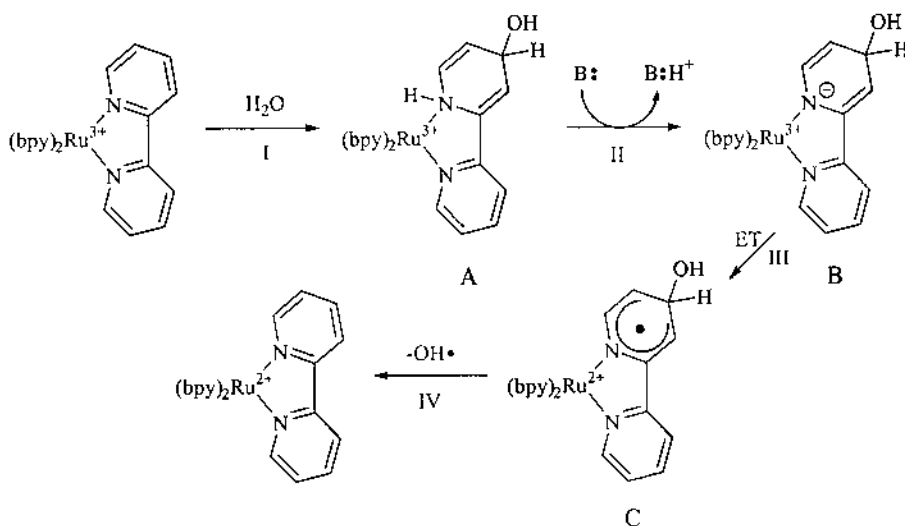


**Fig. 91** Proposed mechanism for reduction of  $\text{Ru}(\text{bpy})_3^{3+}$  with water.

bpy ligand making it amenable to the nucleophilic attack by water (step I, Fig. 91). The scheme also explains the reason why reduction of  $\text{Ru}(\text{bpy})_3^{3+}$  by water is so slow in neutral or acidic aqueous solutions since transformation of intermediate A to B (step II) in Fig. 91 requires base catalysts.

The addition of  $\text{MV}^{2+}$  in the  $\text{Ru}(\text{bpy})_3^{3+}$ -encapsulating Y further accelerates the photoassisted reduction of the Ru(III) complex by water, and this accompanies generation of 3-pyridone (Fig. 92) (214). The formation of 3-pyridone is initiated by attack of hydroxy radical on the 3-position of  $\text{MV}^{2+}$ , as schematically shown in Fig. 92. Thus,  $\text{MV}^{2+}$  acts as the hydroxy radical scavenger from the intermediate C in Fig. 91, and this explains why reduction of  $\text{Ru}(\text{bpy})_3^{3+}$  by water is also promoted in the presence of  $\text{MV}^{2+}$ .

### C. Reduction of $\text{Ru}(\text{bpy})_3^{3+}$ by Zeolite Framework

As was demonstrated in detail in the previous sections, zeolite frameworks are by no means inert compartments and in fact actively participate as electron donors to various acceptors. It was also revealed that  $\text{Ru}(\text{bpy})_3^{3+}$  is reduced to  $\text{Ru}(\text{bpy})_3^{2+}$  by the framework of Y and the reduced amount of  $\text{Ru}(\text{bpy})_3^{3+}$  increases as the donor strength of the framework increases (221). For instance, the hexafluorophosphate ( $\text{PF}_6^-$ ) salt of  $\text{Ru}(\text{bpy})_3^{3+}$ , which is indefinitely stable in rigorously dried acetonitrile, is reduced to  $\text{Ru}(\text{bpy})_3^{2+}$  in the presence of rigorously dried  $\text{M}^+\text{Y}$  ( $\text{M}^+ = \text{Li}^+, \text{Na}^+, \text{K}^+, \text{Rb}^+, \text{and Cs}^+$ ). The produced amount of  $\text{Ru}(\text{bpy})_3^{2+}$  increases with increasing size of the cation:  $\text{Li}^+$ ; 0.46,  $\text{Na}^+$ ; 1.75,  $\text{K}^+$ ; 2.5,  $\text{Rb}^+$ ; 5.01, and  $\text{Cs}^+$ ; 26.2 per unit cell of Y. Thus, there exists a linear relationship between the yield of  $\text{Ru}(\text{bpy})_3^{2+}$  and the estimated negative partial charge of the framework oxygen, consistent with the fact that the framework is the source of electron. Further, considering the high crystallinity of Y, the reduced amounts of

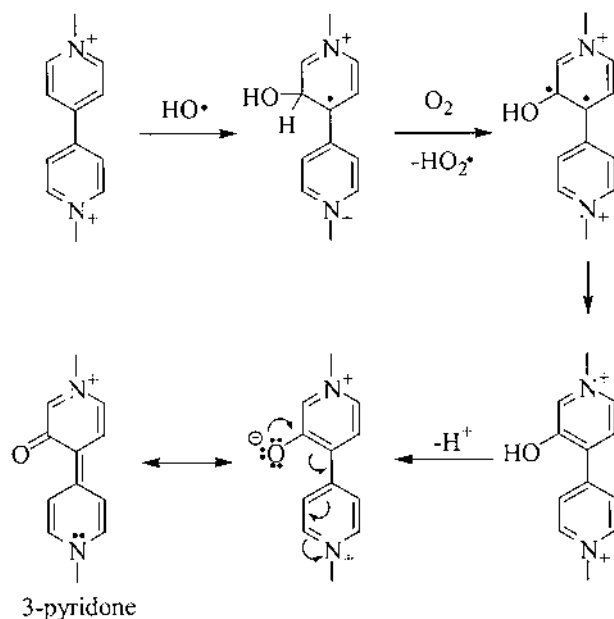


**Fig. 92** Proposed mechanism for formation of 3-pyridone from the reaction of  $\text{MV}^{2+}$  with hydroxy radical ( $\text{HO}\cdot$ ).

$\text{Ru}(\text{bpy})_3^{3+}$  are too large for the defect sites to be attributed as the electron sources. Therefore, the valence band of the zeolite framework should be concluded as the genuine source of electron. This further indicates that the  $E_{1/2}^{\text{Ox}}(\text{ZO}^-)$  value can be decreased even to 1.26 V (vs. NHE) from the previously estimated value of 1.52 V (see page 685), which was deduced by applying Rehm-Weller equation to PYR which readily forms  $\text{PYR}^{\bullet-}$  upon photoexcitation in zeolites.

The fact that  $\text{Ru}(\text{bpy})_3^{3+}$  is reduced by the zeolite framework is also important since this indicates that zeolite-encapsulated  $\text{Ru}(\text{bpy})_3^{2+}$  behaves not only as a photosensitized donor in aqueous solutions but also as a photosensitized relay for ET from the framework to size-excluded acceptors placed in nonaqueous supernatant solutions. For instance, in the model D-A system depicted in Fig. 93A, where  $\text{Ru}(\text{bpy})_3^{2+}$  is the photosensitized donor encapsulated in the supercage of Y and the hexafluorophosphate ( $\text{PF}_6^-$ ) salt of *N*-[3-(dicyclohexylmethyl)oxypropyl]-*N'*-methyl-4,4'-bipyridinium [ $\text{DCH-MV}^{2+}(\text{PF}_6^-)_2$ ] is the size-excluded electron acceptor dissolved in acetonitrile, the yield of  $\text{DCH-MV}^{\bullet+}$  reaches up to 50% of the total amount of  $\text{Ru}(\text{bpy})_3^{2+}$  assembled in the zeolite upon visible irradiation. This occurs despite the fact that the amount of the Ru(II) complex located on the outermost supercages corresponds to only  $\sim 1\%$  of the total amount of the Ru(II) complex and the zeolite does not contain any electron relays that can help transport electron from the  $^*\text{Ru}(\text{bpy})_3^{2+}$  complexes located in the interior to the size-excluded  $\text{DCH-MV}^{2+}$  in the supernatant solution (221).

The above phenomenon occurs according to the scheme shown in Fig. 93B. Thus, the  $\text{Ru}(\text{bpy})_3^{2+}$  in the outermost supercage is photosensitized to  $^*\text{Ru}(\text{bpy})_3^{2+}$  (step I), which in turn transfers an electron to  $\text{DCH-MV}^{2+}$  in the supernatant solution (step II), perhaps through the opening of the supercage, and becomes  $\text{Ru}(\text{bpy})_3^{3+}$ . The  $\text{Ru}(\text{bpy})_3^{3+}$  is then reduced back to  $\text{Ru}(\text{bpy})_3^{2+}$  by the surrounding zeolite framework (step III). As a

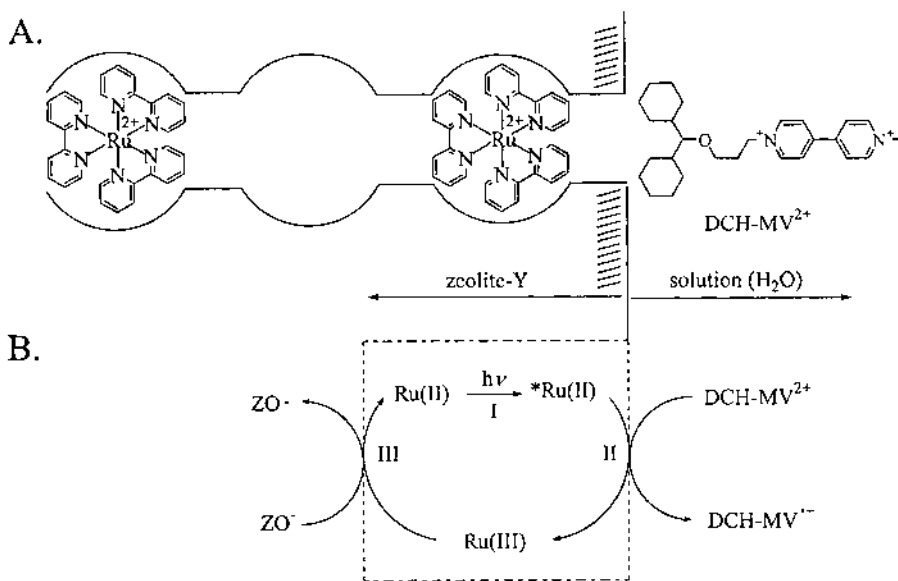


**Fig. 93** Spatial arrangement of  $\text{Ru}(\text{bpy})_3^{2+}$  and  $\text{DCH-MV}^{2+}$  in Y and in solution ( $\text{CH}_3\text{CN}$ ) (A) and the schematic illustration of electron flow (B). (Adapted from Ref. 221.)

result, the yield of DCH-MV<sup>•+</sup> becomes much higher than the amount of the Ru(bpy)<sub>3</sub><sup>2+</sup> located in the outermost supercages of Y.

It is interesting to note the similarity between the scheme shown in Fig. 93B and those shown in Figs. 80, 85, and 90. In all cases, the Ru(II) complexes behave as photocatalysts for ET from a secondary donor to the corresponding acceptor either in the supernatant solution or in zeolite. The difference lies in the nature of the secondary donor, PMZ<sup>+</sup>, Ru(4m-bpy)<sub>3</sub><sup>2+</sup>, water, or the zeolite framework, depending on the nature of the solvent, i.e., aqueous or nonaqueous. When the PET from Ru(bpy)<sub>3</sub><sup>2+</sup> to an acceptor is carried out in aqueous solutions, the *E*<sup>0</sup> of the deliberately added secondary donors should be lower than that of water (1.23 V vs. NHE) for them to be effective. Otherwise, water participates as the secondary donor. In nonaqueous systems, the zeolite framework participates as the secondary donor unless there are deliberately added secondary donors with *E*<sup>0</sup> values smaller than 1.26 V (vs. NHE).

In the cases where water or the zeolite framework serves as the secondary donor the reduction of Ru(bpy)<sub>3</sub><sup>3+</sup> by the secondary donor is slow. While the reason for the slowness of the reduction of Ru(bpy)<sub>3</sub><sup>3+</sup> by water is already discussed in the previous section (p. 704), the reason for the slow reduction of Ru(bpy)<sub>3</sub><sup>3+</sup> by the zeolite framework is yet to be resolved. From the fact that even the reduction of independently prepared free Ru(bpy)<sub>3</sub><sup>3+</sup> by the zeolite framework is slow in acetonitrile, it can be inferred that the propagation of the hole centers through the framework is slow, and this seems to be the reason for the slow rate.

Interestingly, Ru(bpy)<sub>3</sub><sup>3+</sup> can remain stable in Na<sup>+</sup>Y that was treated with chlorine gas (Cl<sub>2</sub>) (96,213,214). In fact, generation of Ru(bpy)<sub>3</sub><sup>3+</sup> in Na<sup>+</sup>Y has been carried out by treating the dried Ru(bpy)<sub>3</sub><sup>2+</sup>-encapsulating Na<sup>+</sup>Y with chlorine gas. However, chlorine oxidizes not only Ru(bpy)<sub>3</sub><sup>2+</sup> but also the zeolite framework. Considering the fact that the *E*<sup>0</sup> of Cl<sub>2</sub> is 1.36 V (vs. NHE), which is higher than that of Ru(bpy)<sub>3</sub><sup>2+</sup> (*E*<sup>0</sup> = 1.26 V), it is expected that chlorine will oxidize the zeolite framework more readily than Ru(bpy)<sub>3</sub><sup>3+</sup> does. Indeed, formation of Cl<sub>2</sub><sup>-</sup> has been observed from dry X and M upon introduction of Cl<sub>2</sub> (222). Therefore, it is likely that all of the valence electrons that could possibly be used to reduce Ru(bpy)<sub>3</sub><sup>3+</sup> are removed by chlorine, allowing the zeolite framework to host Ru(bpy)<sub>3</sub><sup>3+</sup>.

#### D. Simultaneous Flow of Cocations with Electrons and Retardation of Reverse Flow of Cations for Long-Lived CS

In the previously described systems attention has been paid only to the transport of electron. However, in order to maintain the overall charge balance, the electron transport should accompany transport of charge-balancing cations as described earlier (pp. 635–655). For instance, a zeolite-encapsulated Ru(bpy)<sub>3</sub><sup>2+</sup> ion balances two negative charges on the framework. Since the degree of incorporation of Ru(bpy)<sub>3</sub><sup>2+</sup> in the zeolite is limited due to its large size, the rest of the framework negative charges are normally balanced by alkali metal ions, typically Na<sup>+</sup>. When an electron is transferred from a \*Ru(bpy)<sub>3</sub><sup>2+</sup> complex to an acceptor in the supernatant solution, the Ru complex becomes triply charged and thus can balance three negative centers of the framework. As a result, a positive charge should be removed from the zeolite framework to maintain the overall charge balance, both in zeolite and in solution.

For instance, when K<sup>+</sup> ions are the charge-balancing cations, a K<sup>+</sup> ion should leave the zeolite when an electron is transferred from a \*Ru(bpy)<sub>3</sub><sup>2+</sup> complex to DCH-MV<sup>2+</sup> in the supernatant solution as shown in Fig. 94 (221). When crown ether (CE) such as

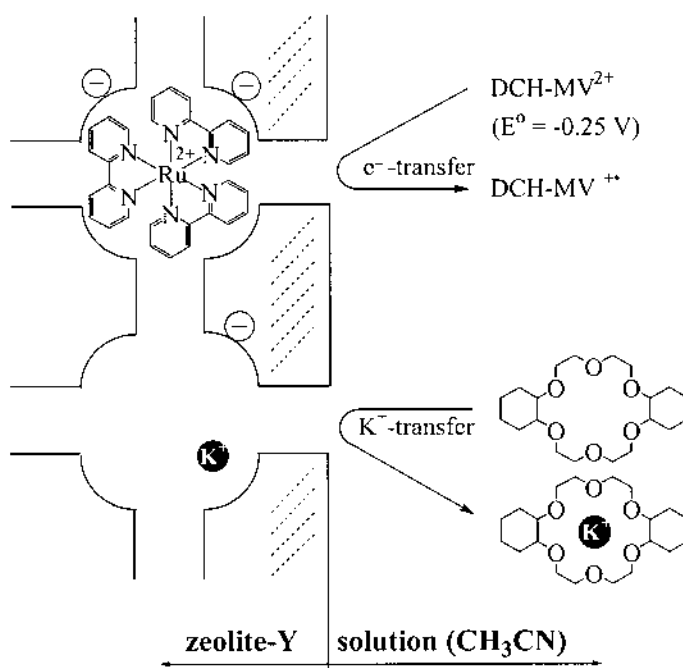


**Fig. 94** Schematic illustration showing the simultaneous transfer of both an electron and a K<sup>+</sup> ion from Ru(bpy)<sub>3</sub><sup>2+</sup> and zeolite framework to DCH-MV<sup>2+</sup> and DCH-18-C-6, respectively. (Adapted from Ref. 221.)

dicyclohexyl-18-crown-6 (DCH-18-C-6), 18-crown-6 (18-C-6), or 15-crown-5 (15-C-5) is present in the supernatant solution, the liberated K<sup>+</sup> and CE form strong host-guest complexes, as typically shown in Fig. 94 for the case of DCH-18-C-6. In the meantime, the initially generated Ru(bpy)<sub>3</sub><sup>3+</sup> is reduced back to Ru(bpy)<sub>3</sub><sup>2+</sup> by the framework leaving a hole center in the framework (vide supra). Now for the electron residing in DCH-MV<sup>•+</sup> to return to the hole center in the zeolite framework, a charge-balancing cation should also return to the zeolite system to maintain the overall charge balance. However, since the K<sup>+</sup>-CE complex is too big (kinetic diameter > 10.3 Å) to pass through the supercage window, the K<sup>+</sup> ion should first be decomplexed from CE to be allowed to enter the supercage. Therefore, the lifetime of CSS, and therefore the photoyield of DCH-MV<sup>•+</sup>, increases as the formation constant for K<sup>+</sup>-CE complexation [K<sub>f</sub>(K<sup>+</sup>)<sub>CE</sub>] increases in the order 15-C-5 < 18-C-6 < DCH-18-C-6. A linear relationship exists between the photoyield and K<sub>f</sub>(K<sup>+</sup>)<sub>CE</sub>.

The above example establishes two facts: (a) ET accompanies cation transfer at the zeolite interface and (b) prevention of the liberated cation from the zeolite from returning back to the zeolite is an alternative way to achieve long-lived CSSs.

### E. Application

Attempts have been made to exploit the advantages of the spatial separation of donors and acceptors across the zeolite-solution interface for practical applications such as H<sub>2</sub> generation from water (223,224) and wastewater treatment (225,226). Although the efficiencies are not yet high enough for the systems to be practically applicable, the results

show that the use of zeolites as the organizing media for interfacial PET bears a great potential for the development of the devices that are practically useful for water splitting and wastewater treatment. In fact, the successful development of an efficient method to split water into  $H_2$  and  $O_2$  has been considered as one of the Holy Grails in chemistry (227). Therefore, the readers are urged to pay more attention to the development of zeolite-based water-splitting devices.

The scheme of the system that was first designed for water splitting is shown in Fig. 95 (223). As the photosensitized donor,  $Zn^{II}Por^{4+}$  [Por = tetrakis(*N*-methyl-4-pyridyl)porphyrin] is exchanged on the surface of L, which is incorporating pre-exchanged  $MV^{2+}$  and small aggregates of platinum (0.001–0.004 wt %) within the channels. The platinum aggregates are incorporated into the channels prior to exchange of  $MV^{2+}$  and  $Zn^{II}Por^{4+}$ . Evolution of hydrogen takes place when the zeolite is irradiated in the visible region in aqueous solution containing ethylenediaminetetraacetic acid (EDTA) as the sacrificial electron donor. Thus,  $Zn^{II}Por^{4+}$  acts as a photosensitized electron relay from EDTA to proton, an ultimate acceptor.  $MV^{2+}$  ions work as electron mediators and Pt aggregates function as both electron conductors and catalysts for the efficient ET from  $MV^{*+}$  to  $H^+$ . The related zinc-porphyrin with no pendant *N*-methylpyridinium groups does not induce hydrogen evolution. This indicates that the ET quenching of the singlet state of  $Zn^{II}Por^{4+}$  ( $^1Zn^{II}Por^{4+}$ ) by  $MV^{2+}$  occurs *via* contact interaction ( $\pi$  overlap) between the *N*-methylpyridinium groups of the  $Por^{2+}$  ligands incorporated into the channels and  $MV^{2+}$  ion through close positioning of the two molecules at high loading of  $MV^{2+}$ . The importance of close positioning of the above two molecules is further supported by the fact that at low loading of  $MV^{2+}$  ( $< 0.4 MV^{2+}$  per cage), where the  $\pi$  overlap between the *N*-methylpyridinium unit and  $MV^{2+}$  is likely to be absent, both hydrogen evolution and singlet state quenching do not occur.

Although the quenching of  $^1Zn^{II}Por^{4+}$  with  $MV^{2+}$  occurs within a 10- to 100-ps time scale, the overall quantum yield for  $H_2$  evolution is only 0.003%. This suggests that the BET process is even more fast and efficient. However, the BET process usually does not proceed completely. For instance,  $MV^{*+}$  persists in solution after continuous irradiation of the nonplatinized zeolites for 10 h in the absence of EDTA. Interestingly, under the same experimental condition, triplet state quenching is not effective despite the

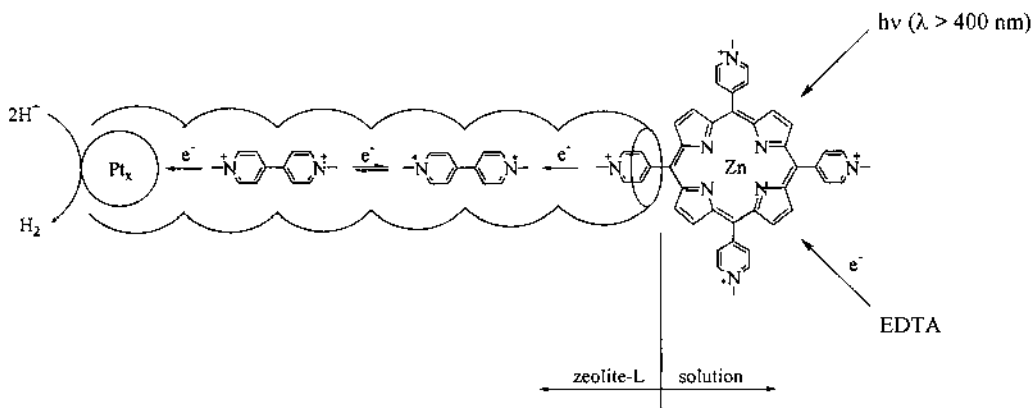


**Fig. 95** Spatial arrangement of  $Zn(Por)^{2+}$ ,  $MV^{2+}$ , platinum aggregates ( $Pt_x$ ), and EDTA in zeolite and in solution.

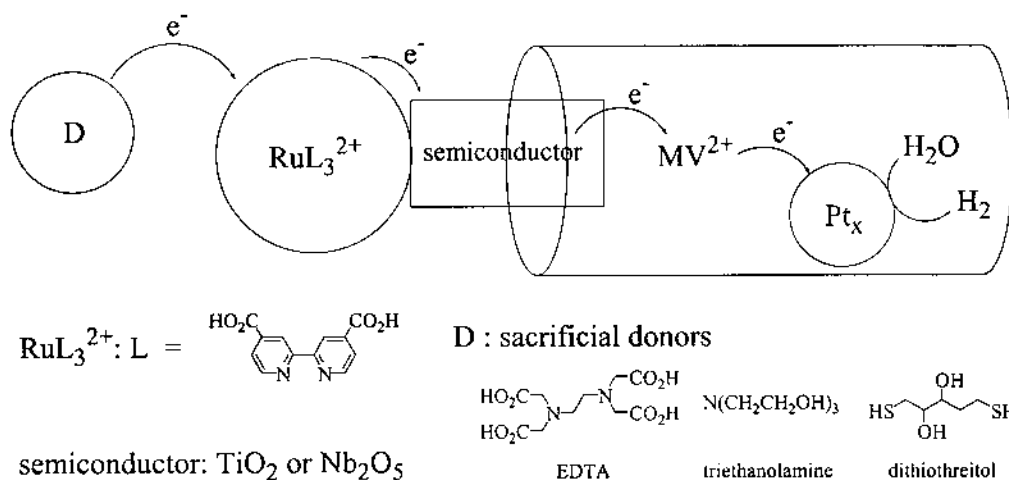


**Fig. 96** Spatial arrangement of the sacrificial donor (D), Ru(II) complex,  $\text{TiO}_2$  or  $\text{Nb}_2\text{O}_5$  semiconductor,  $\text{MV}^{2+}$ , and Pt aggregates ( $\text{Pt}_x$ ) in solution and zeolite L.

fact that the processes are exoergic in homogeneous solution and in micelles. The noneffectiveness is attributed to the shift of ground state redox potentials of porphyrins adsorbed onto zeolite surfaces to more positive values by about 200 mV (207).

Incorporation of  $\text{TiO}_2$  or  $\text{Nb}_2\text{O}_5$  semiconductor as the electron mediator between the photosensitized electron relay and  $\text{MV}^{2+}$  leads to a marked increase in the quantum yield (224). For instance, the quantum yield for  $\text{H}_2$  evolution obtainable from the system depicted in Fig. 96 reaches about 1% at 450 nm, which corresponds to an approximately 330-fold increase with respect to that of the previous system (Fig. 95).

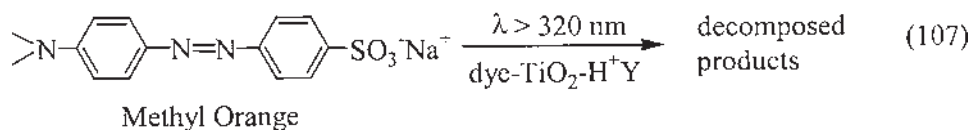
All of the components except  $\text{MV}^{2+}$  are essential for  $\text{H}_2$  evolution. However, in the absence of  $\text{MV}^{2+}$ , the yield decreases fivefold. This indicates that some semiconductor mediators have direct contact with Pt aggregates. In the above system,  $\text{RuL}_3^{2+}$  ( $\text{L} = 4,4'$ -dicarboxy-2,2'-bipyridine) only adheres to the semiconductor surfaces that are exposed to the exteriors of the zeolite hosts but does not adhere onto the bare zeolite surfaces presumably due to the carboxylic groups of the ligands. The system requires UV irradiation (314–414 nm) in order to generate  $\text{H}_2$  in the absence of  $\text{RuL}_3^{2+}$ . Under this condition,  $\text{Nb}_2\text{O}_5$  shows higher activity than  $\text{TiO}_2$ . Regardless of the wavelengths of the light, careful positioning of the semiconductors such that some parts of them are exposed to the exteriors of the zeolite hosts is important for higher photoefficiencies.

Although the above system is more efficient in terms of photoefficiency than the previous one, the resulting quantum yield is not yet satisfactory. Several factors, such as slow kinetics for reduction of the oxidized Ru complex ( $\text{RuL}_3^{3+}$ ) by the sacrificial donor, low loading (0.01–0.1 wt %) and low activity of Pt aggregates, and the midgap states of  $\text{TiO}_2$  in the composite which can trap electrons photoinjected by  $^*\text{RuL}_3^{2+}$ , seem to be responsible for the low efficiency.

While photolysis of water using oxide semiconductors and sacrificial electron donors is of basic interest, a practical solar energy conversion scheme demands nonsacrificial electron donors that can be recycled chemically or electrochemically. However, despite spatial separation of the  $\text{H}_2$  evolution catalyst and electron donors, the above system becomes ineffective when reversible electron donors such as iodide, 2,5-dihydroxy-1,4-benzenedisulfonic acid, hydroquinonesulfonic acid, sodium 4-methoxybenzeneamine *N,N*-

bis(ethylsulfonate), and potassium phenylenediamine-*N,N,N',N'*-tetrakis(ethylsulfonate) are employed.

Dye and TiO<sub>2</sub>-incorporating H<sup>+</sup>Y (dye-TiO<sub>2</sub>-H<sup>+</sup>Y) has been shown to be effective photocatalyst for decomposition of methyl orange, a model organic contaminant, dissolved in water [Eq. (107)] (225,226).



As for the dye, Nile red (NR) and 4-(dimethylamino)benzoic acid (DMA-BA) have been employed. For instance, the decomposition of methyl orange proceeds eight times faster with NR-TiO<sub>2</sub>-H<sup>+</sup>Y than with TiO<sub>2</sub>-H<sup>+</sup>Y as the photocatalyst, as shown in Fig. 97. Interestingly, NR remains intact under the irradiating conditions, and the control experiments show that the simultaneous incorporation of NR and TiO<sub>2</sub> into H<sup>+</sup>Y is essential for high efficiency. The above process is likely to proceed by electron injection from the photoexcited dye to the conduction band of TiO<sub>2</sub> followed by ET from TiO<sub>2</sub> to methyl orange. Although the optimal configuration of the above system and the detailed mechanism for the above process are yet to be elucidated, the above system bears advantages over the conventional dye-TiO<sub>2</sub> mixtures in terms of higher efficiency and the recyclability of the photocatalyst.

## V. CONCLUDING REMARKS

As have been demonstrated in this chapter, zeolites are indeed highly versatile media to assemble or organize supramolecular arrays of various donors and acceptors across the zeolite-solution interfaces as well as within the pores. This provides us valuable opportunities to explore new PET reactions within zeolite pores and across the zeolite-solution

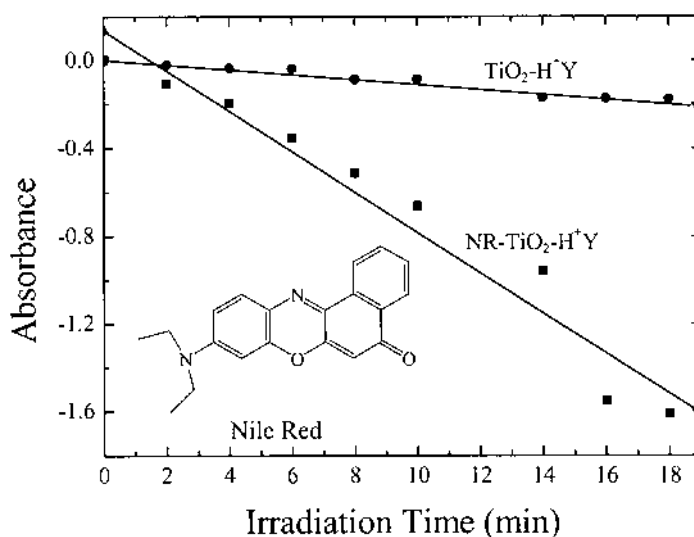


Fig. 97 Effect of Nile red (NR) on the efficiency of methyl orange decomposition.

interfaces. In particular, the high efficiencies demonstrated by zeolites in achieving the remarkable long-lasting CSSs warrant success in the future for practical applications of zeolites for water splitting, wastewater treatment, solar cells, and many others.

The characteristic features of zeolites that made possible the exciting results demonstrated in this chapter can generally be classified into four: the confinement effect, the strong electric field, the donor property of the framework, and the acceptor property of the cation. First of all, the confinement effect imposed by the rigid intracrystalline voids makes it possible to permanently immobilize various donors, acceptors, and photosensitizers. This effect is highlighted by the remarkable efficiency achieved in elongation of the CSS across the zeolite–solution interface and protection of the encapsulated photosensitizer from the attack by highly reactive species. The strong electric field within the zeolite pores created by the cations and the negatively charged framework contributes to the stabilization of the charged species. This leads to a dramatic increase in the lifetimes of the positively charged transient species and the red shift of O<sub>2</sub>-hydrocarbon CT bands that allow highly selective autoxidation of the hydrocarbons induced by visible lights. The acidity (acceptor property) and basicity (donor property) by the charge-balancing cations and the framework, respectively, can be sensitively varied by the nature of the cation and the Si/Al ratio, respectively. Now, coupled with the strong electric field provided by the cation and the framework, the finely tunable acidity and basicity of the zeolite further furnish high diversity to the pathway and, eventually, the selectivity of the PET reactions. Deprotonation from the radical cations of the arene compounds with ring-substituted methyl groups is a good example of the active participation of the zeolite framework in the shaping of products. The triad interaction of intercalated acceptor with both the guest donor and zeolite (either the framework or the cation), such as MV<sup>2+</sup> with both the arene donor and the framework, and TCNB and cyanopyridiniums with the arene donor and the cation also provide the opportunity to design various multiad supramolecular systems in zeolite. The realization that counteranions simultaneously migrate to the directions where electrons are moving will allow design of novel approaches for long-lived CS. This chapter also provides novel insights into the fascinating properties of zeolite frameworks and charge-balancing cations.

## ACKNOWLEDGMENTS

I am grateful to Prof. Jay K. Kochi at the University of Houston, Texas, who first stimulated and encouraged me to enter into the field covered by this chapter. I would like to express my sincere thanks to Dr. Yong Soo Park for his immeasurable help in preparing this chapter. I also would like to extend my sincere thanks to Yun Shim Kang, Hyun Sung Kim, Nak Cheun Jeung, Jin Seok Lee, Jin Sun Park, Sung Yun Choi, Sang Ho Lim, You Seok Seo, Min Jeong Kim, and Hwa Yoon Jung for their help in preparing this chapter.

## REFERENCES

- 1a. AC Graham. Occasional Paper and Monograph Series No 6: Yin-Yang and the Nature of Correlative Thinking. The Institute of East Asian Philosophies, 1986.
- 1b. E Wong. Harmonizing Yin and Yang: The Dragon-Tiger Classic. Random House (P), 1997.
  2. JK Kochi. Acta Chem Scand 44:409–432, 1990.
- 3a. HA Benesi, JH Hildebrand. J Am Chem Soc 71:2703–2707, 1949.
- 3b. WB Person. J Am Chem Soc 87:167–170, 1965.

- 4a. RS Mulliken. *J Am Chem Soc* 74:811–824, 1952.
- 4b. RS Mulliken. *Recl Trav Chim Pays-Bas* 75:845–852, 1956. (c) RS Mulliken. *J Am Chem Soc* 72:600–608, 1950.
- 5a. MA Fox, M Chanon. *Photoinduced Electron Transfer*. New York: Elsevier, 1988.
- 5b. L Eberson. *Electron Transfer Reactions in Organic Chemistry*. Berlin: Springer-Verlag, 1987.
- 6a. V Ramamurthy. *Photochemistry in Organized and Constrained Media*. New York: VCH, 1991.
- 6b. SL Holt. *Inorganic Reactions in Organized media*. Washington, DC: ACS Symposium Series 177, 1981. (c) K Kalyanasundaram. *Photochemistry in Microheterogeneous Systems*. New York: Plenum Press, 1987.
- 7a. V Ramamurthy, KS Schanze, KB Yoon. *Solid State and Surface Photochemistry: Charge and Electron Transfer Reactions in Zeolites*. New York: Marcel Dekker, 2000, pp 143–251.
- 7b. KB Yoon. *Chem Rev* 93:321–339, 1993.
- 7c. PK Dutta, M Ledney. In: KD Karlin, ed. *Progress in Inorganic Chemistry*, Vol 44: GJ Meyer, ed. *Molecular Level Artificial Photosynthetic Materials*, Special Volume. John Wiley & Sons, 1997, pp 209–271.
- 7d. JR Kincaid. *Chem Eur J* 6:4055–4061, 2000.
8. SY Choi, YS Park, SB Hong, KB Yoon. *J Am Chem Soc* 118:9377–9386, 1996.
9. YS Park, SY Um, KB Yoon. *J Am Chem Soc* 121:3193–3200, 1999.
- 10a. X Liu, KK Iu, JK Thomas. *J Phys Chem* 98:7877–7884, 1994.
- 10b. X Liu, KK Iu, JK Thomas. *Chem Phys Lett* 204:163–167, 1993.
11. S Hashimoto, N Hagiwara, T Asahi, H Masuhara. *Langmuir* 15:3123–3133, 1999.
12. S Hashimoto, *J Chem Soc Faraday Trans* 93:4401–4408, 1997.
13. HJD McManus, C Finel, L Kevan. *Radiat Phys Chem* 45:761–764, 1995.
14. M Alvaro, H Garcia, S Garcia, F Marquez, JC Scaiano. *J Phys Chem B* 101:3043–3051, 1997.
15. N Ulagappan, H Frei. *J Phys Chem A* 104:490–496, 2000.
- 16a. J Turkevich, Y Ono. *Adv Catal* 20:135–152, 1969.
- 16b. Y Ono, H Tokunaga, T Keii. *J Phys Chem* 79:752–756, 1975. (c) BD Flockhart, MC Megarry, RC Pink. In: WM Meier, JB Uytterhoeven, ed. *Molecular Sieves. The Third International Conference*, 1973, pp 509–517.
- 17a. BD Flockhart, L McLoughlin, RC Pink. *J Catal* 25:305–313, 1972.
- 17b. KC Khulbe, RS Mann, A Manoogian. *Zeolites* 3:360–364, 1983.
- 17c. RI Samoilova, AA Shubin, MK Bowman, J Hüttermann, SA Dikanov. *Chem Phys Lett* 316:404–410, 2000.
- 18a. KB Yoon, JK Kochi. *J Am Chem Soc* 111:1128–1130, 1989.
- 18b. KB Yoon, JK Kochi. *J Phys Chem* 95:3780–3790, 1991.
- 18c. KB Yoon, TJ Huh, DR Corbin, JK Kochi. *J Phys Chem* 97:6492–6499, 1993.
19. M Alvaro, H Garcia, S Garcia, L Fernández. *Tetrahedron Lett* 37:2873–2876, 1996.
20. KB Yoon, TJ Huh, JK Kochi. *J Phys Chem* 99:7042–7053, 1995.
21. HW Offen. In: R Foster, ed. *In Molecular Complexes*. London: Elek Science, 1973, Vol 1, p.117 ff.
22. HG Drickamer. *Annu Rev Mater Sci* 20:1, 1990.
- 23a. HA Staab, C Krieger, P Wahl, KY Kay. *Chem Ber* 120:551–558, 1987.
- 23b. H Bauer, J Briaire, HA Staab. *Angew Chem Int Ed* 22:334–335, 1983.
- 23c. H Bauer, J Briaire, HA Staab. *Tetrahedron Lett* 26:6175–6178, 1985.
24. H Kadhim, HW Offen. *J Am Chem Soc* 89:1805–1809, 1967.
- 24b. ZG Soos, RC Hughes. *J Chem Phys* 46:253–259, 1967.
- 24c. AH Ewald. *Trans Faraday Soc* 64:733–743, 1968.
- 24d. AH Kadhim, HW Offen. *J Chem Phys* 48:749–753, 1968.
25. DW Breck, WG Eversole, RM Milton, TB Reed, TL Thomas. *J Am Chem Soc* 78:5963–5977, 1956.
26. A Gedeon, T Ito, J Fraissard. *Zeolites* 8:376–380, 1988.

27. DR Corbin, WC Seidel, L Abrams, N Herron, GD Stucky, CA Tolman. *Inorg Chem* 24:1800–1803, 1985.
28. K Nakamoto. *Infrared and Raman Spectra of Inorganic and Coordination Compounds*, 3rd ed. New York: Wiley, 1978.
29. JF Haw, MB Hall, AE Alvarado-Swaisgood, EJ Munson, Z Lin, LW Beck, T Howard. *J Am Chem Soc* 116:7308–7318, 1994.
- 30a. CJ Blower, TD Smith. *J Chem Soc Faraday Trans* 90:931–934, 1994.
- 30b. CJ Blower, TD Smith. *J Chem Soc Faraday Trans* 90:919–929, 1994.
- 30c. CL Angell, MV Howell. *J Phys Chem* 73:2551–2554, 1969.
- 31a. S Sankararaman, KB Yoon, T Yabe, JK Kochi. *J Am Chem Soc* 113:1419–1421, 1991.
- 31b. KB Yoon, SM Hubig, JK Kochi. *J Phys Chem* 98:3865–3871, 1994.
32. SM Hubig. *J Phys Chem* 96:2903–2909, 1992.
- 33a. RA Marcus. *Annu Rev Phys Chem* 15:155–196, 1964.
- 33b. RA Marcus, N Sutin. *Biochim Biophys Acta* 811:265–322, 1985.
- 34a. CJ Schlessener, C Amatore, JK Kochi. *J Am Chem Soc* 106:3567–3577, 1984.
- 34b. CJ Schlessener, JK Kochi. *J Org Chem* 49:3142–3150, 1984.
- 35a. EM Kosower, PE Klinedinst. *J Am Chem Soc* 78:3493–3497, 1956.
- 35b. EM Kosower. *J Am Chem Soc* 80:3253–3260, 1958.
- 35c. KM Harmon, FE Cummings, DA Davis, DJ Diestler. *J Am Chem Soc* 84:3349–3355, 1962.
36. KB Yoon, JK Kochi. *J Phys Chem* 95:1348–1356, 1991.
- 37a. R Foster, ed. *Molecular Complexes*. New York: Crane, 1974, Vols 1, 2.
- 37b. LJ Andrews, RM Keefer. *Molecular Complexes in Organic Chemistry*. San Francisco: Holden-Day, 1964.
38. C Reichardt. *Solvent Effects in Organic Chemistry*. Weinheim: Verlag Chemie, 1979.
- 39a. KMC Davis. In: R Foster, ed. *Molecular Association*. London: Academic Press, 1975, Vol 1, p. 151 ff.
- 39b. R Foster. *Organic Charge Transfer Complexes*. London: Academic, 1969, p 62 ff.
40. KB Yoon, JK Kochi. *J Am Chem Soc* 110:6586–6588, 1988.
41. JA Rabo, CL Angell, PH Kasai, V Schomaker. *Discuss Faraday Soc* 41:328–349, 1966.
- 42a. DW Breck. *Zeolite Molecular Sieves*. New York: Wiley, 1974.
- 42b. RM Barrer. *Hydrothermal Chemistry of Zeolites*. London: Academic Press, 1982.
- 42c. NY Chen, WE Garwood, FG Dwyer. *Shape Selective Catalysis in Industrial Applications*. New York: Marcel Dekker, 1989.
43. KB Yoon, YS Park. *J Chem Soc Chem Commun*:552–523, 1993.
- 44a. J Greenberg, BR Sundheim. *J Chem Phys* 29:1029–1032, 1958.
- 44b. M Smith, MCR Symons. *J Chem Phys* 25:1074–1075, 1956.
- 44c. HY Chen, WS Sheu. *J Am Chem Soc* 122:7534–7542, 2000.
- 44d. WS Sheu, PJ Rosky. *J Am Chem Soc* 115:7729–7735, 1993.
- 44e. MJ Blandamer, MF Fox. *Chem Rev* 70:59–93, 1970.
45. EJ Lee, YS Park, KB Yoon. *Chem Commun* 1882–1883, 2001.
46. V Ramamurthy, DR Corbin, DF Eaton. *J Org Chem* 55:5269–5278, 1990.
47. S Hashimoto. *Tetrahedron* 56:6957–6963, 2000.
48. C Kirschhock, H Fuess. *Micropor Mater* 8:19–28, 1997.
49. IK Lednev, N Mathivanan, LJ Johnston. *J Phys Chem* 98:11444–11451, 1994.
- 50a. S Hashimoto, S Ikuta, T Asahi, H Masuhara. *Langmuir* 14:4284–4291, 1998.
- 50b. V Ramamurthy. *Mol. Cryst. Liq. Cryst.* New York: Gordon and Breach, Vol 240 1994, pp 53–71.
- 50c. V Ramamurthy. *J Am Chem Soc* 116:1345–1351, 1994.
- 51a. SL Suib, A Kostapapas. *J Am Chem Soc* 106:7705–7710, 1984.
- 51b. X Liu, KK Iu, JK Thomas. *J Phys Chem* 93:4120–4128, 1989.
- 51c. V Ramamurthy, DR Sanderson, DF Eaton. *J Phys Chem* 97:13380–13386, 1993.
- 52a. H Miyasaka, S Ojima, N Mataga. *J Phys Chem* 93:3380–3382, 1989.
- 52b. S Ojima, H Miyasaka, N Mataga. *J Phys Chem* 94:4147–4152, 1990.

- 53a. JM Masnovi, JK Kochi, EF Hilinski, PM Rentzepis. *J Am Chem Soc* 108:1126–1135, 1986.
- 53b. S Sankararaman, WA Haney, JK Kochi. *J Am Chem Soc* 109:7824–7838, 1987.
- 53c. S Sankararaman, JK Kochi. *J Chem Soc Perkin Trans 2*:165–174, 1991.
- 54a. H Sun, F Blatter, H Frei. *Catal Lett* 44:247–253, 1997.
- 54b. F Blatter, H Sun, H Frei. *Chem Eur J* 2:385–389, 1996.
- 54c. H Sun, F Blatter, H Frei. In: BK Warren, ST Oyama, ed. *Selective Photooxidation of Small Hydrocarbons by O<sub>2</sub> with Visible Light in Zeolites: Ch 31. ACS Symposium Series 638*, 1996.
- 54d. F Blatter, H Sun, S Vasenkov, H Frei. *Catal Today* 41:297–309, 1998.
- 54e. H Frei, F Blatter, H Sun. *Chemtech* 26:24–30, 1996.
55. H Sun, F Blatter, H Frei. *J Am Chem Soc* 118:6873–6879, 1996.
- 56a. H Sun, F Blatter, H Frei. *J Am Chem Soc* 116:7951–7952, 1994.
- 56b. AG Panov, RG Larsen, NI Totah, SC Larsen, VH Grassian. *J Phys Chem B* 104:5706–5714, 2000.
- 57a. KB Myli, SC Larsen, VH Grassian. *Catal Lett* 48:199–202, 1997.
- 57b. Y Xiang, SC Larsen, VH Grassian. *J Am Chem Soc* 121:5063–5072, 1999.
- 57c. F Blatter, H Sun, H Frei. *Catal Lett* 35:1–12, 1995.
- 58a. S Vasenkov, H Frei. *J Phys Chem B* 102:8177–8182, 1998.
- 58b. S Vasenkov, H Frei. *J Phys Chem B* 101:4539–4543, 1997.
- 58c. F Blatter, F Moreau, H Frei. *J Phys Chem* 98:13403–13407, 1994.
- 58d. F Blatter, H Frei. *J Am Chem Soc* 115:7501–7502, 1993.
- 58e. F Blatter, H Frei. *J Am Chem Soc* 116:1812–1820, 1994.
59. H Takeya, Y Kuriyama, M Kojima. *Tetrahedron Lett* 39:5967–5970, 1998.
60. P Lakshminarasimhan, KJ Thomas, LJ Johnston, V Ramamurthy. *Langmuir* 16:9360–9367, 2000.
- 61a. H Tsubomura, RS Mulliken. *J Am Chem Soc* 82:5966–5974, 1960.
- 61b. K Onodera, GI Furusawa, M Kojima, M Tsuchiya, S Aihara, R Akaba, H Sakuragi, K Tokumaru. *Tetrahedron* 41:2215–2220, 1985.
62. M Itoh, RS Mulliken. *J Phys Chem* 73:4332–4334, 1969.
63. AJ Rest, K Salisbury, JR Sodeau. *J Chem Soc Faraday Trans* 52:265–273, 1977.
- 64a. S Hashimoto, H Akimoto. *J Phys Chem* 90:529–532, 1986.
- 64b. S Hashimoto, H Akimoto. *J Phys Chem* 91:1347–1354, 1987.
- 64c. S Hashimoto, H Akimoto. *J Phys Chem* 93:571–577, 1989.
- 65a. EC Lim, VL Kowalski. *J Chem Phys* 36:1729–1732, 1962.
- 65b. JB Birks, E Pantos, TDS Hamilton. *Chem Phys Lett* 20:544–546, 1973.
66. R Foster. *Organic Charge Transfer Complexes*. London: Academic Press, 1969, p 66 ff.
67. R Foster. *Organic Charge Transfer Complexes*. London: Academic Press, 1969, p 64 ff.
- 68a. YY Huang, JE Benson, M Boudart. *Ind Eng Chem Fund* 8:346–353, 1969.
- 68b. E Dempsy. In *Molecular Sieves; Society of Chemical Industry*. London, 1968, pp 293–305.
- 68c. MA Spackman, HP Weber. *J Phys Chem* 92:794–796, 1988.
69. H Sugihara, K Shimokoshi, I Yasumori. *J Phys Chem* 81:669–673, 1977.
70. SB Liu, BM Fung, TC Yang, EC Hong, CT Chang, PC Shih, FH Tong, TL Chen. *J Phys Chem* 98:4393–4401, 1994.
- 71a. KK Iu, JK Thomas. *J Phys Chem* 95:506–509, 1991.
- 71b. JK Thomas. *Chem Rev* 93:301–320, 1993.
72. F Wilkinson, DR Worrall, SL Williams. *J Phys Chem* 99:6689–6696, 1995.
73. S Hashimoto, T Mutoh, H Fukumura, H Masuhara. *J Chem Soc Faraday Trans* 92:3653–3660, 1996.
74. F Gessner, JC Scaiano. *J Photochem Photobiol A Chem* 67:91–100, 1992.
75. FL Cozens, R Bogdanova, M Régimbald, H García, V Martí, JC Scaiano. *J Phys Chem B* 101:6921–6928, 1997.
76. LJ Johnston, NP Schepp. *J Am Chem Soc* 115:6564–6571, 1993.

77. L Brancalèon, D Brousmiche, VJ Rao, LJ Johnston, V Ramamurthy. *J Am Chem Soc* 120:4926–4933, 1998.
- 78a. KT Ranjit, L Kevan. *J Phys Chem B* 105:118–122, 2001.
- 78b. S Sinlapadech, RM Krishna, Z Luan, L Kevan. *J Phys Chem B* 105:4350–4355, 2001.
- 78c. KT Ranjit, Z Chang, RM Krishna, AM Prakash, L Kevan. *J Phys Chem B* 104:7981–7986, 2000.
79. JY Bae, KT Ranjit, Z Luan, RM Krishna, L Kevan. *J Phys Chem B* 104:9661–9669, 2000.
- 80a. Z Luan, JY Bae, L Kevan. *Chem Mater* 12:3202–3207, 2000.
- 80b. Z Chang, R Koodali, RM Krishna, L Kevan. *J Phys Chem B* 104:5579–5585, 2000.
81. Y Kim, JR Choi, M Yoon. *J Phys Chem B* 105:8513–8518, 2001.
82. S Hashimoto, N Fukazawa, H Fukumura, H Masuhara. *Chem Phys Lett* 219:445–451, 1994.
83. H Yao, T Okada, N Mataga. *J Phys Chem* 93:7388–7394, 1989.
84. S Hashimoto. *Chem Phys Lett* 252:236–242, 1996.
85. X Li, V Ramamurthy. *Tetrahedron Lett* 37:5235–5238, 1996.
- 86a. G Calzaferri, N Gfeller. *J Phys Chem* 96:3428–3435, 1992.
- 86b. D Wohrle, G Schulz-Ekloff. *Adv Mater* 6:875, 1994.
- 87a. GN Lewis, J Bigeleisen. *J Am Chem Soc* 65:520–526, 1943.
- 87b. E Rabinowitch, LF Epstein. *J Am Chem Soc* 63:69–78, 1941.
- 87c. WG Herkstroeter, PA Martic, S Farid. *J Am Chem Soc* 112:3583–3589, 1990.
- 87d. SJ Isak, EM Eyring. *J Phys Chem* 96:1738–1742, 1992.
88. A Corma, V Fornes, H Garcia, MA Miranda, J Primo, MJ Sabater. *J Am Chem Soc* 116:2276–2280, 1994.
89. W Adam, A Corma, MA Miranda, MJ Sabater-Picot, C Sahin. *J Am Chem Soc* 118:2380–2386, 1996.
90. V Fornés, H García, MA Miranda, F Mojarrad, MJ Sabater, NNE Suliman. *Tetrahedron* 52:7755–7760, 1996.
91. A Corma, V Fornés, H García, MA Miranda, MJ Sabater. *J Am Chem Soc* 116:9767–9768, 1994.
92. A Sanjuán, M Alvaro, G Aguirre, H García, JC Scaiano. *J Am Chem Soc* 120:7351–7352, 1998.
93. A Sanjuán, G Aguirre, M Alvaro, H García. *Appl Catal* 15:247–257, 1998.
94. AW Sendelbach. *J Org Chem* 58:5310–5315, 1993.
95. ML Cano, A Corma, V Fornés, H García, MA Miranda, C Baerlocher, C Lengauer. *J Am Chem Soc* 118:11006–11013, 1996.
- 96a. W DeWilde, G Peeters, JH Lunsford. *J Phys Chem* 84:2306–2310, 1980.
- 96b. WH Quayle, G Peeters, GLD Roy, EF Vansant, JH Lunsford. *Inorg Chem* 21:2226–2231, 1982.
- 96c. WH Quayle, JH Lunsford. *Inorg Chem* 21:97–103, 1982.
- 97a. PK Dutta, JA Incavo. *J Phys Chem* 91:4443–4446, 1987.
- 97b. W Turbeville, DS Robins, PK Dutta. *J Phys Chem* 96:5024–5029, 1992.
98. M Sykora, JR Kincaid, PK Dutta, NB Castagnola. *J Phys Chem B* 103:309–320, 1999.
99. P Lainé, M Lanz, G Calzaferri. *Inorg Chem* 35:3514–3518, 1996.
100. JJ Verdonck, RA Schoonheydt, PA Jacobs. *J Phys Chem* 85:2393–2398, 1981.
101. SH Bossmann, C Turro, C Schnabel, MR Pokhrel, LM Payawan, B Baumeister, M Worner. *J Phys Chem B* 105:5374–5382, 2001.
102. JA Incavo, PK Dutta. *J Phys Chem* 94:3075–3081, 1990.
103. NB Castagnola, PK Dutta. *J Phys Chem B* 105:1537–1542, 2001.
104. NB Castagnola, PK Dutta. *J Phys Chem B* 102:1696–1702, 1998.
105. AA Bhuiyan, JR Kincaid. *Inorg Chem* 38:4759–4764, 1999.
106. K Maruszewski, DP Strommen, K Handrich, JR Kincaid. *Inorg Chem* 30:4579–4582, 1991.
107. AA Bhuiyan, JR Kincaid. *Inorg Chem* 40:4464–4471, 2001.
108. K Maruszewski, DP Strommen, JR Kincaid. *J Am Chem Soc* 115:8345–8350, 1993.

109. M Sykora, K Maruszewski, SM Treffert-Ziemelis, JR Kincaid. *J Am Chem Soc* 120:3490–3498, 1998.
110. K Maruszewski, JR Kincaid. *Inorg Chem* 34:2002–2006, 1995.
111. WS Szulbinski, JR Kincaid. *Inorg Chem* 37:859–864, 1998.
112. M Sykora, JR Kincaid. *Nature* 387:162–164, 1997.
- 113a. F Barigelletti, P Belser, AV Zelewsky, A Juris, V Balzani. *J Phys Chem* 89:3680–3684, 1985.
- 113b. RS Lumpkin, TJ Meyer. *J Phys Chem* 90:5307–5312, 1986.
114. MA Coutant, TLN Castagnola, PK Dutta. *J Phys Chem B* 104:10783–10788, 2000.
115. PK Dutta, W Turbeville. *J Phys Chem* 96:9410–9416, 1992.
116. M Vitale, NB Castagnola, NJ Ortins, JA Brooke, A Vaidyalngam, PK Dutta. *J Phys Chem B* 103:2408–2416, 1999.
117. CRC Handbook of Chemistry and Physics, 55th ed. Orlando: CRC Press, 1994, p F-60.
118. KB Yoon, YS Park, JK Kochi. *J Am Chem Soc* 118:12710–12718, 1996.
- 119a. DR Rolison, CA Bessel. *Acc Chem Res* 33:737–744, 2000.
- 119b. DR Rolison. *Chem Rev* 90:867–878, 1990.
- 119c. DR Rolison. In: JC Jansen, M Stöcker, HG Karge, J Weitkamp, ed. *Studies in Surface Science and Catalysis*, Vol 85, *Advanced Zeolite Science and Applications*. New York: Elsevier Science, pp 543–586.
- 119d. C Senaratne, J Zhang, MD Baker, CA Bessel, DR Rolison. *J Phys Chem* 100:5849–5862, 1996.
- 120a. G Calzaferri, M Lanz, JW Li. *J Chem Soc Chem Commun*: 1313–1314, 1995.
- 120b. JW Li, K Pfanner, G Calzaferri. *J Phys Chem* 99:2119–2126, 1995.
- 120c. JW Li, G Calzaferri. *J Electroanal Chem* 377:163–175, 1994.
- 120d. JW Li, G Calzaferri. *J Chem Soc Chem Commun*: 1430–1432, 1993.
- 120e. A Walcarius, L Lamberts, EG Derouane. *Electrochim Acta* 38:2257–2266, 1993.
121. LR Faulkner, SL Suib, CL Renschler, JM Green, PR Bross. In: RG Wymer, OL Keller, eds. *Chemistry in Energy Production*. Washington, DC: ACS Symposium Series, 1982, p 99 ff.
122. PK Dutta, M Borja. *J Chem Soc Chem Commun*: 1568–1569, 1993.
123. WS Szulbinski. *Inorg Chem Acta* 269:253–259, 1998.
- 124a. PP Edwards, PA Anderson, JM Thomas. *Acc Chem Res* 29:23–29, 1996.
- 124b. PP Edwards, LJ Woodall, PA Anderson, AR Armstrong, M Slaski. *Chem Soc Rev* 22:305–312, 1993.
125. PH Kasai. *J Chem Phys* 43:3322–3327, 1965.
126. JA Rabo, CL Angell, PH Kasai, V Schomaker. *Disc Faraday Soc* 41:328–349, 1966.
127. RM Barrer, JF Cole. *J Phys Chem Solids* 29:1755–1758, 1968.
128. AR Armstrong, PA Anderson, LJ Woodall, PP Edwards. *J Am Chem Soc* 117:9087–9088, 1995.
129. Y Kim, YW Han, K Seff. *J Phys Chem* 97:12663–12664, 1993.
130. AR Armstrong, PA Anderson, LJ Woodall, PP Edwards. *J Phys Chem* 98:9279–9284, 1994.
- 131a. T Sun, K Seff, NH Heo, VP Petranovskii. *Science* 259:495–497, 1993.
- 131b. NH Heo, K Seff. *J Chem Soc Chem Commun*:1225–1226, 1987.
- 131c. NH Heo, K Seff. In: WH Flank, TE Whyte, eds. *Perspectives in Molecular Sieve Science: Ch 11*. ACS Symposium Series 368, 1988, pp 177–191.
132. T Sun, K Seff. *J Phys Chem* 98:10156–10159, 1994.
133. T Sun, K Seff. *J Phys Chem* 97:10756–10760, 1993.
134. X Liu, JK Thomas. *Chem Phys Lett* 192:555–559, 1992.
135. X Liu, JK Thomas. *Langmuir* 8:1750–1756, 1992.
136. X Liu, KK Iu, JK Thomas. *J Phys Chem* 98:13720–13728, 1994.
137. KK Iu, X Liu, JK Thomas. *J Phys Chem* 97:8165–8170, 1993.
138. X Liu, G Zhang, JK Thomas. *J Phys Chem* 99:10024–10034, 1995.
139. X Liu, KK Iu, JK Thomas. *Chem Phys Lett* 224:31–37, 1994.
140. X Liu, JK Thomas. *J Chem Soc Faraday Trans* 91:759–765, 1995.
141. S Takatani, H Fukumura, H Masuhara, S Hashimoto. *J Phys Chem B* 101:3365–3369, 1997.

142. YS Park, SY Um, KB Yoon. *Chem Phys Lett* 252:379–383, 1996.
143. KK Iu, JK Thomas. *Colloids Surf* 63:39–48, 1992.
144. PH Kasai, RJ Bishop. *J Phys Chem* 77:2308–2312, 1973.
- 145a. PH Kasai, RJ Bishop. In: JA Rabo, ed. *Zeolite Chemistry and Catalysis*. ACS Monograph Vol 171, 1976, p 350.
- 145b. B Xu, L Kevan. *J Phys Chem* 96:2642–2645, 1992.
- 145c. B Xu, L Kevan. *J Phys Chem* 96:3647–3652, 1992.
146. PP Edwards, MR Harrison, J Klinowski, S Ramdas, JM Thomas, DC Johnson, CJ Page. *J Chem Soc Chem Commun*:982–984, 1984.
147. MR Harrison, PP Edwards, J Klinowski, DC Johnson, CJ Page. *J Solid State Chem* 54:330–341, 1984.
148. PA Anderson, RJ Singer, PP Edwards. *J Chem Soc Chem Commun*:914–915, 1991.
149. PA Anderson, PP Edwards. *J Chem Soc Chem Commun*:915–917, 1991.
150. U Westphal, G Geismar. *Anorg Allg Chem* 508:165–175, 1984.
151. JBAF Smeulders, MA Hefni, AAK Klaassen, E de Boer, U Westphal, G Geismar. *Zeolites* 7:347–352, 1987.
152. VI Srdanov, K Haug, H Metiu, GD Stucky. *J Phys Chem* 96:9039–9043, 1992.
153. REH Breuer, E de Boer, G Geismar. *Zeolites* 9:336–340, 1989.
154. B Xu, L Kevan. *J Chem Soc Faraday Trans* 87:2843–2847, 1991.
155. B Xu, X Chen, L Kevan. *J Chem Soc Faraday Trans* 87:3157–3161, 1991.
156. LRM Martens, PJ Grobet, PA Jacobs. *Nature* 315:568–570, 1985.
157. LRM Martens, PJ Grobet, WJM Vermeiren, PA Jacobs, *Proc. 7th Int. Zeolite Conf.* 935–941, 1986.
158. LRM Martens, WJM Vermeiren, PJ Grobet, PA Jacobs. *Stud Surf Sci Catal* 31:531–542, 1987.
159. YS Park, YS Lee, KB Yoon. *J Am Chem Soc* 115:12220–12221, 1993.
- 160a. PA Anderson, D Barr, PP Edwards. *Angew Chem Int Ed Engl* 30:1501–1502, 1991.
- 160b. GD Stucky, L Iton, T Morrison, G Shenoy, S Suib, RP Zerger. *J Mol Catal* 27:71–80, 1984.
161. KB Yoon, JK Kochi. *J Chem Soc Chem Commun*:510–511, 1988.
162. CP Ursenbach, PA Madden, I Stich, MC Payne. *J Phys Chem* 99:6697–6714, 1995.
163. JC Thompson. *Electrons in Liquid Ammonia*. New York: Oxford University Press, 1976.
- 164a. X Liu, G Zhang, JK Thomas. *J Phys Chem B* 101:2182–2194, 1997.
- 164b. G Zhang, X Liu, JK Thomas. *Radiat Phys Chem* 51:135–152, 1998.
- 164c. X Liu, Y Mao, SA Ruetten, JK Thomas. *Solar Energy Mater Solar Cells* 38:199–219, 1995.
165. PA Anderson, PP Edwards. *J Am Chem Soc* 114:10608–10618, 1992.
166. H Nakayama, DD Klug, CI Ratcliffe, JA Ripmeester. *J Am Chem Soc* 116:9777–9778, 1994.
167. AR Armstrong. *J Solid State Chem* 111:178–189, 1994.
- 168a. T Kodaira, Y Nozue, S Ohwashi, T Goto, O Terasaki. *Phys Rev B* 48:12245–12252, 1993.
- 168b. T Kodaira, Y Nozue, T Goto. *Mol Cryst Liq Cryst* 218:55–60, 1992.
- 168c. Y Nozue, T Kodaira, S Ohwashi, T Goto, O Terasaki. *Phys Rev B* 48:12253–12261, 1993.
169. MW Simon, JC Edwards, SL Suib. *J Phys Chem* 99:4698–4709, 1995.
- 170a. WJ Mortier, RA Schoonheydt. *Porg Solid St Chem* 16:1–125, 1985.
- 170b. WJ Mortier. *J Catal* 55:138–145, 1978.
- 170c. WJ Mortier, SK Ghosh, S Shankar. *J Am Chem Soc* 108:4315–4320, 1986.
- 170d. KA Van Genechten, WJ Mortier. *Zeolites* 8:273–283, 1988.
- 170e. L Uytterhoeven, D Dompas, WJ Mortier. *J Chem Soc Faraday Trans* 88:2753–2760, 1992.
- 170f. R Heidler, GOA Janssens, WJ Mortier, RA Schoonheydt. *J Phys Chem* 100:19728–19734, 1996.
- 171a. PJ O'malley, J Dwyer. *Chem Phys Lett* 143:97–100, 1988.
- 171b. EG Derouane, JG Fripat. *J Phys Chem* 91:145–148, 1987.
- 172a. D Barthomeuf In: J Fraissard, L Petrakis, ed. *Acidity and Basicity of Solids: Basicity in Zeolites*. Dordrecht: Kluwer Academic, NATO ASI Series C Vol 444, 1994, pp 181–197.
- 172b. H Hattori. *Chem Rev* 95:537–558, 1995.

- 173a. AD Mallmann, D Barthomeuf. *J Phys Chem* 93:5636–5637, 1989.
- 173b. S Dzwigaj, AD Mallmann, D Barthomeuf. *J Chem Soc Faraday Trans* 86:431–435, 1990.
- 173c. D Barthomeuf, BH Ha. *J Chem Soc Faraday Trans* 69:2158–2165, 1973.
- 173d. AD Mallmann, D Barthomeuf. *Zeolites* 8:292–301, 1988.
- 174a. D Barthomeuf. *J Phys Chem* 88:42–45, 1984.
- 174b. C Mirodatos, AA Kais, JC Vedrine, P Pichat, D Barthomeuf. *J Phys Chem* 80:2366–2370, 1976.
- 174c. D Murphy, P Massiani, R Franck, D Barthomeuf. *J Phys Chem* 100:6731–6738, 1996.
- 174d. C Mirodatos, P Pichat, D Barthomeuf. *J Phys Chem* 80:1335–1342, 1976.
- 175a. M Huang, S Kaliaguine. *J Chem Soc Faraday Trans* 88:751–758, 1992.
- 175b. M Huang, A Adnot, S Kaliaguine. *J Am Chem Soc* 114:10005–10010, 1992.
- 176a. TL Barr, MA Lishka. *J Am Chem Soc* 108:3178–3186, 1986.
- 176b. TL Barr, LM Chen, M Mohsenian, MA Lishka. *J Am Chem Soc* 110:7962–7975, 1988.
- 176c. TL Barr. *Zeolites* 10:760–765, 1990.
- 176d. Y Okamoto, M Ogawa, A Maezawa, T Imanaka. *J Catal* 112:427–436, 1988.
- 176e. VK Kaushik, SGT Bhat, DR Corbin. *Zeolites* 13:671–677, 1993.
177. KT No, H Chon, T Ree, MS Jhon. *J Phys Chem* 85:2065–2070, 1981.
178. R Rathore, SV Lindeman, JK Kochi. *J Am Chem Soc* 119:9393–9404, 1997.
179. PA Jacobs, WJ Mortier, JB Uytterhoeven. *J Inorg Nucl Chem* 40:1919–1923, 1978.
180. M Alvaro, GA Facey, H García, S García, JC Scaiano. *J Phys Chem* 100:18173–18176, 1996.
- 181a. A Nakahara, JH Wang. *J Phys Chem* 67:496–500, 1963.
- 181b. R Haque, WR Coshov, LF Johnson. *J Am Chem Soc* 91:3822–3827, 1969.
- 181c. AJ Macfarlane, RJP Williams. *J Chem Soc (A)*:1517–1520, 1969.
- 182a. HJD Mcmanus, C Finel, L Kevan. *Radiat Phys Chem* 45:761–xxx, 1995.
- 182b. YS Park, K Lee, C Lee, KB Yoon. *Langmuir* 16:4470–4477, 2000.
183. EK Kim, JK Kochi. *J Am Chem Soc* 113:4962–4974, 1991.
184. DW Breck, ed. *Zeolite Molecular Sieves: Ch 7, Ion Exchange Reactions in Zeolites*. New York: John Wiley and Sons, 1974, pp 529–592.
- 185a. J Kleinberg, AW Davidson. *Chem Rev* 42:601–609, 1948.
- 185b. EM Voigt. *J Phys Chem* 72:3300–3305, 1968.
- 186a. HA Benesi, JH Hildebrand. *J Am Chem Soc.* 71:2703–2707, 1949.
- 186b. JH Hildebrand. *Science* 150:441–450, 1965. (c) J Walkley, DN Glew, JH Hildebrand. *J Chem Phys* 33:621–623, 1960.
187. SH Hastings, JL Franklin, JC Schiller, FA Matsen. *J Am Chem Soc* 75:2900–2905, 1953.
- 188a. S Nagakura. *J Am Chem Soc* 80:520–524, 1958. 188b. RS Drago. *Physical Methods for Chemists*, 2nd ed. Ft Worth: Saunders College Publishing, 1992, pp 133–137.
- 189a. K. Seff, DP Shoemaker. *Acta Crystallogr.* 22:162, 1967.
- 189b. RM Barrer, S Wasilewski. *Trans Faraday Soc* 57:1140–1163, 1961.
190. N Mataga, Y Murata. *J Am Chem Soc* 91:3144–, 1969.
191. A Zweig, JE Lehnsen, WG Hodgson, WH Jura. *J Am Chem Soc* 85:3937–, 1963.
- 192a. SM Hubig, JK Kochi. *J Phys Chem* 99:17578–, 1995.
- 192b. S Iwata, J Tanaka, S Nagakura. *J Am Chem Soc* 89:2813–, 1967.
193. IR Gould, D Noukakis, L Gomez-Jahn, RH Young, JL Goodman, S Farid. *Chem Phys* 176:439–456, 1993.
- 194a. D Rehm, A Weller. *Isr J Chem* 8:259–, 1970.
- 194b. GJ Kavarnos, NJ Turro. *Chem Rev* 86:401–449, 1986.
195. *CRC Handbook of Chemistry and Physics*, 70th ed. Boca Raton: CRC Press, p D-160.
- 196a. DW Werst, AD Trifunac. *Acc Chem Res* 31:651–657, 1998.
- 196b. DW Werst, P Han, SC Choure, EI Vinokur, L Xu, AD Trifunac, LA Eriksson. *J Phys Chem B* 103:9219–9230, 1999.
- 196c. DW Werst, P Han, AD Trifunac. *Chem Phys Lett* 269:333–340, 1997.
- 196d. EA Picos, DW Werst, AD Trifunac, LA Eriksson. *J Phys Chem* 100:8408–8417, 1996.
- 196e. DW Werst, EE Tartakovsky, EA Picos, AD Trifunac. *J Phys Chem* 98:10249–10257, 1994.

- 196f. DW Werst, EA Picos, EE Tartakovsky, AD Trifunac. *Chem Phys Lett* 229:421–428, 1994.
- 197a. MV Barnabas, AD Trifunac. *Chem Phys Lett* 187:565–570, 1991.
- 197b. MV Barnabas, AD Trifunac. *Chem Phys Lett* 193:298–304, 1992.
- 197c. MV Barnabas, DW Werst, AD Trifunac. *Chem Phys Lett* 204:435–439, 1993.
- 197d. MV Barnabas, DW Werst, AD Trifunac. *Chem Phys Lett* 206:21–24, 1993.
198. YH Kim, TE Mallouk. *J Phys Chem* 96:2879–2885, 1992.
199. PK Ghosh, AJ Bard. *J Phys Chem* 88:5519–5526, 1984.
200. JL Colón, CY Yang, A Clearfield, CR Martin. *J Phys Chem* 94:874–882, 1990.
201. K Kalyanasundaram, J Kiwi, M Grätzel. *Helv Chem Acta* 61:2720–2730, 1978.
202. K Kalyanasundaram. *Coord Chem Rev* 46:159–244, 1982.
203. CR Bock, TJ Meyer, DG Whitten. *J Am Chem Soc* 96:4710–, 1974.
204. JS Krueger, JE Mayer, TE Mallouk. *J Am Chem Soc* 110:8232–8234, 1988.
205. EH Yonemoto, YI Kim, RH Schmehl, JO Wallin, BA Shoulders, BR Richardson, JF Haw, TE Mallouk. *J Am Chem Soc* 116:10557–10563, 1994.
206. EH Yonemoto, GB Saupe, RH Schmehl, SM Hubig, RL Riley, BL Iverson, TE Mallouk. *J Am Chem Soc* 116:4786–, 1994.
207. Z Li, TE Mallouk. *J Phys Chem* 91:643–, 1987.
208. M Borja, PK Dutta. *Nature* 362:43–45, 1993.
209. L Kevan, B O'Reagan, A Kay, M Grätzel. *J Electroanal Chem*:291–297, 1993.
210. S Fukuzumi, T Urano, T Suenobu. *Chem Commun*:213–214, 1996.
211. JN Braddock, TJ Meyer. *J Am Chem Soc* 95:3158–3162, 1973.
212. AJ Bard, LR Faulkner. *Electrochemical Methods: Fundamentals and Applications*. New York: John Wiley & Sons, 1980, p 700.
213. M Ledney, PK Dutta. *J Am Chem Soc* 117:7687–7695, 1995.
214. SK Das, PK Dutta. *Langmuir* 14:5121–5126, 1998.
215. A Das, V Joshi, D Kotkar, VS Pathak, V Swayambunathan, PV Kamat, PK Ghosh. *J Phys Chem A* 105:6945–6954, 2001.
216. JM Lehn, JP Sauvage, R Ziessel. *Nouv J Chim* 4:81–, 1980.
217. A Harriman, MA West, ed. *Photogeneration of Hydrogen*. London: Academic Press, 1982.
218. C Creutz, N Sutin. *Proc Natl Acad Sci USA* 72:2858–, 1975.
219. PK Ghosh, BS Brunshwig, M Chou, C Creutz, N Sutin. *J Am Chem Soc* 106:4772–4783, 1984.
- 220a. V Ya Shafirovich, VV Strelets. *Nouv J Chim* 2:1999–, 1978.
- 220b. BS Brunshwig, M Chou, C Creutz, PK Ghosh, N Sutin. *J Am Chem Soc* 105:4832–, 1983.
221. YS Park, EJ Lee, YS Chun, YD Yoon, KB Yoon. *J Am Chem Soc* 124:7123–7135, 2002.
222. JAR Coope, CL Gardner, CA McDowell, AI Pelman. *Mol Phys* 21:1043–1055, 1971.
223. L Persaud, AJ Bard, A Campion, MA Fox, TE Mallouk, SE Webber, JM White. *J Am Chem Soc* 109:7309–7314, 1987.
224. YI Kim, SW Keller, JS Krueger, EH Yonemoto, GB Saupe, TE Mallouk. *J Phys Chem B* 101:2491–2500, 1997.
225. JJ Lee, Y Kim, M Yoon. *J Photosci* 8:27–32, 2001.
- 226a. Y Kim, M Yoon. *J Mol Catal A: Chem* 168:257–263, 2001.
- 226b. Y Kim, BI Lee, M Yoon. *Chem Phys Lett* 286:466–472, 1998.
- 227a. AJ Bard, MA Fox. *Acc Chem Res* 28:141–145, 1995.
- 227b. PA Jacobs, JB Uytterhoeven. *J Chem Soc Chem Commun* 128–129, 1977.